Physics of tidal disruption events around black holes

A thesis
submitted for the degree of

Doctor of Philosophy

in

The Department of Physics,
Pondicherry University,
Puducherry - 605 014, India

by

T. Mageshwaran
Indian Institute of Astrophysics,
Bangalore - 560 034, India

November 2017

Physics of tidal disruption events around black holes

T. Mageshwaran
Indian Institute of Astrophysics

Indian Institute of Astrophysics
Bangalore - 560 034, India

Title of the thesis	:	**Physics of tidal disruption events around black holes**
Name of the author	:	**T. Mageshwaran**
Address	:	Indian Institute of Astrophysics II Block, Koramangala Bangalore - 560 034, India
Email	:	mageshwaran@iiap.res.in
Name of the supervisor	:	**Prof. Arun Mangalam**
Address	:	Indian Institute of Astrophysics II Block, Koramangala Bangalore - 560 034, India
Email	:	mangalam@iiap.res.in

Declaration of Authorship

I hereby declare that the matter contained in this thesis is the result of the investigations carried out by me at the Indian Institute of Astrophysics, Bangalore, under the supervision of Prof. Arun Mangalam. This work has not been submitted for the award of any other degree, diploma, associateship, fellowship, etc. of any other university or institute.

Signed: _____

Date: _____

Certificate

This is to certify that the thesis entitled **'Physics of tidal disruption events around black holes'** submitted to the Pondicherry University by Mr. T. Mageshwaran for the award of the degree of Doctor of Philosophy, is based on the results of the investigations carried out by him under my supervision and guidance, at the Indian Institute of Astrophysics. This thesis has not been submitted for the award of any other degree, diploma, associateship, fellowship, etc. of any other university or institute.

Signed: _____

Date: _____

List of Publications

Refereed Publications

1. *Stellar and gas dynamical model for tidal disruption events in a quiescent galaxy,*

   Mageshwaran T. & Mangalam A. 2015, ApJ 814

   Chapter 5

2. *Accretion and wind dynamics of tidal disruption events,*

   Mageshwaran T. & Mangalam A. 2017, New Frontiers in Black Hole Astrophysics, Proceedings of the International Astronomical Union, IAU Symposium, Volume 324, pp. 134-135. DOI: 10.1017/S1743921317002228

   Chapter 6

3. *Physics and observations of tidal disruption events,*

   Mangalam A. & **Mageshwaran T.** 2018, Bulletin de la Sociètè Royale des Sciences de Liège, in Proceedings of the First Belgo-Indian Network for Astronomy & Astrophysics (BINA) workshop, 87, 307-315

   Chapter 2 & 7

4. *Dynamics of accretion and wind in tidal disruption events,*

   Mageshwaran T. & Mangalam A. 2018, Submitted.

   Chapter 6 & 7

Under Preparation

5. *Black hole demographics from TDE modeling,*

   Mageshwaran T. & Mangalam A. 2018, in preparation.

   Chapter 7

Presentations

1. Poster presentation titled “Stellar, accretion and wind dynamics for TDE" in International Astronomical Union Symposium 324: New Frontiers in Black Hole Astrophysics held at Ljubljana, Slovenia from September 12-16, 2016.

2. Oral presentation titled “Transient jet activity induced by TDEs around Supermassive Black Holes" in Jet Triggering Mechanism in Black Hole Sources, TIFR Mumbai held on 20-24 January 2016.

3. Poster presentation titled “Accretion and wind dynamics of tidal disruption events" in 34th meeting of Astronomical Society of India at University of Kashmir, Srinagar held on 10-13 May 2016.

4. Poster presentation titled “Predictions of event rates for EMRIs" in 28th IAGRG meeting held at Raman Research Institute, Bangalore on March 18-20, 2015.

5. Oral presentation titled “TDEs and its observational implications in quiescent galaxy" in 33rd meeting of Astronomical Society of India at NCRA Pune held on February 17-20, 2015.

6. Poster presentation titled “Stellar disruption around SMBH and implications for observations" in 32nd meeting of Astronomical Society of India at IISER, Mohali held on March 20-24, 2014.

Acknowledgements

The completion of this doctoral dissertation was possible with the support of several people. I would like to express my sincere gratitude to all of them. First of all, I would like to thank Prof. Arun Mangalam, my supervisor, for his guidance, constant encouragement and unconditional support during my PhD. It was a pleasure to work with him.

I am thankful to IIA for providing me an excellent academic environment and the necessary facilities for my research work during my tenure.

I thank the staff of the Vainu Bappu Observatory, Kavalur (Indian Institute of Astrophysics), where some of the work was done, for the hospitality provided during my visits.

I would like to thank my doctoral committee members and the staff at the Pondicherry University for their timely help and relevant suggestions.

I also thank all my friends and fellow students at the IIA for their constant support and encouragement.

Lastly, I would like to thank my parents, my sister, my extended family and my teachers for being a continuous source of support for pursuing a research career.

Dedicated to

my

family, teachers and friends...

Abstract

A nearly self contained and detailed introduction to TDE physics with novel aspects and a summary of observations is provided.

We have constructed a dynamical model of tidal disruption events (TDEs) that includes physical parameters such as black hole (BH) mass $M_\bullet$, specific orbital energy E and angular momentum J, star mass $M_\star$ and radius $R_\star$, and the pericenter of the star orbit $r_p(E,\ J,\ M_\bullet)$. We have calculated the capture rate of stars $\dot{N}_t$, in the galactic center for a stellar density profile $\rho \propto r^{-\gamma}$ with an initial mass function given by Kroupa (2001), by solving the steady state Fokker-Planck equation and integrating over the $\{E,\ J\}$ phase space. Following the steady accretion model of Strubbe and Quataert (2009), we calculate the rise time, the peak bolometric luminosity in terms of these physical parameters and a typical light curve of TDEs which is then compared with the detectors sensitivity to obtain the duration of flare detection. For the standard ΛCDM model, black hole mass function of quiescent galaxies, we calculated the detection rate of TDEs by various surveys such as Large Synoptic Survey Telescope (LSST), Pan-STARRS 3π in optical bands and eROSITA in X-ray band and discuss the follow up of TDEs through observations in various spectral bands from X-rays to radio wavelengths. The crucial point is that the J plays an important role in the stellar dynamical process through $\dot{N}_t$ and the accretion process through pericenter $r_p(E,\ J)$ which impacts the detectable TDE rates; this has not been taken into account in previous calculations.

We have also constructed a self similar model of a time dependent accretion disk in both super and sub-Eddington phase with fallback from outer debris and a general viscosity prescription $\Pi_{r\phi} \propto \Sigma_d^b r^d$ where Σ_d is surface density, r is the radius and b and d are constants that depends on the nature of pressure in the disk. The specific choice of radiative and alpha viscosities and its parameters is decided by the expected

disk luminosity and evolution time scale being in the observed range. The outflow wind structure in super-Eddington phase is modeled analytically using vertical momentum equation. We have also constructed the transition dynamics of disk between the super-Eddington to sub-Eddington phases and modeled the evolutionary track of TDEs. We have fit our time dependent accretion models to the observations in X-ray, UV and optical bands and found that the time dependent model shows a good fit to the observations compared to steady accretion models.

We study the distribution of black hole mass and star mass in redshift obtained from time-dependent models fit described above to the observations and found that the TDEs are dominated by the disruption of low mass star by low mass super-massive black holes with black hole mass $M_\bullet \leq 2.1 \times 10^7\ M_\odot$. We also use the steady accretion model with time varying accretion rate of Mageshwaran & Mangalam (2015) to obtain the peak luminosity L_p with corresponding time t_p in the given spectral bands and assuming luminosity $L \propto t^{-5/3}$, obtained the flare's detection duration which is then compared with the detectors sensitivity to obtain the redshift limit of detection. Using the stellar dynamical model of theoretical capture rate given in Mageshwaran & Mangalam (2015), the Schechter black hole mass function with a duty cycle $\delta(z)$, and the detector survey parameters such as sensitivity f_l, cadence t_{cad} and integration time t_{int}, the expected detection rate was calculated which is then equated with the observed detected rates of TDEs by the previous and ongoing surveys to derive the Schechter parameters. We find that the discrepancy between theoretical and observational capture rates can be explained by the fact that the theoretical TDE rate statitistically galaxy averaged over the black hole mass function is close to the observed values of $\sim 2 \times 10^{-5}$/yr.

Contents

List of Figures

List of Tables

Chapter 1

Introduction

Image: NASA/JPL-Caltech

The black holes, even though invisible, have strong effects on their surroundings leading to various fascinating phenomena. Black holes are found in the universe at all scales from stellar mass black holes in X-ray binaries to supermassive black holes (SMBHs) in the galactic center. It is well known from observations that supermassive black holes (SMBHs) reside at the center of galactic nuclei (Kormendy and Richstone 1995; Kormendy and Ho 2001) and the most luminous active nuclei are called as quasars (quasi stellar objects). The quasars are the most powerful known sources of energy in the universe that converts the mechanical energy of the gas in the surrounding disk into radiation energy. These active quasars that are also called as active galactic nuclei (AGN) are observationally identified through high luminosity, strong emission lines in the spectra, variabilities, and jets (Tadhunter 2008; Padovani *et al.* 2017). The emission in various spectral bands are associated with various physical processes: the emission in X-ray is associated with the accretion disk and corona, ultraviolet (UV) and optical emission are due

to accretion disks, infrared emissions is due to obscuration from dust clouds and molecular disk, γ rays, and radio bands are associated with non-thermal emission of inverse Compton and synchrotron respectively. The observation of AGNs at all redshifts is used to obtain the luminosity function (Schechter 1976; Ueda *et al.* 2003) and study the evolution of black holes in the universe (Natarajan 2011; Shankar *et al.* 2013).

However, all galaxies are not active, there are galaxies whose central black hole has negligible or no surrounding disks and are called dead quasars or inactive galaxies (Esquej *et al.* 2008; Lin *et al.* 2015). The observations of AGNs are insufficient to study the black hole mass distribution as there are inactive galaxies which are comparable or higher in number to the active galaxies in the local universe (Soltan 1982; Shankar *et al.* 2013). The tidal disruption of stars provides the mass for accretion by the black hole leading to emission and thus is a promising phenomenon to observe the inactive nuclei.

A tidal disruption event depends on both the stellar dynamics of stars and the gas dynamics of the disrupted debris. A star orbiting around the black hole experiences gravitational encounters with other stars which results in the change in the energy and angular momentum of the star until it falls in so close to the black hole where the black hole's tidal gravity, $F_g = GM_\bullet R_\star / r_p^3$, exceeds the star's self-gravity, $F_s = GM_\star / R_\star^2$, leading to the tidal disruption of star. The strength of the encounter is given by

$$\eta_t = \left(\frac{F_s}{F_g}\right)^{\frac{1}{2}} = \left(\frac{r_p^3}{GM_\bullet R_\star}\frac{GM_\star}{R_\star^2}\right)^{\frac{1}{2}}, \tag{1.1}$$

and the star is tidally disrupted if $\eta_t \leq 1$ which results in

$$r_p \leq \eta_t^{2/3} \left(\frac{M_\bullet}{M_\star}\right)^{1/3} R_\star, \tag{1.2}$$

so that the tidal radius is given by

$$r_t = \eta_t^{2/3} \left(\frac{M_\bullet}{M_\star}\right)^{1/3} R_\star = 2.2 \times 10^{-6} \eta_t^{\frac{2}{3}} \left(\frac{M_\bullet}{10^6 M_\odot}\right)^{\frac{1}{3}} \left(\frac{M_\star}{M_\odot}\right)^{-\frac{1}{3}} \left(\frac{R_\star}{R_\odot}\right) \text{ pc}, \tag{1.3}$$

with η is typically taken to be unity. In terms of mean density $\bar{\rho}_\star = 3M_\star/(4\pi R_\star^3)$, the tidal radius is given by

$$\frac{r_t}{R_s} \simeq 109 \left(\frac{M_\bullet}{10^6 M_\odot}\right)^{-2/3} \left(\frac{\bar{\rho}_\star}{\rho_\odot}\right)^{-1/3}, \tag{1.4}$$

where $R_s = 2GM_\bullet/c^2$ is the Schwarzchild radius and $\rho_\odot = 1.41$ g cm^{-3} is the average density of sun. For a star to be tidally disrupted, $r_t > R_s$ which yields

$$\frac{\bar{\rho}_\star}{\rho_\odot} < 1.3 \times 10^6 \left(\frac{M_\bullet}{10^6 M_\odot}\right)^{-2}. \tag{1.5}$$

The compact objects such as white dwarf ($\bar{\rho}_\star \sim 10^6$ g cm^{-3}) can be tidally disrupted by low mass super-massive black holes whereas neutron star ($\bar{\rho}_\star \sim 10^{14}$ g cm^{-3}) and black holes ($\bar{\rho}_\star \sim 10^{15}$ g cm^{-3}) have high densities and are directly swallowed by the black hole.

The presence of tidal radius, results in a loss cone in the phase space, such that any star whose velocity vector lies within the cone has its pericenter less than the

tidal radius, leading to the capture of a star. Stars in the galactic center move in the combined potential field of the SMBH and other stars in the galactic center. A star with orbital energy E is tidally captured if the orbital angular momentum is $J \leq J_{lc} = \sqrt{2r_t^2(\Phi(r_t) - E)}$, where J_{lc} is the angular momentum of the loss cone (Frank and Rees 1976) and $\Phi(r)$ is the combined potential of the BH and other stars in the galactic center. The stellar interactions result in the diffusion of the stars into the loss cone. The stellar distribution function (DF) $f(E,\ J)$ obeys the Fokker–Planck (FP) equation (Bahcall and Wolf 1976; Lightman and Shapiro 1977) and the rate of feeding of stars into the loss cone gives the theoretical tidal disruption event (TDE) rate $\dot{N}_t$. The rate of TDE per galaxy depends on the stellar distribution in the galactic center, the SMBH mass $M_\bullet$ and the structure of galactic nuclei that could be axisymmetric, spherical, or triaxial nuclei (Merritt 2013a). Cohn and Kulsrud (1978) obtained the numerical solution to the FP equation for spherical nuclei by means of a detailed boundary layer analysis and applied it to globular clusters. Wang and Merritt (2004) solved the steady state FP equation for the 51 galaxies with the Nuker profile by assuming a single mass star distribution and obtained the $\dot{N}_t \sim 10^{-4} - 10^{-5}\ \mathrm{Yr}^{-1}$. They further predicted that $\dot{N}_t \propto M_\bullet^{-0.25}$ for the isothermal case (also see Merritt (2013b)). Stone and Metzger (2016) employed a stellar mass function, $\xi(m)$, in their DF, and applied it to a sample of 200 galaxies, and obtained $\dot{N}_t \propto M_\bullet^{-0.4}$. Magorrian and Tremaine (1999) solved the steady state FP equation for an axisymmetric nuclei with stars on centrophobic (avoiding the center) orbits and obtained $\dot{N}_t \sim 10^{-4} M_\bullet^{-0.19}\ \mathrm{Yr}^{-1}$.

The star tidally captured is disrupted and the debris following a Keplerian orbit returns to the pericenter (Rees 1988). We consider a star approaching the BH on a parabolic orbit with pericenter distance $R_p \leq R_t$. The star approaches the black hole in dynamical time $t_{dyn} = (R_p^3/(GM_\bullet))^{0.5}$ with a tidal acclera-tion $a = GM_\bullet R_\star/R_p^3$. Thus, the velocity change is given by $\Delta v = at_{dyn} = (GM_\bullet/R_p)^{0.5}(R_\star/R_p) = v_{orb}(R_\star/R_p)$. For $R_\star \ll R_p$, $\Delta E \sim v_{orb}\Delta v \sim GM_\bullet R_\star/R_p^2$ where ΔE is the change in energy of the star debris as shown in Fig 1.1. As a star

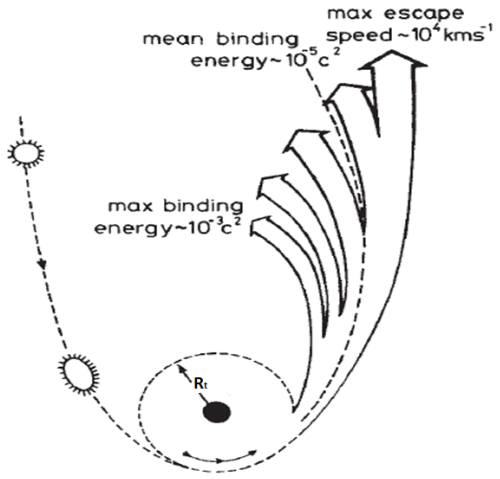

FIGURE 1.1: The disruption of a solar type star is shown for a parabolic orbit. Nearly half of the debris is bound to the black hole and remaining escapes. Courtesy: Rees 1988

comes close to the hole, the gravitational torque will spin up the star to a good fraction to its co-angular velocity so that by the time it gets disrupted, it spins close to its break up angular velocity (Li et.al 2002). To take into account this effect, the spin factor "k" is introduced which is given as (Rees 1988; Alexender & Kumar 2001).

$$k = \begin{cases} 1 & \text{non spin up (no change in angular velocity)} \\ 3 & \text{spin up to break up angular velocity,} \end{cases} \tag{1.6}$$

such that the energy is given by

$$\Delta E = -\frac{kGM_{\bullet}\Delta R}{R_p^2}, \tag{1.7}$$

and the maximum energy is the energy of most tightly bound debris given by

$$\Delta E_{max} = -\frac{kGM_\bullet R_\star}{R_p^2}. \tag{1.8}$$

As the bound material falls back to its pericenter, it loses its energy and angular momentum on time scales much shorter than t and thus accretes into the MBHs and give rise to a flare (Phinney 1989). The total accretion rate of the debris following Keplerian orbits at time t after disruption is given by

$$\frac{\mathrm{d}M}{\mathrm{d}t} = \frac{\mathrm{d}M}{\mathrm{d}\triangle E}\frac{\mathrm{d}\triangle E}{\mathrm{d}r_a}\frac{\mathrm{d}r_a}{\mathrm{d}t} = \frac{1}{3}(2\pi GM_\bullet)^{\frac{2}{3}}\frac{\mathrm{d}M}{\mathrm{d}\triangle E}t^{-\frac{5}{3}}. \tag{1.9}$$

The term $(\mathrm{d}M/\mathrm{d}\triangle E)$ is the energy distribution within the bound matter and depends on the internal structure of the star. The time after which the most tightly bound debris passes through its pericenter after disruption is given by

$$t_{min} = \frac{\pi}{\sqrt{2GM_\bullet}}\frac{R_p^3}{R_\star^{\frac{3}{2}}}k^{-\frac{3}{2}}. \tag{1.10}$$

A schematic representation of the disrupted star is shown in Fig 1.2. The energy spread is maximum for $\triangle R = R_\star$. If $\rho(R)$ is the spherically symmetric mass density of the star, then

$$\frac{dM}{d\triangle E} = \frac{dM}{d\triangle R}\frac{d\triangle R}{d\triangle E} \simeq \frac{dM}{d\triangle R}\frac{R_\star}{\triangle E_{max}} \;\; ; \;\; \frac{dM}{d\triangle R} = 2\pi\int_{\triangle R}^{R_\star}\rho(R)R\,dR \tag{1.11}$$

We then define $\varepsilon = -\triangle E/\triangle E_{max}$ as our dimensionless energy, $x = \triangle R/R_\star$ as our dimensionless pericenter distance and $m = M/M_\star$.

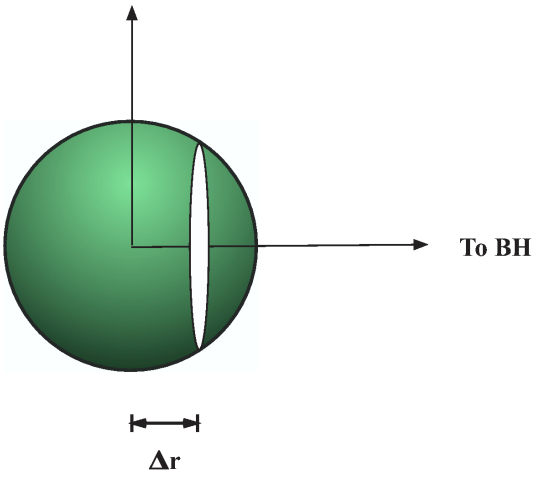

FIGURE 1.2: The schematic represntation of the star disrupted by the black hole. Courtesy: Lodato et al. 2009

The density profile $\rho(R)$ can be obtained from the Lane-Emden equation which is given by

$$\frac{1}{\chi^2}\frac{\mathrm{d}(\chi^2\frac{\mathrm{d}\theta}{\mathrm{d}\chi})}{\mathrm{d}\chi} = -\theta^n \tag{1.12}$$

so that $\rho(R) = \rho_c\theta^n$ where ρ_c is the central density of the star and radius $R = \alpha\chi$. In terms of dimensionless quantities,

$$\varepsilon = x = \tau^{-\frac{2}{3}} \;;\; \frac{\mathrm{d}m}{\mathrm{d}\varepsilon} = \frac{\mathrm{d}m}{\mathrm{d}x} = 2\pi b\int_x^1 \theta^n(x')x'\,\mathrm{d}x' \;;\; \frac{\mathrm{d}m}{\mathrm{d}\tau} = \frac{2}{3}\frac{\mathrm{d}m}{\mathrm{d}\varepsilon}\tau^{\frac{-5}{3}} \tag{1.13}$$

where $\tau = t/t_{min}$ and b is the ratio of central density to mean density. Then, the total mass accretion rate is given by $\dot{M} = (M_\star/t_{min})(\mathrm{d}m/\mathrm{d}\tau)$ and is shown in Fig 1.3 which follows $t^{-5/3}$ at late stages.

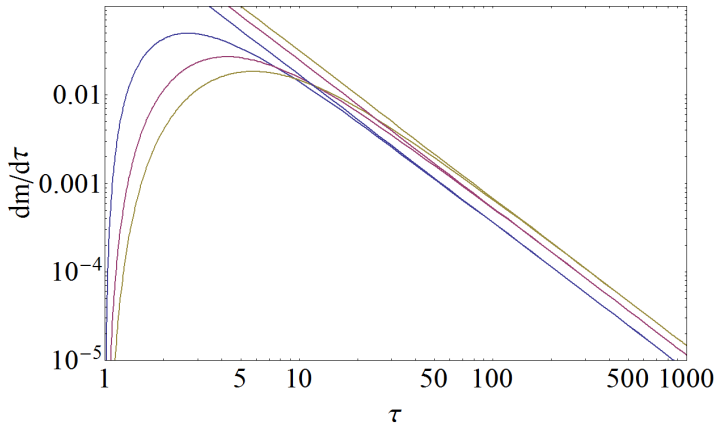

FIGURE 1.3: The evolution of dimensionless accretion rate for various values of $n = 3/2$ (blue), $5/2$ (red) and 3 (yellow). The late accretion rate follows $t^{-5/3}$.

Thus the peak accretion rate and time of peak accretion for a star disrupted at the tidal radius r_t, are given by

$$\dot{M}_p = 7.9 \times 10^{25} \text{ g sec}^{-1} \; k^{\frac{3}{2}} m^{0.8} M_6^{-\frac{1}{2}} \tag{1.14}$$

$$t_p = 38.55 \text{ days } k^{-\frac{3}{2}} m^{0.2} M_6^{\frac{1}{2}}. \tag{1.15}$$

Since the emission is dominated at inner radius r_{in}, the luminosity is given by

$$L = \frac{G M_\bullet \dot{M}}{r_{in}} \zeta, \tag{1.16}$$

and is a function of accretion rate. Assuming that the accretion rate follows the fall back rate, the peak luminosity is given by

$$L_p = 7.1 \times 10^{46} \text{ erg sec}^{-1} \; k^{\frac{3}{2}} \; m^{0.8} \; M_6^{-\frac{1}{2}} \; Z^{-1}(j), \tag{1.17}$$

where r_{in} is taken to be the ISCO given by $r_{ISCO} = R_s Z(j)/2$, with $R_s = 2GM_\bullet/c^2$ is the Schwarzschild radius, j is the black hole spin and $Z(j)$ is given by (Bardeen *et al.* 1972)

$$Z_1(j) = 1 + (1-j^2)^{\frac{1}{3}}\left[(1+j)^{\frac{1}{3}} + (1-j)^{\frac{1}{3}}\right] \tag{1.18a}$$

$$Z_2(j) = \sqrt{3j^2 + Z_1(j)^2} \tag{1.18b}$$

$$Z(j) = 3 + Z_2(j) - \sqrt{(3-Z_1(j))(3+Z_1(j)+2Z_2(j))}. \tag{1.18c}$$

Since the rise of bolometric luminosity is sharp, we assume the rise to be linear such that the total energy released during rising phase is given by

$$E_{\rm rise} = \frac{1}{2} L_p t_p = 1.67 \times 10^{53} \text{ erg } m \ Z^{-1}(j), \tag{1.19}$$

and the total energy released is given by

$$E_T = \zeta \int_{t_{min}}^{\infty} \frac{GM_\bullet \dot{M}}{r_{in}} \, \mathrm{d}t = \zeta \frac{GM_\bullet}{r_{in}} \frac{1}{3} \left(2\pi G M_\bullet\right)^{\frac{2}{3}} \int_{t_{min}}^{\infty} \frac{\mathrm{d}M}{\mathrm{d}\Delta E} t^{-5/3} \, \mathrm{d}t. \tag{1.20}$$

For a constant $\mathrm{d}M/\mathrm{d}\Delta E$ given by

$$\frac{\mathrm{d}M}{\mathrm{d}\Delta E} \simeq \frac{M_\star}{\Delta E} \simeq \frac{\eta^{2/3}}{k} \frac{1}{G} M_\star^{1/3} M_\bullet^{-1/3} R_\star, \tag{1.21}$$

and $t_{min} = \pi\sqrt{r_{in}^3/(2GM_\bullet)}$, the time period of inner orbit, eqn (1.20) gives

$$E_T = \frac{\eta^{2/3}}{k}\frac{GM_\bullet^{5/3}M_\star^{1/3}R_\star}{r_{in}^2}\zeta, \tag{1.22}$$

and employing the ISCO radius as the inner radius, we obtain

$$\begin{aligned} E_T &= \frac{\eta^{2/3}}{k}\frac{c^4}{G}M_\bullet^{-1/3}M_\star^{1/3}R_\star Z^{-2}(j)\zeta & (1.23)\\ &= 8.4\times10^{54}\ \text{erg}\ \left[\frac{\eta^{2/3}}{k}m^{1/3}M_6^{-1/3}\frac{R_\star}{R_\odot}Z^{-2}(j)\zeta\right]. & (1.24)\end{aligned}$$

For a Schwarzschild black hole, $j = 0$, which gives $Z(0) = 6$ and the ratio of energy released to star mass energy $M_\star c^2$ is given by

$$f_R = \begin{cases} \frac{E_R}{M_\star c^2} = 0.0155 & \text{rising phase} \\ \\ \frac{E_T}{M_\star c^2} = 0.129\frac{\eta^{2/3}}{k}m^{-2/3}M_6^{-1/3}\frac{R_\star}{R_\odot}\zeta & \text{total energy,} \end{cases} \tag{1.25}$$

implying that the energy in the falling phase (after the peak) is $E_F = E_T - E_R$.

The debris experience stream collision either due to incoming stream that intersects with the outflowing stream at the pericenter (Kochanek 1994) or due to relativistic precession at the pericenter (Hayasaki *et al.* 2013). These interactions result in circularization of the debris to form an accretion disk (Hayasaki *et al.* 2013; Shiokawa *et al.* 2015; Bonnerot *et al.* 2016). The hydrodynamical simulations by Ramirez-Ruiz and Rosswog (2009) have shown that the debris interactions result in the formation of an accretion disk with mass accretion rate showing deviation from Lodato *et al.* (2009) at early times and following $t^{-5/3}$ in the late stages. Very recently, Bonnerot *et al.* (2016) have performed hydrodynamical simulations

for a star on a highly elliptical orbit with the resulting debris undergoing apsidal precession; they found that the higher the eccentricity (and/or) the deeper the encounter, the faster is the circularization. For an efficient cooling, the debris forms a thin and narrow ring of gas. For an inefficient cooling, they settle in a thick and extended torus, mostly centrifugally supported against gravity. The general relativistic hydrodynamical simulation by Shiokawa *et al.* (2015) have shown that the accretion rate still rises sharply and then decays as a power law. However, its maximum is 10 % smaller than the previous expectation, and timescale of the peak accretion is longer than the previously predicted values. This is due to the mass accumulation at higher radius because of angular momentum exchange at large radii. The overall conclusion is that the resulting debris will form an accretion disk. The thickness of the disk formed and the circularization timescale as a function of stellar parameters and $M_\bullet$ are still need to be evaluated.

The accretion of gas to the black hole depends on the viscous dynamics in the accretion disk and the pressure dominated. The viscosity depends on the nature of pressure dominating in the disk such as α viscosity for gas pressure dominated, the radiative viscosity for radiation pressure dominated, magnetic viscosity and gravitational instability. Shakura and Sunyaev (1973) constructed a thin disk steady accretion model with an α viscosity prescription whereas Pringle (1981) constructed a time-dependent accretion model. The thin disk model is applicable when the accretion rate is smaller than the Eddington rate but once the accretion rate crosses the Eddington rate, the disk gets puffed up and the scale height is comparable to the radius. Such a disk is called slim disk which is radiatively inefficient and some fraction of energy generated due to viscous heating is consumed by the black hole (Paczyńsky and Wiita 1980; Jaroszynski *et al.* 1980; Abramowicz *et al.* 1988). The strong radiation pressure also results in an outflowing wind. The self similar time-dependent accretion model for a sub-Eddington disk was constructed by Mangalam (2001) with a general viscosity prescription $\Pi_{r\phi} \propto \Sigma_d^b r^d$ where Σ_d is

the surface density of the disk, r is the radius and b and d are constants; this subsumes the self similar accretion models derived earlier by (Lin and Pringle 1987; Pringle 1981; Cannizzo *et al.* 1990). The TDE disks are complicated in the sense that not only they simultaneously have accretion by the black hole and the fall back from outer debris, but also a wind. Strubbe and Quataert (2009) constructed a model of a slim disk with a spherical outflowing wind with an accretion rate that follows the fallback rate. Shen and Matzner (2014) constructed a model of TDE disk with and without fallback from disrupted debris by developing a self-similar structure of a non-radiative, advective disk with an outflowing wind and using the self-similar solution of Cannizzo *et al.* (1990) for a radiative thin disk with total angular momentum constant.

The luminosity function (LF) which is the number of galaxies per unit co-moving volume per unit log luminosity is useful in the demographics study of the black holes and is usually obtained from observations of AGNs. The first analytic approximation for the luminosity function was proposed by Schechter (1976) which is fit to the observed profile in optical bands (Turner and Gott 1976; Mobasher *et al.* 1993; Marzke *et al.* 1994; Muriel *et al.* 1995; Lin *et al.* 1996; Brown *et al.* 2001). Ueda *et al.* (2003) investigated a sample of 247 AGNs over a wide flux range in 2-10 keV band to obtain the hard X-ray LF (HXLF) that is modeled by luminosity dependent density evolution model (LDDE) which has a double power-law profile along X-ray luminosity L_X and an evolution factor that depends on redshift and is used by (Shankar *et al.* 2009, 2013) to study the black hole evolution with redshift. Hopkins *et al.* (2007) combined a large set of quasar luminosity function (QLF) measurements from optical, soft and hard X-ray and Infrared bands in the redshift interval $z = 0 - 6$ to obtain the QLF that follows a double power-law profile along luminosity which is a function of redshift and the QLF peaks at $z = 2.15 \pm 0.05$. The BHMF from LF is generally derived assuming the luminosity to be at the Eddington limit. The observed nature of down-sizing in LF at both high and low redshift with a peak at $z = 2 - 3$ (Hopkins *et al.* 2007) implies that the non-active

galaxies dominate at low redshift and low mass SMBHs dominate at high redshift which grows by accretion.

The rate tension between the derived capture rate $\sim 10^{-4}$ yr^{-1} and the observed rate $\sim 10^{-5}$ yr^{-1} depends on the distribution function of stars, the initial mass function of stars, the relaxation mechanism and the structure of the galactic nuclei. The accretion model of the TDEs is crucial to fit the observed light curve to get the black hole mass and star mass. The derived black hole mass is useful to study the demographics of black hole distribution.

1.1 Goals of the thesis

1. To provide a self-contained introduction with novel aspects to the physical theory and observations of TDE.
2. To construct a stellar dynamical model of TDEs that includes the initial mass function of stars to calculate the theoretical capture rate.
3. To construct a self-consistent accretion model of time-dependent TDE disk that includes the flows of accretion, fall back, and the outflowing wind.
4. To fit the accretion model to the observed light curves to deduce the physical parameters such as black hole mass and star mass to study the demographics of black holes.
5. Using the stellar and accretion dynamical model to calculate the TDE detection rate and compare it with the observed rates to deduce the BHMF.
6. To provide a context and approach for future studies in this field.

The pericenter of a star orbit is a function of orbital energy E and angular momentum J. The J plays an important role in the stellar dynamical process through

capture rate $\dot{N}_t(E,\ J,\ m,\ \gamma)$ and the accretion process through the pericenter $r_p(E,\ J,\ M_\bullet,\ m)$ which impacts the detectable TDE rates; this has not been taken into account in previous calculations. The inclusion of J in the calculation includes all the possible stellar orbits and decides the radius upto which debris is bound to the black hole at the moment of disruption and thus the fallback rate of the debris. We have constructed a stellar and gas dynamical model of TDEs that includes J and obtained a mass fallback rate which follows the structure of Lodato *et al.* (2009) for a star with energy $E = 0$ and $r_p = r_t$. Using this, we have constructed an accretion dynamical model of a time-dependent disk that includes all the essential physics of accretion, wind and mass fallback. The detection rate of TDEs depends on the theoretical capture rate, duration of TDE observation, BHMF of non-active galaxies and instrumental parameters such as sensitivity, cadence and integration time. Thus, the reverse can be done, that is by knowing the detection rate of TDEs through observations, one can derive the BHMF.

1.2 The plan of thesis

The chapter-wise plan of the thesis is given below and is shown in Fig 1.4.

In chapter 2, we will discuss the history of transients, the observation of TDEs, the classification of the source and the host galaxy properties. The demographics of black holes from mass estimates in the literature will also be discussed. The discussion on various surveys and the observations of TDEs will be presented.

In chapter 3, we will study the basic dynamics of stars in the galactic center. We will discuss the distribution of stars through the distribution function and the phenomena of gravitational interactions to calculate the diffusion coefficients and

hence the Fokker-Planck equation. The loss cone dynamics and the capture of stars will be calculated.

In chapter 4, we will study the basic accretion dynamics and the viscous stress for the transport of angular momentum. The various viscosity paradigms will be discussed and the accretion models such as standard thin disk and slim disk will be investigated in both steady and time-dependent scenarios.

In chapter 5, we will construct a stellar and gas dynamical model that includes the physical parameters such as black hole mass, star mass, star orbital energy and angular momentum. We will derive the theoretical capture rate and use the steady accretion models to calculate the detectable rate of TDEs by the various survey.

In chapter 6, we will build the time-dependent model of accretion disks using a general viscosity prescription that is a function of the surface density of disk and radius. The choice of viscosity for different disks will be investigated and the transition from one to another disk will be discussed.

In chapter 7, we fit our time-dependent accretion model to observations in various spectral bands and deduce the physical parameters such as black hole mass and star mass to study the demographics of black holes. The detectable rate for various missions will be compared with the observed rate to derive the BHMF.

In chapter 8, we will summarize our work, discuss the novel aspects, and its implications to the observations. The caveats and future theoretical approaches will also be presented.

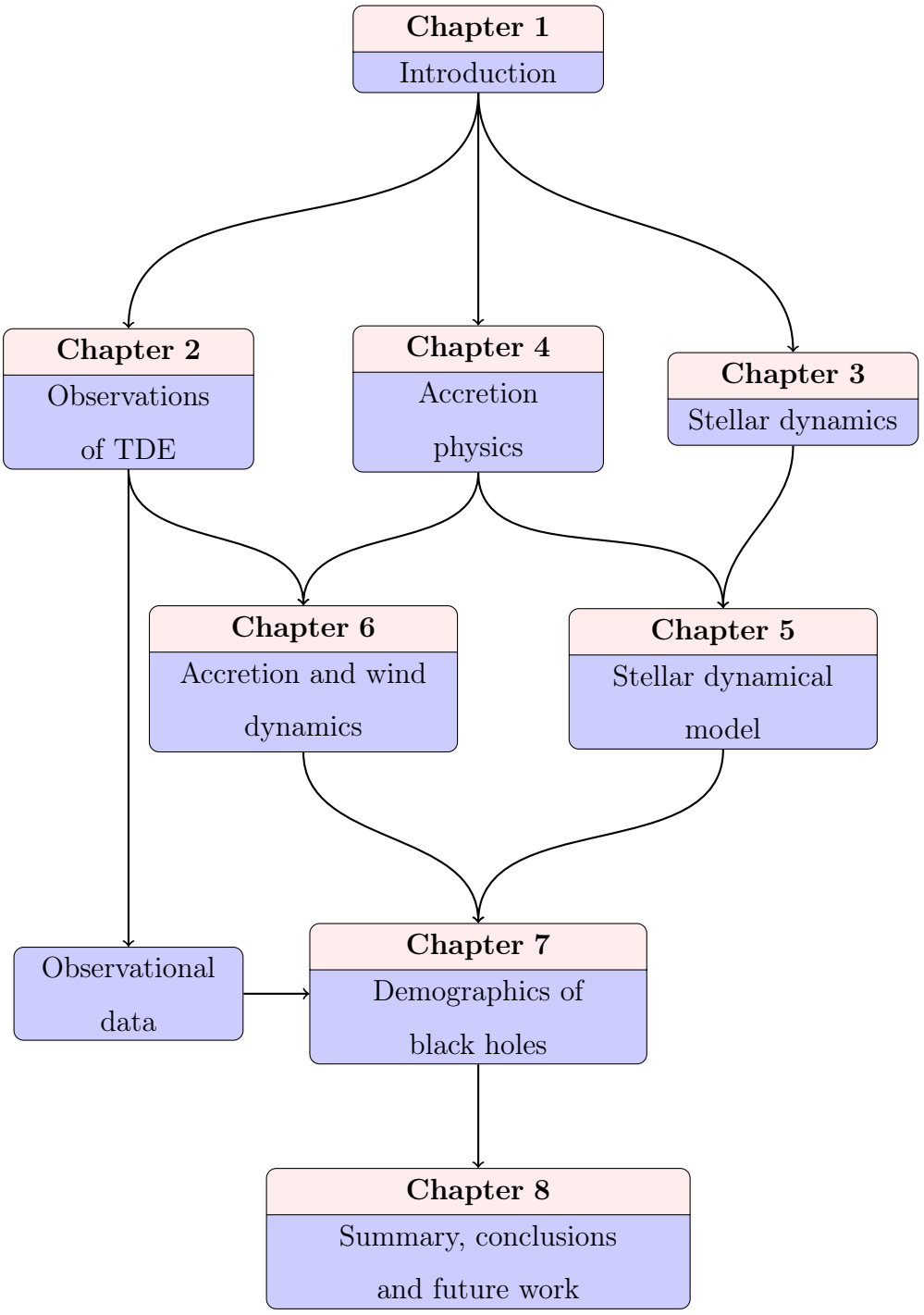

FIGURE 1.4: The plan of the thesis is shown.

Chapter 2

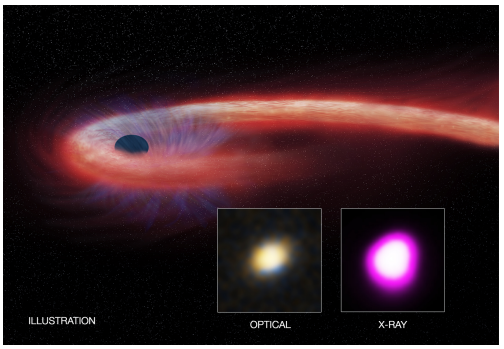

Image: ASAS-SN 14li
NASA/CXC/U. Michigan/J. Miller et al.

Observations of TDEs

2.1 Introduction

The galaxies are classified into two broad categories that are active galactic nuclei (AGN) and quiescent nuclei. In AGNs, the central supermassive black holes (SMBHs) accrete matter from the surrounding disk leading to luminosity in the range $L_{bol} \sim 10^{41} - 10^{48}$ erg sec^{-1} with emission in all spectral bands ranging from X-rays to radio bands and the host nuclei exhibit strong emission line features in their spectra. The nuclei of some galaxies show no evidence of any AGN activity which indicates that the black hole present is starved of fuel and are known as quiescent galaxies which can be observed through the emission from the accretion of debris by tidally disrupted stars leading to a transient event.

The Universe consists of various transient events such as gamma ray burst (GRB),

cataclysmic variable star, kilonovae, supernovae, X-ray binaries, tidal disruption events and AGN variability. The classification of the source in either of the category depends on the luminosity, timescale, and spectral properties. GRBs are highly luminous short duration events whose timescales varies from few seconds to days with the luminosity $\sim 10^{51} - 10^{54}$ erg sec^{-1}. The cataclysmic variable stars are binary stars in which a high-density star consumes matter from the normal star and the timescale varies over months. Kilonova is the merging of two neutron star and is dominated in optical and infrared bands whereas supernova where a star undergoes thermonuclear explosion, occurs on a timescale of hours to months. The X-ray binaries where a black hole accretes matter from the companion star emits in all spectral bands with X-ray luminosity $\sim 10^{38}$ erg sec^{-1} and timescale varies over few days. The AGN variability is long duration transient which shows substantial variability over multiple timescales extending to years and even decades. The tidal disruption events also vary over a timescale of months to years and can be separated out from the AGN variability by its non-repetitive nature unless the disruption of a star is partial as seen in case of TDE IC3599 with a gap of 20 years in successive peak luminosity. The TDEs and AGN variability can also be classified on the basis of spectral properties where the AGN spectra are dominated by narrow emission lines and TDE spectra are dominated by broad emission lines.

Any transient event detected by an All-Sky Survey or Deep Imaging Survey is followed up by ground and space-based detectors with observations ranging from X-rays to radio and the classification of the source depends on the light curve profile and spectral properties. Since the TDE transients are nuclear transients, it is necessary to subtract the background galaxy to extract the source. The analysis for transient source requires source file and reference files which are the observations later or prior to the detection of the transient. The difference imaging analysis (DIA) is performed where the source file is subtracted from the reference file by modeling the alignment difference, the point spread function (PSF), exposure time, atmospheric extinction and sky background between them that results in

the removal of all non-varying sources leaving out the varying sources. The source offset from the galactic center is measured by getting the position of the source from DIA and the centroid of galaxies based on the stacks of previous observations. The emission is considered to be nuclear if the source lies within a few arcseconds from the center.

The detection of the host galaxy of the source prior to the event is necessary to quantify the nature of the source and the host galaxy. In those galaxies whose archival spectrum is unavailable, one has to wait until the transient fades away. If there are no X-ray observations from the galactic center prior to the transients, then the galaxy is considered to be non-active or weak AGN whose classification depends on the spectral properties. To extract the spectral features from the galactic center, the contribution from stellar population needs to be removed. The stellar population synthesis (SPS) model (Bruzual and Charlot 2003) is fit to the host galaxy emission assuming an extinction law, declining star formation history and an initial mass function (mostly Salpeter mass function is considered). The SPS model fit provides us the star formation rate, the age of the stellar population and the template spectrum that is to be subtracted from the host spectrum to extract the spectrum from the central region. If the host spectrum is dominated by absorption lines such as Balmer lines (Hα 6563 Å, Hβ 4861 Å), Ca I G band (4304 Å), Mg I (5175 Å), Na I (5894 Å), Ca H (3934 Å) & K (3969 Å) and 4000Å break lines, the galaxy is populated with the intermediate-age and old stellar populations. The strength of the 4000Å break caused by the blanket absorption of high-energy radiation from metals in stellar atmospheres is the characteristic of the old stellar population in the galaxies. There are some TDEs whose host galaxy spectra shows the emission lines such as Hα, Hβ, HeII , OII, OIII, NII and SII with low intensity which suggests that the host could be a weak AGN.

2.2 Classification of host galaxies

AGN comprises of a broad class that includes a large variety of subtypes with the luminosity range $L_{bol} \sim 10^{41} - 10^{48}$ erg sec^{-1}. Seyfert galaxies were the first and most common class of AGN we observe in the local universe with highly ionized emission lines such as Hα, Hβ, Hγ and forbidden lines such as OIII, OII, OI, NIII, NeV, NII. If the Balmer emission lines are broader (FWHM $10^3 - 10^4$ km sec^{-1}) than the forbidden lines, the galaxy is Seyfert class 1 whereas the galaxy is Seyfert class 2 if the forbidden and Balmer lines show the same narrow width. The presence of strong FeII at 4570Å in the optical spectra is an indication of Seyfert class 1. There are also intermediate Seyfert class subtypes known as Seyfert 1.2, 1.5, 1.8 and 1.9 according to their Balmer characteristic (Osterbrock 1977). The Seyfert 1.2 is a Seyfert galaxy with broad Balmer lines but slightly less broad Hβ lines. In Seyfert 1.5, the strength of Hα and Hβ are comparable whereas Seyfert 1.8 shows weak broad Balmer lines. The Seyfert 1.9 has a broad Hα line and narrow Hβ line. A subset of Seyfert 1 galaxies are the Narrow-Line Seyfert 1 (NLS1) galaxies which are strong X-ray emitters but their Hα lines are broad, their Hβ line is narrow (FWHM < 2000 km sec^{-1}) and possess weak CIV and CIII emission lines. A class of galaxies known as low-ionization nuclear emission line regions (LINER) galaxies have low luminosity core ($L_{bol} \sim 10^{40}$ erg sec^{-1}) and strong emission lines originating from the low ionized non-stellar gas with line widths FWHM $200 - 400$ km sec^{-1}. LINER's have strong emission lines NII (6584 Å), SII (6731 Å) as compared to the Hα line. LINER galaxies properties are similar to Seyfert 2 galaxies but have low luminosity which suggests that the LINER is accreting with low radiative efficiency or at a low rate compared to Seyferts. Some galaxies with emission line spectra similar to Seyfert 2 galaxies with massive gas clouds of ionized hydrogen, the so called HII galaxies are preferentially spiral galaxies and often exhibit strong forbidden oxygen lines compared to the Balmer lines with OIII(5007 Å)/H$\beta > 3$.

An efficient way to classify the various subtypes of AGNs is to use diagnostic diagrams that compare various line ratios which depend on the nature of the ionizing medium (stellar or non-stellar) (Baldwin *et al.* 1981; Kauffmann *et al.* 2003; Kewley *et al.* 2006). These diagrams are commonly known as Baldwin−Phillips−Terlevich (BPT) diagrams and are based on the four optical line ratios OIII/Hβ, NII/Hα, SII/Hα and OI/Hα. Kewley *et al.* (2001) created a maximum starburst line on the BPT diagram by considering the upper limit of the theoretical pure stellar photoionization models and using the multiple stellar population models. Galaxies lying above the starburst line are dominated by AGN and below are dominated by star formation. Their models include a wide range of metallicity, ionization parameter, and dust depletion, and also make allowances for the effects of shock excitation by supernovae. Kauffmann *et al.* (2003) based on the observational study of 22623 narrow line AGN observed in SDSS in redshift range $0.02 < z < 0.3$, obtained an empirical relation which is lower than the maximum starburst line by Kewley *et al.* (2001). Kewley *et al.* (2006) selected their sample of galaxies in redshift range $0.04 < z < 0.1$, from the 567486 galaxies observed in SDSS data release 4 assuming the signal to noise ratio > 3 for accurate classification of AGN and star-forming galaxies as shown in Fig 2.1. The star-forming galaxies have low OIII/Hβ and NII/Hα lines and the sequence from low metallicities (low NII/Hα, high OIII/Hβ) to high metallicities (high NII/Hα, low OIII/Hβ) is the star-forming sequence (Kewley *et al.* 2006). The mixing of AGN with star-forming occurs at high metallicity and extends towards high values of NII/Hα and OIII/Hβ. Galaxies that lies close to the starburst lines are classified as composite galaxies that are likely to contain a metal-rich stellar population plus AGN. Galaxies with high star-formation rate and intense narrow emission lines are called as starburst galaxies whose X-ray, UV, optical and radio properties are accounted by the collection of young stars or supernova remnants (Weedman *et al.* 1981; Feldman *et al.* 1982). The presence of strong Balmer absorption lines but no significant OII line implies that the star-formation is ceased. The central structure of these galaxies are consistent with a power law early type galaxies and their spectra are a superposition

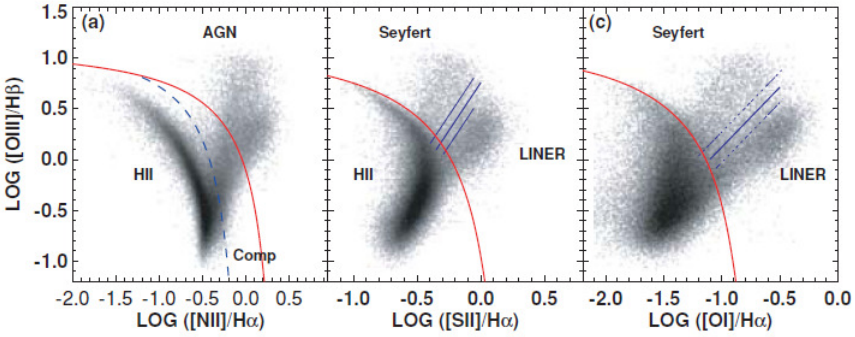

FIGURE 2.1: The BPT diagram shows the classification schemes based in the emission lines. The Kewley *et al.* (2001) maximum starburst line (red solid line), the Kauffmann *et al.* (2003) pure star formation line (blue dashed line), and the Kewley *et al.* (2006) Seyfert−LINER line (blue solid line) are used to separate galaxies into HII -region-like, Seyferts, LINERs, and composite HII AGN types whose spectra contain significant contributions from both AGN and star formation.
Courtesy: Kewley *et al.* (2006)

of a young stellar population represented by A stars and an old population characterized by K stars. These post-starburst galaxies are known as E (for elliptical) +A galaxies (Dressler and Gunn 1983; Yang *et al.* 2004).

2.3 Black hole mass estimation

The black hole mass is calculated either using the galaxy relations such as $M_\bullet - \sigma$ relation given by $M_\bullet \propto \sigma^p$ where σ is the velocity dispersion with $p = 4.86$ (Ferrarese and Ford 2005), 4.24 (Gültekin *et al.* 2009), or 5.64 (McConnell and Ma 2013), and $M_\bullet - M_{\rm bulge}$ relation given by $M_\bullet \propto M_{\rm bulge}^n$ where $M_{\rm bulge}$ is the bulge mass with $n = 1.05$ (McConnell and Ma 2013) and $M_\bullet - L$ relation given by $M_\bullet \propto L^q$ where L is the luminosity with $q = 1.18$ (Marconi and Hunt 2003) in K band, 1.11 (McConnell and Ma 2013) in V band or using the fit to the light curve by the emission model.

2.4 TDE sources

ROSAT surveys made the early discoveries of TDEs in the 1990s as an X-ray outbursts from quiescent galaxies (Bade *et al.* 1996; Komossa and Bade 1999). The TDEs in X-rays were also observed by XMM-Newton (Esquej *et al.* 2007; Saxton *et al.* 2012, 2014, 2017) and Chandra X-ray Observatory (Maksym *et al.* 2010, 2013). Apart from X-rays, the TDEs are also observed in the optical bands (Gezari *et al.* 2008, 2012; van Velzen *et al.* 2011; Holoien *et al.* 2014, 2016b,a; Chornock *et al.* 2014; Arcavi *et al.* 2014; Blagorodnova *et al.* 2017) and in UV (Gezari *et al.* 2008, 2009; Holoien *et al.* 2014). The radio observations of TDEs such as Swift J1644+57 (Burrows *et al.* 2011) and Swift J2058.4+0516 (Cenko *et al.* 2012b) provides an evidence of an associated jet. Since all TDEs do not have an associated jet, the detection of jetted TDEs has opened new challenges in the field of TDE dynamics. The multi-wavelength observations of TDEs with their high-resolution spectra provides deeper insights into the accretion disk and the properties of the star (Holoien *et al.* 2014; Wyrzykowski *et al.* 2017).

From the study of multiple TDEs, the spectrum of TDE transient is dominated by broad Hα, Hβ and sometimes He broad emission lines for TDEs. The TDEs with broad Hα and Hβ lines are associated with the disruption of main sequence star whereas TDEs such as PTF09ge, PS1-10jh, ASAS-SN 14li and ASAS-SN 15oi shows broad HeII strong lines at the initial stage which suggests that the star disrupted is an evolved star. Some TDEs such as OGLE16aaa, iPTF16fnl, iPTF16axa, ASAS-SN 14ae show both strong He and H lines.

Some TDEs are found to have an associated radio counterpart which are due to non-thermal synchrotron emission. The synchrotron emission model fit to the radio emission provides the density of the surrounding medium, magnetic field, and velocity of the outflow ejecta. SWIFT J1644+57 was the first observed jetted TDE shown in Fig 2.3, with $\beta = v/c = 0.55$ where v is the velocity, making this

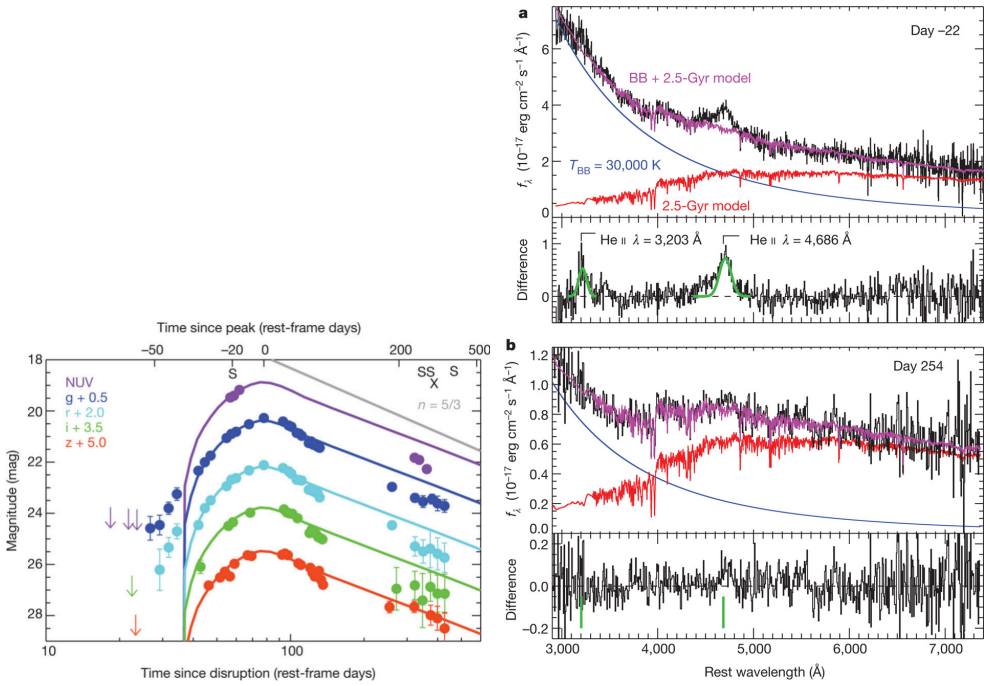

(a) (b)

FIGURE 2.2: (Left) The observed light curve profiles in various spectral bands for TDE PS1-10jh at the redshift of $z = 0.1696$. (Right) The observed spectrum of the source at time t = -22 days and 254 days measured from the time of peak emission. The spectrum is dominated with HeII line and the absence of H lines suggest that the disrupted star is helium rich evolved star. The spectrum is subtracted with a combination (magenta) consist of continuum through blackbody fit (blue) and stellar spectrum template of 2.5 Gyr old star population (red) computed using Bruzual and Charlot (2003).
Courtesy: Gezari *et al.* (2012)

to be a relativistic jetted TDE (Zauderer *et al.* 2011). The radio observations of ASAS-SN 14li and their fit to synchrotron model provides outflow ejecta with $\beta \sim 0.11$ measured at five different epochs suggesting that the outflow is non-relativistic. XMMSL1 J074008.2-853927 was observed in radio bands 592 days after its discovery and is consistent with the synchrotron model which gives $\beta \sim 0.097$ making it the second non-relativistic outflow TDE. SWIFT J2058+0516 was also observed in radio bands and due to high redshift, it provides only a constrained value of $\beta \geq 0.88$ (Cenko *et al.* 2012b) which declines with time to a

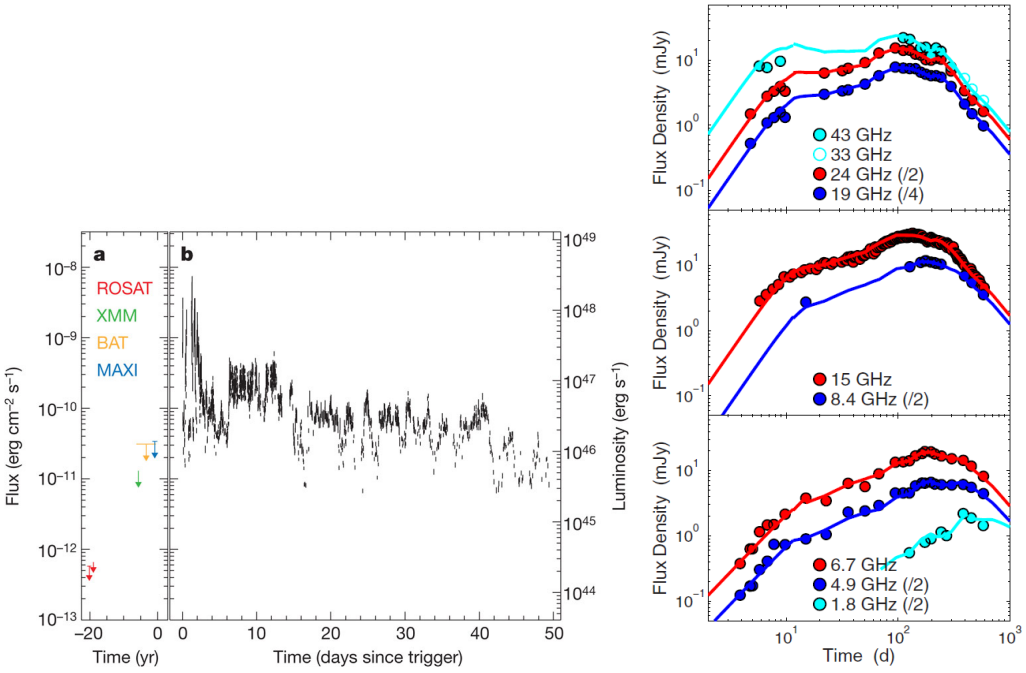

(a) (b)

FIGURE 2.3: The X-ray observation of Swift J1644+57 (left) and it's radio counterpart (right) is shown with the observation from the trigger time 28 March 2011 at the redshift of $z = 0.354$and the prior observations by X-ray missions such as ROSAT, XMM, BAT and MAXI are at their limiting sensitivity. Courtesy: Burrows *et al.* (2011); Zauderer *et al.* (2013)

faint unresolvable source in 40 days after discovery (Pasham *et al.* 2015).

The variability in X-ray for TDE sources can be misinterpreted as the AGN variability. The spectral properties of the host galaxy classify the nature of the galaxy for various TDE sources. The TDEs such as XMM J152130+0.74916, SWIFT J1644+57, SWIFT J2058+0516, XMMSL1 J061927.1-655311, XMMSL1 J074008.2-853927 and ASASSN-14li have X-ray observations which varies over timescales of months to year. Auchettl *et al.* (2017) have shown, by comparing the X-ray TDEs to the AGN candidates, that the observed peak luminosity of TDEs are higher than the AGN at that redshift which is because TDEs are less

obscured due to surrounding medium are compared to AGN because of weak outflows leading to a low-density atmosphere. The luminosity of the TDEs and AGN are of similar order but the power index n (luminosity $L \propto t^n$, where t is time) shows a large variation in time in case of AGN due to the highly variable nature suggesting that the TDEs decays more coherently than the AGN. The hardness ratio HR= $(H - S)/(H + S)$, where H is hard X-ray photon count, and S is soft X-ray photon count, indicate that the TDEs are soft in nature (HR < 0.3) and does not change significantly compared to AGN for which HR can go from -1 (thermal) to +1 (non-thermal). Thus the X-ray TDEs can be distinguished from AGN variability by (1) the nature of host galaxy, (2) low power index n suggesting coherent decay, and (3) low HR suggesting soft nature of TDEs.

The observed TDE candidates are given in Table 2.1. Below we study the spectral properties of TDEs and the classification of their host galaxies.

1. NGC 5905 (Bade *et al.* 1996; Komossa and Bade 1999)

   It is the earliest TDE detected by ROSAT on July 11, 1990, in soft X-ray band. The post-outburst spectra showed a strong emission line in the continuum with deep absorption lines due to stellar content in the nucleus which suggests that the stellar content dominates the spectrum. The emission lines such as OI, OIII, NII and SII are detected whereas the high ionization lines HeII and FeX are absent with FWHM 270-300 km sec^{-1}.

   Li *et al.* (2002) assuming the light curves to follow $L \propto \dot{M}$, where $\dot{M}$ is the mass fallback rate, obtained the black hole mass $M_\bullet = 10^7 - 10^8\ M_\odot$ and star mass $M_\star = 0.6 - 1\ M_\odot$. Using the stellar velocity dispersion in bulge $\sigma = 174.6 \pm 9.0$ km sec^{-1} (Ho *et al.* 2009) and $M_\bullet - \sigma$ relation given in Gültekin *et al.* (2009), the black hole mass obtained is $M_\bullet \sim 10^7\ M_\odot$ (Raichur *et al.* 2015).

2. IC 3599 (Komossa and Bade 1999)

IC-3599 was detected on December 10, 1990, by ROSAT and whose host galaxy spectra have emission lines such as Balmer lines, OIII, HeII and FeVII. The width of Balmer lines are larger than the forbidden lines OIII and SII and thus we classify the host to be Seyfert 1.9.

Grupe *et al.* (2015) using the K band luminosity obtained through 2MASX and black hole mass- K band luminosity (Marconi and Hunt 2003), obtained $M_\bullet = (2-12) \times 10^6\ M_\odot$. Campana *et al.* (2015) using the hydrodynamic simulation code of Guillochon and Ramirez-Ruiz (2013) obtained $M_\bullet \sim 3 \times 10^6\ M_\odot$ with $M_\star \geq 1.5\ M_\odot$.

3. NGC 3599 (Esquej *et al.* 2008)

   The source was detected on November 22, 2003, by XMM-Newton in X-ray bands. The starlight component obtained using single stellar population synthesis model was subtracted from the optical spectrum taken on February 5, 2000, which shows Hα luminosity to be $\sim 10^{39}$ erg sec^{-1} suggesting the host galaxy to be low luminosity AGN. The line ratios OIII/Hβ=3.5 and NII/Hα=1.1 and using the BPT diagram shown in Fig 2.1, the galaxy is located in the transition region between Seyfert and LINER. From the optical spectrum of the host galaxy, they obtained the velocity dispersion $\sigma = 73.2$ km sec^{-1} and using $M_\bullet - \sigma$ relation from Ferrarese and Ford (2005) obtained $M_\bullet = (1.3 \pm 0.6) \times 10^6\ M_\odot$.

4. XMM J152130+0.74916 (Lin *et al.* 2015)

   The spectrum taken on May 28, 2011 (source detected on August 23, 2000) shows absorption lines indicating the host to be inactive. The upper limit luminosity of OIII (5007 Å) is 1.6×10^{39} erg sec^{-1} which is nearly three orders of magnitude smaller than that required for AGN. This implies that the host is not a strong AGN. The SPS model fit to the SDSS observations indicates the stellar population to be old. By using the hydrodynamic model of Guillochon *et al.* (2014) obtained $M_\bullet \sim 10^6\ M_\odot$ for a solar mass star,.

5. SDSS J132341.97+482701.3 (Esquej *et al.* 2008)

   The source was detected on December 1, 2003, by XMM-Newton in X-ray bands. The host galaxy optical spectrum shows the absorption lines from stars and no emission lines suggesting the galaxy to be inactive. From optical spectrum of the host galaxy, they obtained the velocity dispersion $\sigma = 80$ km sec^{-1} and using $M_\bullet - \sigma$ relation from Ferrarese and Ford (2005) obtained $M_\bullet = (2.2 \pm 0.9) \times 10^6\ M_\odot$.

6. D1-9 and D3-13 (Gezari *et al.* 2008)

   The host spectrum of the source D1-9 detected on August 12, 2004, and D3-13 detected on January 15, 2004, by GALEX shows only stellar absorption lines with no X-ray detections and are classified as early type inactive galaxies. Using the bulge luminosity and black hole mass-bluge luminosity relation of Magorrian *et al.* (1998), they obtained $M_\bullet = (0.3 - 3) \times 10^8\ M_\odot$. Using $M_\bullet - \sigma$, the black hole mass for D3-13 is etsimated to be $M_\bullet = (1 - 4) \times 10^7\ M_\odot$. By considering the luminosity $L = \eta \dot{M} c^2$ where η is the efficiency and taking Lodato *et al.* (2009) model for $\dot{M}$, $M_\bullet$ for the disruption of a solar mass star is found to be $2.4 \times 10^7\ M_\odot$ for D1-9 and $1.2 \times 10^7\ M_\odot$ for D3-13.

7. J234201.40+010629.2 (TDE1) and J232348.61-010810.3 (TDE2) (van Velzen *et al.* 2011)

   TDE1 and TDE2 were detected on November 19, 2005, and November 20, 2006, by SDSS. The host galaxy spectrum of TDE1 taken on November 7, 2009 shows Balmer absorption lines and no emission lines with Hα luminosity $< 4.4 \times 10^{37}$ erg sec^{-1} and OIII luminosity $< 1.3 \times 10^{38}$ erg sec^{-1} which suggests that the host is inactive.

   The host galaxy spectrum of TDE2 taken on November 5, 2010 after stellar template subtraction generated using stellar synthesis model shows Hα luminosity $= 1.2 \times 10^{40}$ erg sec^{-1} with emission line ratio NII/Hα=-0.4 $\pm$ 0.2 and OIII luminosity $< 3.6 \times 10^{39}$ erg sec^{-1}. Using the BPT diagram (Fig

2.1), the observed ratio with broad Hα (FWHM=8000 km sec^{-1}) is consistent with an origin from star-formation and thus the galaxy seems to be a star-forming galaxy.

From the magnitude ratio of bulge to total calculated by Tundo *et al.* (2007) and using the scaling relation by Häring and Rix (2004), the $M_\bullet$ for TDE1 is found to be $(6-20)\times10^6 M_\odot$ and for TDE2 is $(2-10)\times10^7 M_\odot$.

8. D23H-1 (Gezari *et al.* 2009)

   The source was detected on September 4, 2007. The spectrum was taken on September 16, 2007 (13 days prior to peak on September 29, 2007) and after subtracting a template for stellar absorption lines, the emission line ratios are OIII/Hβ=0.6±0.1, NII/Hα=0.41±0.03, SII/Hα=0.22±0.06 and OI/Hα <0.035. In the BPT diagram, the line ratios lie in the region of H II which is a combination of star-formation and AGN and since the OIII/Hβ is small, the star-formation dominates over AGN; thus the BPT diagram classifies the host as a star-forming galaxy. The black hole mass estimated using Lodato *et al.* (2009) model is $M_\bullet = (5.4\pm0.4)\times10^7\ M_\odot$ for the disruption of solar type star.

9. PTF09ge, PTF09djl and PTF09axc (Arcavi *et al.* 2014)

   The source spectrum is calculated at multiple days and is subtracted from the stellar spectral template obtained using SPS model. PTF09ge and PTF09djl shows no sign of an AGN emission lines but PTF09axc shows low OIII luminosity $\sim 2.4\pm0.3\times10^{39}$ erg sec^{-1} with OIII/Hα >3.4 which indicates the presence of weak AGN. In the X-ray observations through SWIFT XRT after five years of the outburst, PTF09ge and PTF09djl have no X-ray flux whereas PTF09axc show a low luminosity 7.13×10^{42} erg sec^{-1}. These three outbursts are not likely due to AGN though PTF09axc may contain an extremely weak AGN.

   The host galaxy spectrum was obtained in 2013 after all the transient emission had faded. All of them display the Balmer absorption features. The

spectrum of PTF09djl and PTF09axc have no strong emission lines implying no or very low ongoing star-formation. PTF09ge show weak Hα emission but no strong emission lines. The Balmer absorption with no strong emission lines is a signature of E+A galaxy. The star-formation rate using Hα luminosity for PTF09ge is 0.10 $M_\odot$ yr^{-1} and PTF09axc is 0.04 $M_\odot$ yr^{-1}.

PTF09ge shows broad HeII emission with FWHM $\sim$ 1000 km sec^{-1} whereas the spectrum of PTF09djl and PTF09axc exhibit broad Hα emission. This implies that the PTF09ge shows the TDE of a He dominated star such as an evolved star whereas PTF09djl and PTF09axc show the TDEs of an H dominated star such as a main sequence star. From spectral energy distribution, the estimated black hole masses for PTF09axc is $(3 \pm 0.1) \times 10^6 M_\odot$, PTF09ge is $(6 \pm 0.1) \times 10^6 M_\odot$ and PTF09djl is $(2.5 \pm 0.5) \times 10^6 M_\odot$.

10. PS1-10jh (Gezari *et al.* 2012)

    The X-ray observation on May 22, 2011 (source detected on May 28, 2010) using Chandra X-ray Observatory detected no X-ray source above the background with a 3σ upper limit. The spectra show no narrow emission line to indicate the star-formation or an AGN. Arcavi *et al.* (2014) obtained the optical spectra on April 29, 2014, and found that the spectra are dominated by Balmer absorption lines with no strong emission lines which indicate E+A galaxy.

    The source spectra contains the broad high-ionization HeII emissions with FWHM 9000 $\pm$ 700 km sec^{-1} and lacks the Balmer emission lines which requires extremely low hydrogen mass fraction < 0.2. Thus the TDE is powered by the accretion of a star that has lost its mass either due to stellar winds or through tidal interaction with supermassive black holes. The black hole mass estimated using Lodato *et al.* (2009) model is $M_\bullet = (2.8 \pm 0.1) \times 10^6$ $M_\odot$ for disruption of star with mass $M_\star = 0.23 M_\odot$ and $R_\star = 0.33 R_\odot$.

11. SDSS J120136.02+300305.5 (Saxton *et al.* 2012)

The optical spectrum taken 12 days after the source detection on July 10, 2010 shows no emission lines and the absorption lines MgI (λ 5167, 5173, 5184 Å) and NaI (λ 5890, 5895 Å) were observed. The second spectra taken after 11 months when almost TDE faded away, showed no emission lines with Hα and Hβ seen in absorption with MgI and NaI. After subtracting the SPS model of an old stellar population, the OIII luminosity is $< 4\times10^{39}$ erg sec^{-1}. The galaxy shows no evidence of previous AGN and is thus inactive. Using the scaling relation between black hole mass and K band luminosity given by Marconi and Hunt (2003), they obtained $M_\bullet = 2 \times 10^7\ M_\odot$.

12. PTF10iya (Cenko *et al.* 2012a)

    Host galaxy spectra show both absorption feature due to stellar population and a series of narrow emission lines with no broad components. The typical galaxy emission lines such as OII, Hβ, OIII, NII, Hα, SII are clearly present. After subtracting the template for stellar contamination generated using SPS model, the line ratios are OIII/Hβ=0.65±0.07, NII/Hα=0.29±0.04, SII/Hα=0.38±0.05 and OI/Hα<0.03. Using BPT diagram, it is found that the galaxy is a star-forming galaxy. The star-formation rate from Hα intensity is found to be 1.5±0.5 $M_\odot$yr^{-1}. Since the galaxy position in BPT diagram is lower than the theoretical separation limit, the narrow emission lines might be due to the photoionization of young massive stars. Following the accretion model of Strubbe and Quataert (2009), an estimate of $M_\bullet \sim 10^7\ M_\odot$ for a solar mass star was made.

13. PS1-11af (Chornock *et al.* 2014)

    The host galaxy spectrum obtained after the event faded away and subtracting the template spectrum obtained using SPS, there are no emission lines observed from Hα, OIII and OII which is the signature of AGN or star formation. The 4000 Å break is present which is a signature of an old stellar population. The SPS models provide the age to be 2.5 Gyr. The star-formation rate is found to be 0.04 $M_\odot$ yr^{-1} and the absence of OIII and OII

line indicates that there is no young stellar population in the host galaxy. The host is not detected in the UV bands prior to transient which is against the presence of an AGN. The host is then a quiescent early type galaxy with no evidence of an AGN or star-formation in their spectra. By fitting the model of Guillochon and Ramirez-Ruiz (2013), the parameters obtained are $M_\bullet = 10^6 M_\odot$ and $M_\star = 0.65 M_\odot$.

14. SWFIT J1644+57 (Burrows *et al.* 2011; Zauderer *et al.* 2011)

    ROSAT All-Sky Survey observed the field of the source between 11 July 1990 and 13 August 1991 with the flux limit $< 2.5 \times 10^{-13}$ erg sec^{-1} cm^{-2} in 1-10 keV which results in luminosity $< 1.01 \times 10^{44}$ erg sec^{-1}. The flux of SWIFT J1644+57 is 2-4 orders of magnitude higher than the ROSAT observations. The optical spectrum taken on April 1.34, 2011 UT and April 4.62, 2011 UT (UT= universal time) shows narrow emission lines Hβ, OIII, Hα along with OII which is for star-forming galaxy but high excitation lines such as NeV (3345, 3425 Å) are absent. No broad Hα line is observed. The line ratios log(OIII/Hβ)$\sim$0.15 and log(NII/Hα)$\sim$ -0.4 place the source in the position of star-forming galaxy in BPT diagram (Fig 2.1). The prominent stellar absorption lines are present. The inferred star-formation rate of the host in 0.5 M$_\odot$ yr^{-1} (Levan *et al.* 2011). The late time spectroscopy taken on March 23 to April 4, 2012, shows the same narrow emission lines of Hβ, OIII, Hα and OII with no evolution. The black hole mass from $M_\bullet - \sigma$ relation is $M_\bullet = 3 \times 10^6\ M_\odot$.

15. SWIFT J2058.4+0516 (Cenko *et al.* 2012b)

    The spectrum taken on June 1, 2011 (source detected on May 27, 2011) reveals a blue continuum with strong absorption features corresponding to MgII (2796, 2803 Å) and FeII (2600, 2587, 2383, 2344 Å). No other significant features were detected. The source redshift is 1.1853 and is the farthest detected TDE till now. Due to high redshift, the standard lines do not fall in the optical bandpass. The second spectrum taken on June 29, 2011, does

not have any significant variations compared to the first spectrum and the same absorption features are present. Due to high redshift, the upper limit of black hole mass through black hole-bulge mass relation is found to be 2×10^8 $M_\odot$.

16. SWIFT J1112-8238 (Brown *et al.* 2015)

    The optical spectroscopy done on December 16, 2012, shows a single weak emission feature observed at 7045 Å which was identified to be O3727 Å at redshift z=0.8901. The late time X-ray observations results in the luminosity $L_X < 10^{44}$ erg sec^{-1} which is fainter than the observed quasar luminosity implying that the ongoing nuclear activity is weak. The observed high X-ray flux of the source places the event in the list of relativistic TDEs. Using the scaling relation by Häring and Rix (2004), $M_\bullet \sim 2 \times 10^6$ $M_\odot$ is obtained.

17. XMMSL1 J061927.1-655311 (Saxton *et al.* 2014)

    The source spectrum taken on December 3, 2012, shows broad Hα and Hβ and weak narrow low ionization Balmer lines and lines of OIII, NII and SII. The line ratios are OIII/Hβ=3.1±1.3, NII/Hα=0.85±0.15 and SII/Hα=1.0±0.3. The BPT diagram places the source on the boundary between a LINER and a Seyfert galaxy. The width of the Balmer line Hα and Hβ are 5716 and 5714 km sec^{-1} respectively are greater than the forbidden lines such as OIII=330 km sec^{-1} and NII=292 km sec^{-1} which classify the host as Seyfert I galaxy. The second spectrum taken on October 18, 2013, shows the same features of broad Balmer lines and weak narrow lines. Using the H_α luminosity width, the black hole mass is estimated to be 3×10^7 $M_\odot$.

18. XMMSL1 J074008.2-853927 (Saxton *et al.* 2017)

    The host spectrum taken on January 17, 2002 (source detected on April 1, 2014) after subtraction from the SPS template spectra shows no emission lines with OIII flux $< 4 \times 10^{-15}$erg sec^{-1} cm^{-2}. The host is an inactive

galaxy. Using the K band luminosity of the host galaxy and the scaling relation of Marconi and Hunt (2003), $M_\bullet = (6 \pm 2) \times 10^6\ M_\odot$ is estimated.

19. ASASSN-14ae (Holoien *et al.* 2014)

    The host spectrum is dominated by absorption lines, Balmer lines, CaI G band, MgI, NaI and 4000 Å break making the stellar population to be old. There is no strong emission lines and the OIII luminosity is 2.4×10^{39}erg sec^{-1} suggesting a low level of star-formation and the line ratios suggest a weak AGN.

    The source spectrum shows a blue continuum with broad Balmer lines in emission (FWHM Hα >8000 km sec^{-1}) which are not present in host galaxy spectrum and the broad Hα become stronger at the later epoch. The He emission is also present whose intensity increases compared to Balmer lines as the time progresses. With both He and H present in the spectra, the source falls in the middle of He rich to H rich star disruption. From the stellar synthesis model fit to the spectrum, the total mass of star distribution is obtained and considering it to be the bulge mass, and using the scaling relation between black hole mass and bulge mass given by McConnell and Ma (2013), $M_\bullet \sim 10^{6.8}\ M_\bullet$ is obtained.

20. ASASSN-14li (Holoien *et al.* 2016b)

    The host galaxy was not observed in ROSAT survey suggesting that the host does not have a strong AGN. Detection of the host in archival Wide-field Infrared Survey Explorer (WISE) gives W3 band magnitude to be 12.367±0.439 corresponding to a luminosity of $L_{w3} \sim 2 \times 10^7 L_\odot$, where $L_\odot$ is the solar luminosity. The host galaxy is also detected in radio band with luminosity 2.96 ± 0.15 mJy for 1.4 GHz. This along with non-detection in X-ray implies that AGN activity, if any, is weak. The SPS model fit to the SDSS magnitude of host galaxy provides the star-formation rate to be < 0.009 M$_\odot$ yr^{-1}. The archival host galaxy spectrum shows no Hα or OII in emission but the luminosity of OIII is $\sim 4.4 \times 10^5\ L_\odot$ and of NII is

$\sim 3.6 \times 10^5\ L_\odot$. This indicates that the host is a low luminosity AGN with weak nuclear activity.

The source spectrum contains strong blue continuum with broad Balmer and helium lines in emission. The blue continuum weakens over time. The spectra show HeII earlier compared to the ASAS-SN14ae where it appears at late stages. Both helium and Balmer emission narrow as time progresses. With both He and H present in the spectra, the source falls in the middle of He-rich to H rich star disruption. From the stellar synthesis model fit to the spectrum, the total mass of star distribution is obtained and considering it to be the bulge mass, using the scaling relation between black hole mass and bulge mass given by McConnell and Ma (2013), $M_\bullet \sim 10^{6.7}\ M_\bullet$ is obtained.

21. ASASSN-15oi (Holoien *et al.* 2016a)

    The source spectrum shows string blue continuum and broad helium lines in emission but little to no H emission. The emission features are broad and asymmetric which narrows over time and HeII dominates at the late time. The absence of H lines suggests that the disrupted star is a helium rich. The host galaxy is not detected in ROSAT survey suggesting the host not to be a weak AGN. The spectrum taken when the transient fades away shows no blue continuum and absorption lines. The absence of Balmer absorption lines is consistent with the host to be a post-starburst galaxy. From the stellar synthesis model fit to the spectrum, the total mass of star distribution is obtained and considering it to be the bulge mass, using the scaling relation between black hole mass and bulge mass given by McConnell and Ma (2013), $M_\bullet \sim 10^{7.1}\ M_\bullet$ is obtained.

22. OGLE16aaa (Wyrzykowski *et al.* 2017)

    The host spectrum shows weak OIII, OII and NII narrow forbidden lines in emission as well as narrow emission lines of Hα and Hβ but no Balmer absorption line series. The line ratios log(OIII/Hβ) is -0.25 and log(NII/Hα)

is -0.43 which indicates that the galaxy is a mixture of star-forming and weak AGN as per BPT diagram.

The source spectrum shows broad emission features around HeII and Hα emission lines. Using the model of Guillochon *et al.* (2014), the obtained parameters are $M_\bullet = 10^{6.2}\ M_\odot$ and star mass $M_\star = 0.1 - 0.8\ M_\odot$.

23. iPTF16axa (Hung *et al.* 2017)

    The position of iPTF16axa coincides with SDSS J170334.34+303536.6 whose photometry measurements in SDSS bands are available. The fit of SPS model to the galaxy photometry indicates that the star-formation is quenched with a star-formation rate of $10^{-6.6}$ $M_\odot$ yr^{-1}. No host galaxy archival spectrum is available and no historical variability activity was noted.

    The source spectrum shows broad emission features around HeII and Hα emission lines. The common AGN lines such as OIII and NII are not present and the broad Balmer lines fade away with time suggesting that the broad lines are associated with the transient. The source spectrum is a mixture of HII and Hα lines and they both evolve with the same trend with the FWHM decreasing with time. The velocity dispersion $\sigma = 101.3 \pm 1.9$ km sec^{-1} obtained using MgIb ($\lambda = 5167,\ 5173,\ 5184$) and using the $M_\bullet - \sigma$ relation from McConnell and Ma (2013), the black hole mass obtained is $(2.7-12.9)\times 10^6\ M_\odot$.

24. iPTF16fnl (Blagorodnova *et al.* 2017)

    The iPTF16fnl was observed multiple times by iPTF and no prior AGN activity was detected. The source spectrum shows the broad HeII and Hα emission lines. Several narrow absorption lines associated with host galaxy were observed such as BaII (6496 Å), NAI (5889, 5896 Å) doublet, MgI (5167, 5173, 5184 Å), FeI (5266, 5324 Å), CaII (3934, 3968 Å) and strong NIR triplet absorption at 8498, 8542, and 8662 Å. Early time spectrum was dominated by blue continuum and broad HeII lines along with Hα and Hβ emission lines. The emission lines fade away with time leaving the HeII

line which gets narrow. With the fading of Balmer lines as transient fade and the presence of high metal absorption lines indicates that the host is a post-starburst E+A galaxy. The presence of HeII line at the late time when other lines fade away means that the disrupted star is a helium rich star. Using the TDE model of Guillochon and Ramirez-Ruiz (2013), the estimate of $M_\bullet = 2 \times 10^6\ M_\odot$ and $M_\star = 0.8 M_\odot$ are made.

Table 2.1 show that the TDEs are dominated at low redshift with the number of TDEs detected depending on the host galaxy properties is shown in Fig 2.4. The TDEs are dominated in low mass supermassive black holes at low redshift with mostly favored in the inactive, weak AGN and star-forming galaxies. The detection of TDEs at different redshift is a probe to study the distribution of black hole masses in the universe and hence the black hole mass evolution. The detection rate of TDEs depends on the theoretical capture rate stars in the galactic center, duration of TDE observations, black hole mass function (BHMF) and instrumental parameters such as sensitivity, cadence and integration time which we will be constructed in chapter 5. Thus, the observed detection rate for various missions can be used to measure the BHMF.

2.5 TDE surveys and follow-ups

The search for TDEs has increased in a decade with the various ASS missions and follow-ups from space and ground-based detectors. The transient is detected through ongoing missions such as Monitor of All-sky X-ray Image (MAXI), Astrosat SSM in X-rays and Zwicky Transient Factory (ZTF; iPTF), Optical Gravitational Lensing Experiment (OGLE), All Sky Automated Survey for Supernova (ASAS SN) and Panoramic Survey Telescope and Rapid Response System (Pan-STARRS) in the optical band. The future surveys such as Large Synoptic Survey

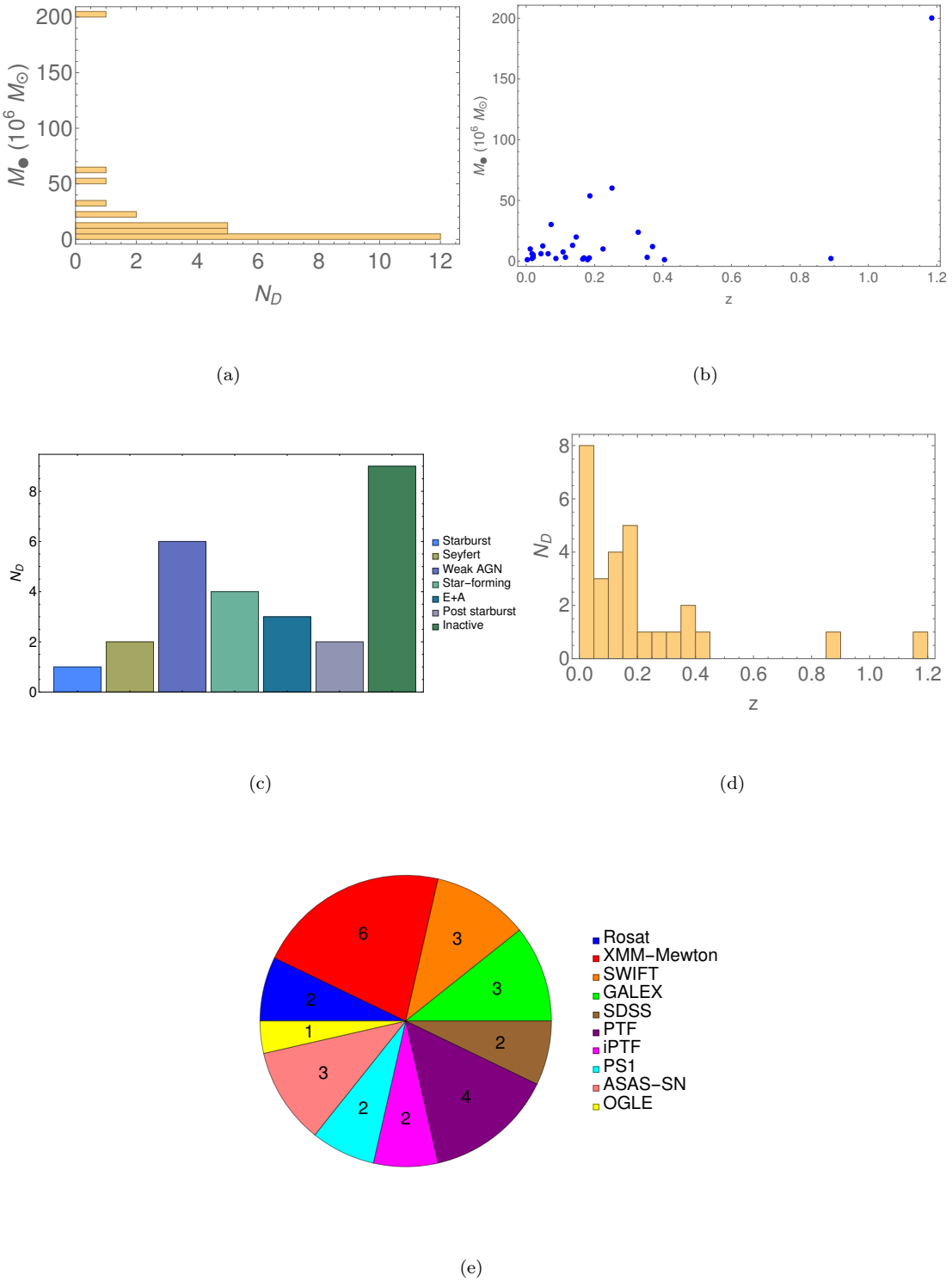

FIGURE 2.4: The distribution of TDEs is shown along black hole mass in (a), host galaxies in (c), redshift in (d) and detected instrument in (e). The distribution in black hole mass and redshift are shown in (b). The TDE detections are dominated in the inactive, weak AGN and star-forming galaxies which comprises of 19 out of 28 TDEs listed with highest in the inactive galaxies with low mass supermassive black hole galaxies at low redshift.

S. No.	Observation	z	t_{trig}	Instrument	Host galaxy	Reference
1	NGC 5905	0.01124	11-7-1990	Rosat	Starbust galaxy	Bade et al. (1996)
2	IC 3599	0.021	10-12-1990	Rosat	Seyfert 1.9 galaxy	Komossa & Bade (1999)
3	XMM J152130+0.74916	0.179	23-8-2000	XMM-Newton	Inactive galaxy	Lin et al. (2015)
4	NGC 3599	0.0028	22-11-2003	XMM-Newton	Low luminosity AGN	Esquej et al. (2008)
5	SDSS J132341.97+482701.3	0.0875	1-12-2003	XMM-Newton	Inactive galaxy	Esquej et al. (2008)
6	D3-13	0.3698	15-1-2004	GALEX UV	Inactive galaxy	Gezari et al. (2008)
7	D1-9	0.327	12-8-2004	GALEX UV	Inactive galaxy	Gezari et al. (2008)
8	J234201.40+010629.2	0.136	19-11-2005	SDSS (g)	Inactive galaxy	Velzen et al. (2011)
9	J232348.61-010810.3	0.251	20-11-2006	SDSS (g)	Star-forming galaxy	Velzen et al. (2011)
10	D23H-1	0.1855	4-9-2007	GALEX UV	Star-forming galaxy	Gezari et al. (2009)
11	PTF09ge	0.064	7-5-2009	PTF (R)	E+A galaxy	Arcavi et al. (2014)
12	PTF09axc	0.1146	20-6-2009	PTF (R)	E+A galaxy	Arcavi et al. (2014)
13	PTF09djl	0.184	24-7-2009	PTF (R)	Weak AGN	Arcavi et al. (2014)
14	PS1-10jh	0.1696	31-5-2010	PS1-MDS (g)	E+A galaxy	Gezari et al. (2012)
15	SDSS J120136.02+300305.5	0.146	10-6-2010	XMM-Newton	Inactive galaxy	Saxton et al. (2012)
16	PTF10iya	0.224	11-6-2010	PTF (R)	Star-forming galaxy	Cenko et al. (2012)
17	PS1-11af	0.4046	30-12-2010	PS1 (g)	Inactive galaxy	Chornock et al. (2014)
18	SWFIT J1644+57	0.354	28-3-2011	SWIFT BAT	Star-forming galaxy	Burrows et al. (2011)
19	SWIFT J2058+0516	1.1853	27-5-2011	SWIFT BAT		Cenko et al. (2012)
20	SWIFT J1112.2-8238	0.89	16-6-2011	SWIFT BAT	Weak AGN	Brown et al. (2015)
21	XMMSL1 J061927.1-655311	0.0729	12-11-2012	XMM-Newton	Seyfert 1 galaxy	Saxton et al. (2014)
22	XMMSL1 J074008.2-853927	0.0173	1-4-2014	XMM-Newton	Inactive galaxy	Saxton et al. (2017)
23	ASASSN-14ae	0.0436	25-1-2014	ASAS-SN (V)	Weak AGN	Holoein et al. (2014)
24	ASASSN-14li	0.0206	22-11-2014	ASAS-SN (V)	Weak AGN	Holoein et al. (2016)
25	ASASSN-15oi	0.0484	14-8-2015	ASAS-SN (V)	Post starbust galaxy	Holoein et al. (2016)
26	OGLE16aaa	0.1655	2-1-2016	OGLE IV (I)	Weak AGN	Wyrzykowski et al. (2017)
27	iPTF16axa	0.108	29-5-2016	iPTF (g)	Inactive galaxy	Hung et al. (2017)
28	iPTF16fnl	0.016328	29-8-2016	iPTF (R)	Post starbust galaxy	Blagorodonova et al. (2017)

TABLE 2.1: The TDEs detection catalog is shown with the detection time, the detected instrument and the host galaxy properties.

Telescope (LSST) in optical and eROSITA in X-rays will further boost the detection rate of TDEs. The follow up of detected TDEs are done in X-rays by XMM-Newton, Swift XRT, and Chandra X-ray telescope, in UV bands by XMM-Newton Optical Monitors and Swift UVOT and in optical by XMM-Newton Optical Monitors, Swift UVOT and Pan-STARRS as shown in Fig 2.5.

India's multiwavelength space mission ASTROSAT has payloads such as SSM for

monitoring the sky in nearly every six hours with a sensitivity of ∼30 mcrab, besides UVIT to observe in far ultraviolet (FUV) and near ultraviolet (NUV), and soft X-ray telescope (SXT) to observe in X-ray 0.2-10 keV bands. The 4m International Liquid Mirror Telescope (ILMT) in Devasthal, India is entirely dedicated to photometry and astrometry direct imaging surveys. ILMT points toward the zenith and scans the strip of the sky every night with limiting magnitude of 22 in i band and sub-arcsecond resolution. With a cadence of one night and higher sensitivity in single integration, ILMT provides a potential mission for TDE search. The 3.6 m Devasthal Optical Telescope (DOT) observes in optical and near-infrared bands with a high sensitivity. The 4k × 4k CCD imager (5 -10 arcmin) covers UVBRI bands with a limiting magnitude of 24 in the R band. The 2 m Himalayan Chandra Telescope (HCT) performs imaging in Bessell UBVRI bands with a limiting magnitude of 22.2 in R band and spectroscopy with a resolution of 300 and a limiting magnitude of 18.5 in V band using HFOSC. The Hanle Echelle Spectrograph (HESP) in HCT covers the entire optical wavelength with a spectral resolution of 30000 and 60000.

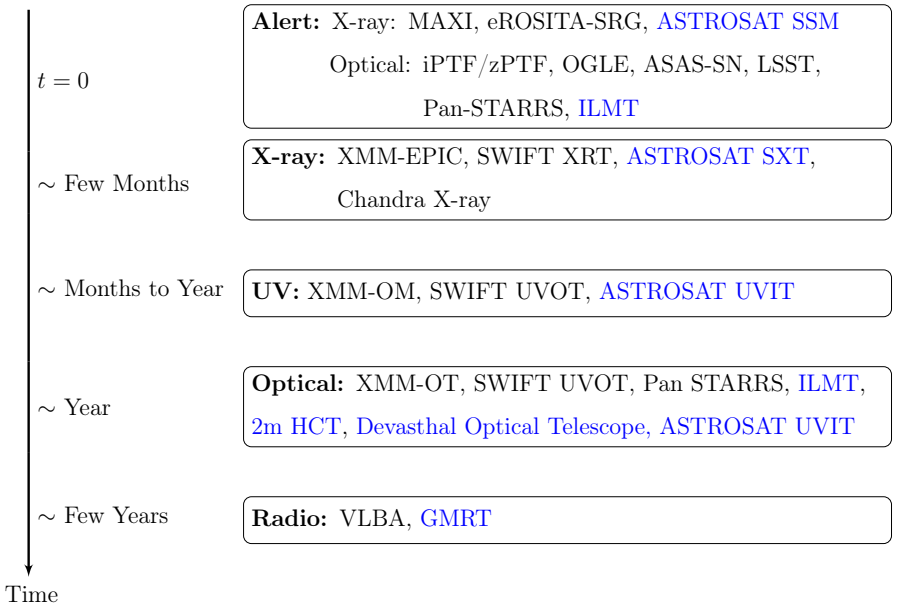

FIGURE 2.5: The detection and follow up missions for TDEs are shown along with the typical timescale of observations in various spectral bands starting from the time of the alert. The blue color highlights Indian observatories.

Given that a high detectable event rate will become possible soon with eROSITA in X-rays and iPTF/ZTF, ASAS SN and Pan-STARRS in the optical, there are several opportunities available currently and in the future. In the Indian context, it is possible that ILMT can be used for picking up these events. Once a trigger is received, there could be follows up in X-rays (SXT), UV (UVIT), Optical (DOT, HCT) and in Radio (GMRT) at the appropriate times given in Fig. 2.5. With the DOT we can probe TDEs longer and also study fainter sources.

The ratio of tidal radius to schwarzchild radius $\frac{r_t}{R_s} \simeq 109 \left(\frac{M_\bullet}{10^6 M_\odot}\right)^{-2/3} \left(\frac{\rho_\star}{\rho_\odot}\right)^{-1/3}$, where $\rho_\star$ is the mean density of star. For high density stars such as neutron stars and white dwarfs, the star is directly consumed rather than disrupted. The inspiralling of star around black holes emits gravitational radiation and is known as EMRIs. For a separation of radius r, the frequency of emission is $\nu \sim c/r$ and since $r > R_S = 2GM_\bullet/c^2$, $\nu < 0.1\ M_6$ Hz, which is less than the detectable range of Laser Interferometer Gravitational-Wave Observatory (LIGO). The future mission European Laser Interferometer Space Antenna (eLISA) will be able to detect these EMRIs. This multi observations that includes the electromagnetic radiation and gravitational radiation will be useful in studying the dynamics close to black holes.

2.6 Summary

The TDEs are observed in various spectral bands ranging from X-ray to radio. The TDEs are characterized by the broad Hα, Hβ and in some cases He emission lines. The dominance of He line in the spectra indicates the disruption of an evolved main sequence star. The nature of host galaxies is obtained through the spectra taken before or after the TDE fade away. The absence of X-ray observations of the galactic center prior to an event is an indication of inactive galaxies. The

host galaxy of TDEs need not necessarily be an inactive galaxy and can be a weak AGN or star-forming galaxy. The TDEs are dominated at low redshift by low mass supermassive black holes. The follow-ups of these TDEs after an alert from all-sky survey mission should be instantaneous to catch the event during its initial phase and peak luminosity in X-ray band which is close to the bolometric luminosity. The imaging and the spectroscopy of the source and the host galaxy (prior to or after fading of transient) is required to confirm the transient as TDE. The accretion model of TDEs is important to obtain the physical parameters such as black hole mass $M_\bullet$ and star mass $M_\star$.

We will construct the dynamical model to calculate the TDE rates in chapter 5 and accretion models in chapter 6. The aim of the theoretical models is to reproduce the observed light curves and deduce parameters such as $M_\bullet$, $M_\star$, E, J, black hole spin j and other model-dependent parameters. From the parameters obtained through a fit to observations, we can study black hole mass demographics such as BHMFs and occurrence of host galaxies as a function of redshift. This exercise is done in chapter 7.

Chapter 3

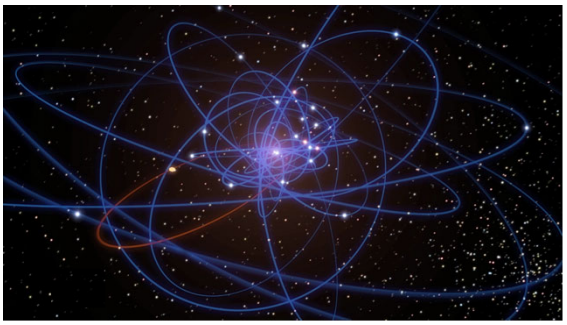

Image: ESO/MPE/M. Schartmann

Stellar dynamics around black holes

In this chapter, we introduce the basic equations of dynamics of stars around black holes. We will discuss the evolution of stars in phase space (E, J) and describe the phenomena of the loss cone: a hole in phase space where the stars are lost into the black hole. The continuous supply of stars into this hole is made possible due to gravitational encounters which is described by the Fokker-Planck equation. We will discuss various approaches to the problem starting from sub-thermal diffusion (Peebles 1972) leading upto the theory of Cohn and Kulsrud (1978), and more modern approaches with their caveats.

3.1 Introduction

The dynamics of stars in the galaxy depends on the black hole at the galactic center and the other stars. The distribution function (DF) of stars depends on

the structure of galactic nuclei which can be symmetric, axis-symmetric or triaxial nuclei (Merritt 2013a). The spherical distribution of stars is the simplest approximation as the potential and the density is a function of radius r only (Peebles 1972; Bahcall and Wolf 1976; Wang and Merritt 2004; Stone and Metzger 2016). The potential is dominated by the black hole at the inner radius and by stars at the outer radius far away to the black hole. The black hole potential is given by

$$\Phi_\bullet = -\frac{GM_\bullet}{r}, \tag{3.1}$$

whereas the stellar potential depends on the density distribution $\rho_\star$ of stars and is given by Poisson equation,

$$\nabla^2\Phi_\star = 4\pi G\rho_\star, \tag{3.2}$$

where G is gravitational constant. The total potential is given by $\Phi = \Phi_\bullet + \Phi_\star$. The radius below which the black hole potential dominates over stellar potential is the radius of influence r_h which is calculated assuming that the stellar distribution is virialized (Rees 1988; Phinney 1989).

3.2 Virial theorem

A stellar system consisting of N stars have kinetic energy K given by

$$K = \sum_{i=1}^{N} \frac{1}{2} m_i v_i^2, \tag{3.3}$$

and potential energy W given by

$$W = -\frac{G}{2}\sum_{i\neq j}\frac{m_i\, m_j}{r_{ij}}, \tag{3.4}$$

where m_i is the star mass with velocity v_i and $r_{ij} = r_i = r_j$ is the separation between i_{th} and j_{th} star where the distance is measured from the galactic center. The moment of inertia is given by

$$I = \sum_{i=1}^{N} m_i r_i^2, \tag{3.5}$$

and differentiating twice with time t gives

$$\frac{1}{2}\frac{\mathrm{d}^2 I}{\mathrm{d}t^2} = \sum_{i=1}^{N} m_i \left[\dot{r}_i^2 + r_i\ddot{r}_i\right], \tag{3.6}$$

where dot represents derivative with time. Using eqn (3.3), $\dot{r}_i = v_i$, $\sum_{i=1}^{N} m_i\dot{r}_i^2 = 2K$. The force on the i_{th} star is given by $F_i = m_i\ddot{r}_i = -\nabla\Phi_\star|_{r=r_i}$ and using potential given by

$$\Phi_\star(r_i) = -G\sum_{j=1}^{N}\frac{m_i\, m_j}{|r_i - r_j|}, \tag{3.7}$$

we obtain

$$\sum m_i \ddot{r}_i r_i = -\frac{G}{2} \sum_{i \neq j} \frac{m_i \, m_j}{|r_i - r_j|} = W. \tag{3.8}$$

Thus eqn (3.6) is given by

$$\frac{1}{2} \frac{\mathrm{d}^2 I}{\mathrm{d}t^2} = 2K + W, \tag{3.9}$$

and taking an average over time T gives

$$\frac{1}{2} \left\langle \frac{\mathrm{d}^2 I}{\mathrm{d}t^2} \right\rangle = 2 \langle K \rangle + \langle W \rangle , \tag{3.10}$$

where

$$\langle A \rangle = \frac{1}{T} \int_0^T A \, \mathrm{d}T, \tag{3.11}$$

and A is $\mathrm{d}^2 I / \mathrm{d}t^2, K$ and W. For a virialized system, the stars would settle in an equilibrium state such that the time average variation of I is too small to be negligible and is taken to be zero such that $2 \langle K \rangle + \langle W \rangle = 0$ (Chandrasekhar 1939). Thus, the total energy of a virialized system is given by

$$E = K + W = \frac{W}{2} = -K. \tag{3.12}$$

The velocity of the virialized system is given by velocity dispersion σ which results in the stellar potential $\Phi_\star = -\sigma^2$. The black hole potential dominates if $\Phi_\bullet > \Phi_\star$,

which results in $r < GM_\bullet/\sigma^2$ and the radius of influence is given by

$$r_h = \frac{GM_\bullet}{\sigma^2}. \tag{3.13}$$

3.3 Distribution function (DF)

The stellar dynamics depends on the star's energy E, angular momentum J and distribution of stars in the galactic center. The distribution function of stars $f(\boldsymbol{X},\ \boldsymbol{v},\ t)$ in the six dimensional phase space whose coordinates are three spatial coordinates ($\boldsymbol{X} = \{x,\ y,\ z\}$) and three velocity coordinates ($\boldsymbol{v} = \{v_x,\ v_y,\ v_z\}$), is defined as the number of stars in phase space volume $\mathrm{d}^3\boldsymbol{X}\mathrm{d}^3\boldsymbol{v}$. The number density distribution of the star is given by

$$n = \int\int\int \mathrm{d}^3\boldsymbol{v}\ f(\boldsymbol{X},\ \boldsymbol{v},\ t). \tag{3.14}$$

We have considered the stellar distribution to be spherical in nature such that the spatial volume in spherical coordinate $(r,\ \theta,\ \phi)$ is given by $\mathrm{d}^3\boldsymbol{X} = r^2 \sin\theta \mathrm{d}r\mathrm{d}\theta\mathrm{d}\phi$. The velocity of star is given by $\boldsymbol{v} = (v_r,\ v_\theta,\ v_\phi)$ and the distribution is isotropic if $v_r = v_\theta = v_\phi$. The velocity volume is given by $\mathrm{d}^3\boldsymbol{v} = 2\pi v_t \mathrm{d}v_t \mathrm{d}v_r$, with radial velocity v_r and tangential velocity $v_t = \sqrt{v_\theta^2 + v_\phi^2}$ with total velocity $v^2 = v_r^2 + v_t^2$.

The energy E and the angular momentum J per unit mass of an orbit is given by

$$E = \Phi(r) - \frac{v^2}{2} = \Phi(r) - \frac{1}{2}\left(v_r^2 + v_t^2\right) \quad \text{and} \quad J = rv_t, \tag{3.15}$$

where E is taken such that $E > 0$ corresponds to bound orbit requiring $\Phi(r) > 0$. The Jacobian transformation from $(v_r,\ v_t)$ to $(E,\ J)$ is given by

$$\mathrm{d}v_r \mathrm{d}v_t = \begin{vmatrix} \frac{\mathrm{d}v_r}{\mathrm{d}E} & \frac{\mathrm{d}v_r}{\mathrm{d}J} \\ \frac{\mathrm{d}v_t}{\mathrm{d}E} & \frac{\mathrm{d}v_t}{\mathrm{d}J} \end{vmatrix} \mathrm{d}E\mathrm{d}J = -\frac{1}{r}\frac{1}{\sqrt{2(\Phi(r) - E) - \frac{J^2}{r^2}}}\mathrm{d}E\mathrm{d}J \tag{3.16}$$

Using eqn (3.14) and (3.16), we obtained

$$n(r) = 2\pi \int_0^{\Phi(r)} \mathrm{d}E \int_0^{\sqrt{2r^2(\Phi(r)-E)}} \mathrm{d}J \frac{J}{r^2} \frac{f(E,\ J)}{\sqrt{2(\Phi(r) - E) - \frac{J^2}{r^2}}}. \tag{3.17}$$

The density of stellar distribution is an observable parameter, so we need an inversion to obtain the distribution function for the observed density structure. For an isotropic distribution, $\mathrm{d}^3\boldsymbol{v} = 4\pi v^2 \mathrm{d}v$, the distribution function is a function of energy alone, $f(E,\ J) = f(E)$, and using eqn (3.15), eqn (3.14) reduces to

$$n(r) = 4\sqrt{2}\pi \int_0^{\Phi(r)} \mathrm{d}E f(E) \sqrt{\Phi(r) - E}. \tag{3.18}$$

Using Abel's inversion given by

$$h(x) = \int_0^x \mathrm{d}t \ \ \frac{g(t)}{(x-t)^\alpha} \quad \Rightarrow \quad g(t) = \frac{\sin \pi\alpha}{\pi} \frac{\mathrm{d}}{\mathrm{d}t} \int_0^t \mathrm{d}x \frac{h(x)}{(t-x)^{1-\alpha}}, \tag{3.19}$$

for $0 < \alpha < 1$, we obtain using eqn (3.18) the distribution function $f(E)$ given by

$$f(E) = \frac{1}{\sqrt{8}\pi^2}\frac{\mathrm{d}}{\mathrm{d}E}\int_0^E \frac{\mathrm{d}\Phi}{\sqrt{E-\Phi}}\frac{\mathrm{d}n_\star}{\mathrm{d}\Phi}. \tag{3.20}$$

This is called as Eddington's formula (eg. Binney and Tremaine 2008) and using this one can generate the distribution function provided the density is given for an isotropic spherical distribution of stars.

For a stellar distribution $n(r) = n_0(r/r_0)^{-\gamma}$ with potential Φ dominated by the black hole (eqn 3.1) where n_0 and r_0 are constants, the density is given by $n = n_0 r_0^\gamma (GM_\bullet)^{-\gamma}\Phi^\gamma$ and using eqn (3.20), the distribution function is given by

$$f(E) = \frac{n_0 r_0^\gamma}{\sqrt{8}\pi^{3/2}}(GM_\bullet)^{-\gamma}\frac{\Gamma(\gamma+1)}{\Gamma(\gamma-1/2)}E^p, \tag{3.21}$$

with constraints $\gamma > 1/2$ for $f(E) > 0$ and $p = \gamma - 3/2$. The more general solution for a single power law density model that includes the stellar potential will be shown in chapter 5.

Peebles (1972) has considered a single stellar population where the black hole potential dominates and assumed a distribution function $f(E) = KE^p$; this implies that the density, using eqn (3.18) is given by

$$n(r) = \frac{\sqrt{2}\pi^{3/2}K}{1+p}\frac{\Gamma(2+p)}{\Gamma(p+5/2)}(GM_\bullet)^{p+3/2}r^{-p-3/2}, \tag{3.22}$$

and the mean square velocity is given by

$$\left\langle v^2 \right\rangle = \frac{1}{n(r)} \int \mathrm{d}^3 v \; v^2 f(E) = \frac{3\sqrt{2}\pi^{3/2} K}{(1+p)(2+p)} \frac{\Gamma(3+p)}{\Gamma(7/2+p)} \frac{(GM_\bullet)^{p+5/2}}{n(r)} r^{-p-5/2} \tag{3.23a}$$

$$= \frac{6}{5+2p} \frac{GM_\bullet}{r} \tag{3.23b}$$

Thus the mean energy is given by

$$\langle E \rangle (r) = \frac{GM_\bullet}{r} - \frac{\langle v^2 \rangle}{2} = \frac{2+2p}{5+2p} \frac{GM_\bullet}{r}. \tag{3.24}$$

In a thermal equilibrium, the $\langle v^2 \rangle$ is constant which results in $n(r)|_{th} \propto r^{-p-5/2}$ and is lower than the actual density derived in eqn (3.22). The density gradient $\mathrm{d} \log(n(r))/\mathrm{d}r$ in thermal equilibrium declines faster than the actual gradient implying that the system is sub-thermal and this leads to the diffusion of the stars.

Peebles (1972) showed that the number rate of star diffusion is $\mathrm{d}N(E)/\mathrm{d}t \propto E^{2p-3/2}$. In a steady state, he assumed that the rate of star diffusion is constant which results in $p = 3/4$ and the density $n(r) \propto r^{-9/4}$.

Bahcall and Wolf (1976) assumed a distribution function similar to Peebles (1972) for an isotropic single star mass distribution and derived a diffusion equation by taking into account the star-star interaction which is the Fokker-Planck equation in energy space as will be discussed in §3.5. They showed that the in a steady state, the $p = 3/4$ leads to an infinite negative energy flux $\mathrm{d}E/\mathrm{d}t$ that results in

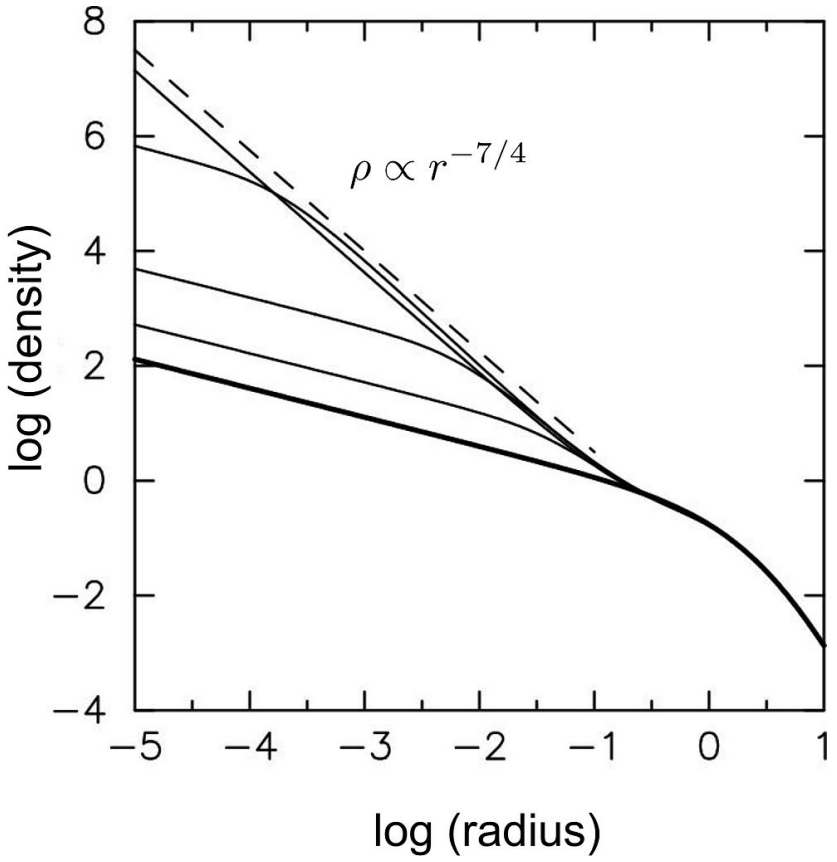

FIGURE 3.1: The number density of star distribution along radius that increases with time as shown in various curves and attain a density structure similar to Bahcall-Wolf cusp implying that the galactic center attained a steady state. Courtesy: Merritt (2013b)

a rapid outward diffusion of stars which is unphysical and thus instead of number rate being constant in a steady state, the energy flux should be constant, which results in $p = 1/4$ with density $n(r) \propto r^{-7/4}$. This is called as the Bahcall-Wolf cusp and is shown in Fig 3.1.

3.4 Stellar systems

Consider a system composed of N gravitationally interacting point mass of mass M and the number density of the star distribution is n. A star moving with velocity

v in the gravitational field of other star experience a force GM/b^2, where b is the impact parameter for an interaction time $\sim 2b/v$. Then the change in velocity in perpendicular direction is given by

$$\delta v_\perp \sim \frac{GM}{b^2}\frac{2b}{v} = \frac{2GM}{bv}. \tag{3.25}$$

The average rate of change in velocity is given by

$$\frac{\mathrm{d}}{\mathrm{d}t}\left\langle \delta v_\perp^2 \right\rangle = \int_{b_{min}}^{b_{max}} \delta v_\perp^2 \, nv2\pi b \, \mathrm{d}b, \tag{3.26}$$

where b_{min} and b_{max} are the minimum and maximum impact parameters. The eqn (3.26) using eqn (3.25) is given by

$$\frac{\mathrm{d}}{\mathrm{d}t}\left\langle \delta v_\perp^2 \right\rangle = \int_{b_{min}}^{b_{max}} \left(\frac{2GM}{bv}\right)^2 nv2\pi b \, \mathrm{d}b = \frac{8\pi G^2 M^2 n}{v} \ln\left(\frac{b_{max}}{b_{min}}\right). \tag{3.27}$$

The b_{max} is the maximum radius of the system and since $\delta v_\perp < v$, we get $b > 2GM/v^2$ which gives the b_{min} given by

$$b_{min} \simeq GM/v^2. \tag{3.28}$$

The maximum radius of the system $R = GM_T/c^2$, where total mass $M_T = NM$ and using this we obtain $b_{min} = R/N$ which reduces the eqn (3.27) to

$$\frac{\mathrm{d}}{\mathrm{d}t}\left\langle \delta v_{\perp}^{2}\right\rangle = \frac{8\pi G^{2}M^{2}n}{v}\ln N. \tag{3.29}$$

For an isotropic distribution of stars, the relaxation time is the time required to change $\langle \delta v_{\perp}^{2}\rangle = v^{2}$ and by considering $(\mathrm{d}/\mathrm{d}t)\langle \delta v_{\perp}^{2}\rangle = \langle \delta v_{\perp}^{2}\rangle / t_{r}$, the relaxation time t_r is given by

$$t_{r} = \frac{v^{3}}{8\pi G^{2}M^{2}n\ln N}. \tag{3.30}$$

The crossing time of the system is given by

$$t_{c} = \frac{R}{v}. \tag{3.31}$$

The ratio of relaxation time to crossing time is given by

$$\frac{t_{r}}{t_{c}} = \frac{v^{3}}{8\pi G^{2}m^{2}n\ln N}\frac{v}{R} = \frac{v^{4}R^{2}}{8\pi G^{2}M^{2}N\ln N}\frac{4\pi}{3}, \tag{3.32}$$

where $n = N/(4\pi R^{3}/3)$ and for a virilized system $v^{2} = GM_{T}/R$, which gives

$$\frac{t_{r}}{t_{c}} = \frac{1}{6}\frac{M_{T}^{2}}{M^{2}}\frac{1}{N\ln N} = \frac{N}{6\ln N}. \tag{3.33}$$

A more detailed calculation gives $t_r = (N/(10\ln N))t_c$. The relaxation timescale and the crossing time scales for various systems are given in Table 3.1.

Object	N	t_c (yr)	t_r (yr)
Galaxy	10^{11}	10^8	10^{16}
Galactic nuclei	10^8	10^4	10^{10}
Globular cluster	10^6	10^5	10^9

TABLE 3.1: The relaxation time and the crossing time for various objects are shown.

In the course of gravitational encounters, the stars may come too close for a face off collision. The collision time $t_{coll} \sim (n\Sigma v_\star)^{-1}$, where number density $n = N/r^3$, Σ is cross section $= \pi(2R_\star)^2$ where $R_\star$ is the radius of star, and $v_\star$ is the velocity. The ratio of collision time to crossing time is

$$\frac{t_{coll}}{t_c} = \frac{R^2}{4\pi N R_\star^2}, \tag{3.34}$$

and for a virialized system $v^2 = GNM/r$ and star velocity $v_\star = \sqrt{2GM/R_\star}$ which results in

$$\frac{t_{coll}}{t_c} = 0.02N \left(\frac{v_\star}{v}\right)^4. \tag{3.35}$$

The ratio of t_{coll} and the t_r is given by

$$\frac{t_{coll}}{t_r} = 0.2 \left(\frac{v_\star}{v}\right)^4 \ln N, \tag{3.36}$$

and $t_{coll} \gg t_r$ which means that the inelastic scattering plays a little role in structure.

Since the galactic center contains multiple star type, the evolution of galactic center can lead to different evolution time and density structure which leads to mass segregation. The segregation timescale for stars of mass $M_\star$ is of the same order as the relaxation timescale, and scales with $M_\star$ as

$$t_S \sim t_r \frac{\langle M_\star \rangle}{M_\star}, \tag{3.37}$$

where $\langle M_\star \rangle$ is the average mass in the galactic center and this concludes that the high mass stars attain a steady state earlier than the low mass stars.

3.4.1 Characterstic scales

The dynamics of stars in the galactic center are governed by various lengthscale. We now compare the various length scales.

1. Schwarzschild radius is horizon of a non-rotating black hole and is given by

$$R_s = \frac{2GM_\bullet}{c^2} = 3 \times 10^{11} \left(\frac{M_\bullet}{10^6 M_\odot}\right) \text{cm} \tag{3.38}$$

2. Radius of influence, r_h is the radius below which BHs gravity dominate over other stars gravity, given by

$$r_h = \frac{GM_{BH}}{\sigma^2} = 3.38 \times 10^{17} \left(\frac{M_\bullet}{10^6 M_\odot}\right) \left(\frac{\sigma}{200\text{kmSec}^{-1}}\right)^{-2} \text{ cm} \tag{3.39}$$

3. Tidal radius R_t is the maximal distance from the MBH where the tidal forces of the MBH can overwhelm the stellar self-gravity and tear the star apart:

$$r_t = \eta_t^{2/3} \left(\frac{M_\star}{M_\odot}\right)^{1/3} R_\star \simeq 6.96 \times 10^{12} \eta^{-1/3} \left(\frac{M_\bullet}{10^6 M_\odot}\right)^{\frac{1}{3}} \left(\frac{M_\star}{M_\odot}\right)^{-\frac{1}{3}} \left(\frac{R_\star}{R_\odot}\right) \text{cm} \tag{3.40}$$

4. A critical mass is implied and is given by the condition $R_t = R_s$

$$M_c \simeq 3 \times 10^8 M_\odot \left(\frac{M_\star}{M_\odot}\right)^{-\frac{1}{2}} \left(\frac{R_\star}{R_\odot}\right)^{\frac{3}{2}} \tag{3.41}$$

5. Collision radius is the minimal distance from the MBH where large angle deflections by close gravitational encounters are possible. Closer to the SMBH the relative velocity v between the interacting stars exceeds the escape velocity from the stellar surface, v_{esc}, and the distance of closest approach required for a large angle deflection becomes smaller than the stellar radius (i.e. when $v_{esc}^2 \sim GM_\star/R_\star < GM_\bullet/r \sim v^2$)

$$r_{col} \simeq 7 \times 10^{16} \left(\frac{M_\bullet}{10^6 M_\odot}\right) \left(\frac{M_\star}{M_\odot}\right)^{-1} \left(\frac{R_\star}{R_\odot}\right) \text{cm} \tag{3.42}$$

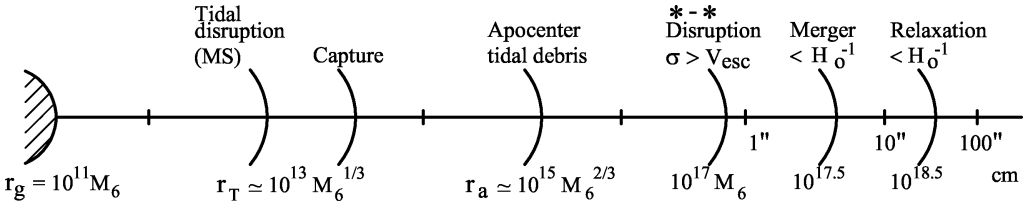

FIGURE 3.2: Shows various radii of physical importance.

The length scales are shown in Fig 3.2 and 3.3 and it can be seen that the tidal radius lies much below the radius of influence but is smaller than the Schwarzschild radius for higher mass black hole

3.5 Fokker-Planck equation

The distribution function of N body is $f^N(W_1, ..., W_N,\ t)$ can be reduced to k body distribution function through

$$f^k(W_1, ..., W_k,\ t) = \int \mathrm{d}^6 W_{k+1} ..... \mathrm{d}^6 W_N f^N(W_1, ..., W_N,\ t), \tag{3.43}$$

and

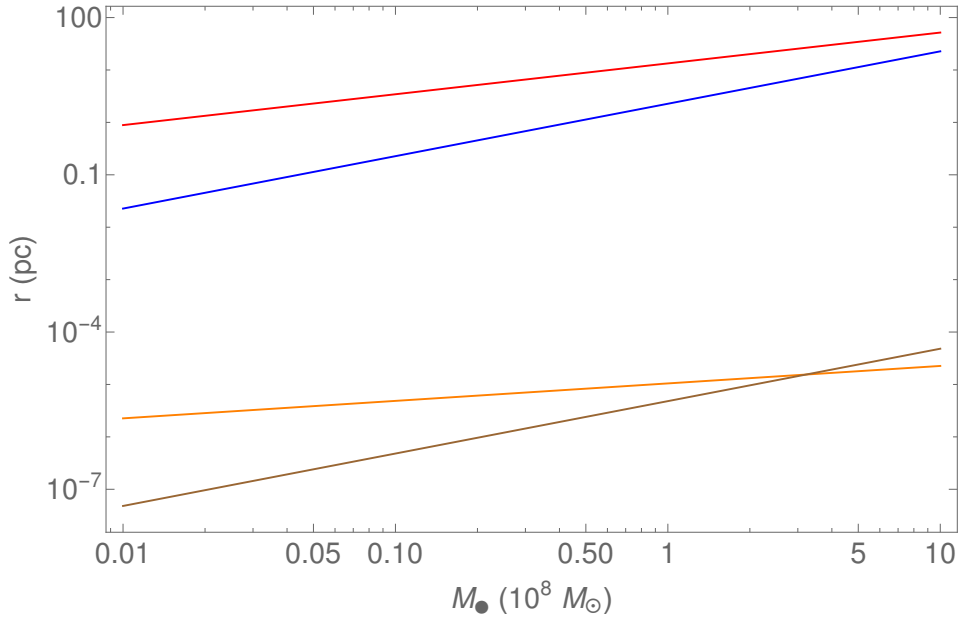

FIGURE 3.3: The plot shows the run of various radii vs mass of the black hole: from top to bottom, the collision radius r_c (blue), the radius of influence, r_h (red), the tidal radius, r_t (orange) with $\eta_t = 1$ and the Schwarzschild radius, R_s (brown). The star mass is taken to be solar mass.

$$\int \mathrm{d}^6W_1....\mathrm{d}^6W_k f^k(W_1,....,W_k,\ t) = 1. \tag{3.44}$$

We write the

$$f^1(W,\ t) = \int \mathrm{d}^6W_1....\mathrm{d}^6W_k f^k(W_1,....,W_k,\ t), \tag{3.45}$$

and a 2 body distribution function can be written in the form

$$f^2(W_1,\ W_2,\ t) = f(W_1,\ t)f(W_2,\ t) + g(W_1,\ W_2,\ t), \tag{3.46}$$

where $g(W_1,\ W_2,\ t)$ is a 2 body correlation function. The probability of finding a particular star in a unit volume of phase space centered on W_1 is

$$f(W_1|W_2) = \frac{f^2(W_1,\ W_2)}{\int \mathrm{d}^6W_1' f^2(W_1',\ W_2)} = \frac{f(W_1)f(W_2) + g(W_1,\ W_2,\ t)}{f(W_2) + \int \mathrm{d}^6W_1' g(W_1,\ W_2)}. \tag{3.47}$$

If $g(W_1,\ W_2) = 0$, then $f(W_1|W_2) = f(W_1)$. The kinetic energy of the system is given by

$$\langle K\rangle = \frac{1}{2}M\int \mathrm{d}^6W_1..\mathrm{d}^6W_N f^N(W_1,....,W_N,t)\sum_{\alpha=1}^{N} v_\alpha^2 = \frac{1}{2}NM\int \mathrm{d}^6W_1 f(W_1,\ t)v_1^2, \tag{3.48}$$

and the average potential is given by

$$\langle W\rangle \;= -\tfrac{1}{2}\int \mathrm{d}^6W_1..\mathrm{d}^6W_N f^N(W_1,....,W_N,t)\sum_{\alpha,\ \beta=1,\ \&\ \alpha\neq\beta}^{N}\frac{GM^2}{|\boldsymbol{X}_\alpha-\boldsymbol{X}_\beta|} \tag{3.49}$$

$$\tfrac{1}{2}M^2N(N-1)\int \mathrm{d}^6W_1\mathrm{d}^6W_2\frac{f^2(W_1,\ W_2,\ t)}{|X_2-X_1|}. \tag{3.50}$$

If correlation function is small such that $g(W_1,\ W_2,\ t) \ll f(W_1,\ t)f(W_2,\ t)$ and for $N \gg 1$, the potential energy is

$$W = -\frac{1}{2}GM^2N^2\int \mathrm{d}^6W_1\mathrm{d}^6W_2\frac{f(W_1,\ t)f(W_2,\ t)}{|X_2-X_1|} = \frac{1}{2}\int \mathrm{d}^3X\rho(X)\Phi(X). \tag{3.51}$$

Let $\Psi(W,\ \Delta W)\mathrm{d}^6(\Delta W)\Delta t$ be the probability that W is scattered to $W+\Delta W$, the distribution function evolution is given by the master equation

$$\frac{\mathrm{d}f}{\mathrm{d}t} = \Gamma(f) = \int \mathrm{d}^6(\Delta W)\left[\Psi(W-\Delta W,\Delta W)f(W-\Delta W) - \Psi(W,\Delta W)f(W)\right]. \tag{3.52}$$

In case of weak encounters $\delta v \ll v$, we expand the function $\Psi(W-\Delta W,\Delta W)f(W-\Delta W)$ in Taylor series so that

$$\Psi(W-\Delta W,\Delta W)f(W-\Delta W) = \Psi(W,\Delta W)f(W) - \sum_{i-1}^{6}\Delta W_i\frac{\partial}{\partial W_i}\left[\Psi(W,\Delta W)f(W)\right] + \frac{1}{2}\sum_{i,\ j=1}^{6}\Delta W_i\Delta W_j\frac{\partial^2}{\partial W_i\partial W_j}\left[\Psi(W,\Delta W)f(W)\right] + \mathcal{O}(\Delta W^3), \tag{3.53}$$

leading to

$$\frac{\mathrm{d}f}{\mathrm{d}t} = -\sum_{i=1}^{6} \frac{\partial}{\partial W_i} \left\{ D[\Delta W_i] f(W) \right\} + \frac{1}{2} \sum_{i=1}^{6} \frac{\partial^2}{\partial W_i \partial W_j} \left\{ D[\Delta W_i \Delta W_j] f(W) \right\}, \quad (3.54)$$

where $D[\Delta W_i]$ and $D[\Delta W_i \Delta W_j]$ are the diffusion coefficients given by

$$D[\Delta W_i] = \int \mathrm{d}^6(\Delta W) \Psi(W,\ \Delta W) \Delta W_i \quad (3.55)$$

$$D[\Delta W_i \Delta W_j] = \int \mathrm{d}^6(\Delta W) \Psi(W,\ \Delta W) \Delta W_i \Delta W_j. \quad (3.56)$$

The eqn (3.52) and (3.54) are the Fokker-Planck equations which is different from the diffusion equation given by

$$\frac{\partial f}{\partial t} = \sum_{i,\ j=1}^{6} \frac{\partial}{\partial W_i} \left(c_{ij} \frac{\partial}{\partial W_j} f(W) \right), \quad (3.57)$$

where c_{ij} are the diffusion coefficients. In action-angle variables $(J,\ \theta)$, the Hamiltonian $H(J,\ t)$ and distribution function is taken to be $f(J,\ t)$. Thus

$$\frac{\mathrm{d}f}{\mathrm{d}t} = \frac{\partial f}{\partial t} + \dot{J}_i \frac{\partial f}{\partial J_i} + \dot{\theta}_i \frac{\partial f}{\partial \theta_i} = \Gamma(f). \quad (3.58)$$

The Hamilton's equation are $\dot{J}_i = -\partial H / \partial \theta_i = 0$ and $\dot{\theta}_i = \partial H / \partial J_i =$ constant are applied to give

$$\frac{\partial f}{\partial t} = \frac{1}{(2\pi)^3}\int \mathrm{d}^3\theta\Gamma(f) \tag{3.59}$$

$$= -\frac{\partial}{\partial J_i}\left\{f\bar{D}[\Delta J_i]\right\} + \frac{1}{2}\frac{\partial^2}{\partial J_i \partial J_j}\left\{d\bar{D}[\Delta J_i \Delta J_j]\right\}, \tag{3.60}$$

where the orbit averaged diffusion coefficients are given by

$$\bar{D}[\Delta J_i] = \frac{1}{(2\pi)^3}\int \mathrm{d}^3\theta D[\Delta J_i] \tag{3.61}$$

$$\bar{D}[\Delta J_i \Delta J_j] = \frac{1}{(2\pi)^3}\int \mathrm{d}^3\theta D[\Delta J_i \Delta J_j]. \tag{3.62}$$

Let the number of stars in a volume V be given by $N_V(t)$, then

$$N_V(t) = N\int_V \mathrm{d}^3 J \int \mathrm{d}^3\theta f(J,\ t) = (2\pi)^3 N \int_V \mathrm{d}^3 J f(J,\ t). \tag{3.63}$$

Thus the number rate of stars is given by

$$\frac{\mathrm{d}N_V}{\mathrm{d}t} = (2\pi)^3 \int_V \mathrm{d}^3 J \frac{\partial f}{\partial t} = -\int_V \mathrm{d}^3 J \frac{\partial F_i}{\partial J_i}, \tag{3.64}$$

where F_i is given by

$$F_i = (2\pi)^3 \left[f\bar{D}[\Delta J_i] - \frac{1}{2}\frac{\partial}{\partial J_i}\left\{f\bar{D}[\Delta J_i \Delta J_j]\right\}\right], \tag{3.65}$$

and using the Gauss divergence theorem, we find

$$\frac{\mathrm{d}N_V}{\mathrm{d}t} = -\oint_S \mathrm{d}^2 S_i F_i, \tag{3.66}$$

where S is the surface element in angular momentum phase space.

3.5.1 Fokker-planck in $\{E,\ J\}$ phase space

The evolution of DF due to the star-star interaction results in the diffusion of stars due to the change in velocities which causes a change in energy and angular momentum is given by the Fokker-Planck equation. We derive the Fokker-Planck equation in terms of the energy E and dimensionless angular momentum $R = J^2/J_c^2$, where $J = rv_t$ and $J_c^2 = GM_\bullet/2E$ is the circular angular momentum. The transition probability $\psi(E;\Delta E,\ R;\Delta R)\mathrm{d}\Delta E\mathrm{d}\Delta R$ for a star with E and R to change by ΔE and ΔR in time Δt, so that the changed distribution function is given by (Lightman and Shapiro 1977; Cohn and Kulsrud 1978)

$$f(E,\ R,\ t+\Delta t) = \int f(E-\Delta E,\ R-\Delta R,\ t)\psi(E;\Delta E,\ R;\Delta R)\ \mathrm{d}\Delta E\mathrm{d}\Delta R. \tag{3.67}$$

Expanding $f(E,\ R,\ t+\Delta t)$ using Taylor series in Δt and $f(E-\Delta E,\ R-\Delta R,\ t)$ and $\psi(E;\Delta E,\ R;\Delta R)$ using Taylor series in ΔE and ΔR, we obtain the Fokker-Planck equation given by (eg. Lightman and Shapiro 1977)

$$\frac{\partial f(E,\ R,\ t)}{\partial t} + \mathcal{O}(\Delta t) = -\frac{\partial}{\partial E}\left(f(E,\ R,\ t)\left\langle \Delta E\right\rangle_t\right) - \frac{\partial}{\partial R}\left(f(E,\ R,\ t)\left\langle \Delta R\right\rangle_t\right) + \frac{1}{2}\frac{\partial^2}{\partial E^2}\left(f(E,\ R,\ t)\left\langle (\Delta E)^2\right\rangle_t\right) + \frac{1}{2}\frac{\partial^2}{\partial R^2}\left(f(E,\ R,\ t)\left\langle (\Delta E)^2\right\rangle_t\right) + \frac{\partial^2}{\partial E \partial R}\left(f(E,\ R,\ t)\left\langle \Delta E \Delta R\right\rangle_t\right) + \mathcal{O}[\left\langle (\Delta E)^3\right\rangle_t] + \mathcal{O}[\left\langle (\Delta R)^3\right\rangle_t] + \mathcal{O}[\langle (\Delta E \Delta R)\rangle_t], \tag{3.68}$$

where the diffusion coefficients are given by (Lightman and Shapiro 1977)

$$\left\langle \Delta X\right\rangle_t = \frac{1}{\Delta t}\int \psi(E;\Delta E,\ R;\Delta R)\Delta X\ \mathrm{d}\Delta E \mathrm{d}\Delta R, \tag{3.69a}$$

$$\left\langle (\Delta X)^2\right\rangle_t = \frac{1}{\Delta t}\int \psi(E;\Delta E,\ R;\Delta R)(\Delta X)^2\ \mathrm{d}\Delta E \mathrm{d}\Delta R, \tag{3.69b}$$

$$\left\langle \Delta X \Delta Y\right\rangle_t = \frac{1}{\Delta t}\int \psi(E;\Delta E,\ R;\Delta R)\Delta X \Delta Y\ \mathrm{d}\Delta E \mathrm{d}\Delta R, \tag{3.69c}$$

with X and Y are E and R. The higher order terms are neglected as they are small compared to the first and second order terms as will be justified later, which results in

$$\frac{\partial f(E,\ R,\ t)}{\partial t} = -\frac{\partial}{\partial E}\left(f(E,\ R,\ t)\left\langle \Delta E\right\rangle_t\right) - \frac{\partial}{\partial R}\left(f(E,\ R,\ t)\left\langle \Delta R\right\rangle_t\right) + \frac{1}{2}\frac{\partial^2}{\partial E^2}\left(f(E,\ R,\ t)\left\langle (\Delta E)^2\right\rangle_t\right) + \frac{1}{2}\frac{\partial^2}{\partial R^2}\left(f(E,\ R,\ t)\left\langle (\Delta E)^2\right\rangle_t\right) + \frac{\partial^2}{\partial E \partial R}\left(f(E,\ R,\ t)\left\langle \Delta E \Delta R\right\rangle_t\right). \tag{3.70}$$

Next section, we calculate the diffusion coefficients in terms of velocity and convert it in terms of E and R.

3.5.2 Gravitational scattering

We consider a test star with mass m and velocity $\boldsymbol{v}$ that encounter a field star with mass m_f and velocity $\boldsymbol{v_f}$. The separation between the test and field star is $\boldsymbol{r} = \boldsymbol{r}_s - \boldsymbol{r}_f$ where $\boldsymbol{r}_s$ and $\boldsymbol{r}_f$ is the position of test and field star given by

$$\boldsymbol{r}_s = \boldsymbol{r}_{cm} + \frac{m_f}{m + m_f}\boldsymbol{r}, \tag{3.71a}$$

$$\boldsymbol{r}_f = \boldsymbol{r}_{cm} - \frac{m}{m + m_f}\boldsymbol{r}, \tag{3.71b}$$

where $\boldsymbol{r}_{cm}$ is the center of mass. In the center of mass coordinate, $\dot{\boldsymbol{r}}_{cm} = 0$ and hence the velocities are given by

$$\boldsymbol{v} = \frac{m_f}{m + m_f}\boldsymbol{u}, \tag{3.72a}$$

$$\boldsymbol{v}_f = -\frac{m}{m + m_f}\boldsymbol{u}, \tag{3.72b}$$

where $\boldsymbol{u} = \dot{\boldsymbol{r}} = \boldsymbol{v} - \boldsymbol{v}_f$ is the relative velocity and the equation of motion is given by

$$\ddot{\boldsymbol{r}} = -\frac{G(m+m_f)}{r^3}\boldsymbol{r}. \tag{3.73}$$

This equation represents the orbit of a star around an object of mass $M_c = m+m_f$. We use the Lagrangian dynamics to calculate the orbit of the star where the Lagrangian, $L(q,\ \dot{q}\ ,t) = T(q,\ \dot{q}\ ,t) - V(q,\ \dot{q}\ ,t)$, where T is the kinetic energy, V is the potential energy, q is the generalized coordinates and the Lagrangian equation of motion is given by

$$\frac{\partial}{\partial t}\left(\frac{\partial L(q,\ \dot{q}\ ,t)}{\partial \dot{q}}\right) - \frac{\partial L(q,\ \dot{q}\ ,t)}{\partial q} = 0. \tag{3.74}$$

For a Keplerian orbit in a plane and using spherical coordinate such that $q = (r,\ \theta)$, $T = (1/2)m(\dot{r}^2 + r^2\dot{\theta}^2)$ and the $V = -GM_cm/r$. The equation of motion is given by

$$\ddot{r} - r\dot{\theta}^2 + \frac{GM_c}{r^2} = 0 \tag{3.75a}$$

$$\dot{\theta} = \frac{J}{r^2}, \tag{3.75b}$$

where J is constant equal to the angular momentum of the orbit. Using $x = 1/r$, the eqn (3.75a) and (3.75b) gives

$$\frac{\mathrm{d}^2x}{\mathrm{d}\theta^2} = \frac{GM_c}{J^2} - x, \tag{3.76}$$

whose solution is the well known Kepler's equation

$$x = \frac{1}{r} = C\cos(\theta - \theta_0) + \frac{GM_c}{J^2}, \tag{3.77}$$

where C and θ_0 are the constants decided by the initial conditions. Let the initial separation that is perpendicular to the initial relative velocity vector $\boldsymbol{u}_0$ be b, the impact parameter of the encounter, the conserved angular momentum $J = bu_0$; hence the eqn (3.77) is given by

$$\frac{1}{r} = C\cos(\theta - \theta_0) + \frac{G(m+m_f)}{b^2u_0^2}. \tag{3.78}$$

As $t \to -\infty$, $r \to \infty$ and $\theta = 0$ which gives $\cos\theta_0 = -G(m+m_f)/(b^2u_0^2C)$. Thus, $\tan\theta_0 = -bu_0^2/(G(m+m_f))$. The velocity is given by $u = \dot{r} = Cu_0b\sin(\theta - \theta_0)$ and for $\theta = 0$, $u = -u_0$ which gives $\sin\theta_0 = 1/(bC)$. The point of closest approach is $\theta = \theta_0$ and the reduced particle velocity is deflected by an angle $\theta_{defl} = 2\theta_0 - \pi$. The deflection angle is $\pi/2$ at the impact parameter

$$b_{90} = \frac{G(m+m_f)}{u_0^2}, \tag{3.79}$$

and thus the deflection angle is given by $\theta_{defl} = 2\tan^{-1}(b_{90}/b)$. By energy conservation, the relative speed after the encounter is equal to the initial speed u_0.

Hence the parallel and perpendicular component of the $\boldsymbol{\Delta u}$ is given by

$$|\Delta u_{\perp}| = u_0 \sin\theta_{defl} = 2u_0 \frac{\tan(\theta_{defl}/2)}{1+\tan^2(\theta_{defl}/2)} = 2u_0 \frac{b/b_{90}}{1+(b/b_{90})^2}, \tag{3.80a}$$

$$|\Delta u_{||}| = u_0(1-\cos\theta_{defl}) = 2u_0 \frac{\tan^2(\theta_{defl}/2)}{1+\tan^2(\theta_{defl}/2)} = 2u_0 \frac{1}{1+(b/b_{90})^2}, \tag{3.80b}$$

and therefore the change in test star velocity is given by

$$|\Delta v_{\perp}| = 2\frac{m_f}{m+m_f} u_0 \frac{b/b_{90}}{1+(b/b_{90})^2}, \tag{3.81a}$$

$$|\Delta v_{||}| = 2\frac{m_f}{m+m_f} u_0 \frac{1}{1+(b/b_{90})^2}. \tag{3.81b}$$

3.5.3 Diffusion coefficients

An interaction of test star with mass m and velocity $\boldsymbol{v}$ to the field star with mass m_f and velocity $\boldsymbol{v_f}$ where the velocities are defined in coordinate system $(\hat{e}_1,\ \hat{e}_2,\ \hat{e}_3)$, results in the change in the velocity vectors which results in a change in the energy and angular momentum leading to the diffusion of stars in the phase space. We define a coordinate system $(\hat{e}_1^{'},\ \hat{e}_2^{'},\ \hat{e}_3^{'})$ such that

$$\hat{e}_1^{'} = \frac{\boldsymbol{u}}{u}, \quad \boldsymbol{u}.\hat{e}_2^{'} = 0, \quad \boldsymbol{u}.\hat{e}_3^{'} = 0, \tag{3.82}$$

where $\boldsymbol{u} = \boldsymbol{v} - \boldsymbol{v}_f = u_1\hat{e}_1 + u_2\hat{e}_2 + u_3\hat{e}_3$, is the relative velocity vector before interaction. Let $\boldsymbol{u}^{'} = u_1^{'}\hat{e}_1^{'} + u_2^{'}\hat{e}_2^{'} + u_3^{'}\hat{e}_3^{'}$, be the relative velocity after interaction such that the change in relative velocity is

$$\Delta u = |\boldsymbol{u}^{'} - \boldsymbol{u}| = \sqrt{u'^2 + u^2 - 2u'u\cos\theta} = 2u\sin\left(\frac{\theta}{2}\right), \tag{3.83}$$

where it is assumed that the interaction changes the velocity vector by an angle θ with $u^{'} = u$. The change in individual component of $u^{'}$ is

$$\Delta u_1^{'} = 2u\sin^2\left(\frac{\theta}{2}\right), \tag{3.84a}$$

$$\Delta u_2^{'} = 2u\sin\left(\frac{\theta}{2}\right)\cos\left(\frac{\theta}{2}\right)\cos\phi, \tag{3.84b}$$

$$\Delta u_3^{'} = 2u\sin\left(\frac{\theta}{2}\right)\cos\left(\frac{\theta}{2}\right)\sin\phi, \tag{3.84c}$$

such that $\boldsymbol{\Delta u^{'}} = -\Delta u_1^{'}\hat{e}_1^{'} - \Delta u_2^{'}\hat{e}_2^{'} + \Delta u_3^{'}\hat{e}_3^{'}$ (Binney and Tremaine 2008) and ϕ is the angle between projection of Δu on $\hat{e}_2^{'} - \hat{e}_3^{'}$ plane and $\hat{e}_2^{'}$. Thus, the change in velocity of test star using eqn (3.72) is given by

$$\Delta v_1^{'} = 2\frac{m_f}{m+m_f}u\sin^2\left(\frac{\theta}{2}\right) = 2\frac{m_f}{m+m_f}u\frac{1}{1+(b/b_{90})^2}, \tag{3.85a}$$

$$\Delta v_2^{'} = 2\frac{m_f}{m+m_f}u\sin\left(\frac{\theta}{2}\right)\cos\left(\frac{\theta}{2}\right)\cos\phi = 2\frac{m_f}{m+m_f}u\frac{b/b_{90}}{1+(b/b_{90})^2}\cos\phi, \tag{3.85b}$$

$$\Delta v_3^{'} = 2\frac{m_f}{m+m_f}u\sin\left(\frac{\theta}{2}\right)\cos\left(\frac{\theta}{2}\right)\sin\phi = 2\frac{m_f}{m+m_f}u\frac{b/b_{90}}{1+(b/b_{90})^2}\sin\phi, \tag{3.85c}$$

The velocity change in $(\hat{e}_1,\ \hat{e}_2,\ \hat{e}_3)$ coordinate is given by

$$\Delta v_\mu = \hat{e}_\mu . \hat{e}'^{\alpha} \Delta v'_\alpha, \tag{3.86a}$$

$$\Delta v_\mu \Delta v_\nu = \hat{e}_\mu . \hat{e}'^{\alpha} \hat{e}_\nu . \hat{e}'^{\beta} \Delta v'_\alpha \Delta v_\beta. \tag{3.86b}$$

For the field star distribution $f(v_f)$, the diffusion coefficients are given by

$$\langle \Delta v_\mu \rangle_t = \int \mathrm{d}^3 v_f\ f(v_f) \int \mathrm{d}b\ 2\ \pi\ b\ u\ \Delta v_\mu, \tag{3.87a}$$

$$\langle \Delta v_\mu \Delta v_\nu \rangle_t = \int \mathrm{d}^3 v_f\ f(v_f) \int \mathrm{d}b\ 2\ \pi\ b\ u\ \Delta v_\mu \Delta v_\nu, \tag{3.87b}$$

and by taking an average over ϕ, integrating over b in limit $\{b_{min},\ b_{max}\}$ and using eqn (3.81), we obtain (Binney and Tremaine 2008)

$$\langle \Delta v_\mu \rangle_t = 2\pi G^2 m_f (m + m_f) \int \mathrm{d}^3 v_f f(v_f) \frac{v_\mu}{u^3} \log\left(1 + \Lambda^2\right), \tag{3.88a}$$

$$\langle \Delta v_\mu \Delta v_\nu \rangle_t = 8\pi G^2 m_f^2 \int \mathrm{d}^3 v_f\ f(v_f) \frac{1}{u} \left[\frac{u_\mu}{u} \left(-\frac{1}{2} \right) \frac{1}{1+\Lambda^2} + \right. \tag{3.88b}$$
$$\left. \frac{1}{4} \left\{ \frac{1}{1+\Lambda^2} + \log\left(1 + \frac{1}{1+\Lambda^2}\right) \left(\delta_{\mu\nu} - \frac{u_\mu u_\nu}{u^2} \right) \right\} \right],$$

where $\Lambda = b_{max}u^2/(G(m+m_f))$. For typical values of $b_{max} = 1$ pc, $u = 200$ km sec^{-1} and $m = m_f = M_\odot$, it follows that $\Lambda = 4.6 \times 10^6$, so that we can neglect $1/(1+\Lambda^2)$ keeping the log term only. If one neglects the velocity dependency of the logarithmic term (Chandrasekhar 1943), then eqn (3.88) reduces to

$$\langle \Delta v_\mu \rangle_t = 4\pi G^2 m_f (m+m_f) \log\Lambda \frac{\mathrm{d}}{\mathrm{d}v^\mu} h(v), \tag{3.89a}$$

$$\langle \Delta v_\mu \Delta v_\nu \rangle_t = 4\pi G^2 m_f^2 \log\Lambda \frac{\mathrm{d}^2}{\mathrm{d}v_\mu \mathrm{d}v_\nu} g(v), \tag{3.89b}$$

where $h(v)$ and $g(v)$ are Rosenbluth potentials given by (Rosenbluth *et al.* 1957)

$$h(v) = \int \mathrm{d}^3 v_f \frac{f(v_f)}{|\boldsymbol{v} - \boldsymbol{v_f}|}, \tag{3.90a}$$

$$g(v) = \int \mathrm{d}^3 v_f \; f(v_f) |\boldsymbol{v} - \boldsymbol{v_f}|. \tag{3.90b}$$

Since the Rosenbluth potentials depends on the velocity only, we can use the relation $\mathrm{d}/\mathrm{d}v_\mu = (v_\mu/v)\mathrm{d}/\mathrm{d}v$ and $\mathrm{d}^2/(\mathrm{d}v_\mu \mathrm{d}v_\nu) = (\delta_{\mu\nu}/v - v_\mu v_\nu/v^3)\mathrm{d}/\mathrm{d}v + (v_\mu v_\nu/v^2)\mathrm{d}^2/\mathrm{d}v^2$. If the velocity vector $\boldsymbol{v}$ is along the $\hat{e}_1$ axes, then $v_1 = v$ and $v_2 = v_3 = 0$. The

diffusion coefficients are then given by (Binney and Tremaine 2008)

$$\left\langle \Delta v_{||} \right\rangle_t = \langle \Delta v_1 \rangle_t = 4\pi G^2 m_f (m + m_f) \log\Lambda \, \frac{\mathrm{d}h(v)}{\mathrm{d}v}, \tag{3.91a}$$

$$\left\langle (\Delta v_{||})^2 \right\rangle_t = \left\langle (\Delta v_1)^2 \right\rangle_t = 4\pi G^2 m_f^2 \log\Lambda \, \frac{\mathrm{d}^2 g(v)}{\mathrm{d}v^2}, \tag{3.91b}$$

$$\left\langle (\Delta v_{\perp})^2 \right\rangle_t = 2\left\langle (\Delta v_2)^2 \right\rangle_t = 2\left\langle (\Delta v_3)^2 \right\rangle_t = 4\pi G^2 m_f^2 \log\Lambda \frac{1}{v}\frac{\mathrm{d}g(v)}{\mathrm{d}v}, \tag{3.91c}$$

which reduces the eqn (3.89) to (Binney and Tremaine 2008)

$$\langle \Delta v_\mu \rangle_t = \frac{v_\mu}{v} \left\langle \Delta v_{||} \right\rangle_t, \tag{3.92a}$$

$$\langle \Delta v_\mu \Delta v_\nu \rangle_t = \frac{v_\mu v_\nu}{v^2} \left[\left\langle (\Delta v_{||})^2 \right\rangle_t - \frac{1}{2} \left\langle (\Delta v_{\perp})^2 \right\rangle_t \right] + \frac{1}{2}\delta_{\mu\nu} \left\langle (\Delta v_{\perp})^2 \right\rangle_t. \tag{3.92b}$$

The higher order diffusion coefficients $\langle \Delta v_{i,1} .... \Delta v_{i,n} \rangle$ will have terms $(\Delta v_{||})^c (\Delta v_{\perp})^d$ where $c + d = n$ and $0 \leq c \leq n$. Using eqn (3.81), for $b \gg b_{90}$, $\Delta v_{||} \propto b^{-2}$ and $\Delta v_{\perp} \propto b^{-1}$ whereas for $b \ll b_{90}$, $\Delta v_{||}$ is constant and $\Delta v_{\perp} \propto b$. Therefore $(\Delta v_{||})^c (\Delta v_{\perp})^d \propto b^{-n-c}$ for $b \gg b_{90}$ and is $\propto b^{n-c}$ for $b \ll b_{90}$. The diffusion coefficients is proportional to the integration over the impact parameter which gives $\int \mathrm{d}b \, b^{1-n-c}$ for $b \gg b_{90}$ and $\int \mathrm{d}b \, b^{1+n-c}$ for $b \ll b_{90}$. For $n > 2$, the integration will result in some power of $1/\Lambda$ and there will be no $\log\Lambda$ terms. Since we have seen that the Λ is a large quantity, the higher order diffusion coefficients are small compared to the coefficients for $n = 1$ and 2. Thus the higher order diffusion coefficients are neglected.

For an isotropic distribution in velocity space $\mathrm{d}^3 v_f = v_f^2 \sin\theta \mathrm{d}v_f \mathrm{d}\theta \mathrm{d}\phi$, the Rosenbluth potentials using eqn (3.90) are given by

$$h(v) = 4\pi \left[\int_0^v \mathrm{d}v_f \ \frac{v_f^2}{v} f(v_f) + \int_v^\infty \mathrm{d}v_f \ v_f f(v_f) \right], \tag{3.93a}$$

$$g(v) = \frac{4\pi}{3} \left[\int_0^v \mathrm{d}v_f \ \left(3v_f^2 v + \frac{v_f^4}{v} \right) f(v_f) + \int_v^\infty \mathrm{d}v_f \ \left(3v_f^3 + v^2 v_f \right) f(v_f) \right], \tag{3.93b}$$

and using eqn (3.91), we have

$$\left\langle \Delta v_{||} \right\rangle_t = -\frac{16\pi^2 G^2 m_f (m + m_f) \log\Lambda}{v^2} \int_0^v \mathrm{d}v_f \ v_f^2 f(v_f), \tag{3.94a}$$

$$\left\langle (\Delta v_{||})^2 \right\rangle_t = \frac{32\pi^2 G^2 m_f^2 \log\Lambda}{3} \left[\int_0^v \mathrm{d}v_f \frac{v_f^4}{v^3} f(v_f) + \int_v^\infty \mathrm{d}v_f v_f f(v_f) \right], \tag{3.94b}$$

$$\left\langle (\Delta v_\perp)^2 \right\rangle_t = \frac{32\pi^2 G^2 m_f^2 \log\Lambda}{3} \left[\int_0^v \mathrm{d}v_f \left(3\frac{v_f^2}{v} - \frac{v_f^4}{v^3} \right) f(v_f) + 2\int_v^\infty \mathrm{d}v_f v_f f(v_f) \right]. \tag{3.94c}$$

The diffusion coefficients in terms E and R using eqn (3.92) are given by

$$\langle \Delta E \rangle_t = -\frac{1}{2}\left\langle (\Delta v_{||})^2 \right\rangle_t - \frac{1}{2}\left\langle (\Delta v_{\perp})^2 \right\rangle_t - v\left\langle \Delta v_{||} \right\rangle \tag{3.95a}$$

$$\left\langle (\Delta E)^2 \right\rangle_t = v^2 \left\langle (\Delta v_{||})^2 \right\rangle_t \tag{3.95b}$$

$$\langle \Delta R \rangle_t = \frac{R}{v^2}\left(1 - \frac{5v^2}{2E}\right)\left\langle (\Delta v_{||})^2 \right\rangle_t + \left[\frac{r^2}{J_c^2} - \frac{R}{2v^2}\left(1 - \frac{v^2}{E}\right)\right]\left\langle (\Delta v_{\perp})^2 \right\rangle_t + 2\frac{R}{v}\left[1 - \frac{v^2}{2E}\right]\left\langle \Delta v_{||} \right\rangle \tag{3.95c}$$

$$\left\langle (\Delta R)^2 \right\rangle_t = \frac{4R^2}{v^2}\left[1 - \frac{9v^2}{8E}\right]\left\langle (\Delta v_{||})^2 \right\rangle_t + \left[2R\frac{r^2}{J_c^2} - 2\frac{R^2}{v^2}\left(1 - \frac{v^2}{4E}\right)\right]\left\langle (\Delta v_{\perp})^2 \right\rangle_t - R^2\frac{v}{E}\left\langle \Delta v_{||} \right\rangle \tag{3.95d}$$

$$\langle \Delta E \Delta R \rangle_t = -2R\left[1 - \frac{v^2}{2E}\right]\left\langle (\Delta v_{||})^2 \right\rangle_t . \tag{3.95e}$$

Spitzer (1987) has shown that for a Maxwellian distribution of field stars $f(v_f) = (n/(2\pi\sigma_f)^{3/2})\exp[-v_f^2/(2\sigma_f^2)]$ whose $v_{rms} = \sqrt{3}\sigma_f$, the parallel component diffusion coefficient $\left\langle (\Delta v_{||})^2 \right\rangle_t = \langle \Delta v_1 \Delta v_1 \rangle_t$ is given by $\left\langle (\Delta v_{||})^2 \right\rangle_t = \sqrt{2}(n\Gamma/\sigma_f)G(x)/x$, where $\Gamma = 4\pi^2 G^2 m_f^2 \log\Lambda$, $G(x) = (\mathrm{Erf(x)} - x\mathrm{d}_x\mathrm{Erf}(x))/(2x^2)$ and $x = v/(\sqrt{2}\sigma_f)$. The relaxation time is defined to be

$$t_r = \frac{1}{3}\frac{v_{rms}^2}{\left\langle (\Delta v_{||})^2 \right\rangle_t |_{v=v_{rms}}}, \tag{3.96}$$

and works out to be

$$t_r = 0.065 \frac{v^3}{G^2 m_f^2 n \log \Lambda}, \tag{3.97a}$$

$$= 3.4 \times 10^9 \text{ yr } \left(\frac{v}{\text{km sec}^{-1}}\right)^3 \left(\frac{n}{\text{pc}^{-3}}\right)^{-1} \left(\frac{m_f}{M_\odot}\right)^{-2} \log^{-1} \Lambda. \tag{3.97b}$$

The number rate of stars diffusion can be approximated as $\dot{N} \approx n(r) r^3 / t_r$ and following Peebles (1972) argument that in steady state, the number rate, $\dot{N}$, is constant in the physical space, and using eqn (3.97), the mean velocity $v^2 = GM_\bullet / r$, it is seen that $n(r) \propto r^{-9/4}$. Similarly the energy rate can be written as $\dot{E} = n(r) r^3 v^2 M_\star / t(r)$ and following Bahcall and Wolf (1976), $n(r) \propto r^{-7/4}$. In phase space, the number rate of stars is given by $\dot{N} = f(E)\Gamma(E)E/t_r$ where the distribution function $f(E) \propto E^p$, the phase space volume per energy $\Gamma(E) \propto r^3 v^3 \propto r^(3/2) \propto E^{-3/2}$ obtained using eqn (3.24), and $t_r(E) \propto v^3/n \propto 1/f(E) \propto E^{-p}$. Using this, the number rate $\dot{N} \propto E^{2p-1/2}$, and assuming that the number rate remain constant in phase space, we get $p = 1/4$. Thus the Bahcall and Wolf (1976) solution suggest that the number rate of star flow should be constant in phase space and not in coordinate space as shown by Peebles (1972).

3.6 Loss cone dynamics

The presence of tidal radius puts a constraint on the angular momentum J and the star is tidally captured if $J \leq J_{lc}$, where loss cone angular momentum J_{lc} as shown in Fig 3.4, is given by (Frank and Rees 1976)

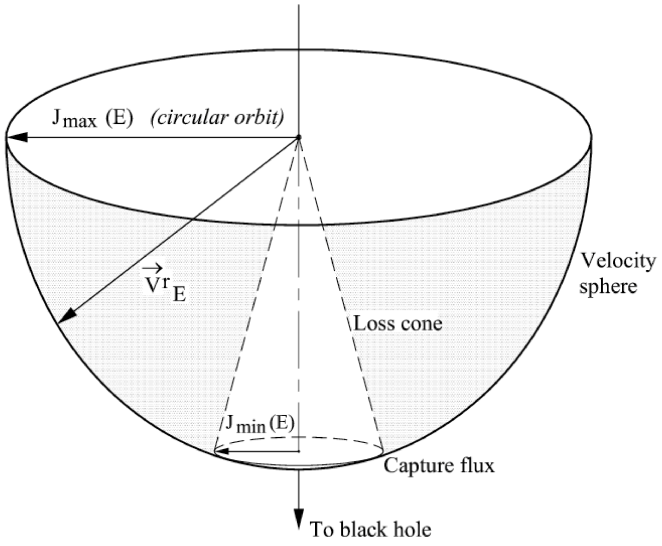

FIGURE 3.4: The loss cone geometry in velocity space is shown. If the stars angular momentum is less than $J_{min} = J_{lc}$, then the star is tidally disrupted. courtesy: Lightman and Shapiro (1977)

$$J_{lc} = \sqrt{2r_t^2(\Phi(r_t) - E)}. \tag{3.98}$$

The radius of a circular orbit $r_c = GM_\bullet/(2E)$ and the velocity is $v_c^2 = GM_\bullet/r_c$. The maximum angular momentum J_{max} of an orbit is the circular angular momentum given by $J_{max}^2 = J_c^2 = r_c^2 v_c^2 = GM_\bullet/(2E)$. The ratio of J_{lc} and J_{max} obtained using eqn (3.15) is given by

$$\frac{\frac{GM_\bullet}{r_t} - E}{\frac{GM_\bullet}{r} - E} = \left(\frac{J_{lc}}{J_{max}}\right)^2 \frac{r^2}{r_t^2}, \tag{3.99}$$

where $E = GM_\bullet/r - \langle v^2 \rangle /2$, $J_{lc}/J_{max} = \sin\theta_{lc}$ and θ_{lc} is the loss cone angle and with $r \gg r_t$, we obtain

$$\sin^2\theta_{lc} = 2\frac{r_t}{r^2}\frac{GM_\bullet}{\langle v^2\rangle}. \tag{3.100}$$

Thus $\langle v^2\rangle$ is given by

$$\left\langle v^2\right\rangle = 3\sigma^2 \begin{cases} \frac{r_h}{r} & r < r_h \\ 1 & r \geq r_h, \end{cases}$$

where σ^2 is the line of sight velocity dispersion and this results in loss cone angle given by

$$\theta_{lc} = f \begin{cases} \sqrt{\frac{2}{3}\frac{r_t}{r}} & r < r_h \\ \sqrt{\frac{2}{3}\frac{r_t r_h}{r^2}} & r \geq r_h, \end{cases} \tag{3.101a}$$

$$= 1.9\times10^{-5}\left(\frac{M_\bullet}{10^6 M_\odot}\right)^{-\frac{1}{3}}\left(\frac{M_\star}{M_\odot}\right)^{-\frac{1}{6}}\left(\frac{R_\star}{R_\odot}\right)^{\frac{1}{2}}\left(\frac{\sigma}{200\text{ km sec}^{-1}}\right) f \begin{cases} \sqrt{\frac{r_h}{r}} & r < r_h \\ \frac{r_h}{r} & r \geq r_h, \end{cases}$$

where the factor f takes account that stars with larger impact factor can be lost from the cusp due to tidal capture and is taken to be 2 (Frank and Rees 1976). Using eqn (3.89), the change in $v_\perp$ in time t is given by $\Delta v_\perp = \sqrt{\langle(\Delta v_\perp)^2\rangle_t\, t}$ and hence the change in angular momentum $\Delta J = r\Delta v_\perp = r\sqrt{\langle(\Delta v_\perp)^2\rangle_t\, t}$. The time-scale on which a star can survive in a loss cone is the dynamical time-scale t_{dyn}. The diffusion angle θ_D is given by

$$\theta_D^2 = \left(\frac{\Delta J}{J_{max}}\right)^2 = \frac{\langle(\Delta v_\perp)^2\rangle_t\, t_{dyn}}{v^2} = \frac{t_{dyn}}{t_R}, \tag{3.102}$$

where the dynamical time is given by

$$t_{dyn} = \begin{cases} \sqrt{\frac{r^3}{GM_\bullet}} & r < r_h \\ \frac{r}{\sigma} & r \geq r_h \end{cases} = \frac{r_h}{\sigma} \begin{cases} \left(\frac{r}{r_h}\right)^{\frac{3}{2}} & r < r_h \\ \frac{r}{r_h} & r \geq r_h. \end{cases} \tag{3.103}$$

Using eqn (3.97) along with $v = \sigma(r/r_h)^{-1}$ for $r < r_h$ and $v = \sigma$ for $r \geq r_h$, θ_D given by

$$\theta_D^2 = 15.38 G^2 M_f^2 \log\Lambda \frac{r_h}{\sigma^4} n(r) \begin{cases} \left(\frac{r}{r_h}\right)^3 & r < r_h \\ \left(\frac{r}{r_h}\right) & r \geq r_h. \end{cases} \tag{3.104}$$

For $r \gg r_h$, the cluster mass $M_c = nr^3 M_\star$ where n is the stellar density is higher than the black hole mass and hence from virialization theorem, $\sigma \simeq (GM_\star n_c r_c^2)^{1/2}$ where n_c is the density and r_c is the core radius. Assuming the density to be $n(r) = n_c(r/r_h)^{-7/4}$ (Bahcall & Wolf cusp) for $r < r_h$ and $n(r) = n_c$ for $r \geq r_h$ with $M_f = M_\star$, θ_D using eqn (3.104) given by (Frank and Rees 1976)

$$\theta_D = 3.9 \times 10^{-4} \left(\frac{M_\bullet}{10^6 M_\odot}\right)^{\frac{1}{2}} \left(\frac{M_\star}{M_\odot}\right)^{-\frac{1}{2}} \left(\frac{n_c}{10^4\ \mathrm{pc}^{-3}}\right)^{-1} \left(\frac{r_c}{10\ \mathrm{pc}}\right)^{-3} \cdot \log\Lambda \begin{cases} \left(\frac{r}{r_h}\right)^{\frac{5}{8}} & r < r_h \\ \left(\frac{r}{r_h}\right)^{\frac{1}{2}} & r \geq r_h. \end{cases} \tag{3.105}$$

The ratio $q = \theta_{lc}/\theta_D$ is given by (Frank and Rees 1976)

$$q = 3.13 \left(\frac{M_\bullet}{10^6 M_\odot}\right)^{-\frac{5}{6}} \left(\frac{M_\star}{M_\odot}\right)^{\frac{5}{6}} \left(\frac{R_\star}{R_\odot}\right)^{\frac{1}{2}} \left(\frac{n_c}{10^4\ \mathrm{pc}^{-3}}\right)^{\frac{3}{2}} \left(\frac{r_c}{10\ \mathrm{pc}}\right)^4 \cdot \frac{f}{\sqrt{\log\Lambda}} \begin{cases} \left(\frac{r}{r_h}\right)^{-\frac{9}{8}} & r < r_h \\ \left(\frac{r}{r_h}\right)^{-\frac{3}{2}} & r \geq r_h. \end{cases} \tag{3.106}$$

The stars on the loss cone are consumed on the dynamical timescale and the filling of loss cone depends on the diffusion time-scale which depends on the diffusion angle. The loss cone is said to be full loss cone if $q < 1$ as the stars move in and out of the loss cone whereas the loss cone is empty if $q > 1$ and the stars have to diffuse into the loss cone. The angular diffusion of stars to the loss cone is similar to the heat conduction in a hemispherical shell such that the heat conduction rate is given by $\mathrm{d}Q/\mathrm{d}t = -\kappa A \nabla T$, where Q energy, κ is thermal conductivity, $A = 2\pi r^2 \sin\theta$ is the surface area and T is the temperature. For a constant $\mathrm{d}Q/\mathrm{d}t$, it is found that $T \propto -\log(\tan(\theta/2)) \sim \log(2/\theta)$ and thus the heat conduction rate $\mathrm{d}Q/\mathrm{d}t \propto (T_2 - T_1)/\log(2/\theta)$ where T_1 and T_2 is the temperature at the equator and co-latitude θ respectively. Based on similar arguments, the number rate of stars in diffusive regime is $\propto 1/\log(2/\theta_{lc}) = N/(t_R \log(2/\theta_{lc}))$, where N is the total number of stars and thus we can say that the angular diffusion time to be $\sim t_R \log(2/\theta_{lc})$.

The radius at which $q = 1$ is the critical radius r_{crit} and separate the full loss cone regime to the empty loss cone regime. The critical radius using eqn (3.107) is given by (Frank and Rees 1976)

$$\frac{r_{crit}}{r_h} = \begin{cases} r_{crit} < r_h : \\ 2.75 \left(\frac{M_\bullet}{10^6 M_\odot}\right)^{-\frac{20}{27}} \left(\frac{M_\star}{M_\odot}\right)^{\frac{20}{27}} \left(\frac{R_\star}{R_\odot}\right)^{\frac{4}{9}} \left(\frac{n_c}{10^4\ \mathrm{pc}^{-3}}\right)^{\frac{4}{3}} \left(\frac{r_c}{10\ \mathrm{pc}}\right)^{\frac{32}{9}} \left(\frac{f}{\sqrt{\log\Lambda}}\right)^{\frac{8}{9}} \\ r_{crit} \geq r_h : \\ 2.13 \left(\frac{M_\bullet}{10^6 M_\odot}\right)^{-\frac{5}{9}} \left(\frac{M_\star}{M_\odot}\right)^{\frac{5}{9}} \left(\frac{R_\star}{R_\odot}\right)^{\frac{1}{3}} \left(\frac{n_c}{10^4\ \mathrm{pc}^{-3}}\right) \left(\frac{r_c}{10\ \mathrm{pc}}\right)^{\frac{8}{3}} \left(\frac{f}{\sqrt{\log\Lambda}}\right)^{\frac{2}{3}}. \end{cases} \tag{3.107}$$

Inside r_{crit}, the star diffuses into the loss cone whereas outside r_{crit} the loss cone loses its significance as the given star drift in and out of it in dynamical time. The mean energy $E(r) = (3/2)v^2 = (3/2)GM_\bullet/r$ and thus the critical energy is $E(r_{crit})$. The capture rate of a star due to diffusion into loss-cone orbits follows directly from the angular diffusion time scale and star density at r_{crit}, is given by

$$\dot{N} = 4n(r)r^2v(r)\theta_{lc}^2$$

$$= \begin{cases} r_{crit} < r_h : \\ 1.1 \times 10^{-6}\ \mathrm{yr}\ \frac{f^{\frac{8}{9}}}{(\log\Lambda)^{\frac{5}{9}}} \left(\frac{n_c}{10^4\ \mathrm{pc}^{-3}}\right)^{-\frac{7}{6}} \left(\frac{r_c}{10\ \mathrm{pc}}\right)^{-\frac{49}{9}} \left(\frac{M_\bullet}{10^6 M_\odot}\right)^{\frac{61}{27}} \left(\frac{M_\star}{M_\odot}\right)^{-\frac{95}{54}} \left(\frac{R_\star}{R_\odot}\right)^{\frac{4}{9}} \\ r_{crit} \geq r_h : \\ 4 \times 10^{-6}\ \mathrm{yr}\ f^2 \left(\frac{n_c}{10^4\ \mathrm{pc}^{-3}}\right)^{\frac{1}{2}} \left(\frac{r_c}{10\ \mathrm{pc}}\right)^{-1} \left(\frac{M_\bullet}{10^6 M_\odot}\right)^{\frac{4}{3}} \left(\frac{M_\star}{M_\odot}\right)^{-\frac{5}{6}} \left(\frac{R_\star}{R_\odot}\right), \end{cases} \tag{3.108a}$$

The number of stars using the distribution function $f(E)$ and eqn (3.16) is given by

$$N = 4\pi^2 \int \mathrm{d}E f(E) \int \mathrm{d}J^2 \int \frac{\mathrm{d}r}{v_r}, \tag{3.109}$$

and taking the radial period $P(E) = \int \mathrm{d}r/v_r$ and integrating over J, the number of stars in the loss cone and total number of stars in the energy range E and $E + \mathrm{d}E$ are given by

$$N_{lc}(E) = 4\pi^2 f(E) J_{lc}^2(E) P(E) \tag{3.110a}$$

$$N(E) = 4\pi^2 f(E) J_{max}^2(E) P(E). \tag{3.110b}$$

Thus $N_{lc}(E) = N(E) J_{lc}^2/J_{max}^2$. In the full loss cone model, the stars are captured in dynamical time which is the radial period and using the balance of angular momentum diffusion time scale with the supply rate of stars, $J_{lc}^2/J_{max}^2 \simeq (P(E)/t_r)$ and thus the capture rate $\dot{N} = \int \mathrm{d}E\ N_{lc}(E)/P(E) = \int \mathrm{d}E\ N(E)/t_r$. For a power law galaxy with the assumptions that total number of stars in $r \leq r_h$ is $N(< r_h) = 2M_\bullet/M_\star$ and that the potential is dominated by black hole, the density is given by $n(r) = (3-\gamma)/(2\pi)(M_\bullet/M_\star) r_h^{-3} (r/r_h)^{-\gamma}$ and using eqn (3.22), the distribution function is given by

$$f(E) = \frac{3-\gamma}{2\sqrt{2}\pi^{5/2}} \frac{\Gamma(\gamma+1)}{\Gamma(\gamma-1/2)} (GM_\bullet)^{-\gamma} \frac{M_\bullet}{M_\star} r_h^{\gamma-3} r_h^{\gamma-3} E^{\gamma-3/2}. \tag{3.111}$$

For $1/2 < \gamma < 3$ and the capture rate per energy $F(E)$ is given by

$$F(E) = 2(3-\gamma)\sqrt{\frac{2}{\pi}} \frac{\Gamma(\gamma+1)}{\Gamma(\gamma-1/2)} G^{-2} \frac{M_\bullet^{-\frac{2}{3}}}{M_\star^{\frac{4}{3}}} R_\star \sigma^{6-2\gamma} \left(1 - \frac{r_t E}{GM_\bullet}\right) E^{\gamma-3/2}, \tag{3.112}$$

which is integrated over energy E to get total capture rate $\dot{N}$, between the limits $\{\Phi(r_h) = GM_\bullet/r_h,\ \infty\}$ and the solution is diverging for $\gamma > 1/2$. However a crude way to get the capture rate is $\dot{N} = N_{lc}/P(E = \Phi(r_h))$, where N_{lc} is the total number of stars in loss cone obtained by integrating eqn (3.110), $P(E)$ is taken to be Kepler orbital period and $J_{lc} = \sqrt{2GM_\bullet r_t}$; this gives

$$\dot{N}_f = \sqrt{\frac{2}{\pi}}\ \frac{3-\gamma}{2-\gamma}\frac{\Gamma(\gamma+1)}{\Gamma(\gamma-1/2)}\left(\frac{M_\bullet}{M_\star}\right)^{\frac{4}{3}} R_\star \frac{\sigma^5}{(GM_\bullet)^2} \tag{3.113a}$$

$$= 0.03 \text{ yr}\ \frac{3-\gamma}{2-\gamma}\frac{\Gamma(\gamma+1)}{\Gamma(\gamma-1/2)}\left(\frac{M_\bullet}{10^6 M_\odot}\right)^{-\frac{2}{3}}\left(\frac{M_\star}{M_\odot}\right)^{-\frac{4}{3}}\left(\frac{R_\star}{R_\odot}\right)\left(\frac{\sigma}{200 \text{ km sec}^{-1}}\right)^5,$$

where $\dot{N}_f$ is full loss cone rate.

Even though this method is approximate, it gives an estimate of the rate of capture in the full loss cone regime. The stars experience scattering due to gravitational encounters which results in a change in their energy and angular momentum. By solving the Fokker-Planck equation, one obtains the evolution of distribution function and the inflow rate of stars to the loss cone calculated at the tidal radius gives the net capture rate.

3.6.1 Diffusion equation

If we consider that change in angular momentum over an orbital period due to gravitational interaction is higher than the change in energy, then eqn (3.70) is given by

$$\frac{\mathrm{d}}{\mathrm{d}t}f(E,\ R,\ t) = -\frac{\partial}{\partial R}\left(f(E,\ R,\ t)\left\langle \Delta R\right\rangle_t\right) + \frac{1}{2}\frac{\partial^2}{\partial R^2}\left(f(E,\ R,\ t)\left\langle (\Delta R)^2\right\rangle_t\right), \tag{3.114}$$

and in the limit $R \to 0$, the eqn (3.95) gives

$$\left\langle \Delta R\right\rangle_t = \frac{\left\langle (\Delta R)^2\right\rangle_t}{2R}, \tag{3.115}$$

which reduces the eqn (3.114) to

$$\frac{\mathrm{d}}{\mathrm{d}t}f(E,\ R,\ t) = \frac{\partial}{\partial R}\left[R\frac{\partial}{\partial R}\left(f(E,\ R,\ t)\left\langle \Delta R\right\rangle_t\right)\right]. \tag{3.116}$$

Thus the Fokker-Planck equation reduces to simple diffusion equation with diffusion occurring along R. In steady state $\partial f(E,\ R,\ t)/\partial t = 0$ and thus $\mathrm{d}f(E,\ R,\ t)/\mathrm{d}t = v_r \partial f(E,\ R,\ t)/\partial r$ and eqn (3.116) is given by

$$v_r\frac{\partial}{\partial r}f(E,\ R,\ t) = \frac{\partial}{\partial R}\left[R\frac{\partial}{\partial R}\left(f(E,\ R,\ t)\left\langle \Delta R\right\rangle_t\right)\right]. \tag{3.117}$$

In terms of variable $j = J^2/J_c^2(\mathcal{E})$ and χ defined by

$$\chi = \frac{1}{\langle D(\mathcal{E})\rangle}\int_{r_p}^{r}\lim_{j\to 0}\frac{\langle(\Delta j)^2\rangle}{2j}\frac{\mathrm{d}r}{v_r} \quad \text{and} \quad y = \frac{j}{\langle D(\mathcal{E})\rangle} \tag{3.118}$$

where $\langle D(\mathcal{E})\rangle = \oint \lim_{j\to 0} \frac{\langle(\Delta j)^2\rangle}{2j} \frac{\mathrm{d}r}{v_r}$ is the orbit averaged angular momentum diffusion coefficient and y_{lc} is y at $j = j_{lc}$, the eqn (3.117) is recast as

$$\frac{\mathrm{d}f(\chi,\ y)}{\mathrm{d}\chi} = \frac{\mathrm{d}}{\mathrm{d}y}\left(y\frac{\mathrm{d}f(\chi,\ y)}{\mathrm{d}y}\right). \tag{3.119}$$

Cohn and Kulsrud (1978) have calculated the steady state solution of FP equation numerically for spherically symmetric and isotropic distribution. For a steady state with diffusion in angular momentum space only, the FP equation reduces to the equation describing a transfer of heat in a cylinder. The phase space density ($f(\chi,\ y)$ where χ and y are timelike and angular momentum variables respectively) was considered to vary along an orbit with the boundary condition given by

$$\text{boundary condition} = \begin{cases} f(0,y) = f(1,y) & y \geq y_{lc} \\ f(0,y) = 0 & y \leq y_{lc} \\ f(1,y) \geq 0 & \end{cases}$$

In this boundary conditions, the solution of eqn (3.119) is given by

$$f(\chi,\ y) = f(y_{lc})\left[1 - \frac{2}{\sqrt{y_{lc}}}\sum_{m=1}^{\infty}\frac{e^{-\beta_m^2\chi/4}}{\beta_m}\frac{J_0(\beta_m\sqrt{y})}{J_1(\beta_m\sqrt{y_{lc}})}\right], \tag{3.120}$$

where J_0 and J_1 are Bessel functions of the first kind and β_m gives consecuitve zeros of $J_0(\beta\sqrt{y_{lc}}) = 0$. Thus the average flux travelling across y_{lc} is

$$F(E) = 4\pi^2 P(E)\,\langle D(\mathcal{E})\rangle\, J_c^2(E) \int_0^{y_{lc}} f(1,\ y)\,\mathrm{d}y \tag{3.121}$$

$$= 4\pi^2 J_c^2(E) R_{lc} f(R_{lc}) \left[1 - 4\sum_{m=1}^{\infty} \frac{e^{-\alpha_m^2 q/4}}{\alpha_m^2}\right], \tag{3.122}$$

where $R_{lc} = J_{lc}^2/J_c^2$ and q is given by

$$q(E) = \frac{P(E)\,\langle D(\mathcal{E})\rangle}{R_{lc}(E)}, \tag{3.123}$$

where $P(E)$ is the orbital period. For smoothness of $f(\chi,\ y)$ at $y = 0$, we take the condition $\partial f(\chi,\ y)/\partial\sqrt{y} = 0$. Using this condition, the $f(R_{lc})$ is given by

$$f(R_{lc}) = \frac{f(1)}{1 + q^{-1}\xi(q)\ln(1/R_{lc})}, \tag{3.124}$$

where

$$\xi(q) = 1 - 4\sum_{m=1}^{\infty} \frac{e^{-\alpha_m^2 q/4}}{\alpha_m^2}. \tag{3.125}$$

Thus the flux is given by

$$F(E) = 4\pi^2 J_c^2(E) R_{lc} \frac{\bar{f}(E)}{\xi(q)^{-1} + q^{-1}\ln(1/R_{lc})} = 4\pi^2 q J_c^2 R_{lc} \frac{\bar{f}(E)}{\ln(1/R_0)}, \tag{3.126}$$

where $f(1) = \bar{f}(E) = \int_0^1 f(E,\ R)\,\mathrm{d}R$ and $R_0 = R_{lc}e^{-q/\xi(q)}$. Cohn and Kulsrud (1978) suggested the value of R_0 to be

$$R_0(q) = R_{lc}\begin{cases} e^{-q} & q \gg 1 \\ e^{-0.186q-0.824\sqrt{q}} & q \ll 1 \end{cases} \tag{3.127}$$

The limits of $q \ll 1$ and $q \gg 1$ in the previous equation are regime of empty and full loss cone respectively. The eqn (3.126) in the limits of q is given by (Merritt 2013b)

$$F = F_{max}\begin{cases} q|\ln R_{lc}|^{-1} & q \ll -\ln R_{lc} \\ 1 & q \gg -\ln R_{lc}, \end{cases} \tag{3.128}$$

where $F_{max} = 4\pi^2 J_c^2 R_{lc}\bar{f}(E)$. The transition from empty to full loss cone regime occurs at the critical energy E_{crit} when $q(E_{crit}) = \ln R_{lc}(E_{crit})$.

Cohn and Kulsrud (1978) also obtained the steady state 2D ($E,\ R$) solution of FP equation where the time dependent part of FP equation was written as $\mathrm{d}f/\mathrm{d}t = (\mathrm{d}f/\mathrm{d}t)_{scat} + (\mathrm{d}f/\mathrm{d}t)_{coll}$, where $(\mathrm{d}f/\mathrm{d}t)_{scat}$, $(\mathrm{d}f/\mathrm{d}t)_{coll}$ is scattering by star-star interaction and physical collision term respectively. They included the physical collision term $(\mathrm{d}f/\mathrm{d}t)_{coll} = -\nu_{coll}f$ where $\nu_{coll} = 4\pi R_\star^2 g(v) + 4\pi G M_\star R_\star h(v)$ is the collision frequency, into the FP equation and obtained the rate of loss cone feeding to be

$$\dot{N} = 3\times10^{-7}\ \mathrm{Yr}^{-1}\left(\frac{M_\bullet}{10^3 M_\odot}\right)^{2.33}\left(\frac{n}{5\times10^4\ \mathrm{pc}^{-3}}\right)^{1.6}\left(\frac{\sigma^2}{100\ \mathrm{km}^2\ \mathrm{sec}^{-2}}\right)^{-2.88}. \tag{3.129}$$

Syer and Ulmer (1999) using the assumption of spherical symmetry, power law distribution and loss cone mechanism, calculated a rough event rate for both main sequence star and red giant star. Red giants may enter the loss cone in the same manner as main-sequence stars: they diffuse towards an empty loss cone for orbits below a critical radius, and above that radius, they scatter on to a full loss cone. There is an additional contribution to the red giant capture rate. Red giants also grow on to the loss cone as they expand. As the loss cone angle $\theta_{lc}^2 \propto R_t$, and $R_{t_{Giant}} \gg R_{t_{MS}}$, the number of red giants susceptible to capture may be significant. In order to calculate the red giant capture rates, it is important to determine their birth rate and their number density. The fraction of red giant stars $f_{RG} = (\mathrm{d}\dot{N}_{new}/\mathrm{d}N)t_{RG}$ where $\dot{N}_{new}$, t_{RG} are birth rate and evolutionary time of red giant stars. They used the Salpeter mass function $\mathrm{d}N/\mathrm{d}m = 1.6m^{-1.35}$, the lifetime of main sequence star $t_{MS} = 10^{10}m^{-2.5}$ yr where $m = M_\star/M_\odot$, $\mathrm{d}\dot{N}_{new}/\mathrm{d}N = (\mathrm{d}N/\mathrm{d}M_\star)(M_\star/t_{MS})$ and the red giant star lifetime $t_{RG} \sim 7 \times 10^8$ yr. It is also important to obtain the maximum radius R_{max}, and minimum radius R_{min}, of a giant star, because it is the radius of a star that decides the size of loss cone and is taken to be $R_{max} = 200R_\odot$ and $R_{min} = 3R_\odot$. So, the capture rate of red giant stars depends on the number of new giant stars formed and diffused into the loss cone. It also depends on the number of stars that evolve to the red giant while they are in loss cone. These authors assumed that all stars within the loss cone that evolve to the red giant are disrupted, then the rate of red giant captures within loss cone is $\mathrm{d}\dot{N}_{RG}/\mathrm{d}N = \theta_{lc_{RG}}^2(\mathrm{d}\dot{N}_{new}/\mathrm{d}N)$. The total capture rate per star is then given by

$$\frac{\mathrm{d}\dot{N}_{RG}}{\mathrm{d}N} = \frac{\mathrm{d}\dot{N}_{new}}{\mathrm{d}N}\left[\int_{R_{min}}^{R_t}\frac{R}{R_\odot}\frac{\theta_{lc}^2}{t_{dyn}}\,dt + \int_{R_t}^{R_{max}}\frac{1}{t_R\log(2/\theta_{lc})}\,dt + \frac{R_{max}}{R_\odot}\theta_{lc}^2\right] \quad (3.130)$$

where θ_{lc} is the loss cone for main sequence stars. So the total capture rate is given by

$$\dot{N}_{RG} = f_{RG} \int \frac{\mathrm{d}\dot{N}_{RG}}{\mathrm{d}N} n(r) r^2 \, dr \tag{3.131}$$

For a Nuker density profile (Byun *et al.* 1996; Faber *et al.* 1997), they obtained the capture rate to be $\dot{N} \simeq 10^{-8} (M_\bullet / (10^6 M_\odot)\ \mathrm{yr}^{-1}$.

Wang and Merritt (2004) solved the steady Fokker-Planck equation for a spherically symmetric nuclei with an isothermal density form $\rho(r) = M_\star n(r) = \sigma^2/(2\pi G r^2)$, and total potential as sum of black hole and stellar potentials. They obtained $\dot{N} \propto \sigma^{7/2} M_\bullet^{-1}$ and using $M_\bullet - \sigma$ relation given by $M_\bullet = 1.48 \times 10^8 M_\odot (\sigma/(200\,\mathrm{km\ sec}^{-1}))^{4.65}$ (Merritt and Ferrarese 2001), they obtained the theoretical event rate given by

$$\dot{N} = 6.5 \times 10^{-4} \left(\frac{M_\bullet}{10^6 M_\odot} \right)^{-0.25} \ \mathrm{yr}^{-1}. \tag{3.132}$$

Wang and Merritt (2004) have also numerically solved the steady state Fokker-Planck equation for a sample of 51 galaxies by assuming a single mass distribution and obtained the capture rate shown in Fig 3.5. The consumption rate for power-law galaxies is higher than that of core galaxies because the number of stars is higher at lower radii for power-law galaxies.

The previous models use a single stellar mass distribution to calculate the capture rate. Stone and Metzger (2016) employed a stellar mass function, $\xi(m)$ given by Kroupa (2001), the Kroupa mass function, in their distribution function, and applied it to a sample of 200 galaxies with Nuker profiles, and by using the steady Fokker-Planck equation, they obtained $\dot{N}_t \propto M_\bullet^{-0.4}$.

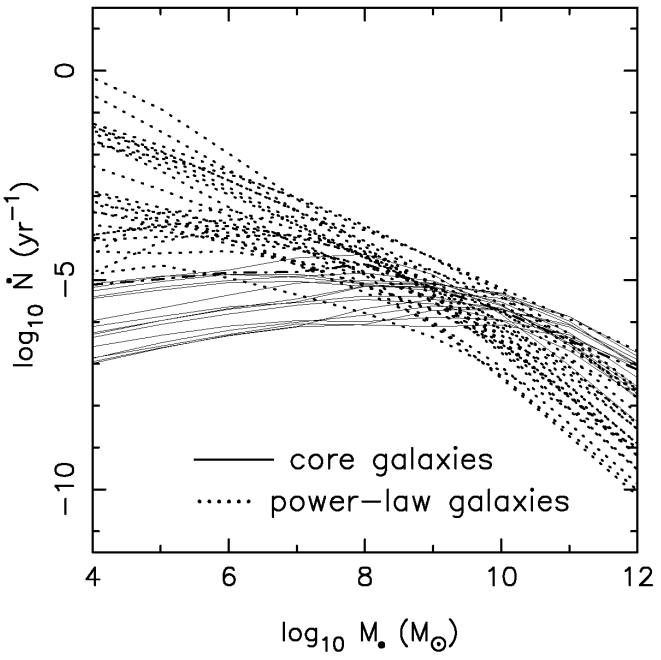

FIGURE 3.5: Consumption rate for core galaxies and power law galaxies as function of $M_\bullet$ for the sample of 51 galaxies.
Courtsey: Wang and Merritt (2004)

Apart from spherical nuclei, the galactic nuclei may be either axisymmetric or triaxial. The potential of such non-spherical nuclei are complicated and apart from Keplerian orbits, various other orbits are possible. The stars orbit precession can lead to the capture of stars by the black hole (orbit draining). Stars in the loss cone are drained in time t_{dyn} and if the $t_{dyn} < t_{prec}$, then the loss cone is empty else the loss cone is full. These centrophilic orbits (orbits that are capable of coming too close to the black hole even in the absence of gravitational encounters or any other effect that drives the star close to the black hole) can have a dramatic effect on the consumption rate, because stars with $J \gg J_{lc}$ can precess into the loss cone so long as $|J_z| < J_{lc}$. Crudely speaking, the loss cone is replaced by a loss wedge with the same extent $|J_z| < J_{lc}$ in the J_z direction of phase space, but stretched in the J direction to some $J > J_{lc}$.

Magorrian and Tremaine (1999) solved the FP equation which is taken to be in J_z

direction and obtained the capture rate is found to be $\dot{N} \propto M_{\bullet}^{-0.188}$. Vasiliev and Merritt (2013) assuming the deviation of galactic nuclei from spherical structure to be small and doing a detailed analysis of orbital structure and solving the Fokker-Planck equation obtained $\dot{N} \sim 10^{-4} - 10^{-6}\,\mathrm{yr}^{-1}$.

The orbital evolution in the galactic nuclei is more complicated in the presence of triaxial potentials, which support two distinct families of tube orbits circulating about the long and short axes of the triaxial figure (Merritt and Vasiliev 2011). In addition, there is a new class of centrophilic orbits called the pyramids, and the defining feature of the pyramid orbit is that the minimum of J=0 and a star on such an orbit will eventually find its way into the SBH even without the assistance of collisional relaxation (Merritt and Valluri 1999). Feeding rates due to collisional loss cone refilling are very large in such galaxies compared with the spherical galaxies (Merritt and Poon 2004). A flow-chart of various model and their references are given in Fig 3.6.

3.7 Summary

A star orbiting around the black hole experiences gravitational scattering from neighbor star leading to change in energy and angular momentum. These interaction results in the diffusion of stars and the evolution of stellar system through Fokker-Planck equation. However, there exists a tidal radius beyond which the star is lost to the black hole. The presence of tidal radius results in a loss cone such that a star with angular momentum less than the loss cone angular momentum is fed to the black hole where the star is shredded by the black hole. This feeding rate of star to the black hole is called as the theoretical capture rate and is constrained by the ratio of loss cone angular momentum to diffusion angular momentum defined by parameter q. The loss cone is empty if $q > 1$ and full

if $q < 1$. The capture rate is calculated using the steady loss cone theory for spherical galactic nuclei and is found to be $\sim 10^{-4}$ yr^{-1} which is higher than the observed rate of 10^{-5} yr^{-1} leading to the rate tension.

3.8 Caveats

We discuss some caveats below (Merritt 2006)

1. The distribution function varies with the density model of a star as the total potential is a sum of the black hole and stellar potentials; thus the choice of density model is crucial.

2. The loss cone dynamics discussed here is a solution of a steady Fokker-Planck equation. The dependence of f on J near the loss cone boundary will be different from the steady form for the time-dependent Fokker-Planck equation and thus the capture rate may vary.

3. The structure of galactic nuclei is crucial to decide the orbit of stars and the geometry of loss cone such as it is a cone in spherical galactic nuclei and a wedge in axisymmetric nuclei. This will also affect the capture rate.

4. The distribution function assumed here is isotropic but in general, the distribution is anisotropic which also affects the stellar distribution and thus the capture rate.

5. Galactic nuclei may undergo catastrophic changes due to galaxy mergers, star formation, infall of star cluster or black holes. These changes will have a substantial effect on the feeding rates.

The dynamical model considered here is for a star on a parabolic orbit however the crucial point is that the J plays an important role in the stellar dynamical process through pericenter radius r_p. In chapter 5, we have discussed a dynamical model that includes both energy and angular momentum to solve the steady Fokker-Planck equation for spherical galactic nuclei with a power-law density profile and the Kroupa's initial stellar mass function.

We enlist the discussion points of this chapter below:

- Basic concepts of stellar dynamics around black holes: virial theorem, DF, important time scales and radii.
- The master equation, Fokker-Planck equation and diffusion in phase space.
- The Fokker-Planck equation in $\{E,\ J\}$ space for spherical systems.
- Derivations of the diffusion coefficients.
- Loss cone dynamics.
- Solution to Fokker-Planck with a loss cone boundary.
- Discussion of capture rates and caveats.

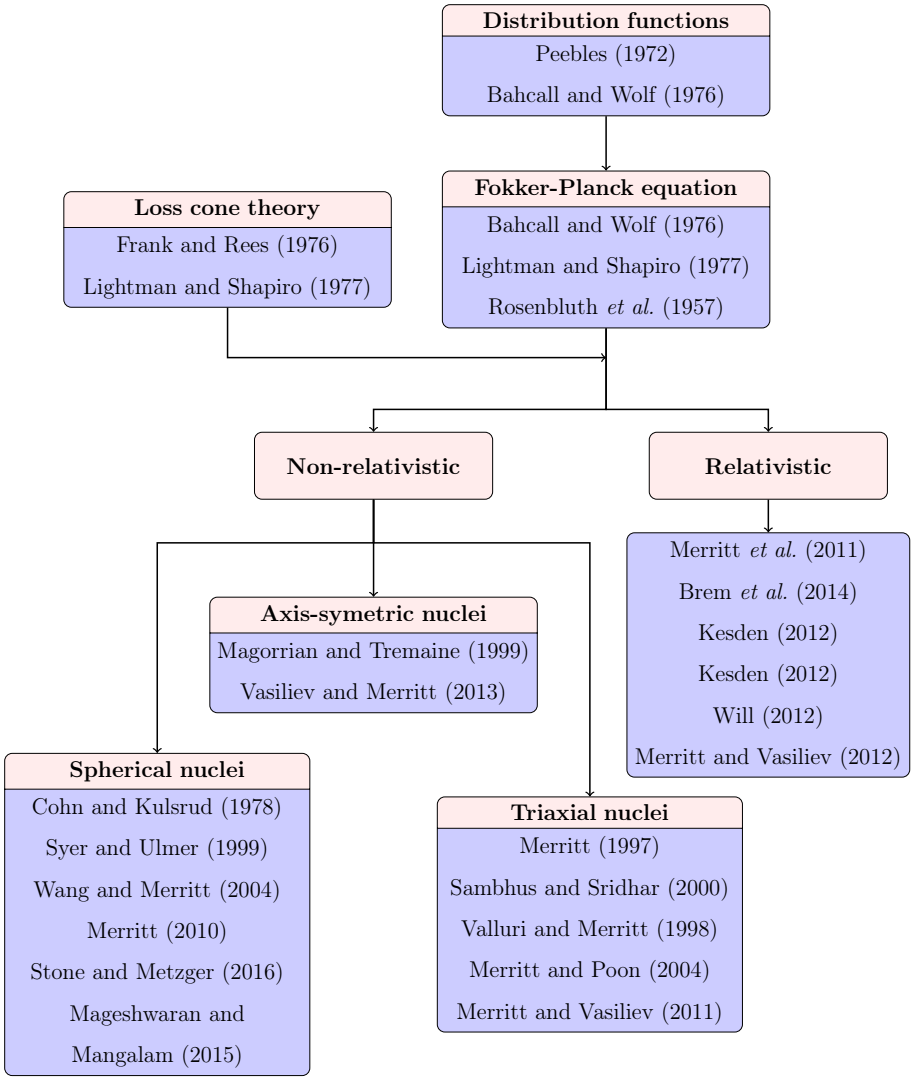

FIGURE 3.6: The BH stellar dynamical literature flow chart and their contextual interplay.

Chapter 4

Accretion physics

Image: ESO / ESA / Hubble / M. Kornmesser.

4.1 Introduction

The energy source for luminous quasars is the accretion of matter from the surrounding disk by the massive black holes. The simplest picture is that the source of energy is the extraction of potential energy through an accretion of the material from the disk. A mass element ΔM at a radius r is accreted by the black hole $M_\bullet$ and the energy released is $\Delta E = GM_\bullet \Delta M(1/R_s - 1/r)$, where R_s is the Schwarzschild radius. The luminosity from the source is given by

$$L = \frac{\Delta E}{\Delta t} = \frac{GM_\bullet}{R_s}\frac{\Delta M}{\Delta t}\left(1 - \frac{R_s}{r}\right) = \frac{GM_\bullet \dot{M}}{R_s}\left(1 - \frac{R_s}{r}\right) = \eta \dot{M} c^2, \qquad (4.1)$$

where $\dot{M}$ is the accretion rate and $\eta = (1/2)(1 - R_s/r)$ is the efficiency. At

high luminosity, the accretion rate is controlled by the radiation pressure from the photons to the accreting material through scattering and absorption. When the radiation pressure overcomes the gravity from the black hole, the accretion halts and the luminosity reaches the Eddington luminosity.

This simple accretion picture above involves the direct fall of matter into the black hole, whereas in general, the gas in the disk is rotating and thus it is necessary to remove the angular momentum to spiral down the matter into the black hole. The viscosity acting within the gas layers is the source of angular momentum exchange and depends on the nature of pressure dominating in the disk; this viscosity heats up the disk which is then emitted in the form of radiation. In this chapter, we will discuss various viscosity models, the accretion disk structure, the luminosity emitted and discuss the appropriate model for TDEs.

4.2 Equations of gas dynamics

The matter in the accretion disk is in a gaseous form consisting of free electrons and various species of ions that interacts within themselves through collision. The collision of a gas particle with another particle results in the change in the state of motion and these interactions occur over a length scale of mean free path. For a uniform gas distribution, these random interactions result in some mean velocity that is the velocity of the gas. Since we are interested in the length-scale $\gg$ mean free path, we can neglect these microscopic interactions and consider the fluid to be continuous with density ρ having velocity $\boldsymbol{v}$ and temperature T.

4.2.1 Equation of continuity

For a fluid density ρ in volume V_0, the total mass is $\int \rho \, \mathrm{d}V$ where the integration is over volume V_0. The mass of the fluid moving out of the surface $\mathrm{d}\boldsymbol{f}$ along the normal with velocity $\boldsymbol{v}$ is given by $\rho\boldsymbol{v} \cdot \mathrm{d}\boldsymbol{f}$, then the total mass of fluid flowing out from V_0 is $\oint_{V_0} \rho\boldsymbol{v} \cdot \mathrm{d}\boldsymbol{f}$. Thus the change in the fluid mass in volume V_0 due to fluid leaving V_0 is given by

$$\frac{\partial}{\partial t} \int \rho \, \mathrm{d}V = - \oint_{V_0} \rho\boldsymbol{v} \cdot \mathrm{d}\boldsymbol{f}, \tag{4.2}$$

which then using the Gauss divergence theorem, gives (Landau and Lifshitz 1959)

$$\frac{\partial \rho}{\partial t} + \boldsymbol{\nabla} \cdot (\rho\boldsymbol{v}) = 0. \tag{4.3}$$

4.2.2 Euler's equation

For a pressure P acting on the fluid in volume V_0, the total force is given by $\boldsymbol{F_p} = \oint \boldsymbol{P} \cdot \mathrm{d}\boldsymbol{f} = - \int \boldsymbol{\nabla}(P) \mathrm{d}V$. If the fluid is in gravitational field, then the gravitational force is given by $\boldsymbol{F_g} = \int \rho\boldsymbol{g} \, \mathrm{d}V$ such that the total force is $\boldsymbol{F} = \boldsymbol{F_p} + \boldsymbol{F_g}$. The equation of motion using $\boldsymbol{F} = \int \rho(\mathrm{d}\boldsymbol{v}/\mathrm{d}t) \, \mathrm{d}V$ gives (Landau and Lifshitz 1959)

$$\rho \frac{\mathrm{d}\boldsymbol{v}}{\mathrm{d}t} = -\boldsymbol{\nabla} P + \rho\boldsymbol{g} \tag{4.4}$$

The change in velocity $\mathrm{d}\boldsymbol{v}$ in time $\mathrm{d}t$ consists of change with t at a fixed point in space and the difference in velocity at two points separated out by $\mathrm{d}\boldsymbol{r}$ at the same

time t where $\mathrm{d}\boldsymbol{r}$ is the distance travelled by fluid in $\mathrm{d}t$. Then the net change in velocity is given by

$$\frac{\mathrm{d}\boldsymbol{v}}{\mathrm{d}t} = \frac{\partial \boldsymbol{v}}{\partial t} + (\boldsymbol{v}\cdot\boldsymbol{\nabla})\boldsymbol{v}. \tag{4.5}$$

Using eqns (4.3, 4.4, 4.5), the momentum flux is given by

$$\frac{\partial(\rho v_i)}{\partial t} = -\frac{\partial \Pi_{ik}}{\partial x_k} + \rho \boldsymbol{g}, \tag{4.6}$$

where $\Pi_{ik} = P\delta_{ik} + \rho v_i v_k$ is the momentum flux density tensor, v_i is the velocity component of $\boldsymbol{v}$ and x_k is the spatial component.

The Euler equation shown in eqn (4.4) is for an ideal fluid whereas there is a viscosity in real fluids. We now include the viscosity term in the Euler equation. The viscosity provides an irreversible transfer of momentum from high velocity to a low-velocity region and thus the equation of motion for a viscous fluid can be obtained by adding the viscosity stress tensor $-\sigma^{'}_{ik}$ to Π_{ik} given by $\Pi_{ik} = P\delta_{ik} + \rho v_i v_k - \sigma^{'}_{ik}$. Since the viscosity occurs when the different fluid particles move with different velocities so that there is a relative motion between various particles, the viscosity tensor should be a function of space derivative of the velocity, that is $\sigma^{'}_{ik} \propto \mathrm{d}v_i/\mathrm{d}x_k$. For a uniformly rotating fluid in which the velocity $\boldsymbol{v} = \boldsymbol{\Omega} \times \boldsymbol{r}$, where Ω is angular velocity, there is no friction which implies that $\sigma^{'}_{ik} = 0$ which is possible if $\sigma^{'}_{ik} = \mathrm{d}v_i/\mathrm{d}x_k + \mathrm{d}v_k/\mathrm{d}x_i$. Thus using the above conditions, the most general tensor is given by

$$\sigma^{'}_{ik} = \eta\left[\frac{\partial v_i}{x_k} + \frac{\partial v_k}{\partial x_i} - \frac{2}{3}\delta_{ik}\frac{\partial v_\ell}{\partial x_\ell}\right] + \zeta\delta_{ik}\frac{\partial v_\ell}{\partial x_\ell}, \tag{4.7}$$

where η and ζ are coefficients of viscosity, independent of bulk velocities and both are positive. Thus momentum equation for a viscous fluid using eqn (4.6) is given by

$$\rho\left[\frac{\partial v_i}{\partial t}+v_k\frac{\partial v_i}{\partial x_k}\right]=-\frac{\partial P}{\partial x_k}+\frac{\partial}{\partial x_k}\left[\eta\left(\frac{\partial v_i}{\partial x_k}+\frac{\partial v_k}{\partial x_i}-\frac{2}{3}\delta_{ik}\frac{\partial v_\ell}{\partial x_\ell}\right)\right]+\delta_{ik}\frac{\partial}{\partial x_k}\left(\zeta\frac{\partial v_\ell}{\partial x_\ell}\right)+\rho\boldsymbol{g}, \tag{4.8}$$

which for constant η and ζ is given by

$$\rho\frac{\mathrm{d}\boldsymbol{v}}{\mathrm{d}t}=-\boldsymbol{\nabla}P+\eta\nabla^2\boldsymbol{v}+\left(\zeta+\frac{\eta}{3}\right)\boldsymbol{\nabla}(\boldsymbol{\nabla}\cdot\boldsymbol{v})+\rho\boldsymbol{g}. \tag{4.9}$$

For an incompressible fluid, $\boldsymbol{\nabla}\cdot\boldsymbol{v}=0$, which reduces eqn (4.9) to (Landau and Lifshitz 1959)

$$\rho\frac{\mathrm{d}\boldsymbol{v}}{\mathrm{d}t}=-\boldsymbol{\nabla}P+\eta\nabla^2\boldsymbol{v}+\rho\boldsymbol{g}, \tag{4.10}$$

and this is called as Navier-Stokes equation.

4.2.3 Energy equation

For an adiabatic fluid, the entropy s is constant and using the law of thermodynamics given by

$$\mathrm{d}w = T\mathrm{d}s + V\mathrm{d}P, \tag{4.11}$$

where w is the enthalpy (heat function per unit mass of fluid), $V = 1/\rho$ is the volume per unit mass and P is the pressure. Since entropy is constant, we have

$$\mathrm{d}w = V\mathrm{d}P = \frac{\mathrm{d}P}{\rho}, \tag{4.12}$$

and using eqn (4.4), we have

$$\frac{\partial \boldsymbol{v}}{\partial t} + (\boldsymbol{v}\cdot\boldsymbol{\nabla})\boldsymbol{v} = -\boldsymbol{\nabla}w + \boldsymbol{g}. \tag{4.13}$$

Using vector identity $(1/2)\boldsymbol{\nabla}v^2 = \boldsymbol{v}\times(\boldsymbol{\nabla}\times\boldsymbol{v}) + (\boldsymbol{v}\cdot\boldsymbol{\nabla})\boldsymbol{v}$, eqn (4.13) is given by

$$\frac{\partial \boldsymbol{v}}{\partial t} - \boldsymbol{v}\times(\boldsymbol{\nabla}\times\boldsymbol{v}) = -\boldsymbol{\nabla}\left(w + \frac{v^2}{2} + \Phi(\boldsymbol{r})\right), \tag{4.14}$$

where $\boldsymbol{g} = -\boldsymbol{\nabla}\Phi(\boldsymbol{r})$ and $\Phi(\boldsymbol{r})$ is the potential of gravitational field. For a steady stream line flow along stream direction line ℓ, eqn (4.14) is given by

$$\frac{\partial}{\partial \ell}\left(w + \frac{v^2}{2} + \Phi(\boldsymbol{r})\right) = 0, \tag{4.15}$$

which gives $w+(1/2)v^2+\Phi(\boldsymbol{r}) =$ constant and this is called as Bernoulli's equation.

The energy of unit volume of fluid is $(1/2)\rho v^2 + \rho\epsilon$, where $(1/2)\rho v^2$ and $\rho\epsilon$ are the fluid's kinetic and internal energies. Using eqns (4.3), (4.9) and (4.12), we have

$$\frac{\partial}{\partial t}\left(\frac{1}{2}\rho v^2\right) = -\frac{1}{2}v^2\boldsymbol{\nabla}\cdot(\rho\boldsymbol{v}) - \rho\boldsymbol{v}\cdot\boldsymbol{\nabla}\left(\frac{1}{2}v^2 + w\right) + \rho T\boldsymbol{v}\cdot\boldsymbol{\nabla}s - \rho(\boldsymbol{v}\cdot\boldsymbol{\nabla})\Phi(\boldsymbol{r}) + v_i\frac{\partial\sigma_{ik}^{'}}{\partial x_k}, \tag{4.16}$$

and since enthalpy $w = \epsilon + P/\rho$, by using eqn (4.12) and (4.3), we obtain

$$\frac{\partial}{\partial t}(\rho\epsilon) = -w\boldsymbol{\nabla}\cdot(\rho\boldsymbol{v}) - \rho T\boldsymbol{v}\cdot\boldsymbol{\nabla}s. \tag{4.17}$$

Employing eqns (4.16) and (4.17), we have

$$\frac{\partial}{\partial t}\left(\frac{1}{2}\rho v^2 + \rho w\right) = -\boldsymbol{\nabla}\cdot\left[\rho\boldsymbol{v}\left(w + \frac{1}{2}v^2\right)\right] - \rho(\boldsymbol{v}\cdot\boldsymbol{\nabla})\Phi(\boldsymbol{r}) + v_i\frac{\partial\sigma_{ik}^{'}}{\partial x_k}. \tag{4.18}$$

Applying the vector identity $\boldsymbol{\nabla}\cdot(\psi\boldsymbol{A}) = \psi\boldsymbol{\nabla}\cdot\boldsymbol{A} + \boldsymbol{A}\cdot\boldsymbol{\nabla}\psi$, $\rho(\boldsymbol{v}\cdot\boldsymbol{\nabla})\Phi(\boldsymbol{r}) = \boldsymbol{\nabla}\cdot(\rho\boldsymbol{v}\Phi) + \partial(\rho\Phi)/\partial t - \rho\partial\Phi/\partial t$ and since $\Phi(\boldsymbol{r})$ is independent of time, eqn (4.18) reduces to

$$\frac{\partial}{\partial t}\left[\rho\left(\frac{1}{2}v^2 + w + \Phi(\boldsymbol{r})\right)\right] = -\boldsymbol{\nabla}\cdot\left[\rho\boldsymbol{v}\left(w + \frac{1}{2}v^2 + \Phi(\boldsymbol{r})\right) - \boldsymbol{v}\cdot\boldsymbol{\sigma}^{'}\right] - \sigma_{ik}^{'}\frac{\partial v_i}{\partial x_k}. \tag{4.19}$$

By integrating eqn (4.19) over a volume V, we obtain (Landau and Lifshitz 1959)

$$\frac{\partial}{\partial t}\int\left[\rho\left(\frac{1}{2}v^2+w+\Phi(\boldsymbol{r})\right)\right]\mathrm{d}V=-\oint\left[\rho\boldsymbol{v}\left(w+\frac{1}{2}v^2+\Phi(\boldsymbol{r})\right)-\boldsymbol{v}\cdot\boldsymbol{\sigma}^{'}\right]\cdot\mathrm{d}\boldsymbol{f}-\int\sigma^{'}_{ik}\frac{\partial v_i}{\partial x_k}\mathrm{d}V, \quad (4.20)$$

where the first term on right hand side gives the rate of change of energy of the fluid in V due to energy flux and the second term shows the decrease per unit time in energy due to dissipation.

4.3 Viscous tensor in curvilinear coordinates

The structure of an accretion disk is taken to be either cylindrical or spherical to solve the fluid equations. Thus, the viscous tensor in cylindrical and spherical coordinates are given below (Landau and Lifshitz 1959).

4.3.1 Cylindrical coordinates

In cylindrical coordinates $r,\ \phi,\ z$ the components of stress tensor is given by

$$\sigma^{'}_{rr}=2\eta\frac{\partial v_r}{\partial r}, \qquad \sigma^{'}_{r\phi}=\eta\left(\frac{1}{r}\frac{\partial v_r}{\partial\phi}+\frac{\partial v_\phi}{\partial r}-\frac{v_\phi}{r}\right) \quad (4.21a)$$

$$\sigma^{'}_{\phi\phi}=2\eta\left(\frac{1}{r}\frac{\partial v_\phi}{\partial\phi}+\frac{v_r}{r}\right), \qquad \sigma^{'}_{\phi z}=\eta\left(\frac{\partial v_\phi}{\partial z}+\frac{1}{r}\frac{\partial v_z}{\partial\phi}\right) \quad (4.21b)$$

$$\sigma^{'}_{zz}=2\eta\frac{\mathrm{d}v_z}{\mathrm{d}z}, \qquad \sigma^{'}_{zr}=\eta\left(\frac{\mathrm{d}v_z}{\mathrm{d}r}+\frac{\mathrm{d}v_r}{\mathrm{d}z}\right), \quad (4.21c)$$

Thus the Navier-Stokes equation and the equation of continuity are given by

$$\frac{\partial v_r}{\partial t} + v_r\frac{\partial v_r}{\partial r} + \frac{v_\phi}{r}\frac{\partial v_r}{\partial \phi} + v_z\frac{\partial v_r}{\partial z} - \frac{v_\phi^2}{r} = -\frac{1}{\rho}\frac{\partial P}{\partial r} - \frac{\partial \Phi}{\partial r} + \frac{1}{\rho}\left[\frac{1}{r}\frac{\partial (r\sigma_{rr}^{'})}{\partial r} + \frac{1}{r}\frac{\partial \sigma_{r\phi}^{'}}{\partial \phi} + \frac{\partial \sigma_{rz}^{'}}{\partial z} + \frac{\sigma_{rr}^{'} - \sigma_{\phi\phi}^{'}}{r}\right] \tag{4.22a}$$

$$\frac{\partial v_\phi}{\partial t} + v_r\frac{\partial v_\phi}{\partial r} + \frac{v_\phi}{r}\frac{\partial v_\phi}{\partial \phi} + v_z\frac{\partial v_\phi}{\partial z} + \frac{v_r v_\phi}{r} = -\frac{1}{\rho r}\frac{\partial P}{\partial \phi} - \frac{1}{r}\frac{\partial \Phi}{\partial \phi} + \frac{1}{\rho}\left[\frac{1}{r^2}\frac{\partial}{\partial r}\left(r^2\sigma_{r\phi}^{'}\right) + \frac{1}{r}\frac{\partial \sigma_{\phi\phi}^{'}}{\partial \phi} + \frac{\partial \sigma_{\phi z}^{'}}{\partial z}\right] \tag{4.22b}$$

$$\frac{\partial v_z}{\partial t} + v_r\frac{\partial v_z}{\partial r} + \frac{v_\phi}{r}\frac{\partial v_z}{\partial \phi} + v_z\frac{\partial v_z}{\partial z} = -\frac{\partial P}{\partial z} - \frac{\partial \Phi}{\partial z} + \frac{1}{\rho}\left[\frac{1}{r}\frac{\partial}{\partial r}\left(r\sigma_{zr}^{'}\right) + \frac{1}{r}\frac{\partial \sigma_{z\phi}^{'}}{\partial \phi} + \frac{\partial \sigma_{zz}^{'}}{\partial z} + \frac{\sigma_{zr}^{'}}{r}\right] \tag{4.22c}$$

$$\frac{\partial \rho}{\partial t} + \frac{1}{r}\frac{\partial}{\partial r}(r\rho v_r) + \frac{1}{r}\frac{\partial}{\partial \phi}(\rho v_\phi) + \frac{\partial}{\partial z}(\rho v_z) = 0. \tag{4.22d}$$

4.3.2 Spherical coordinates

In spherical coordinates $(r,\ \theta,\ \phi)$ the components of stress tensor are given by

$$\sigma'_{rr} = 2\eta\frac{\partial v_r}{\partial r}, \qquad \sigma'_{r\phi} = \eta\left[\frac{\partial v_\phi}{\partial r} + \frac{1}{r\sin\theta}\frac{\partial v_r}{\partial \phi} - \frac{v_\phi}{r}\right] \tag{4.23a}$$

$$\sigma'_{\phi\phi} = 2\eta\left[\frac{1}{r\sin\theta}\frac{\partial v_\phi}{\partial \phi} + \frac{v_r}{r} + \frac{v_\theta\cot\theta}{r}\right], \qquad \sigma'_{\phi\theta} = \eta\left[\frac{1}{r\sin\theta}\frac{\partial v_\theta}{\partial \phi} + \frac{1}{r}\frac{\partial v_\phi}{\partial \theta} - \frac{v_\phi\cot\theta}{r}\right] \tag{4.23b}$$

$$\sigma'_{\theta\theta} = 2\eta\left[\frac{1}{r}\frac{\partial v_\theta}{\partial \theta} + \frac{v_r}{r}\right], \qquad \sigma'_{\theta r} = \eta\left[\frac{1}{r}\frac{\partial v_r}{\partial \theta} + \frac{\partial v_\theta}{\partial r} - \frac{v_\theta}{r}\right], \tag{4.23c}$$

Thus the Navier-Stokes equation and the equation of continuity are given by

$$\rho\left[\frac{\partial v_r}{\partial t}+v_r\frac{\partial v_r}{\partial r}\frac{v_\theta}{r}\frac{\partial v_r}{\partial \theta}+\frac{v_\phi}{r\sin\theta}\frac{\partial v_r}{\partial \phi}-\frac{v_\theta^2+v_\phi^2}{r}\right]=-\frac{\partial P}{\partial r}-\rho\frac{\partial \Phi}{\partial r}+\frac{1}{r^2}\frac{\partial}{\partial r}(r^2\sigma_{rr}^{'})+\frac{1}{r\sin\theta}\frac{\partial}{\partial \theta}(\sin\theta\sigma_{r\theta}^{'})+\frac{1}{r\sin\theta}\frac{\partial\sigma_{r\phi}^{'}}{\partial\phi}-\frac{\sigma_{\theta\theta}^{'}+\sigma_{\phi\phi}^{'}}{r} \tag{4.24a}$$

$$\rho\left[\frac{\partial v_\theta}{\partial t}+v_r\frac{\partial v_\theta}{\partial r}+\frac{v_\theta}{r}\frac{\partial v_\theta}{\partial \theta}+\frac{v_\phi}{r\sin\theta}\frac{\partial v_\theta}{\partial \phi}+\frac{v_r v_\theta}{r}-\frac{v_\phi^2\cot\theta}{r}\right]=-\frac{1}{r}\frac{\partial P}{\partial\theta}+\frac{\rho}{r}\frac{\partial\Phi}{\partial\theta}+\frac{1}{r}\frac{\partial}{\partial r}(r\sigma_{\theta r}^{'})+\frac{1}{r\sin\theta}\frac{\partial}{\partial\theta}(\sin\theta\sigma_{\theta\theta}^{'})+\frac{1}{r\sin\theta}\frac{\partial\sigma_{\phi\phi}^{'}}{\partial\phi}+\frac{2\sigma_{r\theta}^{'}-\cot\theta\sigma_{\phi\phi}^{'}}{r} \tag{4.24b}$$

$$\rho\left[\frac{\partial v_\phi}{\partial t}+v_r\frac{\partial v_\phi}{\partial r}+\frac{v_\theta}{r}\frac{\partial v_\phi}{\partial \theta}+\frac{v_\phi}{r\sin\theta}\frac{\partial v_\phi}{\partial \phi}+\frac{v_r v_\phi}{r}+\frac{v_\theta v_\phi\cot\theta}{r}\right]=-\frac{1}{r\sin\theta}\frac{\partial P}{\partial\phi}+\frac{\rho}{r\sin\theta}\frac{\partial\Phi}{\partial\phi}+\frac{1}{r}\frac{\partial}{\partial r}(r\sigma_{\phi r}^{'})+\frac{1}{r}\frac{\partial\sigma_{\theta\phi}^{'}}{\partial\theta}+\frac{1}{r\sin\theta}\frac{\partial\sigma_{\phi\phi}^{'}}{\partial\phi}+\frac{2}{r}(\sigma_{r\phi}^{'}+\cot\theta\sigma_{\theta\phi}^{'}) \tag{4.24c}$$

$$\frac{\partial\rho}{\partial t}+\frac{1}{r^2}\frac{\partial}{\partial r}(r^2\rho v_r)+\frac{1}{r\sin\theta}\frac{\partial}{\partial\theta}(\rho v_\theta\sin\theta)+\frac{1}{r\sin\theta}\frac{\partial}{\partial\phi}(\rho v_\phi)=0. \tag{4.24d}$$

4.4 Eddington luminosity

The maximum luminosity of a source in hydrostatic equilibrium is the Eddington luminosity. If the luminosity exceeds the Eddington limit, then the radiation

pressure drives an outflow. The radiation flux is given by

$$\boldsymbol{\mathcal{F}} = -\frac{c}{\kappa}\frac{1}{\rho}\boldsymbol{\nabla} P, \tag{4.25}$$

where κ is the opacity and P is the radiation pressure. From Euler's equation in hydrostatic equilibrium given by eqn (4.4), the mean acceleration of zero implies that

$$\frac{\mathrm{d}\boldsymbol{v}}{\mathrm{d}t} = -\frac{1}{\rho}\boldsymbol{\nabla} P + \boldsymbol{g} = 0, \tag{4.26}$$

while eqn (4.25) then gives

$$\boldsymbol{\mathcal{F}} = \frac{c}{\kappa}\boldsymbol{g}. \tag{4.27}$$

The luminosity of a source bounded by a surface $\boldsymbol{f}$ in a volume V using Gauss's divergence theorem and $\boldsymbol{g} = -\boldsymbol{\nabla}\Phi$, is given by

$$L_E = \int \boldsymbol{\mathcal{F}} \cdot \mathbf{d}\boldsymbol{f} = \int \frac{c}{\kappa}\boldsymbol{g} \cdot \mathbf{d}\boldsymbol{f} = -\frac{c}{\kappa}\int \boldsymbol{\nabla}\Phi \cdot \mathbf{d}\boldsymbol{f} = -\frac{c}{\kappa}\int \nabla^2\Phi \mathrm{d}V, \tag{4.28}$$

and using Poisson equation given by $\nabla^2\Phi = -4\pi G\rho$, the Eddington luminosity is given by (Rybicki and Lightman 1986)

$$L_E = \frac{4\pi G c}{\kappa}\int \rho \mathrm{d}V = \frac{4\pi G M_\bullet c}{\kappa}. \tag{4.29}$$

Thus, using eqn (4.1), the Eddington mass accretion rate is given by

$$\dot{M}_E = \frac{4\pi G M_\bullet}{\eta \kappa c}. \tag{4.30}$$

The opacity κ is a measure of the impenetrability of medium to photons through absorption and scattering of radiation in a medium that depends on the nature of interactions between photons and electrons. The opacity due to elastic scattering of photons by an electron is called as Thomson opacity in which the photon energy $h\nu \ll mc^2$, where m is the particle mass and ν is the frequency of the photon. The Thomson opacity is given by $\kappa_{es} = 0.20(1+X)$ cm^2 g^{-1}, where X is hydrogen mass fraction and for solar composition $X = 0.7$ which gives $\kappa = 0.34$.

The electron passing close to ions experience the acceleration and an accelerating charge emits radiation. This is free-free emission, also called Bremsstrahlung dominates at high temperature where plasma is highly ionized. A free electron can also absorb a photon during a collision with an ion and this is called as free-free absorption. The opacity due to free-free absorption called as Kramers opacity is given by

$$\kappa_{ff} = 3.68 \times 10^{22} g_{ff}(1-Z)(1+X)\frac{\rho}{\text{g cm}^{-3}} T^{-7/2} \text{ cm}^2 \text{ g}^{-1}, \tag{4.31}$$

where g_{ff} is the quantum mechanical correction, Z is the mass fraction of elements higher than hydrogen. Since κ is due to the Thomson scattering, the opacity is taken to be constant in the calculation of Eddington luminosity.

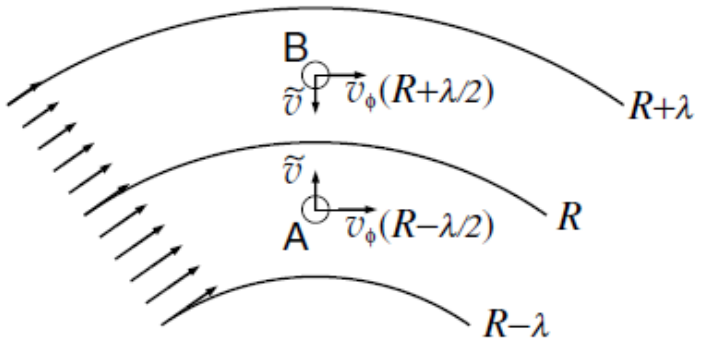

FIGURE 4.1: The exchange of fluid blob in a diffrentially rotating fluid that results in a transfer of angular momentum from inner annulus to the outer.

4.5 Viscous torques

We consider an accretion disk which is rotating with Keplerian velocity $\omega = \sqrt{GM_\bullet/r^3}$ and whose inner radius is r_{in} and outer radius is r_{out}. The matter is accreted by the black hole at the inner radius and the matter at higher radius moves inward. Since the matter is following a Keplerian orbit with specific angular momentum $J = \sqrt{GM_\bullet r}$ and with a value inner radius of $J_{in} = \sqrt{GM_\bullet r_{in}}$, the matter has to lose its angular momentum through some viscous mechanism to move inward.

A rotating accretion disk whose angular velocity ω is a function of radius r has a shear viscosity where the differential rotation results in an orthogonal transport of the momentum to the direction of gas motion which results in an inward flow of mass. We consider an accretion disk in a cylindrical coordinates with density $\rho(r)$ and height $H(r)$, rotating with velocity $v_\phi = r\omega(r)$. Let us consider a surface R through which the mass is flowing due to shear viscosity from both upper and lower layers at a separation of $\lambda/2$ from R with a velocity $\tilde{v}$. Due to chaotic motion of the plasma in an equilibrium flow, the mass flux through the surface is equal from upper and lower layers but this flow of matter results in the transfer of angular momentum with a net angular momentum flux as shown in Fig 4.1. The $\phi-$

momentum flux crossing R from $R+\lambda/2$ is given by $L_{\phi}^{+} = \rho\tilde{v}H(R+\lambda/2)v_{\phi}(R-\lambda/2)$ and from layer $R-\lambda/2$ is given by $L_{\phi}^{-} = \rho\tilde{v}H(R-\lambda/2)v_{\phi}(R+\lambda/2)$. Using a Taylor series expansion for $\lambda \ll 1$, we obtain to first order in λ, a torque per unit length given by (Frank *et al.* 2002)

$$\dot{\mathcal{L}} = -\rho\tilde{v}H\lambda R^2\omega^{'}, \tag{4.32}$$

where $\omega^{'} = \mathrm{d}\omega/\mathrm{d}r$. The non-vanishing component of stress here is the force in $\phi-$ direction and using eqn (4.21), it is found to be $\sigma^{'} = -\eta R\omega^{'}$. By comparing $\sigma^{'}_{r\phi}$ with eqn (4.32), we obtain the kinematic viscosity $\nu = \lambda\tilde{v}$ and torque exerted by the outer layer on the inner layer to be given by

$$\mathcal{G} = 2\pi\nu R\Sigma R^2\omega^{'}, \tag{4.33}$$

where $\Sigma = \rho H$. Since the plasma is in thermal motion, the particles carrying energy and momentum will interact to attain an equilibrium state. Thus, the microscopic properties of this plasma will affect the macroscopic properties through transport process which is important when there is a large gradient in velocity and temperature of the plasma. The net rate of momentum transferred across the surface is given by

$$-\rho\tilde{v}\left(v_{\phi} + \lambda\frac{\partial v_{\phi}}{\partial r}\right) + \rho\tilde{v}\left(v_{\phi} - \lambda\frac{\partial v_{\phi}}{\partial r}\right) = -2\rho\tilde{v}\lambda\frac{\partial v_{\phi}}{\partial r} \tag{4.34}$$

The momentum transferred implies that there is a force acting along r directions which can be obtained by calculating the momentum transferred at r and $r + \mathrm{d}r$

so that

$$\mathrm{d}F_{vis} = 2\rho\tilde{v}\lambda\mathrm{d}A\left(\frac{\partial v_\phi}{\partial r} + \frac{\partial^2 v_\phi}{\partial r^2}\mathrm{d}r\right) - 2\rho\tilde{v}\lambda\mathrm{d}A\frac{\partial v_\phi}{\partial r} \tag{4.35a}$$

$$= 2\rho\tilde{v}\lambda\frac{\partial^2 v_\phi}{\partial r^2}\mathrm{d}A\mathrm{d}r, \tag{4.35b}$$

where $\mathrm{d}A$ is the area element and volume is given by $\mathrm{d}V = \mathrm{d}A\mathrm{d}r$ which results in the viscous force density given by

$$f_{\text{vis, shear}} = 2\rho\tilde{v}\lambda\frac{\partial^2 v_\phi}{\partial r^2}. \tag{4.36}$$

The inertia of the plasma is given by $\rho(\partial_t \boldsymbol{v} + (\boldsymbol{v}\cdot\boldsymbol{\nabla}\boldsymbol{v}))$ and since the velocity is dominated by rotational velocity, the inertia is $\sim \rho v_\phi^2/r$. The Reynolds number is given by

$$R_e = \frac{\text{Interia}}{\text{Viscous}} \sim \frac{v_\phi^2}{r}\frac{1}{2\tilde{v}\lambda v_\phi/r^2} \sim \frac{r v_\phi}{\lambda\tilde{v}} \sim \frac{r v_\phi}{\nu}, \tag{4.37}$$

and the viscosity is important if $R_e \ll 1$.

4.5.1 Molecular viscosity

Any small perturbation from hydrostatic equilibrium propagates through the gas as sound waves with speed $c_s = \sqrt{\mathrm{d}P/\mathrm{d}\rho}$, and for gas pressure dominated system $P = \rho k_B T/(\mu m_p)$, where k_B is the Boltzmann constant, T is the temperature, μ is the mean-molecular weight and m_p is the mass of proton, $c_s = 10(T/10^4\mathrm{K})^{1/2}$ km sec^{-1}. The coloumb interaction energy $e_1 e_2/(4\pi\epsilon_0 b_0)$ where ϵ_0 is the emissivity of the medium, e_1 and e_2 are the charges, is of the order of mean thermal energy $(1/2)mv^2 \sim k_B T$ at the radius b_0 given by

$$b_0 = \frac{e_1 e_2}{4\pi\epsilon_0 k_B T}. \tag{4.38}$$

Thus the mean free path of the interaction $\lambda = 1/(n\pi b_0^2)$ which gives $\lambda = 7 \times 10^5 T^2 n^{-1}$ cm, where $n(\mathrm{cm}^{-3})$ is the density of the medium. With a more detailed analysis of coloumb interactions, the mean free path is given by $\lambda = 7 \times 10^5 T^2 n^{-1} \ln\Lambda$ cm, where $\Lambda = \lambda_D/b_0$ and $\lambda_D = k_B T/(4\pi e^2 n)$. Using the mean velocity $\tilde{v} \sim c_s$ and the Keplerian velocity $v_\phi = r\omega = \sqrt{GM_\bullet/r}$, the Reynolds number is given by

$$R_e = 0.2 \left(\frac{n}{\mathrm{cm}^{-3}}\right) \left(\frac{M_\bullet}{M_\odot}\right)^{\frac{1}{2}} \left(\frac{r}{10^{10}\ cm}\right)^{\frac{1}{2}} \left(\frac{T}{10^4\ \mathrm{K}}\right)^{-\frac{5}{2}}, \tag{4.39}$$

and since density $n \sim 10^{15}$ cm^{-3}, it follows that the $R_e \gg 1$ which in turn implies that the microscopic viscosity is negligible.

4.6 Radiative flux

For annuli of inner radius r and outer radius $r + \mathrm{d}r$, the angular momentum of the fluid changes and thus the rate of working is given by

$$\frac{\partial E}{\partial t} = \omega \frac{\partial \mathcal{G}}{\partial r} \mathrm{d}r = \left[\frac{\partial}{\partial r}(\mathcal{G}\omega) - \mathcal{G}\omega^{'} \right], \mathrm{d}r \tag{4.40}$$

where the first term on RHS is just the rate of convection of rotational energy through the gas by the torques and the second term is the local rate of loss of mechanical energy that must go into internal (heat) energy. Thus the viscous dissipation per unit area is given by (Frank *et al.* 2002)

$$D(r) = \frac{\mathcal{G}\omega^{'}}{4\pi r} = \frac{1}{2}\nu\Sigma(r\omega^{'})^2, \tag{4.41}$$

which is obtained using eqn (4.33). The viscous stress tensor is given by $\sigma^{'}_{r\phi} = 2\nu\rho r\omega^{'}$ and thus using eqn (4.33), $\mathcal{G}/\sigma^{'}_{r\phi} = \pi r^2\Sigma/\rho$ and for $\rho = \Sigma/H$, $\mathcal{G} = \pi r^2 H\sigma^{'}_{r\phi}$. The vertically integrated stress $\Pi_{r\phi} = \int \sigma^{'}_{r\phi}\,\mathrm{d}z = H\sigma^{'}_{r\phi}$, results in $\mathcal{G} = \pi r^2\Pi_{r\phi}$. Then the viscous dissipation is given by

$$D(r) = \frac{\mathcal{G}\omega^{'}}{4\pi r} = \frac{r\omega^{'}\Pi_{r\phi}}{4} = \frac{3}{8}\omega\Pi_{r\phi}. \tag{4.42}$$

In the thin disc approximation, the disc medium is essentially plane-parallel at each radius, so that the temperature gradient is effectively in the z-direction. The flux of radiant energy through a surface at given z is given by (Rybicki and Lightman 1986)

$$F = -\frac{16\sigma_{SB}T^3}{3\kappa\rho}\frac{\partial T}{\partial z} = \frac{4\sigma_{SB}}{3\kappa\rho}\frac{\partial T^4}{\partial z} \simeq \frac{4\sigma_{SB}}{3\tau}T^4(z), \tag{4.43}$$

where the optical depth is given by $\tau = \rho\kappa H = \kappa\Sigma$. The energy radiated per unit volume per unit time is given by

$$\frac{\partial F}{\partial z} = q^-_{rad}. \tag{4.44}$$

The energy balance equation is

$$q^-_{rad} = q^+, \tag{4.45}$$

where q^+ is the volume rate of energy production by viscous dissipation. After integrating, we obtain

$$F(H) - F(0) = \int q^+ \, \mathrm{d}z = D(r). \tag{4.46}$$

Using eqn (4.43), and the fact that the central temperature exceeds the surface temperature such that $T_c^4 \gg T^4(H)$, we obtain

$$\frac{4\sigma_{SB}}{3\tau}T_c^4 = D(r), \tag{4.47}$$

and the radiative rate per unit area is $Q^+_{rad} = \sigma_{SB}T_e^4 = 4\sigma_{SB}T_c^4/(3\tau)$, where T_e is the effective temperature. With the given effective temperature and assuming the

system to have blackbody emission, the emission flux is given by

$$F_\nu = \frac{2h\nu^3}{c^2}\frac{1}{\exp\left[\frac{h\nu}{k_B T_e}\right]-1}, \tag{4.48}$$

where ν is the frequency and h is the Planck constant.

In the above relation, it is assumed that the energy dissipated through viscous heating is radiated away. In some cases, where accretion rate is high, the energy dissipated may be consumed by the black hole through advection. The advection rate per unit volume is given by

$$q^-_{adv} = \frac{\rho v_r}{r} T_c \frac{\mathrm{d}s}{\mathrm{d}\ln r}, \tag{4.49}$$

where s is the entropy and the vertical integration gives the advection rate per unit area, given by

$$Q^-_{adv} = \frac{\Sigma v_r}{r} T_c \frac{\mathrm{d}s}{\mathrm{d}\ln r}. \tag{4.50}$$

Thus the energy conservation equation gives

$$q^+ = q^-_{rad} + q^-_{adv}. \tag{4.51}$$

The following classes of solutions have been investigated earlier:

1. $q^-_{adv} \ll q^+ \approx q^-_{rad}$: cooling dominated accretion flows (Shapiro *et al.* 1976)

2. $q^-_{rad} \ll q^-_{adv} \approx q^+$: Slim disk, advection dominated accretion flows (ADAF) (Narayan and Yi 1995)

3. $q^+ \ll q^-_{rad} \approx -q^-_{adv}$: cooling flows, low angular momentum (Medvedev and Narayan 2000)

4.6.1 α viscosity prescription

The fluid motion is turbulent if $R_e > 1$ where the fluid shows chaotic motion on arbitrary short times and lengthscales. The motion is smooth below the turbulence lengthscale $\lambda_{\rm turb}$ and velocity $v_{\rm turb}$. For an accretion disk with height H, the maximum turbulence scale is $\lambda_{\rm turb} = H$ and for a subsonic flow $v_{\rm turb} \leq c_s$, the turbulent viscosity $\nu \sim \lambda_{\rm turb} v_{\rm turb}$ which gives

$$\nu = \alpha c_s H, \tag{4.52}$$

where α is a constant. This is the $\alpha-$ prescription of Shakura & Sunyaev (1973). For a streamline flow, the viscosity should less than the turbulent viscosity which implies that $\alpha < 1$ and is generally taken to be 0.1. The viscous stress is given by (Shakura and Sunyaev 1973)

$$\Pi_{r\phi} = \alpha_s P_g H, \tag{4.53}$$

where α_s is the constant, H is the scale height and P_g is the gas pressure. Using eqn (6.47) and the radiative loss given by $Q^-_{rad} = \sigma T_e^4 = (4ac/3\kappa)(T_c^4/\Sigma_d)$, the energy conservation equation gives

$$\frac{3}{8}\omega\Pi_{r\phi} = \frac{4ac}{3\kappa}\frac{T_c^4}{\Sigma_d}, \tag{4.54}$$

which together with eqn. (4.53) gives

$$\Pi_{r\phi} = \left(\frac{9}{32}\frac{\kappa\sqrt{GM_\bullet}}{ac}\left(\frac{\alpha_s k_B}{2\mu m_p}\right)^4\right)^{\frac{1}{3}}\Sigma_d^{5/3} r^{-1/2} \tag{4.55}$$

4.6.2 Magnetic viscosity

The local shear tensor due to the magnetic field B, depends on the magnetic density $\sim B^2/(8\pi)$. The magnetic field induces a Lorentz force due to motion of plasma and the shear tensor is given by

$$\Pi_{r\phi} \approx \frac{B^2 H}{8\pi}. \tag{4.56}$$

A strongly magnetized disk would behave according to the viscosity prescription given by eqn (4.56) and in the weak field limit, it is likely to be approximately given by eqn (4.53) with $\alpha \sim 0.01 - 0.1$ as seen in various simulations (King *et al.* 2007; Frank *et al.* 2002).

4.6.3 Gravitational instability

Any perturbation in the disk will induce mass accumulation and these regions with more matter will exert a gravitational force on the neighboring regions which results in the collapsing of the accretion disk. The criteria for the stability of the disk is given by (Toomre 1964)

$$Q_T = \frac{c_s \omega}{\pi G \Sigma} > \frac{1}{2}, \tag{4.57}$$

where Σ_0 is the surface density. For a uniformly rotating isothermal disk, the criteria for stability is $Q_T > 1.06$ (Goldreich and Lynden-Bell 1965). Lin and Pringle (1987) estimated the effective kinematic viscosity due to gravitational instability to be $\nu = \omega \ell^2$, where ℓ is the critical shearing length given by $\ell = G\Sigma\omega^2$ which is the maximum possible size for instability. Hence the viscous stress is given by

$$\Pi_{r\phi} = -\alpha_g \nu \Sigma r \frac{\partial \omega}{\partial r}, \tag{4.58}$$

which for a Keplerian disk is given by (Mangalam 2001)

$$\Pi_{r\phi} = \frac{3}{2} \alpha_g \nu \Sigma^3 \omega^{-2}, \tag{4.59}$$

where $Q_T^2 < \alpha_g < 1$ is a constant parameter.

4.6.4 Radiative viscosity

The photons interact with the electrons through Thomson scattering and the photon is scattered if the interaction lies within the area of cross section σ_T. Thus, the mean free path is $\lambda = 1/(n_e\sigma_T)$, where n_e is the electron density. The x-direction momentum transferred by photon from y-direction is $\lambda(\partial v_x/\partial y)\left\langle E\right\rangle/c^2$, where $\langle E\rangle$ is the average photon energy. For an isotropic distribution of photons, the y flux of photons, that is the number of photons per unit area per unit time is, $\sim \epsilon_\gamma c/(3\left\langle E\right\rangle)$, where ϵ_γ is the energy of a photon. Total x-momentum transported per unit area per unit time is

$$\lambda\frac{\partial v_x}{\partial y}\frac{\epsilon_\gamma}{3c} = \frac{\epsilon_\gamma}{3n_e\sigma_T c}\frac{\partial v_x}{\partial y}. \tag{4.60}$$

The viscous stress is given by $\eta(\partial v_x/\partial y)$ and by comparing with eqn (4.60), we obtain

$$\eta_\gamma = \frac{1}{3}\frac{\epsilon_\gamma}{n_e\sigma_T c}. \tag{4.61}$$

A complete model that includes the Thomson cross section and anisotropic photon distribution gives (Misner 1968; Weinberg 1971)

$$\eta_\gamma = \frac{8}{27}\frac{\epsilon_\gamma}{n_e\sigma_T c}, \tag{4.62}$$

which is close to the value estimated in eqn (4.61) by an order $9/8 = 1.125$. The viscous stress is given by (Mangalam 2003)

$$\Pi_{r\phi} = \eta_\gamma r H \frac{\partial \omega}{\partial r}, \qquad \eta_\gamma = \frac{8}{27} \frac{\epsilon_\gamma}{n_e \sigma_T c}, \tag{4.63}$$

and is called as the radiative viscosity.

We now study the disk structure using the viscosity prescription discussed above and the most commonly used viscosity is the α viscosity.

4.7 Thin disk structure

We consider cylindrical coordinates $(r,\ \phi,\ z)$ where matter lies very close to the mid-plane $z = 0$ and is rotating around the black hole with angular velocity ω. For an axially symmetric disk, $\partial/\partial\phi = 0$ and assuming the dominant viscous stress to be $\Pi_{r\phi}$, the vertical momentum equation of the disk using eqn (4.22) by neglecting other viscous terms is given by

$$\frac{1}{2}\frac{\partial}{\partial z} v_z^2 = -\frac{1}{\rho}\frac{\partial}{\partial z} P - \frac{\partial}{\partial z}\Phi(r, z), \tag{4.64}$$

where for a hydrostatic equilibrium $v_z = 0$, and the vertical structure of disk is given by

$$\frac{1}{\rho}\frac{\partial}{\partial z} P + \frac{\partial}{\partial z}\Phi(r, z) = 0, \tag{4.65}$$

which for $\Phi(r,\ z) = -GM_\bullet/\sqrt{r^2+z^2}$ and for a disk in hydrostatic equilibrium, in the limit scale height $H \ll r$, reduces to

$$H^2 \frac{GM_\bullet}{r^3} = c_s^2 = \left|\frac{\partial P}{\partial \rho}\right|_{z=0}. \tag{4.66}$$

The radial momentum equation of the disk using eqn (4.22) in the limit of $v_r \ll v_\phi$, where v_r is the radial velocity and v_ϕ is the azimuthal velocity, is given by

$$\frac{v_\phi^2}{r} = \frac{1}{\rho}\frac{\partial}{\partial r}P - \frac{\partial}{\partial r}\Phi(r,\ z), \tag{4.67}$$

where $v_\phi = r\omega(r)$. Using eqn (6.8)

$$\frac{1}{\rho}\frac{\partial}{\partial r}P = \frac{1}{\rho}c_s^2\frac{\partial}{\partial r}\rho = \left(\frac{H}{r}\right)^2 \frac{GM_\bullet}{r^2}, \tag{4.68}$$

which is much smaller than the term $\partial_r\Phi(r,\ z)|_{z=0} = GM_\bullet/r^2$; therefore by neglecting pressure term in eqn (4.67), we obtain

$$\omega = \sqrt{\frac{GM_\bullet}{r^3}}. \tag{4.69}$$

We consider the conservation equations for the mass and angular momentum transport in the disc due to the radial drift motions. An annulus of the disc material lying between r and $r + \Delta r$ has total mass $2\pi r\Delta r\Sigma$ and angular momentum $2\pi r\Delta r\Sigma r 2\omega$. The rate of change these quantities is given by the net flow from the neighbouring annuli. For mass conservation,

$$\frac{\partial}{\partial t}(2\pi r\Sigma\Delta r) = 2\pi r\Sigma(r,\ t)v_r(r,\ t) - 2\pi(r+\Delta r)\cdot \Sigma(r+\Delta,\ t)v_r(r+\Delta r,\ t) \quad (4.70)$$

$$= -2\pi\Delta r\frac{\partial}{\partial_r}(r\Sigma\ v_r), \quad (4.71)$$

and in the limit $\Delta r \to 0$, the mass conservation reduces to

$$\frac{\partial\Sigma}{\partial t} = -\frac{1}{r}\frac{\partial}{\partial r}(r\Sigma\ v_r). \quad (4.72)$$

The angular momentum conservation for the net effect of viscous torque $\mathcal{G}(r,\ t)$, is given by

$$\frac{\partial}{\partial t}(2\pi r\Sigma\Delta r r^2\omega) = 2\pi r\Sigma(r,\ t)v_r(r,\ t)r^2\omega - 2\pi(r+\Delta r)\Sigma(r+\Delta,\ t)\cdot v_r(r+\Delta r,\ t)(r+\Delta r)^2\omega(r+\Delta r) + \frac{\partial\mathcal{G}(r,\ t)}{\partial r}\Delta r \quad (4.73)$$

$$= -2\pi\Delta r\frac{\partial}{\partial_r}(r\Sigma\ v_r r^2\omega^{'}) + \frac{\partial\mathcal{G}(r,\ t)}{\partial r}\Delta r, \quad (4.74)$$

where $\mathcal{G}(r,\ t)$ is given by eqn (4.33) and in the limit $\Delta r \to 0$, the eqn (4.74) reduces to

$$r\frac{\partial}{\partial t}(\Sigma r^2\omega) + \frac{\partial}{\partial r}(r\Sigma v_r r^2\omega) = \frac{1}{2\pi}\frac{\partial\mathcal{G}(r,\ t)}{\partial r}. \quad (4.75)$$

Using eqns (5.15), (4.75) and (4.33), the disk evolution equation is given by

$$\frac{\partial \Sigma}{\partial t} = \frac{3}{r}\frac{\partial}{\partial r}\left[r^{1/2}\frac{\partial}{\partial r}(\nu \Sigma r^{1/2})\right], \tag{4.76}$$

and the radial velocity v_r is given by

$$v_r = -\frac{3}{\Sigma r^{1/2}}\frac{\partial}{\partial r}(\nu \Sigma r^{1/2}). \tag{4.77}$$

4.7.1 Steady thin disk

For a stable disc, $\partial/\partial t = 0$ and using the mass conservation given by eqn (5.15), we have $r\Sigma v_r$ = constant and since $v_r < 0$, the accretion rate is given by (Frank *et al.* 2002)

$$\dot{M} = -2\pi r \Sigma v_r. \tag{4.78}$$

Using angular momentum conservation given by eqn (4.75) is

$$r\Sigma v_r r^2 \omega = \frac{\mathcal{G}}{2\pi} + \frac{C}{2\pi}, \tag{4.79}$$

where C is a constant. Since the matter leaves the accretion disk at $r = r_{in}$, the angular velocity $\omega(r_{in}) < \omega_K$, where ω_K is the Keplerian velocity. In this case, the angular velocity of the disc material remains Keplerian and thus increases inwards, until it begins to decrease to the value $\omega(r_{in})$. This implies that at some radius $r_{in} + b$, $\omega^{'}(r_{in} + b) = 0$ which reduces the eqn (4.79) to

$$C = 2\pi\Sigma v_r r_{in}^3 \omega(r_{in} + b), \tag{4.80}$$

and for $b \ll 1$, $C = -\dot{M}(GM_\bullet r_{in})^{1/2}$, which using eqns (4.77) and (4.79) gives

$$\nu\Sigma = \frac{\dot{M}}{3\pi}\left[1 - \sqrt{\frac{r_{in}}{r}}\right]. \tag{4.81}$$

Using eqns (4.78) and (4.98), the radial velocity is given by

$$v_r = -\frac{3\nu}{2r}\left[1 - \sqrt{\frac{r_{in}}{r}}\right]^{-1}. \tag{4.82}$$

We can see that the $v_r \sim \nu/r = \alpha c_s H/r \ll 1$ for the α viscosity prescription given by eqn (4.52). The Mach number $\mathcal{M}$, is defined by

$$\mathcal{M} = \frac{v_\phi}{c_s}. \tag{4.83}$$

For a Keplerian velocity $\omega = \sqrt{GM_\bullet/r^3}$ and using eqn (6.8), we obtain

$$H = \mathcal{M}^{-1} r \tag{4.84}$$

$$v_r = \alpha c_s \mathcal{M}^{-1}. \tag{4.85}$$

Since $H \ll r$, $\mathcal{M} \gg 1$ and thus circular velocity v_ϕ is Keplerian and highly supersonic whereas the radial velocity v_r is subsonic. The radial drift velocity and

vertical scale-height are self-consistently small.

Thus the viscous dissipation for Keplerian velocity is given by

$$D(r) = \frac{9}{8}\nu\Sigma\frac{GM_\bullet}{r^3} = \frac{3}{8\pi}\frac{GM_\bullet\dot{M}}{r^3}\left[1-\sqrt{\frac{r_{in}}{r}}\right], \tag{4.86}$$

and comparing it with the radiation flux, the temperature is given by

$$\sigma_{SB}T_e^4 = \frac{9}{8}\nu\Sigma\frac{GM_\bullet}{r^3} = \frac{3}{8\pi}\frac{GM_\bullet\dot{M}}{r^3}\left[1-\sqrt{\frac{r_{in}}{r}}\right]. \tag{4.87}$$

Following a blackbody assumption, the luminosity is given by

$$L = \int_{r_1}^{r_2} 2\pi r\sigma_{SB}T_e^4\,\mathrm{d}r = \frac{3G\dot{M}M_\bullet}{2}\left[\frac{1}{r_1}\left(1-\frac{2}{3}\left(\frac{r_{in}}{r_1}\right)^{1/2}\right)-\frac{1}{r_2}\left(1-\frac{2}{3}\left(\frac{r_{in}}{r_2}\right)^{1/2}\right)\right]. \tag{4.88}$$

For $r_1 = r_{in}$ and $r_2 \to \infty$, the luminosity is given by

$$L = \frac{1}{2}\frac{GM_\bullet\dot{M}}{r_{in}}, \tag{4.89}$$

which implies that the half of the potential energy at the inner radius in radiated.

The sound speed c_s is given by

$$c_s^2 = \frac{P}{\rho} \tag{4.90}$$

where, in general, the pressure P is the sum of gas and radiation pressures that is given by

$$P = \frac{\rho k_B T_c}{\mu m_p} + \frac{a}{3} T_c^4, \tag{4.91}$$

where T_c is the mid-plane temperature and a is the radiation constant. To obtain the structure of thin disk, we need to solve a complete set of equations that are given below:

$$\begin{aligned}
\rho &= \frac{\Sigma}{H} && (4.92)\\
H &= \frac{c_s r^{3/2}}{\sqrt{GM_\bullet}} && (4.93)\\
c_s^2 &= \frac{P}{\rho} && (4.94)\\
P &= \frac{\rho k_B T_c}{\mu m_p} + \frac{a}{3} T_c^4 && (4.95)\\
\tau &= \Sigma\kappa && (4.96)\\
\frac{4\sigma T_c^4}{3\tau} &= \frac{3GM_\bullet \dot{M}}{8\pi r^3}\left[1 - \sqrt{\frac{r_{in}}{r}}\right] && (4.97)\\
\nu\Sigma &= \frac{\dot{M}}{3\pi}\left[1 - \sqrt{\frac{r_{in}}{r}}\right] && (4.98)\\
\nu &= \alpha c_s H, && (4.99)
\end{aligned}$$

where τ is the optical depth. If we assume that the pressure is dominated by gas and the opacity is Kramers opacity $\kappa = 5 \times 10^{24} \rho T_c^{-7/2}$ cm^2 g^{-1}, using eqns

(4.97) and (4.96), we obtained $T_c^4/(\Sigma\kappa) \propto M_\bullet \dot{M} f^4/r^3$, which using eqns (4.93) and (4.98) results in $T_c^8 \propto D\Sigma^2\sqrt{M_\bullet} r^{-3/2}$, where $f = 1 - \sqrt{r_{in}/r}$ and $D = (3GM_\bullet\dot{M}/(8\pi r^3))f$. Then, using eqns (4.98) and (4.99), the temperature and surface density are given by

$$T_c^8 \propto \Sigma^2 D M_\bullet^{\frac{1}{2}} r^{-\frac{3}{2}} \tag{4.100}$$

$$\Sigma \propto \alpha^{-\frac{4}{5}} \dot{M}^{\frac{7}{10}} M_\bullet^{\frac{1}{4}} r^{-\frac{3}{4}} f^{\frac{14}{5}}. \tag{4.101}$$

A complete solution of Shakura-Sunyaev disk is

$$\Sigma = S_1\ \alpha^{-\frac{4}{5}} \dot{M}^{\frac{7}{10}} M_\bullet^{\frac{1}{4}} r^{-\frac{3}{4}} f^{\frac{14}{5}} \tag{4.102}$$

$$H = S_2\ \alpha^{-\frac{1}{10}} \dot{M}^{\frac{3}{20}} M_\bullet^{-\frac{3}{8}} r^{\frac{9}{8}} f^{\frac{3}{5}} \tag{4.103}$$

$$\rho = S_3\ \alpha^{-\frac{7}{10}} \dot{M}^{\frac{11}{20}} M_\bullet^{\frac{5}{8}} r^{-\frac{15}{8}} f^{\frac{11}{5}} \tag{4.104}$$

$$T_c = S_4\ \alpha^{-\frac{1}{5}} \dot{M}^{\frac{3}{40}} M_\bullet^{\frac{1}{4}} r^{-\frac{3}{4}} f^{\frac{6}{5}}, \tag{4.105}$$

where $S_1,\ S_2,\ S_3,\ S_4$ are the scales and all other parameters are scaled by the numbers given in Table 4.1.

Using eqn (4.103), the H/r ratio is given by

$$\frac{H}{r} = \alpha^{-\frac{1}{10}} \dot{M}^{\frac{3}{20}} M_\bullet^{-\frac{3}{8}} r^{\frac{1}{8}} f^{\frac{3}{5}} \begin{cases} 1.7 \times 10^{-2} & \text{Stellar} \\ 1.7 \times 10^{-3} & \text{AGN} \end{cases} \tag{4.106}$$

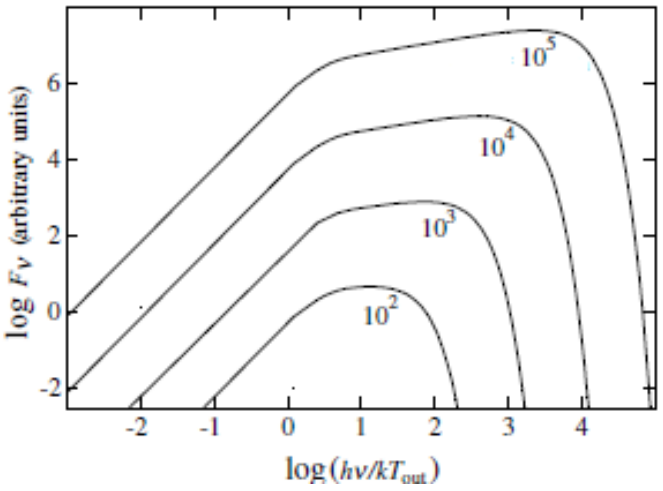

FIGURE 4.2: The continuum spectrum of a steady optically thick accretion disk assuming the disk to be a blackbody with different ratios r_{out}/r_{in}. The frequency is normalized to $k_B T_{out}/h$ where $T_{out} = T(r_{out})$ is temperature at outer radius. Courtesy: Frank *et al.* (2002)

Scale	Stellar	AGN
S_1 (g cm^{-2})	5.2	5.2×10^6
S_2 (cm)	1.7×10^8	1.7×10^{11}
S_3 (g cm^{-3})	3.1×10^{-8}	3.1×10^{-5}
S_4 (K)	1.4×10^4	1.4×10^6

Parameter	Stellar	AGN
$\dot{M}$ (g sec^{-1})	10^{16}	10^{26}
$M_\bullet$ ($M_\odot$)	1	10^8
r (cm)	10^{10}	10^{14}

TABLE 4.1: The scales of the set of equations (left) and the parameters (right) that are given in (4.102−4.105) are shown for stellar mass and AGN black holes.

where the parameters on the RHS are scaled. We have taken the opacity to be Kramers opacity which dominates over the Thomson opacity for the radius $r > r_K$, where r_K is given by

$$\frac{r_K}{\text{cm}} = \dot{M}^{\frac{2}{3}} M_\bullet^{\frac{1}{3}} f^{\frac{8}{3}} \begin{cases} 2.5 \times 10^7 & \text{stellar} \\ 5.4 \times 10^{16} & \text{AGN.} \end{cases} \tag{4.107}$$

and the parameters in the RHS are scaled.

The accretion disk we considered here is a steady disk but in general, the accretion disk is a time-dependent disk where the surface density evolves with time.

4.7.2 Time-dependent thin disk

The time-dependent disk equation is given in eqn (4.76) and for constant viscosity, the equation reduces to (Pringle 1981)

$$\frac{\partial \Sigma}{\partial t} = \frac{3\nu}{r}\frac{\partial}{\partial r}\left\{ r^{1/2}\frac{\partial}{\partial r}(r^{1/2}\Sigma)\right\}, \tag{4.108}$$

and multiplying $r^{1/2}$, eqn (4.108) simplifies to

$$\frac{\partial}{\partial t}(r^{1/2}\Sigma) = \frac{3\nu}{r}\left(r^{1/2}\frac{\partial}{\partial r}\right)^2 (r^{1/2}\Sigma). \tag{4.109}$$

Taking $s = 2r^{1/2}$ and a separable solution such that $r^{1/2}\Sigma = T(t)S(s)$. we obtain

$$\frac{\dot{T}}{T} = \frac{12\nu}{s^2}\frac{1}{S(s)}\frac{\mathrm{d}^2 S(s)}{\mathrm{d}s^2} = \text{constant} = -\lambda^2, \tag{4.110}$$

where λ is a constant and the solution are

$$T(t) \propto e^{-\lambda^2 t} \tag{4.111}$$

and

$$\frac{\mathrm{d}^2 S(s)}{\mathrm{d}s^2} + \frac{\lambda^2}{12\nu} s^2 S(s) = 0. \tag{4.112}$$

Assuming $k^2 = \lambda^2/(12\nu)$, the eqn (4.112) reduces to

$$\frac{\mathrm{d}^2 S(s)}{\mathrm{d}s^2} + k^2 s^2 S(s) = 0, \tag{4.113}$$

Let at the initial time $t = 0$, the mass is constrained into a ring such that the surface density is given by

$$\Sigma(r,\ t = 0) = \frac{m}{2\pi r_0}\delta(r - r_0), \tag{4.114}$$

where $\delta(r - r_0)$ is the Dirac-Delta function. Then the Σ evolution is given by (Pringle 1981)

$$\Sigma(x,\ \tau) = \frac{m}{\pi r_0^2}\tau^{-1}x^{-\frac{1}{4}} \exp\left(-\frac{1+x^2}{\tau}\right) I_{1/4}(2x/\tau), \tag{4.115}$$

where $I_{1/4}$ is the modified Bessel function, $x = r/r_0$ and $\tau = 12\nu t/r_0^2$. The viscosity has the effect of spreading the original ring in radius on a typical viscous timescale given by

$$t_{vis} \sim \frac{r^2}{\nu}. \tag{4.116}$$

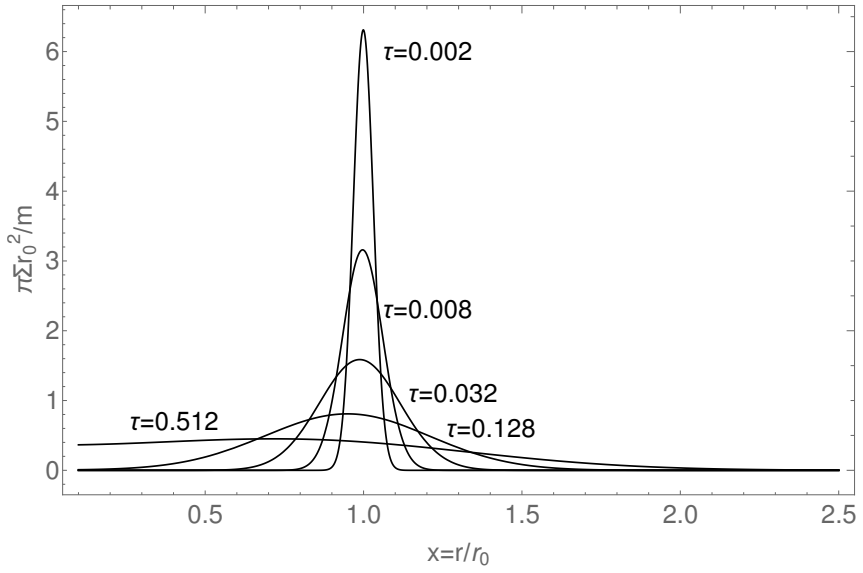

FIGURE 4.3: A ring of mass m kept at $r = r_0$ spreads out due to viscous stress where the outer radius moves outward due to transfer of angular momentum from inward and the viscosity ν is constant.
Courtesy: Pringle (1981)

Using eqn (4.77), the radial velocity is given by

$$v_r = -3\nu \frac{\partial}{\partial r}(\ln(\Sigma r^{\frac{1}{2}})), \tag{4.117}$$

and using eqn (4.115), v_r is given by

$$v_r = -\frac{3\nu}{r_0}\frac{\partial}{\partial x}\left[\frac{1}{4}x - \frac{1+x^2}{\tau} + \ln I_{1/4}(2x/\tau)\right]. \tag{4.118}$$

The asymptotic behavior of $I_{1/4}(z)$ is given by

$$I_{1/4}(z) \propto \begin{cases} z^{-1/2}e^z & z \gg 1 \\ z^{1/4} & z \ll 1, \end{cases} \tag{4.119}$$

such that the radial velocity is given by

$$v_r \sim \frac{3\nu}{r_0} \begin{cases} \left[\frac{1}{4x} + \frac{2x}{\tau} - \frac{2}{\tau}\right] & 2x \gg \tau \\ \\ -\left[\frac{1}{2x} - \frac{2x}{\tau}\right] & 2x \ll \tau. \end{cases} \tag{4.120}$$

Thus, the matter at the outer radius moves outward taking out the angular momentum of the inner parts such that the matter at the inner radius moves inward as one can see from Fig 4.3. Now, τ increases with time t such that the matter that is moving outward starts losing angular momentum to the matter at still larger radii and thus drift inwards. After a very long time ($\tau \gg 1$), all of the angular momenta has been carried to very large radii by a very small fraction of the mass.

4.8 Self-similar evolution of the disk

The time-dependent model we have considered previously is by assuming a constant viscosity. Now in this section, we construct the time-dependent model for a viscous stress that is a function of surface density Σ and radius r. The vertical averaging of eqn (4.22) in the limit $v_r \ll v_\phi$ and for an axially symmetric disk is given by

$$r\frac{\partial \Sigma}{\partial t} = -\frac{\partial}{\partial_r}(r\Sigma\ v_r) \tag{4.121}$$

$$\omega^2 = \frac{1}{r}\frac{\partial \Phi(r,\ z)}{\partial_r}|_{z=0} \tag{4.122}$$

$$\Sigma v_r \frac{\partial}{\partial r}(r^2\omega) = -\frac{1}{r}\ \frac{\partial}{\partial r}(r^2\Pi_{r\phi}). \tag{4.123}$$

We now proceed to calculate a detailed model of self-similar evolution of a disk from the diffusion equation obtained from eqn (4.123) and given by

$$\partial_t \Sigma = \frac{1}{r}\partial_r \left(\frac{1}{\partial_r (r^2 \omega)} \partial_r [r^2 \Pi_{r\phi}] \right), \tag{4.124}$$

where the viscous stress can be parameterized as $\Pi_{r\phi} = K_2 \Sigma^b r^c$ and in addition, the rotation law is assumed to be of the form $\omega = K_1 r^a$. This very useful formulation of a self-similar form is due to Pringle (1981) but only particular analytic solutions to the diffusion equation has been reported for the specific cases of ($a = -3/2, b = c = 3$; Lin and Pringle (1987)) in the context of accretion of a protostellar disk onto a point mass via gravitational instabilities and ($a = -3/2, b = 5/3, c = -1/2$; Cannizzo *et al.* (1990); see §4.6.1) in the context of disk accretion of a tidally disrupted star onto a massive black hole. Note that in CLG, the scaling law for the viscous stress is obtained by the closure of the conditions of local dissipation in an α disk in a Kepler potential and vertical equilibrium. Here, an analytic solution to the general problem of the type ($\Pi_{r\phi} \propto \Sigma^b r^c, \omega \propto r^a$) is presented so that possible viscosity mechanisms discussed earlier and expressible in this way, can be explored within the same formulation. The general solution presented below has a larger utility in contexts other than one considered here (Mangalam 2001).

If $b = 1$, the equation is linear and the general solution is easily found. Proceeding generally, under the assumptions of self-similarity for ($b \neq 1$), one may write the surface density in the following form

$$\Sigma = \Sigma_0 (t/t_0)^\beta g(\xi) \qquad r_f = r_s (t/t_0)^\alpha, \tag{4.125}$$

where $\xi \equiv r/r_f$, and r_s is the associated radius scale. We set the constants

$$t_0 = \frac{K_1}{K_2} r_s^{a+2-c}\Sigma_0,\ M_d = 2\pi l \Sigma_0 r_s^2,\ l = \int_0^1 \xi^2 g(\xi)\mathrm{d}\xi \tag{4.126}$$

where M_d is the initial disk mass. Here we seek a particular solution when there is no external torque, which implies the total angular momentum, J, of the disk is a constant. Using the scaling relations above that are implicit in eqn (4.124) and

$$J = 2\pi K_1 r_s^{4+a}\Sigma_0 j, \qquad j = \int_0^1 \xi^3 g(\xi)\mathrm{d}\xi \tag{4.127}$$

it follows that $\alpha = (4b + ab - 2 - c)^{-1}$ and $\beta = -(a+4)\alpha$. At this point we note that the disk edge travels outward if $2 + c < b(4 + a)$. Substituting into the form for the surface density, as given in (4.125), and simplifying (4.124), we obtain the following ordinary differential equation,

$$-\alpha\xi g' + \beta g = -\frac{1}{(a+2)\xi}\mathrm{d}_\xi\left(\xi^{-(a+1)}\mathrm{d}_\xi(\xi^{2+c}g^b)\right). \tag{4.128}$$

After some algebraic transformations, one can integrate it once to obtain

$$\alpha(a+2)g\xi^{a+4} + (a-c)\xi^{2+c}g^b = b\xi^{3+c}g^{b-1}g' + c_1. \tag{4.129}$$

Now, we apply the boundary condition that the density vanishes at the disk edge, ie.,

$$\Sigma(r = r_f) = 0; \quad g(1) = 0. \tag{4.130}$$

Moreover, if $b > 1$, which is the case for the examples considered here, then $c_1 = 0$. By rearranging terms and integrating, we obtain the following solution

$$g(\xi) = \xi^{(a-c)/b} \left(1 - \xi^{2+\frac{(a-c)}{b}}\right)^{1/(b-1)}. \tag{4.131}$$

Now we consider the particular case of magnetic accretion ($a = -1, b = 4/3, c = -1/3$, Mangalam 2001) which has the solution

$$\alpha = 3/7, \qquad \beta = -9/7, \; g_m(\xi) = \xi^{-1/2} \left[1 - \xi^{3/2}\right]^3. \tag{4.132}$$

Similarly, the accretion due to gravitational instabilities ($a = -1, b = 3, c = 2$) has the solution

$$\alpha = 1/5, \qquad \beta = -3/5, \; g_g(\xi) = \xi^{-1} \left[1 - \xi\right]^{1/2}. \tag{4.133}$$

Fig 4.4 shows the $g(\xi)$ of the self-similar disk for magnetic accretion and gravitational instabilities.

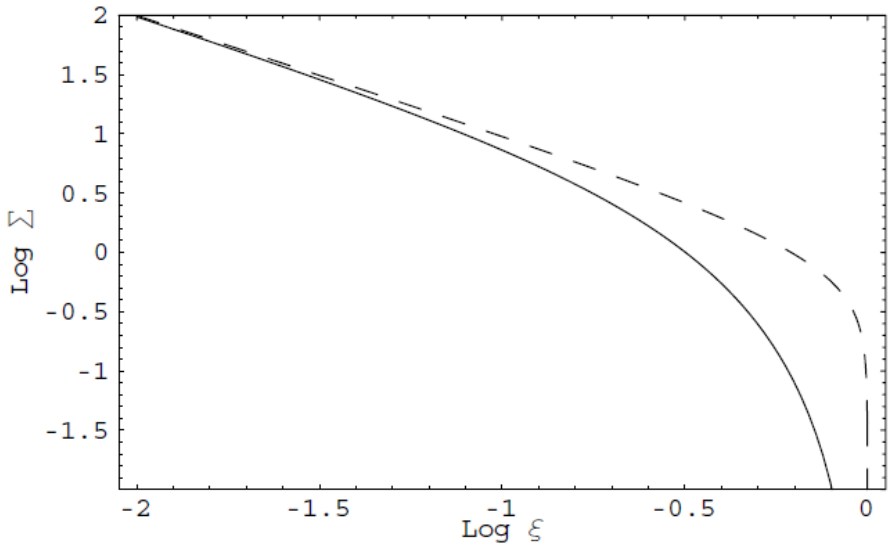

FIGURE 4.4: The structure $g(\xi)$ of the self-similar disk, $\Sigma = \Sigma_0 \left(\frac{t}{t_0}\right)^{\beta} g(\xi)$ where $\xi = r/r_f, r_f = r_s \left(\frac{t}{t_0}\right)^{\alpha}$. The magnetic solution, $g_m(\xi) = \xi^{-1/2}\left[1-\xi^{3/2}\right]^3$ is shown by a solidline, and the solution of the disk with gravitational viscosity, $g_g(\xi) = \xi^{-1}\left[1-\xi\right]^{1/2}$, is shown by a dashed line.
Courtesy: Mangalam (2001)

4.9 Slim disk model

The thin disk approximation breaks down for high accretion rate as $H/r \sim 1$ (eqn 4.106) and the pressure is dominated by the radiation. Such discs puff up to become slim or thick discs and advect the accretion energy with the flow (Paczyńsky and Wiita 1980; Jaroszynski *et al.* 1980; Abramowicz *et al.* 1988).

By integrating eqn (4.4) over a surface $\boldsymbol{f}$ contain in a volume V, we obtain

$$\int \frac{\mathrm{d}\boldsymbol{v}}{\mathrm{d}t} \cdot \mathrm{d}\boldsymbol{f} = \int -\frac{1}{\rho}\boldsymbol{\nabla} P \cdot \mathrm{d}\boldsymbol{f} + \int \boldsymbol{g} \cdot \boldsymbol{f}. \tag{4.134}$$

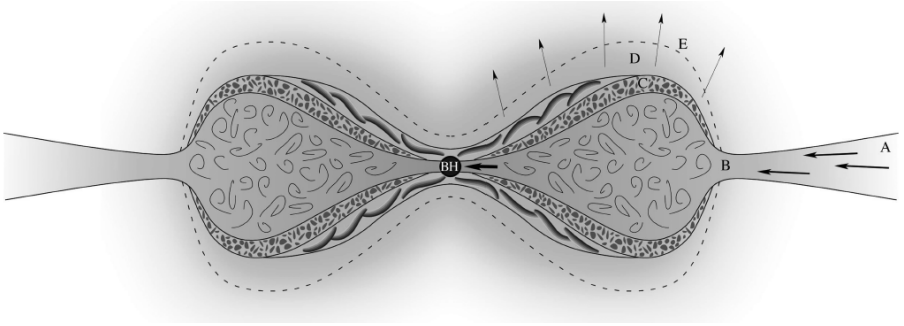

FIGURE 4.5: Different region of slim disk model are: (A) Sub Eddington thin disc. (B) Radiation pressure dominated region. (C) Porus layer forms at less dense region above convection layer. (D) Thin porus layer, wind is accelerated. Courtesy: Dotan and Shaviv (2011)

Using the Gauss divergence theorem, $\boldsymbol{g} = -\boldsymbol{\nabla} \cdot \Phi(r)$, and eqns (4.25, 4.28), the eqn (4.134) is given by

$$\int \boldsymbol{\nabla} \cdot \frac{\mathrm{d}\boldsymbol{v}}{\mathrm{d}t} \, \mathrm{d}V = \frac{\kappa}{c}(L - L_E), \tag{4.135}$$

which shows that when the luminosity exceeds the Eddington luminosity, there is an outward velocity from the volume resulting in an outflow of mass and thus the wind. The structure of a slim disk is shown in Fig 4.5.

A simple steady slim disk model is given by Strubbe and Quataert (2009) where they assumed the disk equations to follow eqns (4.78,4.82, 4.51) and obtained the effective temperature profile given by

$$\sigma_{SB} T_e^4 = \frac{3GM_\bullet \dot{M} f}{8\pi r^3} \left[\frac{1}{2} + \left\{ \frac{1}{4} + \frac{3}{2} f \left(\frac{\dot{M}}{\eta \dot{M}_E} \right)^2 \left(\frac{r}{R_s} \right)^{-2} \right\}^{\frac{1}{2}} \right]^{-1}. \tag{4.136}$$

where $f = 1 - \sqrt{r_{in}/r}$ and R_s is the Schwarzchild radius. The scale height is given by

$$\frac{H}{r} = \frac{3}{4} f \left(\frac{\dot{M}}{\eta \dot{M}_E}\right) \left(\frac{r}{R_s}\right)^{-1} \left[\frac{1}{2} + \left\{\frac{1}{4} + \frac{3}{2} f \left(\frac{\dot{M}}{\eta \dot{M}_E}\right)^2 \left(\frac{r}{R_s}\right)^{-2}\right\}^{\frac{1}{2}}\right]^{-1} . \quad (4.137)$$

Since the pressure is dominated by radiation, the radiation force can exceed the gravity which will result in the luminosity exceeding the Eddington luminosity and this strong radiation pressure results in an out-flowing wind. So the, gas is likely to form an advective accretion disk accompanied by powerful outflows. Strubbe and Quataert (2009) constructed a wind model following a spherically adiabatic outflow. The main assumption is that from the launching radius $R_L \simeq 2R_p$, the wind expands adiabatically and radially with a constant velocity $v_w \sim f_v v_{esc} \sim f_v \sqrt{2GM_\bullet/R_L}$ (Lodato and Rossi 2011). The radiation temperature at the base of the wind $T_L = T(R_L)$ can be derived by energy conservation in the wind. If all the internal energy at the base of the wind is converted into kinetic energy, then $aT_L^4 \sim 0.5\rho(R_L)v_w^2$. We approximate the outflow geometry as spherical with density profile $\rho(R) \sim (\dot{M}_{out}/4\pi R^2 v_w)$ where $\dot{M}_{out} = f_{out}\dot{M}_{fb}$, and the $\dot{M}_{fb}$ is mass accretion rate. The radius of the photosphere (radius at which $R\kappa\rho(R) \sim 1$) is given by

$$R_{ph} \approx 10^{11} \frac{f_{out}}{f_v} M_6^{\frac{2}{3}} \left(\frac{R_\star}{R_\odot}\right)^{\frac{1}{2}} \left(\frac{M_\star}{M_\odot}\right)^{-\frac{1}{6}} \left(\frac{\eta}{0.1}\right)^{-1} \left(\frac{\dot{M}}{\dot{M}_E}\right) \text{ meter} \quad (4.138)$$

Assuming that the wind expands adiabatically, the temperature changes as $T \propto \rho^{1/3}$. Thus, the temperature at the photosphere is given by

$$T_{ph} \approx 1.41\times10^{5} f_{out}^{-\frac{5}{12}} f_{v}^{\frac{11}{12}} M_{6}^{-\frac{1}{18}} \left(\frac{\eta}{0.1}\right)^{\frac{1}{2}} \left(\frac{R_{\star}}{R_{\odot}}\right)^{-\frac{7}{24}} \left(\frac{M_{\star}}{M_{\odot}}\right)^{\frac{7}{72}} \left(\frac{\dot{M}}{\dot{M}_{E}}\right)^{-\frac{5}{12}} \text{K} \quad (4.139)$$

Strubbe and Quataert (2009) have considered the fraction of mass outflows constant. Dotan and Shaviv (2011) have constructed a super-Eddington slim disk model by solving the steady disk equation with α viscosity where the vertical structure of super-Eddington disk is divided into two regions, a hydrostatic region which includes the porous atmosphere, and the region of a continuum driven wind and obtained the fraction of mass outflowing wind f_{out} in terms of accretion rate $\dot{M}$ which we have approximated to the following relation

$$f_{out} = \frac{2}{\pi} \arctan\left[\frac{1}{4.5}\left(\frac{\dot{M}}{\dot{M}_{Edd}} - 1\right)\right] \quad (4.140)$$

In chapter 6, we will derive solutions for a more complicated physics of accretion, wind, and fallback for the case of TDEs.

4.10 Disk structure

The steady poloidal momentum equation is given by

$$(\boldsymbol{v}_p \cdot \boldsymbol{\nabla})\boldsymbol{v}_p = -\frac{1}{\rho}\boldsymbol{\nabla}P - \boldsymbol{\nabla}\Phi + \omega^2 r + \boldsymbol{\nabla}\cdot\sigma^{'}, \quad (4.141)$$

and by neglecting the viscous term $\boldsymbol{\nabla}\cdot\sigma^{'}$, the possible steady accretion flows are

given in Table 4.2. When the pressure in the disk is small compared to the gravity, the rotation of the disk supports gravity which results in a Keplerian thin disk. In case if the disk is non-rotating, there is no force to support the gravity and the disk will collapse resulting in an inward flow. If gravity and pressure dominate with negligible contribution from the rotation, then the source is stars, stellar envelopes, and atmosphere. If the advection dominates along with the gravity and rotation, then the disk is radiatively inefficient and the disk gets puffed to due radiation pressure to form a slim disk. If the radiation pressure is high, the $H > r$ and the disk is a thick disk. In case of Bondi-Hoyle accretion, the matter falls into the black hole radially and thus rotation is negligible. In case of a thick disk, if advection is significant, then the disk is sub-Keplerian and the flow is the accretion dominated advection flow.

Hence, the nature of accretion disk depends on the significance of terms such as advection, pressure, gravity, and rotation. In an accretion disk, different quantities dominate at the different radii: advection dominates at the inner radius, radiation pressure dominates in the inner region and gas pressure dominates in the outer region. The transition from one disk structure to other disk structure is generally obtained by matching the mass accretion rate and the angular momentum exchange rate at the transition radius. However, the nature of transition is poorly understood and is a topic of our research.

4.11 TDE disks

The TDE disks are complicated in structure due to the existence of the accretion by the black hole, fallback from outer debris and the wind outflows in case of super-Eddington accretion. Montesinos Armijo and de Freitas Pacheco (2011) have numerically solved the axisymmetric disk equation with the time-dependent

Physical quantity	Terms	Disk
Gravity + Rotation	$-\boldsymbol{\nabla}\Phi + \omega^2 r = 0$	Thin Keplerian disk
Gravity + Pressure	$-\boldsymbol{\nabla}\Phi - \frac{1}{\rho}\boldsymbol{\nabla}P$	Stars, stellar envelopes and atmosphere
Advection + Gravity	$(\boldsymbol{v}_p \cdot \boldsymbol{\nabla})\boldsymbol{v}_p = -\boldsymbol{\nabla}\Phi$	Gravitational collapse
Advection + Gravity + Rotation	$(\boldsymbol{v}_p \cdot \boldsymbol{\nabla})\boldsymbol{v}_p = -\boldsymbol{\nabla}\Phi + \omega^2 r$	Slim disk
Pressure + Gravity + Rotation	$-\frac{1}{\rho}\boldsymbol{\nabla}P - \boldsymbol{\nabla}\Phi + \omega^2 r = 0$	Thick disks
Advection + Pressure + Gravity	$(\boldsymbol{v}_p \cdot \boldsymbol{\nabla})\boldsymbol{v}_p = -\frac{1}{\rho}\boldsymbol{\nabla}P - \boldsymbol{\nabla}\Phi$	Bondi-Hoyle accretion
Advection + Pressure + Gravity + Rotation	$(\boldsymbol{v}_p \cdot \boldsymbol{\nabla})\boldsymbol{v}_p = -\frac{1}{\rho}\boldsymbol{\nabla}P - \boldsymbol{\nabla}\Phi + \omega^2 r$	Sub-Keplerian ADAF

TABLE 4.2: Shows various possible steady accretion flow with their dominant terms using eqn (4.141).

mass input at the outer radius r_p due to fallback debris, without an outflowing wind and the viscosity prescription given by $\nu = 2\pi r u_\phi / R_y$, where R_y is the Reynolds number characterizing the flow and u_ϕ is the azimuthal velocity. They have considered the disk edges to be constant and showed that the mass accretion rate follows the fallback rate at the late stages. Armijo and de Freitas Pacheco (2013) applied this model to the PS1-10jh observations and deduced a black hole mass $M_\bullet = 6.3 \times 10^6\ M_\odot$. Shen and Matzner (2014) have constructed the model of TDE disk with and without fallback from disrupted debris by developing a self-similar structure of a non-radiative, advective disk with an outflowing wind for general viscosity prescription $\Pi_{r\phi} \propto \Sigma_d^b r^d$ where Σ_d is surface density, r is the radius and b and d are constants that depend on the nature of pressure in the disk. The time-dependent accretion model for sub-Eddington disk was proposed by Cannizzo *et al.* (1990) as a self-similar accretion model with a constant total angular momentum of the disk and α viscosity which is generalized by Mangalam (2001) for other viscosities. The previous TDE models and their underlying assumptions

are summarized in Table 4.3.

In this thesis, we describe a time-dependent disk that includes accretion, fallback, and wind. In chapter 6, we will construct a self-similar model of a time-dependent TDE accretion disk in both sub and super-Eddington phases by taking in account the accretion, fallback, and wind. We will also study the transition dynamics between the phases. This chapter covered the following aspects of accretion physics.

- The basic disk equations.
- Various physical processes that produce viscosity.
- Thin disk and its spectrum.
- A time-dependent model under simplifying assumptions of self-similar disk profiles.
- TDE models.

With this background, we will discuss our new models for TDE accretion in chapter 6.

#	Reference	Application	Disk structure	$\dot{M}_{fb}$	$\dot{M}$	$\dot{M}_w$	Edge radii	Assumptions
1	Mangalam (2001) & (2003)	BH formation at $z = 5$	Time dependent disk Sub-Eddington Super-Eddington	 None None	 None None	 None None	Evolving	Total disk angular momentum is constant $\Pi_{r\phi} \propto \Sigma_d^b r^d$: α disk, gravitational Instability, magnetic stress, radiative stress Super-Eddington: self gravitating disk
2	Strubbe & Quataert (2009) Lodato & Rossi (2011)	TDE	Steady structure disk Sub-Eddington Super-Eddington	 None None	 $\propto t^{-5/3}$ $\propto t^{-5/3}$	 None $\propto t^{-5/3}$	Static	α disk: Standard Shakura-Sunyaev viscosity Sub-Eddington disk: radiative thin disk Super-Eddington disk: slim disk with adiabatic and spherical wind outflow
3	Armijo & Pacheco (2011)	TDE	Time dependent disk Sub-Eddington	 $\propto t^{-5/3}$	 $\propto t^{-5/3}$	 None	Static	β viscous model, $\nu = 2\pi r u_\phi / R_y$ Mass fallback at outer radius Numerical simulation.
4	Shen & Matzner (2014)	TDE	Time dependent disk Sub-Eddington Super-Eddington	 $\propto t^{-5/3}$ $\propto t^{-5/3}$	 $\propto t^{-19/16}$ $\propto t^{-\eta}$	 None $\propto t^{-\eta_1}$	Evolving	$\Pi_{r\phi} \propto \Sigma_d^b r^d$ Sub-Eddington with constant angular momentum Super-Eddington: non radiative advective disk η and η_1 are function of ratio of wind to disk angular momentum.
5	Mageshwaran & Mangalam (2015)	TDE	Steady structure disk Sub-Eddington Super-Eddington	 None None	 $\propto t^{-5/3}$ $\propto t^{-5/3}$	 None $\propto f_{out}(t) t^{-5/3}$	Static	α disk: Standard Shakura-Sunyaev viscosity Star's angular momentum is included Fraction of mass outflow f_{out} is obtained from Dotan & Shaviv (2011)

TABLE 4.3: Various accretion models in the literature with and without steady structure are compared that includes the accretion rate $\dot{M}$, fallback $\dot{M}_{fb}$ and mass outflow rate due to wind $\dot{M}_w$. The accretion model of TDE by Mageshwaran & Mangalam (2015) includes the dynamical parameters E and J whereas the other models of TDE have assumed the initial orbit of disrupted star to be parabolic $E = 0$ and have not included the angular momentum J.

Chapter 5

Image: ASAS-AN 15lh around spinning black hole

Stellar and gas dynamics of TDEs and the event rates

5.1 Introduction

The dynamics of tidal dsiruption events considered previously is for a star on a parabolic orbit. The pericenter of the orbit is a function of both energy E and angular momentum J and thus, it is nessecary to take both in account. In this chapter, we have included J in both stellar dynamical model and accretion dynamical model to calculate the theoretical capture rate and simulate the light curve which is then used to calculate the detectable TDE rates by various surveys.

The energy of the debris E_d depends on the pericenter of the star orbit $r_p(E,\ J,\ M_\bullet,\ m)$. Hence, the mass accretion rate $\dot{M}(E,\ J,\ M_\bullet,\ m)$, the flux, and δt_f depends on E

and J. We build an accretion model based on the initial stellar system parameters and simulate light curve profiles as a function of E and J in the optical and X-ray bands. For a DF that depends on the E only, the stars are diffused into the loss cone through star-star interactions, which leads to the change in orbital angular momentum of the star (Lightman and Shapiro 1977); thus the DF of stars within the loss cone depends on both E and J and we calculate $\dot{N}_t(E,\ J,\ m,\ \gamma)$ and the detectable rates of TDE $\dot{N}_D$ for the various optical and X-ray surveys.

The observed sample of candidate TDE is expanding rapidly, mainly at the optical frequencies due to the advent of the highly sensitive wide-field surveys such as Panoramic Survey Telescope and Rapid Response System (Pan-STARRS), observing in both the medium deep survey (MDS) mode and 3π survey mode (Kaiser *et al.* 2002). The study of TDE will be further revolutionized in the next decade by the Large Synoptic Survey Telescope (LSST) with high sensitivity in optical frequencies (LSST Science Collaboration *et al.* 2009) and the extended Roentgen Survey with an Imaging Telescope Array (eROSITA) in the X-ray band, which performs an all-sky survey (ASS) twice a year (Merloni *et al.* 2012) and can detect hundreds or thousands of TDE per year (Gezari *et al.* 2008; van Velzen and Farrar 2014; Khabibullin *et al.* 2014). We calculate the detectable rate $\dot{N}_D$ for Pan-STARRS 3π, Pan-STARRS MDS, and LSST in the optical g band and eROSITA in soft X-ray band; whose instrument details are given in Table 5.2.

The Figure 5.1 shows the methodology we have adopted to calculate the detectable TDE with the initial parameters $M_\bullet$, $M_\star$, $R_\star$, E, J and redshift z. In Section 2, we solve the steady state FP equation for a power law density profile $\rho(r) \propto r^{-\gamma}$ and stellar mass function $\xi(m)$. We obtain $\dot{N}_t(E,\ J,\ m,\ \gamma)$ for the typical parametric range of density profiles ($\gamma = 0.6\ -\ 1.4$), energy, and angular momentum ($J \leq J_{lc}$), which we use it later to calculate the detection rate, $\dot{N}_D$. In Section 3, we calculate the energy E_d of the disrupted debris and the maximum radius $R_l(E,\ J)$ from the star center to the point where the debris is bound to the BH. We then simulate

$\dot{M}(E,\ J,\ t)$. In Section 4, we compare the accretion t_a, ring formation t_r, viscous t_v and radiation t_R timescales and discuss the conditions for the formation of an accretion disk. In Section 5, by equating the $\dot{M}$ and Eddington mass accretion rate $\dot{M}_E$, we obtain the critical BH mass $M_c(E,\ J)$, such that for $M_\bullet < M_c$, the accretion disk formed has a super Eddington phase. We then simulate the light curve profiles in the optical and X-ray as a function of E, J, and $M_\bullet$, depending on whether the accretion disk is super Eddington or sub Eddington. The flux from the source at a redshift z is compared with the sensitivity of the mission instrument to obtain the δt_f. In Section 6, we calculate $\dot{N}_D$ for optical and X-ray missions by assuming the standard cosmological parameters and BH mass function to obtain the galaxy density. The Table 5.1 shows a glossary of symbols we use in this chapter.

5.2 Theoretical capture rate

Using eqn (1.3) and taking the quantity $\eta_t = 1$, for a main sequence star with the mass-radius relation $R_\star = R_\odot m^n$, where $m = M_\star/M_\odot$, the tidal radius given by

$$r_t(M_\bullet,\ m) \approx 2.25 \times 10^{-6} \left(\frac{M_\bullet}{10^6 M_\odot}\right)^{\frac{1}{3}} m^{n-\frac{1}{3}} \text{ pc} \tag{5.1}$$

and for $n > 1/3$, $r_t(M_\bullet,\ m)$ increases with m. We take $n = 0.8$ for the entire range of stellar masses in our calculations (Kippenhahn and Weigert 1994). We take the lifetime of the main sequence star $t_{MS} \propto M_\star^{-2.5}$ and the dynamical time of the star to fall into the BH $t_{\rm dyn} = \sqrt{a^3/GM_\bullet}$, where a is the semimajor axis of the star to the BH. For a star to be captured during its main sequence lifetime, $t_{\rm dyn} < t_{MS}$, which gives

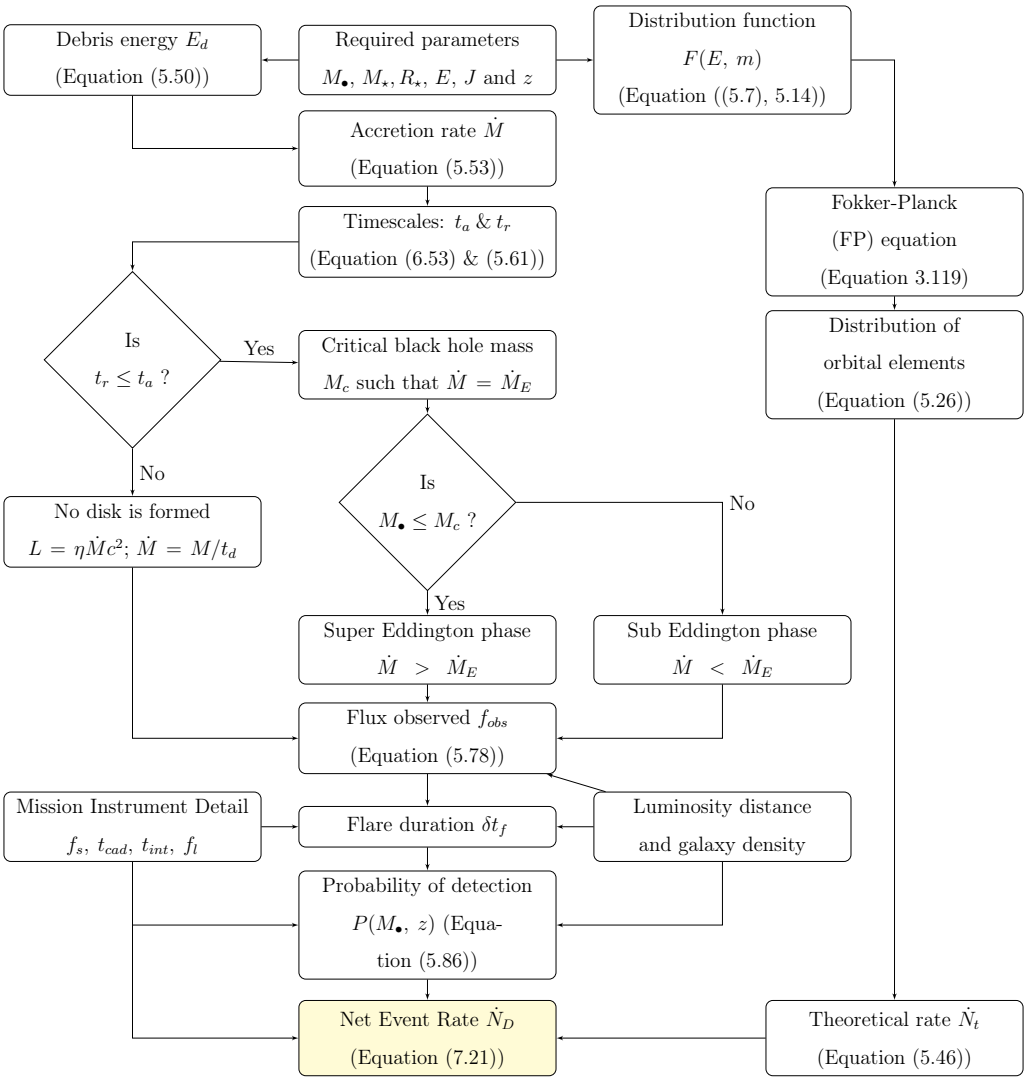

FIGURE 5.1: The flow chart of the procedure we have adopted in the calculation of event rates. The stellar dynamics and gas dynamics are connected by the parameters of specific energy E and specific angular momentum J of the star's initial orbit. The flux $f_{\rm obs}$ is compared with the sensitivity f_l of the detector to obtain flare duration. For the given instrument details, such as cadence $t_{\rm cad}$, integration time $t_{\rm int}$ and fraction of sky observed f_s, we calculate the net detectable TDE rate for the detector. The t_d is the dynamical time of the in-fall of the debris to the black hole.

Common Parameters			
$M_\bullet$	Black hole mass	J	Orbital angular momentum
M_6	$M_\bullet/(10^6 M_\odot)$	J_{lc}	Loss cone angular momentum
$M_\star$	Stellar mass	J_c	Angular momentum of circular orbit
E	Orbital energy	ℓ	J/J_{lc}
$\xi(m)$	Stellar mass function	m	$M_\star/M_\odot$
Stellar Dynamical Parameters			
j	J^2/J_c^2	$\mathcal{E}$	E/σ^2
r_t	Tidal radius	ρ	Galactic density
r_h	Black hole influence radius	γ	Galaxy density power law
s	r/r_h	s_t	r_t/r_h
R_s	Schwarzschild radius	$\Phi_\star$	Stellar potential
r_b	Break radius of Nuker profile	$\Phi_\bullet$	Black hole potential
σ	stellar velocity dispersion	Φ	Total potential= $\Phi_\bullet + \Phi_\star$
q	Diffusion parameter	$t_{\rm MS}$	Main sequence lifetime
$\mathcal{E}_c$	Critical energy for $q = 1$	T_r	Radial period of orbit
$\dot{N}_t$	Theoretical TDE rate	$f_\star$	Probability of main sequence star capture
Accretion Dynamical Parameters			
r_p	Pericenter of the orbit	t_d	dynamical time
$\bar{e}$	$E/(GM_\bullet/r_t)$= $(r_t/r_h)\mathcal{E}$	Γ	Adiabatic index
E_d	Energy of disrupted debris	k	Spin factor
R_l	Maximum radius from star center to bound debris	t_m	Orbital period of inner-most debris
x_l	$R_l/R_\star$	t_a	Accretion timescale
x	$\Delta R/R_\star$	ΔR	Debris radius from star center
ε	E_d/E_{dm}	$E_{\rm dm}$	Energy of inner-most bound debris
μ	$M/M_\star$	M	Debris mass with energy E_d
$\dot{M}$	Mass accretion rate	τ	t/t_m
$\dot{M}_E$	Eddington mass accretion rate	t_r	Ring formation timescale
f_r	Fraction of star mass bound to black hole	t_v	Viscous timescale
M_c	Critical black hole mass	t_R	Radiation timescale
κ	Opacity of the medium	$\mathcal{T}_r$	t_r/t_a
r_c	Circularization radius	$\mathcal{T}_v$	t_v/t_R
r_L	Outflowing wind launch radius	$T_{\rm ph}$	Temperature of photosphere
$r_{\rm ph}$	Radius of photosphere of outflowing wind	T_e	Effective temperature of disk
L_e	Luminosity emitted from the source	L	Luminosity
$\psi(M_\bullet)$	Black hole mass function	L_E	Eddington luminosity
$P(M_\bullet,\ z)$	Probability of detection	z	Redshift
Υ	Detection efficiency of a detector	$\dot{N}_D$	Detectable rate
Instrumental Parameters			
f_l	sensitivity of the detector	$t_{\rm cad}$	Cadence of instrument
$t_{\rm int}$	Integration time of detector	f_s	Fraction of sky survey

TABLE 5.1: Glossary of symbols

$$m_l = \left(t_\odot \sqrt{\frac{GM_\bullet}{a^3}} \right)^{0.4}, \tag{5.2}$$

where $t_\odot$ is the life time of the sun and is shown in Figure 5.2 for $a = r_h$.

Stars in the galactic center move in the potential field of both SMBH and other stars in the galaxy. The DF is assumed to be a function of energy $E = \Phi(r) - v^2/2$

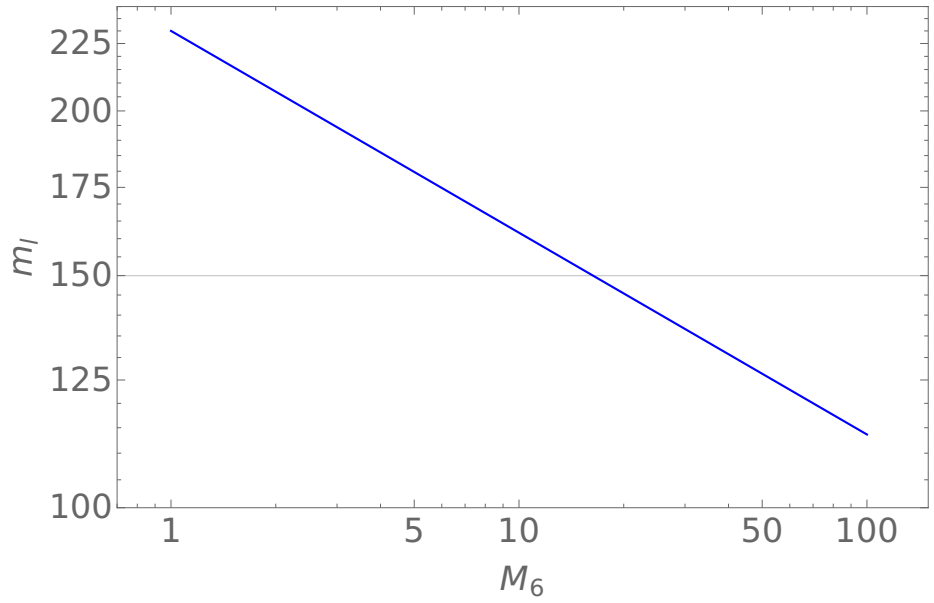

FIGURE 5.2: The mass limit of star m_l as a function of black hole mass $M_\bullet = 10^6 M_\odot M_6$ for $a = r_h$. It is the maximum mass of star in the cluster that can be captured during its main sequence lifetime. The thin gray line shows the maximum mass in the Kroupa (2001) sample of stars.

only and is given by $f(E) \propto E^p$ for $r \leq r_h$ and $\Phi(r) = GM_\bullet/r$, where $r_h = GM_\bullet/\sigma^2$ is the radius of influence and σ is the stellar velocity dispersion and is related to the $M_\bullet$ through the $M_\bullet - \sigma$ relation given by Ferrarese and Ford (2005)

$$M_\bullet = 1.66 \times 10^8 M_\odot \left(\frac{\sigma}{200 \text{ Km sec}^{-1}}\right)^{4.86} \tag{5.3}$$

Bahcall and Wolf (1976) introduced the stellar scattering and diffusion and found that $p = 3/4$ (Peebles 1972) gives a negatively divergent flux; they also obtained $p = 1/4$ for the steady state distribution, which gives a constant energy flux. The stars are tidally captured if the angular momentum is $J \leq J_{lc}(E, r_t)$ where $J_{lc}(E, r_t) = \sqrt{2r_t^2(\Phi(r_t) - E)}$ is the loss cone angular momentum (Frank and Rees 1976). The maximum value of J is $J_{lc}(E, r_t)$. As $J_{lc}(E, r_t) \geq 0$, the maximum value of energy is $E_{\boldsymbol{m}} = \Phi(r_t)$.

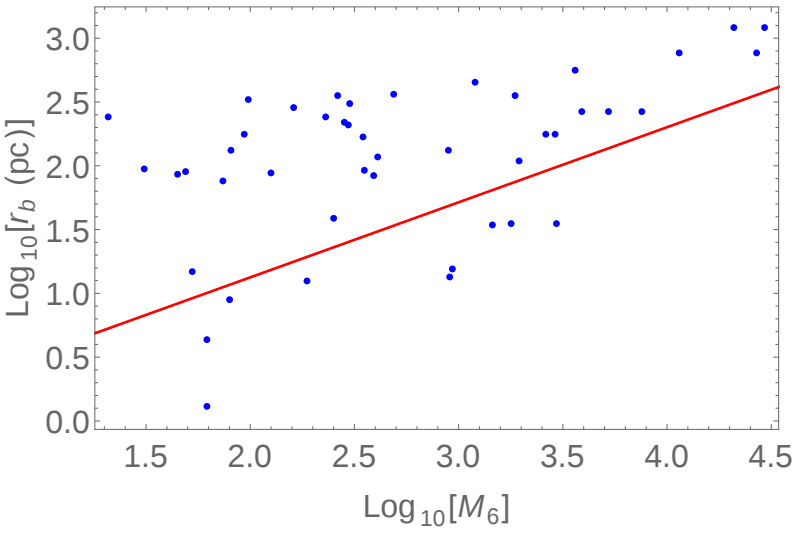

FIGURE 5.3: The blue points show the break radius r_b for the sample of galaxies given in Wang and Merritt (2004). The red line shows the radius of influence r_h. The plot indicates that for most of galaxies $r_b > r_h$, which implies that for $r \leq r_h$, the density $\rho(r)$ can be taken to be a single power law profile.

Because $J_{lc}(E, r_t)$ depends on r_t, which varies with $M_\star$, so we consider a DF that depends on the stellar mass function $\xi(m)$ given by (Kroupa 2001)

$$\xi(m) \approx \begin{cases} Hm^{-1.3} & 0.08 < m < 0.5 \\ Bm^{-2.3} & 0.5 < m < 150 \end{cases} \tag{5.4}$$

where

$$H = 2B \quad , \quad B = \frac{1}{7.91 - 0.77 m_m^{-1.3}} \quad \text{and} \quad m = \frac{M}{M_*},$$

where m_m is the maximum mass of a main sequence star in the stellar distribution, taken to be 150.

Wang and Merritt (2004) and Stone and Metzger (2016) have taken the sample of

galaxies with a Nuker law, which is basically a double power law profile with break radius r_b that separates inner and outer slopes. In Figure 5.3, we have shown the range of r_b and r_h for the sample of galaxies given in Wang and Merritt (2004). For most of the galaxies $r_b > r_h$, which is also true for the sample of galaxies given in Stone and Metzger (2016). Because the stellar dynamics in the galactic center is influenced by the BH for $r \leq r_h$, we consider a single power law density profile $\rho(r) = \rho_0(r/r_0)^{-\gamma}$ for $r \leq r_h$, where γ is the inner slope of the Nuker law. We define the r_h, where $M_\star(r_h) = 2M_\bullet$ (Wang and Merritt 2004), such that

$$\rho_0 r_0^\gamma = \frac{3-\gamma}{2\pi} M_\bullet r_h^{\gamma-3} \tag{5.5}$$

The potential due to the stellar distribution is obtained from the Poisson equation and given by

$$\Phi_\star(r) = 2\sigma^2 \begin{cases} \frac{1}{2-\gamma}\left[1 - \left(\frac{r}{r_h}\right)^{2-\gamma}\right] & \gamma \neq 2 \\ \ln(\frac{r_h}{r}) & \gamma = 2 \end{cases} \tag{5.6}$$

The total potential is given by $\Phi(r) = \Phi_\bullet(r) + \Phi_\star(r)$, where $\Phi_\bullet(r) = GM_\bullet/r$ is the potential due to the BH. We consider the DF as

$$F(E,\, m) = f(E)\xi(m) \tag{5.7}$$

The density of stars for $F(E,\, m)$ is given by

$$\rho(r) = \int \mathrm{d}^3v\; M_\star\, F(E,\, m) = \int \mathrm{d}^3v\; f(E) \int \mathrm{d}m\; \xi(m)\; M_\star, \tag{5.8}$$

where $\mathrm{d}^3v = 2\pi v_t \mathrm{d}v_t \mathrm{d}v_r$ with radial velocity v_r and tangential velocity v_t is given by

$$v_t = \frac{J}{r}; \quad v_r = \sqrt{2(\Phi(r) - E) - \frac{J^2}{r^2}}; \quad \mathrm{d}^3v = \frac{2\pi}{r^2 v_r} J \mathrm{d}E \mathrm{d}J \tag{5.9}$$

For a spherically isotropic galactic center, the function $f(E)$ is obtained through the inverse transform of Equation (5.8), and is known as the Eddington formula, given by (Binney and Tremaine 2008)

$$f(E) = \frac{1}{\sqrt{8}\pi^2 \langle M_\star \rangle} \frac{\mathrm{d}}{\mathrm{d}E} \int_{E_{min}}^{E} \frac{\mathrm{d}\rho}{\mathrm{d}\Phi} \frac{1}{\sqrt{E - \Phi}} \, \mathrm{d}\Phi, \tag{5.10}$$

where

$$\langle M_\star \rangle = \int_{0.08}^{150} M_\star \, \xi(m) \, \mathrm{d}m \tag{5.11}$$

and $E_{\min}$ is the minimum of E taken to be -100. The number of stars in the cluster for a given $F(E,\, m)$ is

$$N = \int \mathrm{d}^3 r \int \mathrm{d}^3 v \int \mathrm{d}m \, F(E,\, m), \tag{5.12}$$

where $\mathrm{d}^3 r = 4\pi r^2 \mathrm{d}r$ for spherical galaxy. In terms of dimensionless variables $\ell = J/J_{lc}$ and $\mathcal{E} = E/\sigma^2$, the number of stars is given by

$$N(\mathcal{E},\,\ell)\,\mathrm{d}\mathcal{E}\,\mathrm{d}\ell = \int \mathrm{d}m\; 8\pi^2\, J_{lc}^2\,\sigma^2\,\ell\, T_r(\mathcal{E},\,\ell)\, F(\mathcal{E},\,m)\,\mathrm{d}\mathcal{E}\,\mathrm{d}\ell \tag{5.13}$$

where $T_r(\mathcal{E},\,\ell) = \oint \dfrac{\mathrm{d}r}{v_r}$ is the radial period. For a spherical geometry, $T_r(\mathcal{E},\,\ell)$ is a function of $\mathcal{E}$ only, and the $N(\mathcal{E},\,\ell)$ increases with ℓ.

From the given stellar density profile and potential $\Phi(r)$, the DF $f(E)$ is given by

$$f(\mathcal{E}) = \frac{M_\bullet}{\langle M_\star\rangle}\frac{1}{r_h^3\sigma^3}g(\mathcal{E}) \tag{5.14}$$

where

$$g(\mathcal{E}) = \frac{1}{4\sqrt{2}\pi^3}\begin{cases} \gamma(3-\gamma)\frac{\mathrm{d}}{\mathrm{d}\mathcal{E}}\int_{s_1}^{s_2}\frac{s^{\gamma-1}}{\sqrt{\mathcal{E}-s-\frac{2}{2-\gamma}(1-s^{\gamma-2})}}\,\mathrm{d}s & \gamma\neq 2 \\ \int_{\mathcal{E}_{\min}}^{\mathcal{E}}\frac{\mathcal{L}(2+\mathcal{L})}{(1+\mathcal{L})^3}\frac{1}{\sqrt{\mathcal{E}-\Psi}}\,\mathrm{d}\Psi & \gamma = 2 \end{cases} \tag{5.15}$$

and $\mathcal{L}$ is the Lambert function given by $\mathcal{L}e^{\mathcal{L}} = (1/2)e^{\Psi/2}$ where $\Psi = \Phi/\sigma^2$, $s = r_h/r$, $\mathcal{E} = E/\sigma^2$ (Wang and Merritt 2004) and s_1 and s_2 are obtained by solving

$$s_1 + \frac{2}{2-\gamma}(1-s_1^{\gamma-2}) = \mathcal{E}_{\min} \tag{5.16a}$$

$$s_2 + \frac{2}{2-\gamma}(1-s_2^{\gamma-2}) = \mathcal{E} \tag{5.16b}$$

The Figure 5.4 shows the plot of $g(\mathcal{E})$ for various γ. For $\gamma = 2$, $g(\mathcal{E})$ corresponds to Equation (17c) of Wang and Merritt (2004). The BH potential dominates over the star potential for $r \ll r_h$ as shown in Figure 5.5 and thus $g(\mathcal{E}) \propto \mathcal{E}^{\gamma-3/2}$ for

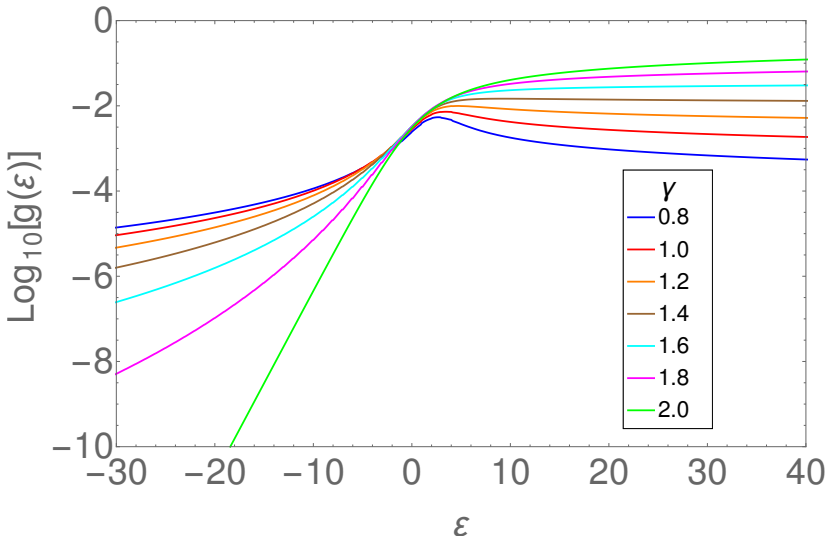

FIGURE 5.4: The dimensionless $g(\mathcal{E})$ is shown for various γ. For $\gamma = 2$, $g(\mathcal{E})$ corresponds to Equation (17c) of Wang and Merritt (2004).

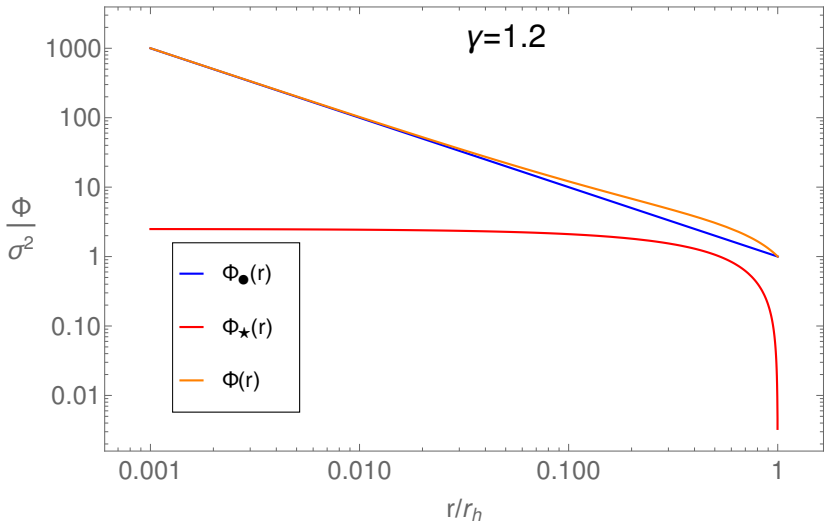

FIGURE 5.5: The stellar potential $\Phi_\star(r)$, black hole potential $\Phi_\bullet(r)$ and total potential $\Phi(r)$ are shown for $\gamma = 1.2$. For $r \ll r_h$, the black hole potential $\Phi_\bullet(r) = GM_\bullet/r$ dominates over the star potential.

$\mathcal{E} \gg 1$.

5.2.1 Loss cone theory

The loss cone is a geometrical region in phase space for which $r_p \leq r_t$. We adopt the Cohn and Kulsrud (1978) formalism for computing the flux of stars into the loss cone in $\mathcal{E}$ and the $j = J^2/J_c^2(\mathcal{E})$ phase space, where $J_c(\mathcal{E})$ is the angular momentum of circular orbit with energy $\mathcal{E}$. We consider the diffusion in the j space only and in the limit $j \to 0$, the steady state FP equation as given in eqn (3.119), is given by (Merritt 2013a)

$$\frac{\mathrm{d}\mathcal{F}(\chi,\, y)}{\mathrm{d}\chi} = \frac{\mathrm{d}}{\mathrm{d}y}\left(y\frac{\mathrm{d}\mathcal{F}(\chi,\, y)}{\mathrm{d}y}\right) \tag{5.17}$$

with the boundary condition

$$\mathcal{F}(0,\, y) = 0 \qquad \forall\ y < y_{lc} \tag{5.18a}$$

$$\mathcal{F}(0,\, y) = \mathcal{F}(1,\, y) \quad \forall\ y \geq y_{lc} \tag{5.18b}$$

where

$$\chi = \frac{1}{\langle D(\mathcal{E})\rangle}\int_{r_p}^{r} \lim_{j\to 0}\frac{\langle(\Delta j)^2\rangle}{2j}\frac{\mathrm{d}r}{v_r} \quad \text{and} \quad y = \frac{j}{\langle D(\mathcal{E})\rangle} \tag{5.19}$$

and $\langle D(\mathcal{E})\rangle = \oint \lim_{j\to 0}\frac{\langle(\Delta j)^2\rangle}{2j}\frac{\mathrm{d}r}{v_r}$ is the orbit averaged angular momentum diffusion coefficient and y_{lc} is y at $j = j_{lc}$. Merritt (2015b) has expressed $\mathcal{F}(\chi,\, y)$ in terms of the distribution of the pericenters r_p and apocenters r_a, and calculated the capture

rate $\dot{N}_t$ in terms of r_a and r_p while we use appropriately scaled values of E and J^2 for calculating r_p and various other parameters required in the gas dynamical calculation in the following sections. Note that in the calculation we use the total potential inclusive of the stars and the BH.

The local diffusion coefficient in the limit $j \to 0$ is given by (Magorrian and Tremaine 1999)

$$\lim_{j\to 0} \frac{\langle (\Delta j)^2 \rangle}{2j} = \frac{r^2}{J_c^2(\mathcal{E})} \left\langle (\Delta v_\perp)^2 \right\rangle \tag{5.20}$$

where $\langle (\Delta v_\perp)^2 \rangle$ is given in Appendix L of Binney and Tremaine (2008). Thus, the orbit averaged diffusion coefficient is given by

$$\langle D(\mathcal{E}) \rangle = \frac{32\sqrt{2}}{3} \frac{\pi^2 G^2 \left\langle M_f^2 \right\rangle \log \Lambda}{J_c^2(\mathcal{E})} \frac{M_\bullet}{\langle M_\star \rangle} \frac{1}{\sigma^2} (2h_1(\mathcal{E}) + 3h_2(\mathcal{E}) - h_3(\mathcal{E})) \tag{5.21}$$

where M_f is the mass of field star with the maximum mass taken to be 150 $M_\odot$, $\Lambda \approx M_\bullet / M_\star$ and

$$\left\langle M_f^2 \right\rangle = M_\odot^2 \int_{0.08}^{150} m_f^2 \xi(m_f)\, \mathrm{d}m_f \tag{5.22a}$$

$$h_1(\mathcal{E}) = \int_0^{s(\mathcal{E})} \mathrm{d}s' \frac{s'^2}{\sqrt{\Psi(s') - \mathcal{E}}} \int_{-\infty}^{\mathcal{E}} \mathrm{d}\mathcal{E}'\, g(\mathcal{E}') \tag{5.22b}$$

$$h_2(\mathcal{E}) = \int_0^{s(\mathcal{E})} \mathrm{d}s' \frac{s'^2}{\Psi(s') - \mathcal{E}} \int_{\mathcal{E}}^{\Psi(s's)} \mathrm{d}\mathcal{E}' \sqrt{\Psi(s') - \mathcal{E}'}\, g(\mathcal{E}') \tag{5.22c}$$

$$h_3(\mathcal{E}) = \int_0^{s(\mathcal{E})} \mathrm{d}s' \frac{s'^2}{(\Psi(s') - \mathcal{E})^2} \int_{\mathcal{E}}^{\Psi(s')} \mathrm{d}\mathcal{E}' (\Psi(s') - \mathcal{E}')^{\frac{3}{2}}\, g(\mathcal{E}') \tag{5.22d}$$

where $s(\mathcal{E})$ is obtained by solving $\Psi(s) = \mathcal{E}$, $s = r/r_h$ and

$$\Psi(s) = \frac{\Phi}{\sigma^2} = \frac{1}{s} + \frac{2}{2-\gamma}(1 - s^{2-\gamma}). \tag{5.23}$$

Now $J_c^2(\mathcal{E})$ is given by

$$J_c^2(\mathcal{E}) = \sigma^2 r_h^2 \left[s_c(\mathcal{E}) + 2s_c^{4-\gamma}(\mathcal{E})\right] \tag{5.24}$$

where $s_c(\mathcal{E})$ is given by

$$\frac{1}{2s_c} + \frac{2}{2-\gamma}(1 - s_c^{2-\gamma}) - s_c^{2-\gamma} = \mathcal{E}. \tag{5.25}$$

The solution of Equation (5.17) with the boundary conditions (5.18) is given by (Merritt 2013a)

$$\mathcal{F}(\chi,\ y) = X(j_{lc}) \left(1 - 2\sum_{n=1}^{\infty} \frac{e^{\frac{-\alpha_n^2 q}{4}\chi}}{\alpha_n} \frac{J_0\left(\alpha_n \sqrt{y/y_{lc}}\right)}{J_1(\alpha_n)}\right) \tag{5.26}$$

where α_n are the consecutive zeros of the Bessel function $J_0(\alpha)$, $q = 1/y_{lc}$, and $X(j_{lc})$ is given by

$$X(j_{lc}) = \frac{f(\mathcal{E})}{1 + q^{-1}\zeta(q)\log\left(\frac{1}{j_{lc}}\right)}; \quad \zeta(q) = 1 - 4\sum_{n=1}^{\infty} \frac{e^{\frac{-\alpha_n^2 q}{4}}}{\alpha_n^2} \tag{5.27}$$

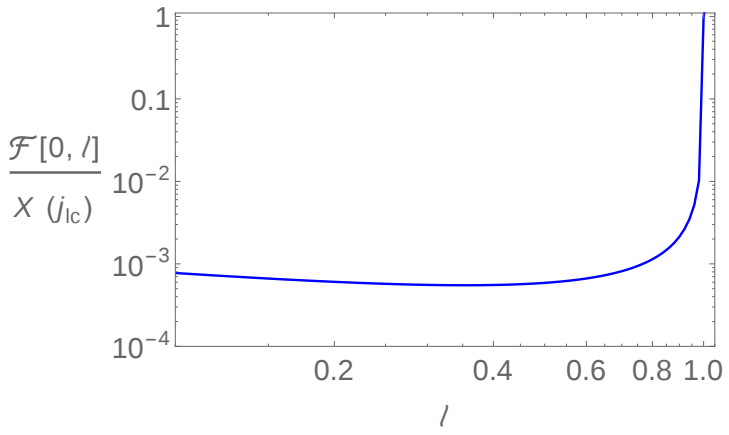

FIGURE 5.6: The $\mathcal{F}(0,\ \ell)$ is obtained by transforming Equation (5.26) from y to $\ell = J/J_{lc}$ space such that $y/y_{lc} = \ell^2$, and calculating for 1000 terms in summation of Equation (5.26). The boundary condition given by Equation (5.18a) shows that $\mathcal{F}(0,\ \ell)$ is a step function with ℓ for $\ell \leq 1$. Thus, taking 1000 terms in summation satisfies the boundary condition within a fraction of about 10^{-3}.

where $f(\mathcal{E})$ is given by Equation (5.14). The Equation (5.26) gives the DF of stars in the loss cone in terms of energy $\mathcal{E}$ and angular momentum $\ell = J/J_{lc} = \sqrt{y/y_{lc}}$. Figure 5.6 shows the plot of $\mathcal{F}(0,\ \ell)$ for 1000 terms in the summation in Equation (5.26), which matches with the boundary condition given by Equation (5.18a) with an accuracy of $\sim 10^{-3}$. With increase in the number of terms in summation, the order of accuracy of $\mathcal{F}(0,\ \ell)$ to Equation (5.18a) increases; however, we use 1000 terms in summation to calculate $\mathcal{F}(\chi,\ \ell)$ beacuse it is in close agreement with the boundary condition.

The approximation to $\zeta(q)$ given by Cohn and Kulsrud (1978) is

$$\zeta(q) \approx \zeta_{CK}(q) = \begin{cases} 1 & q \gg 1 \\ \dfrac{q}{0.186q + 0.824\sqrt{q}} & q \ll 1 \end{cases} \tag{5.28}$$

We have compared the $\zeta(q)$ obtained for a summation of 10,000 terms in Equation (5.27) with $\zeta_{CK}(q)$, and it does not fit very well for q close to unity, as shown in

Figure 5.7. Thus we have used a better approximation to $\zeta(q)$ given by

$$\zeta(q) \approx \begin{cases} 1 & q \geq 4 \\ \dfrac{q}{0.86q^{0.5} + 0.384q - 0.379q^{1.5} + 0.427q^2 - 0.095q^{2.5}} & q < 4 \end{cases} \tag{5.29}$$

which follows Equation (5.28) for $q \ll 1$ and gives a better fit to $\zeta(q)$ for q close to unity. The residual for Equation (5.28) is higher than the residual for Equation (5.29), as shown in Figure 5.7.

The function $q(\mathcal{E})$ given by

$$q(\mathcal{E}) = \frac{\langle D(\mathcal{E}) \rangle}{j_{lc}} = \frac{\langle D(\mathcal{E}) \rangle \, J_c^2(\mathcal{E})}{J_{lc}^2(\mathcal{E}, r_t)} = \frac{\langle D(\mathcal{E}) \rangle \, J_c^2(\mathcal{E})}{2r_t^2(\Phi(r_t) - \mathcal{E}\sigma^2)} \tag{5.30}$$

can be interpreted as the ratio of the orbital period to the timescale for diffusional refilling of the loss cone. The regime $q(\mathcal{E}) > 1$ defines the pinhole or full loss cone in which stellar encounters replenish loss cone orbits much more rapidly than they are depleted, whereas $q(\mathcal{E}) < 1$ defines the diffusive or empty loss cone regime. The Figure 5.8 shows $q(\mathcal{E})$ plotted as a function of $\mathcal{E}$ for $\gamma = 1.0$. The function $q(\mathcal{E})$ decreases with $\mathcal{E}$ which implies that the high energy orbits have smaller diffusion angle. The smaller the diffusion angle, the higher the diffusion time and thus the lower the feeding rate to the loss cone. The critical energy $\mathcal{E}_c$ defined by $q(\mathcal{E}_c) = 1$ decreases with $M_\bullet$, and m is shown in Figure 5.9 for $\gamma = 1$. The $\mathcal{E}_c$ is the energy from which the majority of the loss cone flux originates (Lightman and Shapiro 1977). With an increase in $M_\bullet$, the relaxation time of the galaxy increases; thus the diffusion timescale increases (Frank and Rees 1976) and q decreases, which results in a decrease in $\mathcal{E}_c$. As $r_t(M_\bullet,\, m) \propto m^{n-1/3}$, it increases with m for $n = 0.8$; and

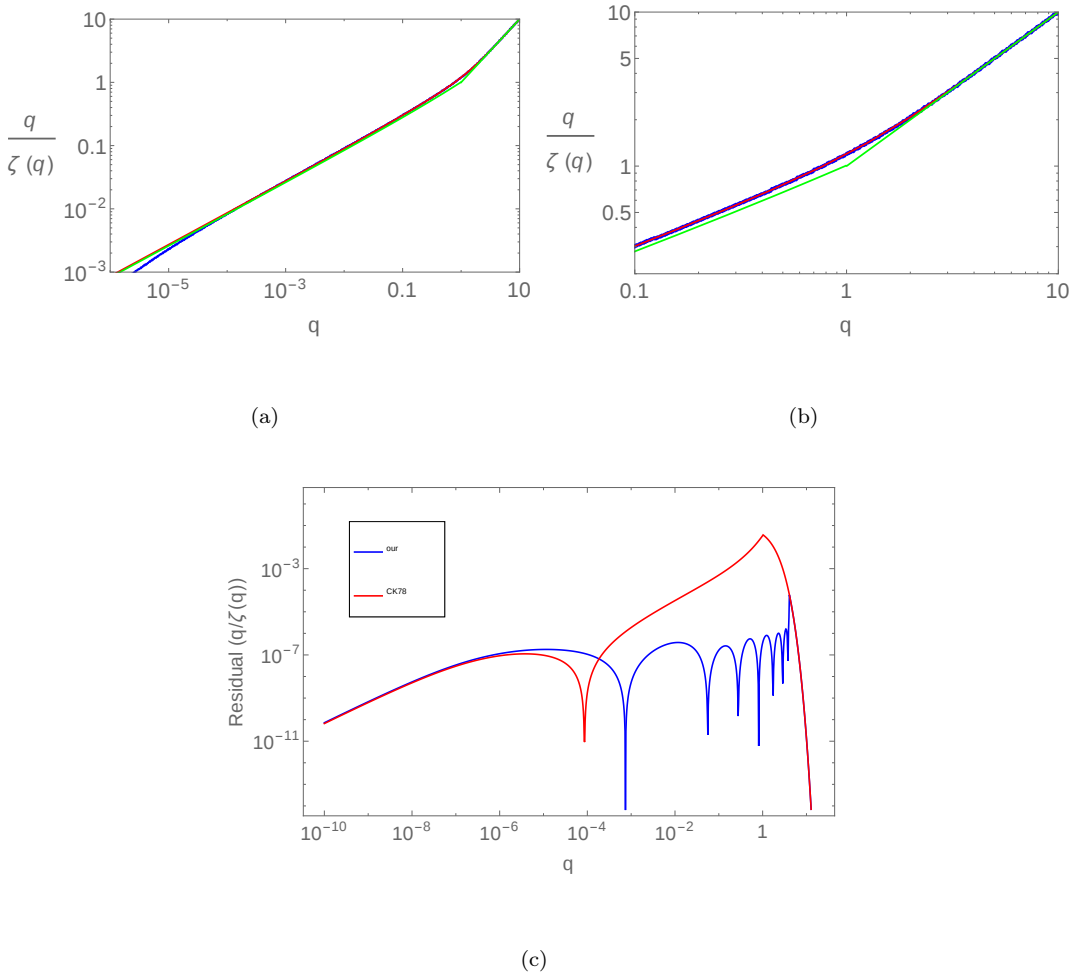

(a) (b)

(c)

FIGURE 5.7: The figure (a) shows $q/\zeta(q)$ as a function of q over all ranges under various approximations. The blue line corresponds to $\zeta(q)$ summed up to 10,000 terms. The red thin line corresponds to our approximation of $\zeta(q)$ given by Equation (5.29). The green line shows the results obtained by Cohn and Kulsrud (1978) and is given by Equation (5.28). Asymptotically, the blue line follows the red thin line. The figure (b) shows $q/\zeta(q)$ that for q close to unity; our approximated formula gives a good fit to $\zeta(q)$. The figure (c) shows the residual of $q/\zeta(q)$ for our approximated equation (blue) and the Cohn and Kulsrud (1978) approximation (red).

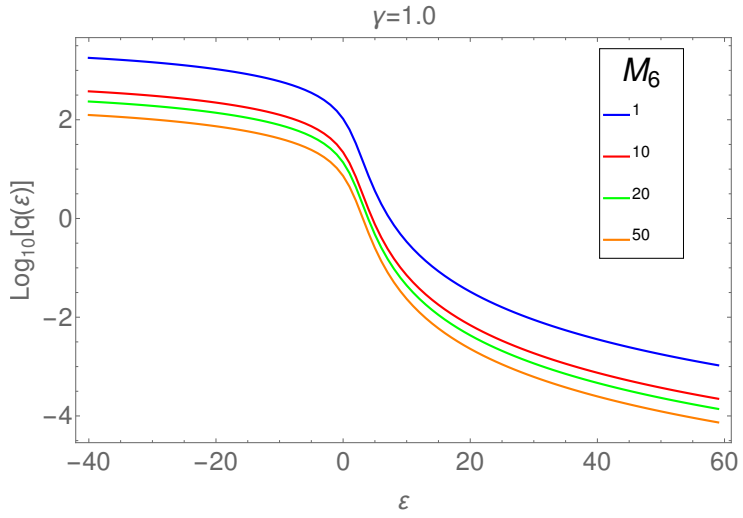

FIGURE 5.8: The function $q(\mathcal{E})$ given by Equation (5.30) is shown as a function of $\mathcal{E}$ for $\gamma = 1.0$ and $m = 1$; $q(\mathcal{E})$ decreases with $\mathcal{E}$ which implies that the high energy orbits have smaller diffusion angle.

J_{lc} increases and so q decreases, which results in a decrease of $\mathcal{E}_c$. As γ increases, the diffusion timescale decreases due to an increase in the number of scatterers, and thus q increases and thus, $\mathcal{E}_c$ increase.

Using Equation (5.26) and the mass function of stars in the galaxy $\xi(m)$ given by Equation (5.4), the loss cone feeding rate is given by (Merritt 2013a)

$$\frac{\mathrm{d}^2\dot{N}_t}{\mathrm{d}E\,\mathrm{d}y} = 4\pi^2 \int \mathrm{d}m\, \xi(m) J_c^2(E)\, \langle D(E)\rangle\, \mathcal{F}(\chi = 1,\, y) \tag{5.31}$$

The corresponding feeding rate in terms of E and j is given in Merritt (2015a).

The Jacobian of the transformation from $\{E,\, y\}$ space to dimensionless variables $\{\mathcal{E},\, \ell^2 = (J/J_{lc}(\mathcal{E}, r_t))^2 = j(J_c(\mathcal{E})/J_{lc}(\mathcal{E}, r_t))^2\}$ is given by

$$\mathrm{d}E\,\mathrm{d}y = \mathrm{Det}\left[\frac{\partial(E,\, y)}{\partial(\mathcal{E},\, \ell^2)}\right] \mathrm{d}\mathcal{E}\,\mathrm{d}\ell^2, \quad \text{where} \quad \frac{\partial(E,\, y)}{\partial(\mathcal{E},\, \ell^2)} = \frac{\partial(E,\, y)}{\partial(E,\, J^2)} \cdot \frac{\partial(E,\, J^2)}{\partial(\mathcal{E},\, \ell^2)} \tag{5.32}$$

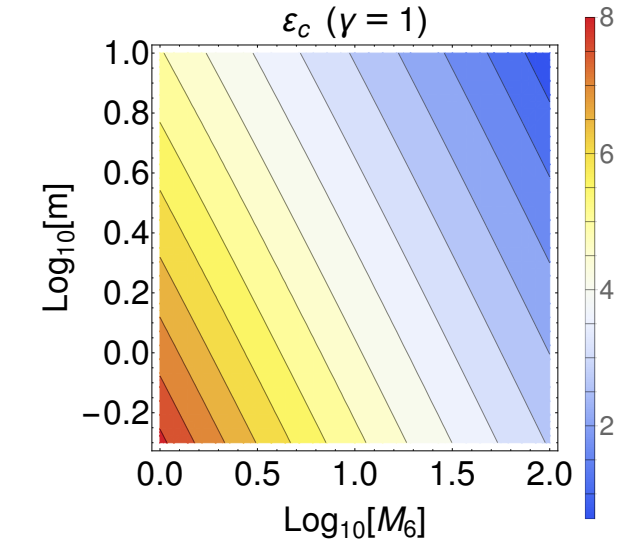

(a)

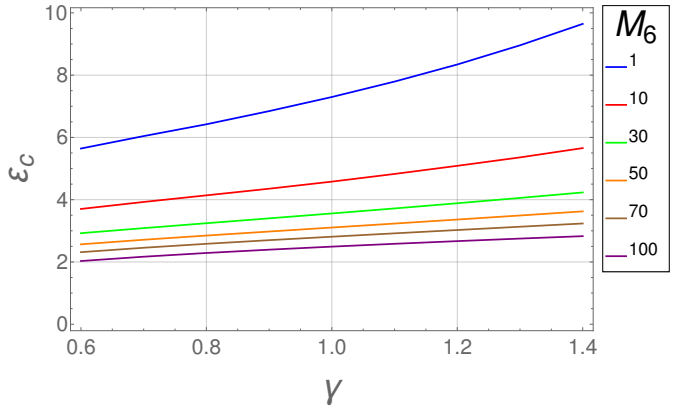

(b)

FIGURE 5.9: The top panel (a) shows $\mathcal{E}_c$ for which $q(\mathcal{E}) = 1$ as function of M_6 and m for $\gamma = 1$. The bottom panel (b) shows the $\mathcal{E}_c$ as a function of γ for a star of unit solar mass and radii that increases with γ.

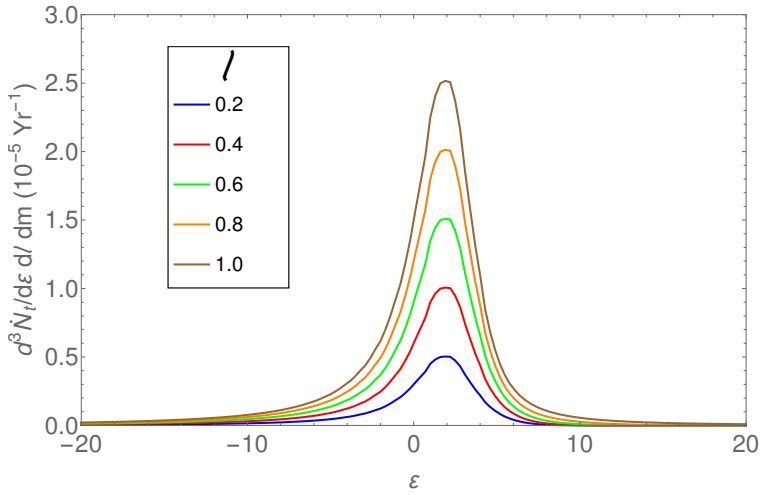

FIGURE 5.10: The theoretical capture rate $\dot{N}_t$ (Equation (5.34)) is shown as a function of $\mathcal{E}$ for various ℓ and for $M_6 = 1$ and $\gamma = 0.8$. The capture rates for high energy orbits are small and increase with ℓ due to an increase in $N(\mathcal{E},\, \ell)$ (see Equation (5.13)).

and the following result is obtained by calculating the product of the determinants of the two Jacobians in the above equation as

$$\mathrm{d}E\ \mathrm{d}y = \sigma^2 \frac{J_{lc}^2(\mathcal{E}, r_t)}{\langle D(\mathcal{E})\rangle\, J_c^2(\mathcal{E})} \mathrm{d}\mathcal{E}\ \mathrm{d}\ell^2. \tag{5.33}$$

Then, the feeding rate is given by

$$\frac{\mathrm{d}^2\dot{N}_t}{\mathrm{d}\mathcal{E}\ \mathrm{d}\ell^2\ \mathrm{d}m} = 4\pi^2\, \sigma^2 \xi(m)\, J_{lc}^2(\mathcal{E})\, \mathcal{F}(\chi = 1,\, \ell) \tag{5.34}$$

Figure 5.10 shows the plot of $\dot{N}_t$ as a function of $\mathcal{E}$ for various ℓ for $M_6 = 1$ and $\gamma = 0.8$. The capture rates decreases with $\mathcal{E}$ because of the decrease in diffusion coefficient $D(\mathcal{E})$ and increases with ℓ due to the increase in $N(\mathcal{E},\, \ell)$ (see Equation (5.13)).

Beacuse $J_{lc}(r_t) = \sqrt{2r_t^2(\Phi(r_t) - E)}$ (see Section 2), this implies that $E < \Phi(r_t)$

and the maximum value of $E = E_m = \Phi(r_t)$. Because $r_t(M_\bullet,\, m)/r_h \sim 10^{-6}-10^{-5}$, and for $r \ll r_h$, the potential is dominated by the BH potential as shown in the Figure 5.5, which implies that $E_m(M_\bullet,\, m) = \Phi(r_t(M_\bullet,\, m)) = GM_\bullet/r_t(M_\bullet,\, m)$. The orbital motion of a star at the turning point of the orbit r_x, is given by

$$E = \Phi(r_x) - \frac{J^2}{2r_x^2} \tag{5.35}$$

where $\Phi(r) = \Phi_\bullet(r) + \Phi_\star(r)$, $\Phi_\bullet(r) = GM_\bullet/r$ and $\Phi_\star(r)$ is given by Equation (5.6). In terms of dimensionless variables, $\ell = J/J_{lc}$ and $\bar{e} = E/E_m$, where $E_m = GM_\bullet/r_t$, such that $\bar{e} = (r_t/r_h)\mathcal{E}$, and the Equation (5.35) using Equation (5.23) is given by

$$\frac{\bar{e}}{s_t} = \frac{s_x - \ell^2 s_t + \frac{2}{2-\gamma}\left[s_x^2(1-s_x^{2-\gamma}) - \ell^2 s_t^2(1-s_t^{2-\gamma})\right]}{s_x^2 - \ell^2 s_t^2} \tag{5.36}$$

where $s_x = r_x/r_h$, $s_t = r_t/r_h$. Since $\bar{e}$ is a monotonically decreasing function of s_x, and both the pericenter and apocenter of the orbit should lie below r_h, the minimum value of $\bar{e}$ is at $s_x = 1$ for $r_x = r_h$; taking $\bar{e}(s_x = 1) = \bar{e}_h$, the Equation (5.36) reduces to

$$\frac{\bar{e}_h}{s_t} = \frac{1 - \ell^2 s_t - \frac{2}{2-\gamma}\ell^2 s_t^2(1-s_t^{2-\gamma})}{1-\ell^2 s_t^2}. \tag{5.37}$$

Now $s_t = r_t/r_h \sim 10^{-5}$–$10^{-6}$, $\bar{e}_h \simeq r_t/r_h$. Beacuse $J_{lc}(r_x) = \sqrt{2r_x^2(\Phi(r_x) - E)}$, this implies that $E < \Phi(r_x)$ and the maximum value of $E = \Phi(r_x) \simeq \Phi(r_t)$, which corresponds to $\bar{e} \simeq 1$ and thus $\bar{e} \lesssim 1$. The total potential is dominated by the BH near r_t, as shown in the Figure 5.5. After ignoring the second term in the numerator in the righthand side of Equation (5.36), which is a factor $s_t = r_t/r_h \simeq$

$10^{-5} - 10^{-6} \ll 1$ lower than the first, the Equation (5.36) reduces to

$$\bar{e} = \frac{x_x - \ell^2}{x_x^2 - \ell^2}, \tag{5.38}$$

where $x_x = s_x/s_t$. If x_p is lower of the two roots of x_x, it is given by

$$x_p = \frac{1}{2\bar{e}} \left(1 - \sqrt{1 - 4\bar{e}(1-\bar{e})\ell^2}\right). \tag{5.39}$$

For a star to be tidally disrupted, $x_p < 1$ which results in

$$(1 - \bar{e})(1 - \ell^2) > 0 \tag{5.40}$$

and $x_p > 0$ results in

$$\ell^2 \bar{e}(1 - \bar{e}) > 0. \tag{5.41}$$

The Equation (5.41) restricts the range of $\bar{e}$ to $\bar{e} < 1$ and thus Equation (5.40) implies that $\ell < 1$. Thus, the applicable ranges are $\bar{e}_h < \bar{e} < 1$ and $0 < \ell < 1$. We derived the turning points s_x by solving Equation (5.36) subject to the constraint $r_p < r_t$ and $r_t < r_a < r_h$, and verified the range for $\bar{e}$ and ℓ derived above.

While we have ignored relativistic effects in the analysis above, we plan to include them in the future.

The lifetime of a main sequence star is $t_{MS} = t_{\odot} m^{-2.5}$ where $t_{\odot} = 10^{10}$ yr is the lifetime of a solar type star and the radial period is given by

$$T_r = \int_{r_p}^{r_a} \frac{1}{v_r} \mathrm{d}r. \tag{5.42}$$

In terms of $s = r/r_h$ and using Equation (5.23), T_r is given by

$$T_r(\bar{e},\ M_\bullet,\ m) = \frac{r_h}{\sqrt{2}\sigma} \int_{s_p}^{s_a} \frac{s\sqrt{s_t}}{\sqrt{s_t\left(s - \ell^2 s_t + \frac{2}{2-\gamma}\left[s^2(1-s^{2-\gamma}) - \ell^2 s_t^2(1-s_t^{2-\gamma})\right]\right) - \bar{e}(s^2 - \ell^2 s_t^2)}} \mathrm{d}s, \tag{5.43}$$

where s_a and s_p are the dimensionless apocenter and pericenter that are obtained by solving Equation (5.36). We find numerically that the radial period T_r is approximated by

$$T_r(\bar{e},\ M_\bullet,\ m) \simeq \frac{\pi}{2\sqrt{2}} \frac{r_h}{\sigma} \begin{cases} 0.57 e^{[0.27(1.47 - \frac{\bar{e}}{s_t})]} & \bar{e} < 1.47 s_t \\ \left(\frac{\bar{e}}{s_t}\right)^{-\frac{3}{2}} & \bar{e} \geq 1.47 s_t \end{cases} \tag{5.44}$$

Because the BH potential dominates at high energy, the corresponding orbits are Keplerian and the radial period $\propto \bar{e}^{(-3/2)}$. Using the $M_\bullet - \sigma$ relation given by Equation (5.3) and $r_h = GM_\bullet/\sigma^2$, the radial period in Keplerian regime is $T_r \propto M_\bullet^{0.38} \mathcal{E}^{-3/2}$, where $\mathcal{E} = \bar{e}/s_t$. The stars on the loss cone orbits are captured in the radial period timescale and the number of stars in the loss cone orbit is $N_{lc}(\mathcal{E})\mathrm{d}\mathcal{E}$ (Merritt 2013a). Thus the capture rate is approximately given by $\dot{N}_t = \int (N_{lc}(\mathcal{E})/T_r(\mathcal{E}))\, \mathrm{d}\mathcal{E} \propto M_\bullet^{-0.38}$ in the regime $\bar{e} > 1.47 s_t$, which is consistent with the average best-fit slope of -0.3 over the entire range of $\bar{e}$ that was found numerically.

A tidally captured star is on main sequence if its main sequence lifetime is $t_{MS} > T_r$, where T_r is the radial period of the orbit. Considering all possible radial phases of the star in an orbit, the probability that a star of mass m is tidally captured as a main sequence is given by

$$f_\star(\bar{e},\ M_\bullet,\ m) = \mathrm{Min}\left[1,\ \frac{t_{MS}(m)}{T_r(\bar{e},\ M_\bullet,\ m)}\right]. \tag{5.45}$$

Using Equations (5.26), (5.34), and $\mathrm{d}\mathcal{E}\,\mathrm{d}\ell^2 = s_t^{-1}\,\mathrm{d}\bar{e}\,\mathrm{d}\ell^2$, the capture rate is given by

$$\frac{\mathrm{d}^2\dot{N}_t}{\mathrm{d}\bar{e}\,\mathrm{d}\ell^2\,\mathrm{d}m} = 4\pi^2\ s_t^{-1}\sigma^2\ \xi(m) f_\star(\bar{e},\ M_\bullet,\ m)\ J_{lc}^2(\bar{e})\ \mathcal{F}(\chi=1,\ \ell). \tag{5.46}$$

Figure 5 of Freitag and Benz (2002) gives the maximum mass of BH as function of mass m of the star that is disrupted. We observe that stars with mass $m > 0.8$ are tidally disrupted in the entire range of BH mass $10^6 M_\odot < M_\bullet < 10^8 M_\odot$ and for $m < 0.8$, a substantial fraction is tidally captured without disruption. Thus we take the effective star mass range to be $0.8 < m < 150$. The net capture rate is given by

$$\dot{N}_t(\gamma,\ M_\bullet) = 4\pi^2\ \int_{0.8}^{150}\mathrm{d}m \int_{\bar{e}_h}^{1}\mathrm{d}\bar{e}\int_0^1 \mathrm{d}\ell^2\ \sigma^2 s_t^{-1}(M_\bullet,\ m)\xi(m) f_\star(\bar{e},\ M_\bullet,\ m)\cdot$$
$$J_{lc}^2(\bar{e})\ \mathcal{F}(\chi=1,\ \ell). \tag{5.47}$$

We solved Equation (5.26) to obtain $\mathcal{F}(1,\ \ell)$ and used it in Equation (5.46) to calculate the capture rate. The integration of Equation (5.46) over the energy

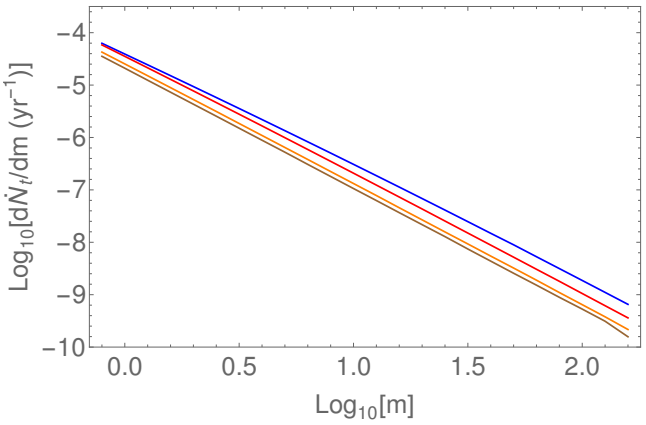

(a)

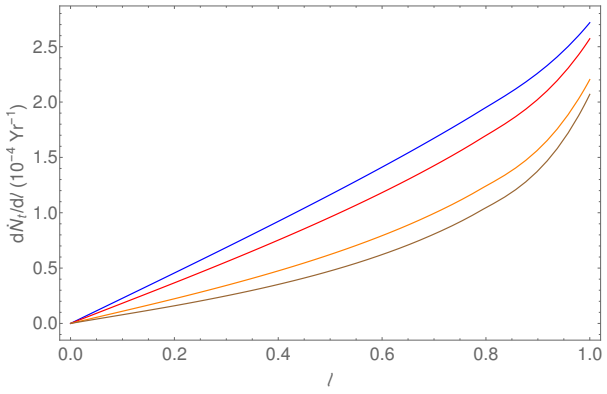

(b)

FIGURE 5.11: For $\gamma = 1.0$ and $M_6 = 1$ (blue), 10 (red), 50 (orange), and 100 (brown). Figure (a) shows $\mathrm{d}\dot{N}_t/\mathrm{d}m$ obtained using Equation (5.26) and integrating Equation (5.46) over $\bar{e}$ and ℓ decreases with m as $\xi(m)$ decreases with m. Figure (b) shows $\mathrm{d}\dot{N}_t/\mathrm{d}\ell$ obtained using Equation (5.26) and integrating Equation (5.46) over $\bar{e}$ and ℓ.

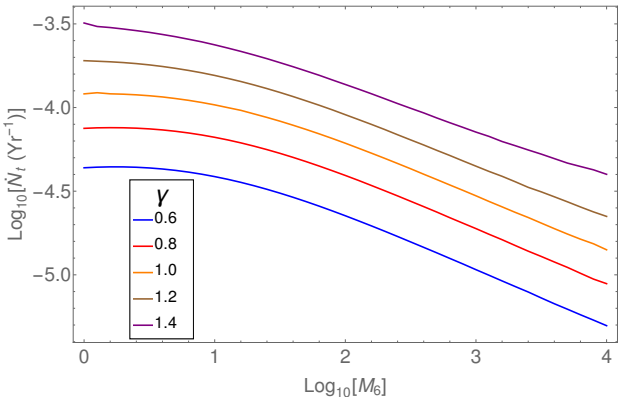

(a)

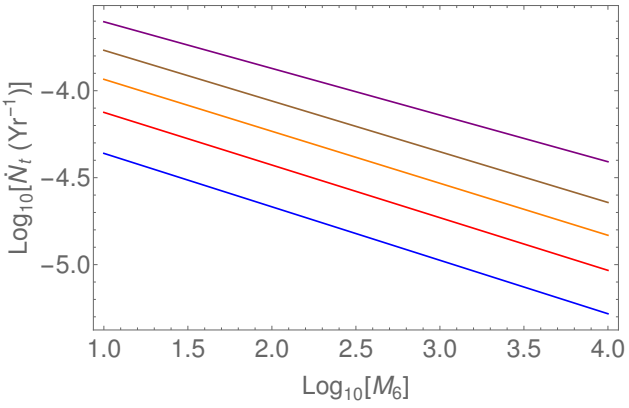

(b)

FIGURE 5.12: Panel (a) shows the net $\dot{N}_t$ obtained using Equations (5.26) and (5.47) as a function of M_6 for various γ. Panel (b) shows $\dot{N}_t$ as a function of M_6 for $M_6 > 10$ and γ=0.6 (blue), 0.8 (red), 1.0 (orange), 1.2 (brown), and 1.4 (purple), and it follows that $\dot{N}_t \propto M_6^{-\beta}$ where $\beta = 0.3 \pm 0.01$.

range $\bar{e}_h < \bar{e} < 1$ and angular momentum range $0 < \ell < 1$ results in a capture rate per unit mass $\mathrm{d}\dot{N}_t/\mathrm{d}m$, which is a decreasing function of m as $\xi(m)$ decreases with m and is shown in Figure 5.11a for various $M_\bullet = 10^6 M_\odot M_6$ and $\gamma = 1.0$. Similarly, integrating Equation (5.46) over energy $\bar{e}_h < \bar{e} < 1$ and test star mass $0.8 < m < 150$ results in $\mathrm{d}\dot{N}_t/\mathrm{d}\ell$, which is an increasing function ℓ as shown in Figure 5.11b.

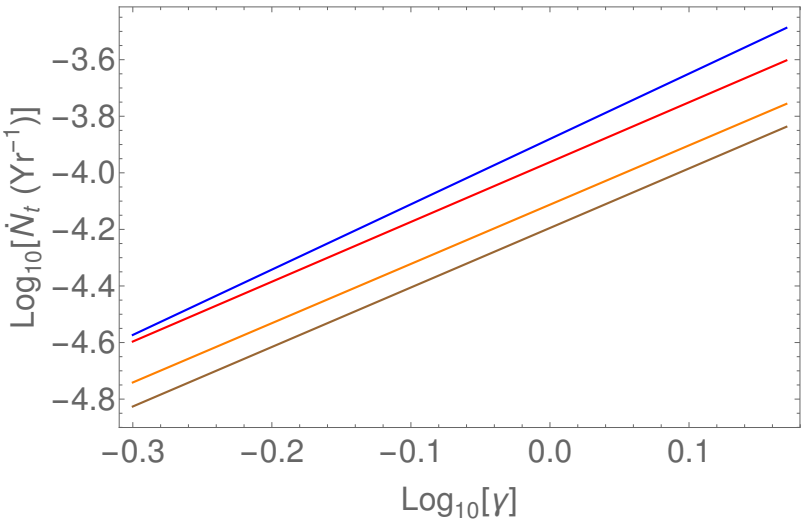

FIGURE 5.13: The figure shows the $\dot{N}_t$ obtained using Equations (5.26) and (5.47) as a function of γ for various M_6=1 (blue), 10 (red), 50 (orange), and 100 (brown), and it follows $\dot{N}_t \propto \gamma^p$ with the best-fit value of $p \sim 2.1$. The $\dot{N}_t$ increases with γ due to an increase in the density of the central stellar population.

The net $\dot{N}_t$ obtained using Equations (5.26) and (5.47) increases with γ and decreases with M_6 as shown in Figure 5.12. For $M_6 \geq 10$, the $\dot{N}_t \propto M_6^{\beta}$ where $\beta = 0.3 \pm 0.01$, as shown in the Figure 5.12b for various γ. The increase with γ is nonlinear as shown in Figure 5.13 and for $\dot{N}_t \propto \gamma^p$, the best-fit value of $p \sim 2.1$. The galaxies with larger γ posses higher rates because their denser central stellar populations naturally feature shorter relaxation times and faster rates of energy and angular momentum diffusion.

5.3 Physics of tidal disruption

The classical description of a TDE was outlined by Rees (1988). In this picture, a star on parabolic orbit is tidally captured and disrupted at the pericenter and the distribution of mass of disrupted debris with respect to specific binding energy $\mathrm{d}M/\mathrm{d}E_d$ is roughly flat, where E_d is the energy of the disrupted debris. For stars on a parabolic orbit, Lodato *et al.* (2009) found that $\mathrm{d}M/\mathrm{d}E_d$ depends on the

properties of the star and adiabatic index Γ. Using Equation (5.39), the pericenter is given by

$$r_p(\bar{e},\ \ell,\ M_\bullet,\ m) = \frac{r_t}{2\bar{e}}\left(1-\sqrt{1-4\bar{e}(1-\bar{e})\ell^2}\right) = r_t\left(\frac{2\ell^2(1-\bar{e})}{1+\sqrt{1-4\ell^2\bar{e}(1-\bar{e})}}\right). \tag{5.48}$$

Equivalently

$$r_p(E,\ J,\ M_\bullet) = \frac{GM_\bullet}{2E}\left[1-\sqrt{1-\frac{2EJ^2}{G^2M_\bullet^2}}\right] = \frac{J^2}{GM_\bullet}\left[1+\sqrt{1-\frac{2EJ^2}{G^2M_\bullet^2}}\right]^{-1}. \tag{5.49}$$

The stars on the loss cone orbits are captured within the dynamical time $t_d = (r_p^3/GM_\bullet)^{0.5}$ with tidal acceleration $a_t = GM_\bullet\Delta R/r_p^3$ where ΔR is the debris distance from the star center at the moment of breakup. Then, the energy of the disrupted debris is given by

$$E_d(\bar{e},\ \ell,\ M_\bullet,\ m,\ \Delta R) \approx \bar{e}E_{\boldsymbol{m}}(M_\bullet,\ m) - \frac{2kGM_\bullet\Delta R}{r_p^2(\bar{e},\ \ell,\ M_\bullet,\ m)} \tag{5.50}$$

where $\Delta R \in \{-R_\star,\ R_\star\}$, the negative sign corresponds to the region toward the BH and k is the spin-up factor due to tidal torque by the SMBH on a star given by (Alexander and Kumar 2001)

$$k = \begin{cases} 1 & \text{non spin up (no change in angular velocity)} \\ 3 & \text{spin up to break up angular velocity} \end{cases}$$

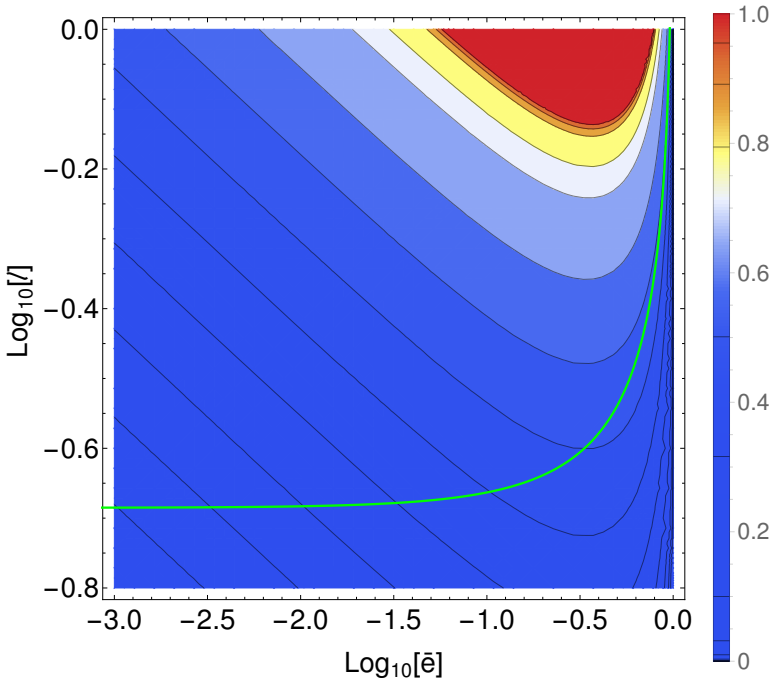

FIGURE 5.14: A contour plot of the maximum distance from the star center $x_l(\bar{e},\, \ell, M_\bullet,\, m) = R_l/R_\star$ (Equation (5.51)) to the point where the debris is bound to the black hole for $M_6 = 1$ and $m = 1$. The green line corresponds to $r_p = R_s$ and for $r_p > R_s$, the contours lie above the green line.

The maximum distance from the center of a star to the point where the debris is bound to the BH at the moment of disruption is obtained by setting $E_d = 0$ in Equation (5.50) and is given by

$$R_l(\bar{e},\, \ell,\, M_\bullet,\, m) = \frac{r_p^2(\bar{e},\, \ell,\, M_\bullet,\, m)\bar{e}}{2kr_t(M_\bullet,\, m)}. \tag{5.51}$$

Figure 5.14 shows the contour plot of $x_l \equiv x_l(\bar{e},\, \ell, M_\bullet,\, m) = R_l(\bar{e},\, \ell, M_\bullet,\, m)/R_\star$ for $M_6 = 1$ and $m = 1$. The value of $r_p(\bar{e},\, \ell,\, M_\bullet,\, m)$ is less than Schwarzschild radius $R_s(M_\bullet)$ for $\ell \leq 0.2$; whereas $x_l(\bar{e},\, \ell, M_\bullet,\, m)$ increases with $\bar{e}$ and the increase with ℓ is significant for high energy orbits. With the increase in the value of $x_l(\bar{e},\, \ell, M_\bullet,\, m)$, the mass of the debris bound to the BH increases and for $x_l(\bar{e},\, \ell, M_\bullet,\, m) = 1$, the entire debris is bound to the BH.

The time taken for the most tightly bound debris to return its pericenter after disruption is given by

$$t_m(\bar{e},\ \ell,\ M_\bullet,\ m) = \frac{2\pi G M_\bullet}{[2E_d(\bar{e},\ \ell,\ M_\bullet,\ m,\ -R_\star)]^{3/2}}. \tag{5.52}$$

As the bound material falls back to its pericenter, it loses its energy and angular momentum, thus accreting into the SMBH and giving rise to the flare (Phinney 1989). The in-fall mass accretion rate at time t after disruption for the debris following Keplerian orbits is given by

$$\frac{\mathrm{d}M}{\mathrm{d}t} = \frac{\mathrm{d}M}{\mathrm{d}E_d}\frac{\mathrm{d}E_d}{\mathrm{d}a}\frac{\mathrm{d}a}{\mathrm{d}t} = \frac{1}{3}(2\pi G M_\bullet)^{\frac{2}{3}}\frac{\mathrm{d}M}{\mathrm{d}E_d}t^{-\frac{5}{3}} \tag{5.53}$$

where a is the semimajor axis of the debris with orbital energy $E_d(\bar{e},\ \ell,\ M_\bullet,\ m,\ \Delta R)$. The term $\mathrm{d}M/\mathrm{d}E_d$ is the energy distribution within the bound matter and depends on the internal structure of the star (Phinney 1989; Lodato *et al.* 2009). We now write it in terms of dimensionless quantities using Equations (5.50) and (5.51), and modify the dimensionless quantities given in Lodato *et al.* (2009) by including the dependence on $r_p(\bar{e},\ \ell,\ M_\bullet,\ m)$ through $R_l(\bar{e},\ \ell,\ M_\bullet,\ m)$ and express

$$\varepsilon = \frac{x_l - x}{x_l + 1}, \qquad x = x_l - \tau^{-2/3}(1 + x_l) \tag{5.54}$$

$$\frac{\mathrm{d}\mu}{\mathrm{d}\varepsilon} = (1 + x_l)\frac{\mathrm{d}\mu}{\mathrm{d}x}, \qquad \frac{\mathrm{d}\mu}{\mathrm{d}\tau} = \frac{2}{3}\frac{\mathrm{d}\mu}{\mathrm{d}\varepsilon}\tau^{\frac{-5}{3}} \tag{5.55}$$

where $\varepsilon(\bar{e},\ \ell,\ M_\bullet,\ m) = E_d(\bar{e},\ \ell,\ M_\bullet,\ m,\ \Delta R)/E_d(\bar{e},\ \ell,\ M_\bullet,\ m,\ -R_\star)$,

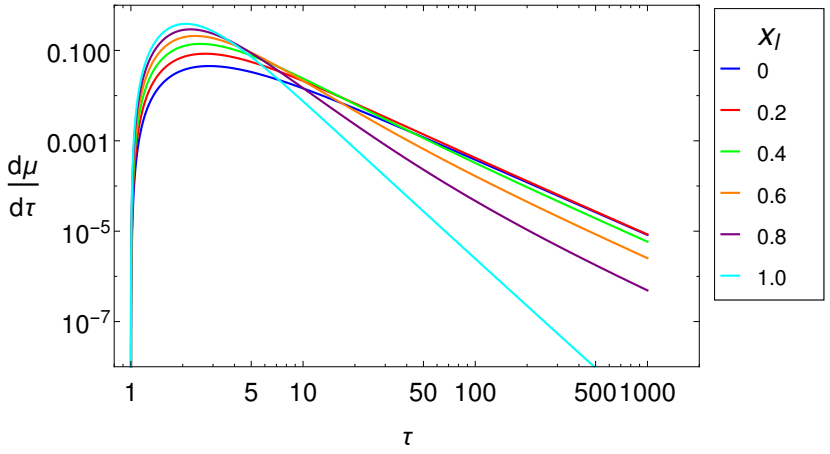

FIGURE 5.15: The dimensionless mass accretion rate given by Equation (5.55), as a function of dimensionless time τ for various x_l. The peak accretion rate increases with x_l whereas the time for peak accretion decreases with x_l.

$x = \Delta R/R_\star$, $\mu = M/M_\star$ and $\tau(\bar{e},\ \ell,\ M_\bullet,\ m) \equiv t/t_m(\bar{e},\ \ell,\ M_\bullet,\ m)$ where $E_{dm} = E_d(\bar{e},\ \ell,\ M_\bullet,\ m,\ -R_\star)$ is the energy of inner-most tightly bound debris. The term $\mathrm{d}\mu$

$$\frac{\mathrm{d}\mu}{\mathrm{d}x} = \frac{3}{2} b \int_x^1 \theta^u(x') x' \,\mathrm{d}x' \tag{5.56}$$

where b is the ratio of central density ρ_c to mean density $\overline{\rho_\star} = 3M_\star/4\pi R_\star^3$ and θ is the solution of Lane–Emden equation for the given polytrope u related to the density by $\rho = \rho_c \theta^u$. The total mass accretion rate is given by $\dot{M}(\bar{e},\ \ell,\ M_\bullet,\ m,\ t) = (M_\star/t_m)(d\mu/d\tau)$ which depends on the orbital parameters through x_l and t_m. We simulated the mass fallback rate for $u = 1.5$, which corresponds to $\Gamma = 5/3$. Figure 5.15 shows the plot of $\mathrm{d}\mu/\mathrm{d}\tau$ for various values of x_l. With an increase in $\bar{e}$, the x_l increases and the orbital period of the debris decreases, which implies that the mass in-fall rate increases. Thus, the peak accretion rate increases with x_l. Next, we examine the conditions for formation of an accretion disk.

5.4 Formation of an accretion disk

The debris of the disrupted star follows a Keplerian orbit around the BH. This debris experiences stream–stream collision either due to an incoming stream that intersects with the outflowing stream at the pericenter (Kochanek 1994) or due to relativistic precession at the pericenter (Hayasaki *et al.* 2013). This stream–stream collision results in a shock breakout which circularizes the debris and forms an accretion disk (Ramirez-Ruiz and Rosswog 2009).

Even though the circularization timescale (time required for the debris to circularize to form an accretion disk) is not accurately known, it is roughly given by $t_c \approx n_{\rm orb} t_m$, where $n_{\rm orb}$ is the minimum number of orbits required for circularization (Ulmer 1999). As the debris falls toward the pericenter, it is accreted with an accretion rate given by Equation (5.53). The formation of an accretion disk depends on t_c and the accretion timescale t_a, which we define as the time required to consume 99% (at the 3σ level) of bound debris. If this timescale is less than t_c, the matter is accreted before the disk is formed. We approximated $\mathrm{d}\mu/\mathrm{d}x$ for convenience with a Gaussian function because it depends on the solution of Lane–Emden equation, which is symmetric about the center of the star and is given by $\mathrm{d}\mu/\mathrm{d}x \simeq 1.192 e^{-4.321x^2}$. The total mass consumed in dimensionless time $\tau_a = t_a/t_m$ is given by

$$\Delta\mu = \int_1^{\tau_a} \frac{\mathrm{d}\mu}{\mathrm{d}\tau}\,\mathrm{d}\tau \tag{5.57}$$

where $\mathrm{d}\mu/\mathrm{d}\tau$ is given by Equation (5.55). If f_r is the fraction of debris bound to the BH, then in time τ_a, the mass accreted by the BH is $\sim 0.99 f_r$. Then, the accretion timescale t_a is given by

$$t_a(\bar{e},\ \ell,\ M_\bullet,\ m) = t_m \left(\frac{1 + x_l}{x_l + \frac{1}{2.0787}\mathrm{Erf}^{-1}[0.997 - 1.962 f_r]} \right)^{\frac{3}{2}} \tag{5.58}$$

where

$$f_r \equiv f_r(\bar{e},\ \ell,\ M_\bullet,\ m) = \int_{-1}^{x_l} \frac{\mathrm{d}\mu}{\mathrm{d}x}\,\mathrm{d}x \tag{5.59}$$

The orbital period of debris will vary due to energy. The energy gradient between the bound debris will fill out a ring and the initial spatial distance between the bound debris will determine the ring formation timescale t_r. Let the dispersion in the energy around the initial energy E be ΔE. A ring is formed in the timescale $t_r = 2\pi/\Delta\Omega$, where $\Delta\Omega$ is the dispersion in the orbital frequency (Hadrava *et al.* 2001). The orbital frequency $\Omega = (2E)^{3/2}/(GM_\bullet)$ and dispersion $\Delta\Omega \propto E^{1/2}\Delta E$ and ΔE are given by

$$\Delta E(\bar{e},\ \ell,\ M_\bullet,\ m) = \frac{2kGM_\bullet}{r_p^2(\bar{e},\ \ell,\ M_\bullet,\ m)}(\mathrm{Min}[R_l(\bar{e},\ \ell,\ M_\bullet,\ m),\ R_\star] + R_\star) \tag{5.60}$$

Then, t_r is given by

$$t_r(\bar{e},\ \ell,\ M_\bullet,\ m) = \frac{\pi}{3\sqrt{2}k} \frac{r_p^2(\bar{e},\ \ell,\ M_\bullet,\ m)}{\bar{e}^{1/2} E_{\boldsymbol{m}}^{1/2}(M_\bullet,\ m)} (R_\star + \mathrm{Min}[R_l(\bar{e},\ \ell,\ M_\bullet,\ m),\ R_\star])^{-1} \tag{5.61}$$

The ratio $\mathcal{T}_r(\bar{e},\ \ell,\ M_\bullet,\ m) = t_r(\bar{e},\ \ell,\ M_\bullet,\ m)/t_a(\bar{e},\ \ell,\ M_\bullet,\ m)$ is given by

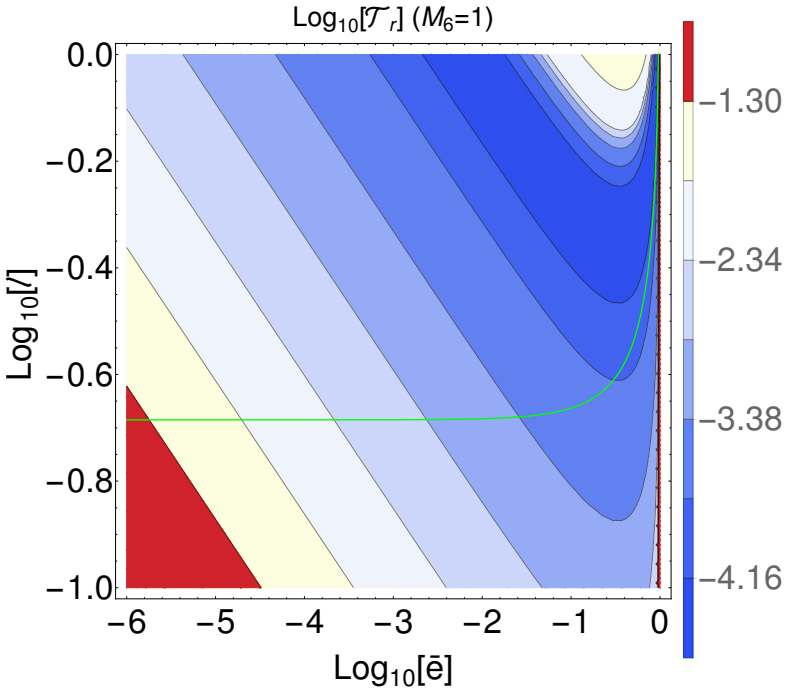

(a)

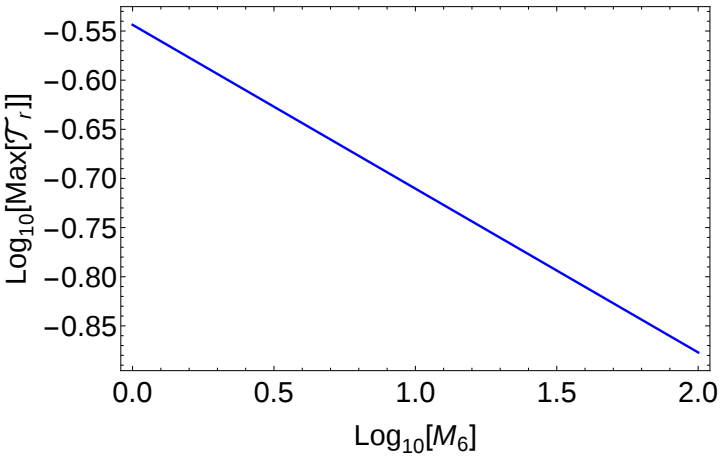

(b)

FIGURE 5.16: The top panel (a) shows a contour plot of the ratio $\mathcal{T}_r(\bar{e},\ \ell,\ M_6,\ m)$ (Equation (5.62)) for $M_6 = 1$ and $m = 1$. The green line corresponds to $r_p = R_s$. For $r_p > R_S$ which lies above green line, $\mathcal{T}_r(\bar{e},\ \ell) < 1$ and thus an accretion disk is formed. The bottom panel (b) shows the Max$[\mathcal{T}_r(\bar{e},\ \ell)]$ as a function of M_6 obtained in the range $10^{-6} \leq \bar{e} \leq 1$ and $0 \leq \ell \leq 1$.

$$\mathcal{T}_r(\bar{e},\ \ell,\ M_\bullet,\ m) = \frac{1}{3\sqrt{2}}\frac{x_l}{1+\mathrm{Min}[1,\ x_l]}\left(\frac{x_l+\frac{1}{2.0787}\mathrm{Erf}^{-1}[0.997-1.962 f_r]}{x_l}\right)^{\frac{3}{2}} \tag{5.62}$$

and an accretion disk is formed if $\mathcal{T}_r(\bar{e},\ \ell,\ M_\bullet,\ m) < 1$. In Figure 5.16, the top panel (a) shows the contour plot of $\mathcal{T}_r(\bar{e},\ \ell,\ M_\bullet,\ m)$ for M_6=1, $m = 1$, and for $r_p(\bar{e},\ \ell,\ M_6,\ m) > R_s$, $\mathcal{T}_r < 1$. The bottom panel (b) shows that Max[$\mathcal{T}_r(\ 10^{-6} \leq \bar{e} \leq 1,\ 0 \leq \ell \leq 1, 1 \leq M_6 \leq 100)$]$< 1$, which implies that the bound debris will form an accretion disk.

The radiation timescale of the disk is given by

$$t_R(\bar{e},\ \ell,\ M_\bullet,\ m) = \frac{f_r M_\star c^2}{\eta \dot{M}(\bar{e},\ \ell,\ M_\bullet,\ m)}\, c^2 \tag{5.63}$$

where c is the light speed, $\dot{M}$ is the accretion rate, and η is the radiative efficiency of the disk. The viscous timescale t_v of the disk formed is given by

$$t_v = \int_{r_{\rm in}}^{r_c} \frac{1}{V_r}\,\mathrm{d}r \tag{5.64}$$

where V_r is the radial inflow velocity of matter in the disk, $r_{\rm in}$ is the inner radius of disk, and the circularization radius obtained using angular momentum conservation is given by

$$r_c(\bar{e},\ \ell,\ M_\bullet,\ m) = 2r_p(1 - r_p\bar{e}/r_t). \tag{5.65}$$

The radial inflow velocity given in eqn (4.82), is given by

$$V_r = -\frac{3}{2}\frac{\nu}{r}\frac{1}{f} \tag{5.66}$$

where $f = 1 - \sqrt{\frac{r_{\rm in}}{r}}$ and ν is the viscosity of the medium given by $\nu = \alpha c_s H$. The parameter α is taken to be 0.1 and $c_s = H\sqrt{GM_\bullet/r^3}$ where H is the disk scale height. Strubbe and Quataert (2009) have calculated the disk scale height for a slim disk (see Section 4.9) to be

$$\frac{H}{r}(\bar{e},\ \ell,\ M_\bullet,\ m,\ r) = \frac{3}{4} f \left(\frac{\dot{M}}{\eta \dot{M}_E}\right)\left(\frac{r}{R_s}\right)^{-1} \cdot \left\{\frac{1}{2} + \left\{\frac{1}{4} + \frac{3f}{2}\left(\frac{\dot{M}}{\eta \dot{M}_E}\right)^2 \left(\frac{r}{R_s}\right)^{-2}\right\}^{\frac{1}{2}}\right\}^{-1} \tag{5.67}$$

where $\dot{M}_E$ is the Eddington mass accretion rate and $\dot{M}$ is taken to be the time averaged accretion rate. Using Equations (5.64) and (5.66), the viscous timescale is given by

$$t_v(\bar{e},\ \ell,\ M_\bullet,\ m) = \frac{2}{3\alpha}\frac{1}{\sqrt{GM_\bullet}} \int_{r_{\rm in}}^{r_c(\bar{e},\ \ell,\ M_\bullet,\ m)} \left(\frac{H(\bar{e},\ \ell,\ M_\bullet,\ m,\ r)}{r}\right)^{-2} \sqrt{r} f \, {\rm d}r \tag{5.68}$$

The ratio $\mathcal{T}_v(\bar{e},\ \ell,\ M_\bullet,\ m) = t_v(\bar{e},\ \ell,\ M_\bullet,\ m)/t_R(\bar{e},\ \ell,\ M_\bullet,\ m)$ is given by

$$\mathcal{T}_v(\bar{e},\ \ell,\ M_\bullet,\ m) = \frac{4}{9\alpha}\frac{1}{\sqrt{GM_\bullet}}\frac{\eta^3}{f_r M_\star}\frac{\dot{M}_E^2}{\dot{M}}\int_{r_{\rm in}}^{r_c}\left(\frac{r}{R_s}\right)^2\frac{\sqrt{r}}{f}\cdot \left(\frac{1}{2}+\left\{\frac{1}{4}+\frac{3f}{2}\left(\frac{\dot{M}}{\eta\dot{M}_E}\right)^2\left(\frac{r}{R_s}\right)^{-2}\right\}^{\frac{1}{2}}\right)^2 {\rm d}r \quad (5.69)$$

where radiative efficiency is typically $\eta = 0.1$ and an accretion disk formed is a slim disk if $\mathcal{T}_v < 1$. The Figure 5.17 shows the contour plot of $\mathcal{T}_v(\bar{e},\ \ell,\ M_\bullet,\ m)$ for $m = 1$ and ℓ=1 and 0.6. We conclude that the accretion disk formed is a slim disk for $M_6 \leq 31.6$. For higher mass SMBHs, a thin disk forms from the disrupted debris of a star on low energy orbit and $\ell \sim 1$, and a thick disk for a star on high energy orbit.

5.5 Accretion disk phase

The Eddington mass accretion rate is given by

$$\dot{M}_E = \frac{4\pi G M_\bullet}{\eta\kappa c} \quad (5.70)$$

where κ is the opacity of the medium taken to be Thompson opacity and η is the radiative efficiency. For a given tidally disrupted star, the accretion disk formed has a super Eddington phase if $M_c(\bar{e},\ \ell,\ m) > M_\bullet$ where $M_c(\bar{e},\ \ell,\ m)$ is the critical BH mass. We have numerically equated the peak accretion rate $\dot{M}_p$ and $\dot{M}_E$, and obtained the $M_c(\bar{e},\ \ell,\ m)$ as shown in Figure 5.18 for $m = 1$. The $M_c(\bar{e},\ \ell,\ m)$ decreases with ℓ and increases with $\bar{e}$. For a given ℓ, an increase in $\bar{e}$ increases

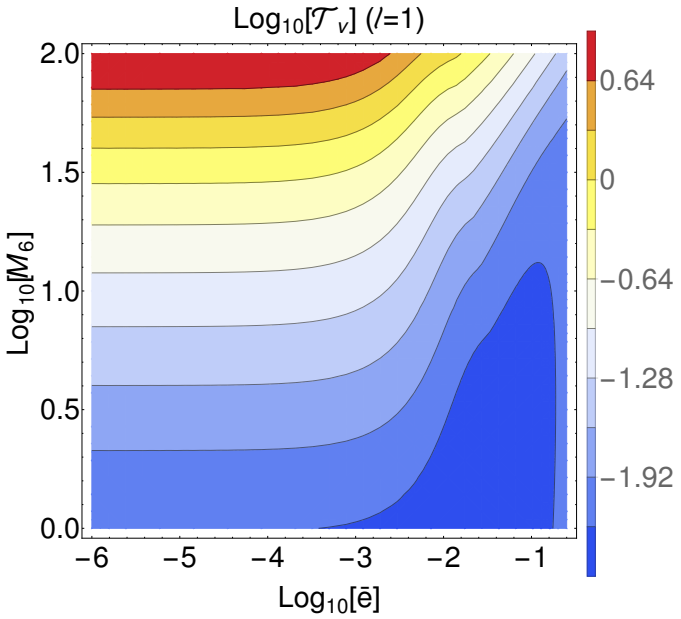

(a)

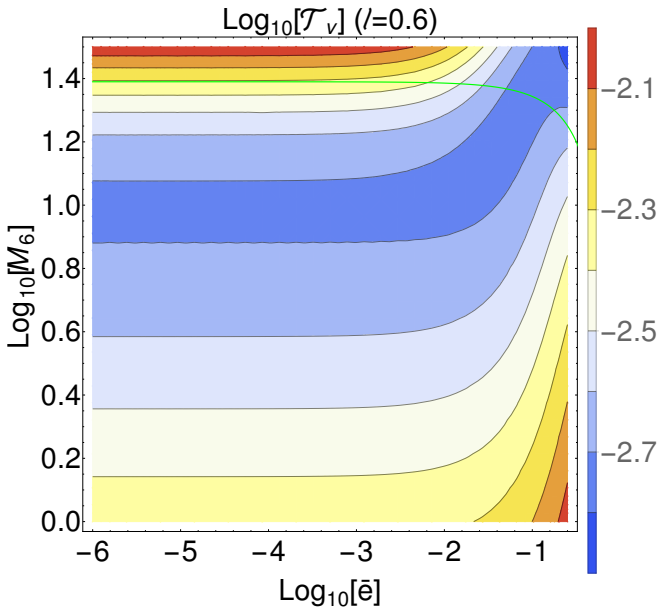

(b)

FIGURE 5.17: The contour plot of $\mathcal{T}_v(\bar{e},\ \ell,\ M_\bullet,\ m)$ (Equation (5.69)) is shown for $\ell = 1$ (top) and $\ell = 0.6$ (bottom) for $m = 1$. The green line corresponds to $r_p = R_s$. For $M_6 \leq 31.6$, the accretion disk formed is a slim disk.

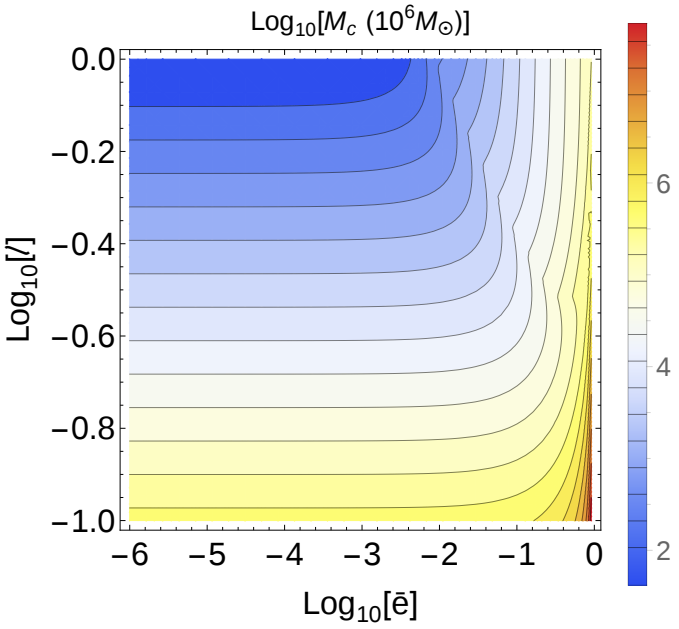

FIGURE 5.18: A contour plot of $M_c(\bar{e},\, \ell,\, m)$ is shown for the disruption of a star of solar mass. The peak $\dot{M}$ increases with a decrease in ℓ and an increase in $\bar{e}$, and thus, the M_c increases with decreasing in ℓ and increasing in $\bar{e}$.

E_d and thus the orbital period of the disrupted debris decreases, which results in an increase in the $\dot{M}$ and hence the peak accretion rate $\dot{M}_p$. For a given $\bar{e}$, the pericenter r_p increases with ℓ, which results in a decrease in E_d and thus $\dot{M}_p$ decreases. For a given $\bar{e}$ and ℓ, $r_p(\bar{e}, \ell, m)$ increases with m, which results in a decrease in E_d. The decrease in E_d implies an increase in fallback time and a decrease in peak accretion rate $\dot{M}_p$ which results in a decrease in $M_c(\bar{e}, \ell, m)$.

5.5.1 Super Eddington Phase

For $M_\bullet \leq M_c(\bar{e},\, \ell,\, m)$, the radiation produced by viscous stress in the rotating disk is trapped by electron scattering and the disk is radiatively inefficient. The time for the photon to diffuse out of the gas is longer than both the inflow time in the disk and the dynamical time for the outflow. Thus, the disk is radiation pressure dominated and the opacity is given by the electron scattering. We assume

that the opacity due to the Thompson scattering and in our flux calculation adopt the work of Strubbe and Quataert (2009). The strong radiative pressure induces an outflowing wind. At the launch radius $r_L(\bar{e},\, \ell,\, M_\bullet,\, m) = r_c(\bar{e},\, \ell,\, M_\bullet,\, m) = 2r_p(1 - r_p\bar{e}/r_t)$, the internal energy is converted into the kinetic energy of the outflows, and the material leaves the disk with the temperature at the launch radius as determined by $aT_L^4 \approx (1/2)\rho(r_L)v_w^2$ (Lodato and Rossi 2011), where a is the radiation constant. The outflow geometry is assumed to be spherical. The photons are trapped up to the radius where $\rho\kappa r \sim 1$ and the radius of photosphere $r_{\rm ph} \sim (\rho\kappa)^{-1}$ is given by

$$r_{\rm ph}(\bar{e},\, \ell,\, M_\bullet,\, m,\, t) = \frac{f_{\rm out}\dot{M}\kappa}{4\pi v_w}, \tag{5.71}$$

where $M_\bullet = M_6 10^6 M_\odot$, $f_{\rm out} = (\dot{M}_{\rm out}/\dot{M})$ and $v_w = f_v\sqrt{GM_\bullet/r_L}$ is the velocity of outflowing wind where f_v is taken to be unity. The outflowing wind is assumed to expand adiabatically so that the density is $\rho(r) \propto T^3(r)$, where T is the temperature of the out flowing wind. Using this scaling relation, the temperature at the photosphere is $T_{\rm ph} = T_L(\rho(r_{\rm ph})/\rho(r_L))^{1/3}$ and using Equation (5.71), $T_{\rm ph}$ is given by

$$T_{\rm ph}(\bar{e},\, \ell,\, M_\bullet,\, m,\, t) = (4\pi)^{\frac{5}{12}}\left(\frac{1}{2a}\right)^{\frac{1}{4}}\kappa^{-\frac{2}{3}} f_{\rm out}^{-\frac{5}{12}} f_v^{\frac{11}{12}}\dot{M}^{-\frac{5}{12}} r_L^{-\frac{7}{24}}(GM_\bullet)^{\frac{11}{24}}. \tag{5.72}$$

Dotan and Shaviv (2011) have calculated the fraction of outflowing material from the super Eddington slim disk with $\dot{M}/\dot{M}_E$=1, 5, 10, and 20 respectively. We approximated their result by the following relation (Lodato and Rossi 2011)

$$f_{\rm out}(\bar{e},\ \ell,\ M_\bullet,\ m,\ t) = \frac{2}{\pi}\arctan\left[\frac{1}{4.5}\left(\frac{\dot{M}}{\dot{M}_E}-1\right)\right]. \tag{5.73}$$

Thus, the luminosity from the outflowing wind is given by $L_\nu^{\rm out}(\bar{e},\ \ell,\ M_\bullet,\ m,\ t) = 4\pi r_{\rm ph}^2 B_\nu(T_{\rm ph})$ and $B_\nu(T_{\rm ph})$ is the intensity obtained assuming the outflowing wind as a black body.

In the super Eddington phase, the time for the photon to diffuse out of the disk is longer than the viscous time, so that the disk that is formed is thick and advective, whereas in the case when $\dot{M} \leq \dot{M}_E$, the disk is thin and cools by radiative diffusion. Strubbe and Quataert (2009) considered a slim disk model by introducing an additional advection term the in energy conservation equation, where the effective temperature profile of the disk as a function of radius is given by (also see §4.9)

$$\sigma_{\rm SB}T_e^4(\bar{e},\ \ell,\ M_\bullet,\ m,\ r,\ t) = 8.54\times10^{17}\ \frac{M_6^{-1}\left(\frac{\eta}{0.1}\right)^{-1}\left(\frac{r}{R_s}\right)^{-3}\left(\frac{\dot{M}}{\dot{M}_E}\right)f}{\frac{1}{2}+\left\{\frac{1}{4}+\frac{3f}{2}\left(\frac{\dot{M}}{\eta\dot{M}_E}\right)^2\left(\frac{r}{R_s}\right)^{-2}\right\}^{\frac{1}{2}}}\ \ {\rm W\,m^{-2}} \tag{5.74}$$

where $f = 1-\sqrt{\frac{r_{\rm in}}{r}}$, $\sigma_{\rm SB}$ is Stefan–Boltzmann constant, $r_{\rm in}$ is the inner radius of the disk and R_s is the Schwarzschild radius BH.

5.5.2 Sub-Eddington Phase

The disk is sub-Eddington for the BH mass $M_\bullet > M_c(\bar{e},\ \ell,\ m)$ and $\dot{M} < \dot{M}_E$. We then consider the disk as the radiative thin disk whose the temperature profile is shown in eqn (4.87) and is given by

$$\sigma_{\rm SB} T_e^4(\bar{e},\ \ell,\ M_\bullet,\ m, r,\ t) = 8.54 \times 10^{17} M_6^{-1} \left(\frac{\eta}{0.1}\right)^{-1} \left(\frac{r}{R_s}\right)^{-3} \left(\frac{\dot{M}}{\dot{M}_E}\right) f \ \ {\rm W\,m^{-2}} \tag{5.75}$$

We see that Equation (5.74) is the modified temperature profile of the thin disk and follows the thin disk for $\dot{M} < \dot{M}_E$. Since the super-Eddington phase exists only for a certain duration, we assume that Equation (5.74) is the temperature profile for the entire duration as it approaches the thin disk model for $\dot{M} < \dot{M}_E$. Assuming the disk to be a black body, the intensity of the disk is given by $B_\nu(T_e(\bar{e},\ \ell,\ M_\bullet,\ m, r,\ t))$ and thus the disk luminosity is given by

$$L_\nu^{\rm Disk}(\bar{e},\ \ell,\ M_\bullet,\ m,\ t) = \int_{r_{\rm in}}^{r_c(\bar{e},\ \ell,\ M_\bullet,\ m)} B_\nu(T_e(\bar{e},\ \ell,\ M_\bullet,\ m, r,\ t)) 2\pi r\, {\rm d}r, \tag{5.76}$$

The total luminosity can be written as

$$L_\nu(\bar{e},\ \ell,\ M_\bullet,\ m,\ t) = \begin{cases} M_\bullet < M_c(\bar{e},\ \ell,\ m): \\ \\ L_\nu^{\rm Disk}(\bar{e},\ \ell,\ M_\bullet,\ m,\ t)\ + L_\nu^{\rm out}(\bar{e},\ \ell,\ M_\bullet,\ m,\ t) \\ \\ M_\bullet \geq M_c(\bar{e},\ \ell,\ m): \\ \\ L_\nu^{\rm Disk}(\bar{e},\ \ell,\ M_\bullet,\ m,\ t) \end{cases}$$

If ν_l and ν_h are the minimum and maximum frequency of the spectral band, then the luminosity of the emitted radiation in the given spectral band in the rest frame of the galaxy is given by

$$L_e(\bar{e},\ \ell,\ M_\bullet,\ m,\ z,\ t) = \int_{\nu_l(1+z)}^{\nu_h(1+z)} L_\nu(\bar{e},\ \ell,\ M_\bullet,\ m,\ t)\,\mathrm{d}\nu \tag{5.77}$$

The observed flux $f_{\rm obs}(\bar{e},\ \ell,\ M_\bullet,\ m,\ z,\ t) = L_e(\bar{e},\ \ell,\ M_\bullet,\ m,\ z,\ t)/(4\pi \mathrm{d}_L^2(z))$, where z is the redshift and d_L is the luminosity distance, and the radiation is observed only if

$$f_l < f_{\rm obs}(\bar{e},\ \ell,\ M_\bullet,\ m,\ z,\ t) = \frac{L_e(\bar{e},\ \ell,\ M_\bullet,\ m,\ z,\ t)}{4\pi d_L^2(z)} \tag{5.78}$$

where f_l is the sensitivity of the detector. The Equation (5.78) is utilized to generate a digital signal $A(t)$ such that

$$A(t) = \begin{cases} 1 & \text{if Equation (5.78) holds true} \\ \\ 0 & \text{if Equation (5.78) does not hold true} \end{cases} \tag{5.79}$$

The width of the digital signal gives the duration of the flare detection used in the event rate calculation (see Section 5.6.3).

As an example, the observed flux in optical g band is shown in Figure 5.19 for $M_6 = 1$, $z = 0.1$, and ℓ= 0.6 (blue), 0.8 (red), 1.0 (orange). For $M_6 = 1$, both the outflowing wind and disk contribute to the observed flux and the flux from wind dominates in the initial time. We can observe a dip in flux due to the outflowing wind whose $r_{\rm ph} \propto \dot{M}$ and $T_{\rm ph} \propto \dot{M}^{-5/12}$ and the occurrence time of dip is nearly at the time of peak accretion rate $\dot{M}_p$ (see Figure 5.15). With an increase in $\bar{e}$, the $\dot{M}_p$ increases, which results in an increase in $r_{\rm ph}$ and a decrease in $T_{\rm ph}$ and thus a decrease in the intensity of radiation $B(T_{\rm ph})$. The flux is due to out flowing wind

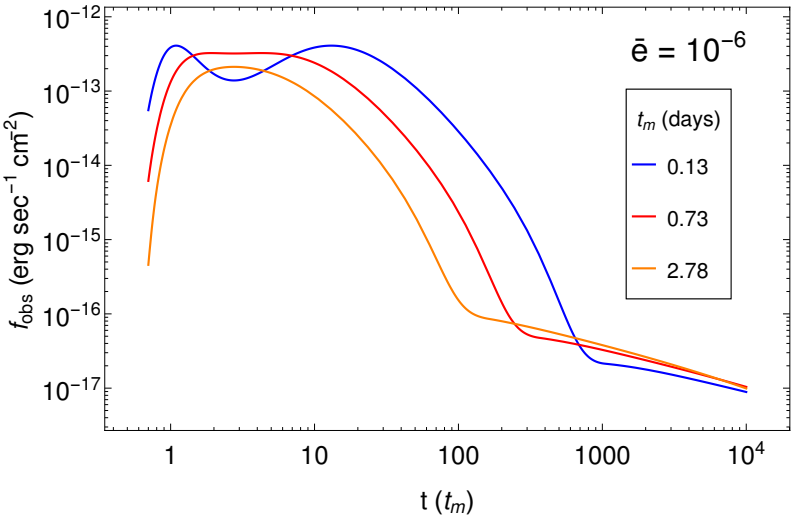

(a)

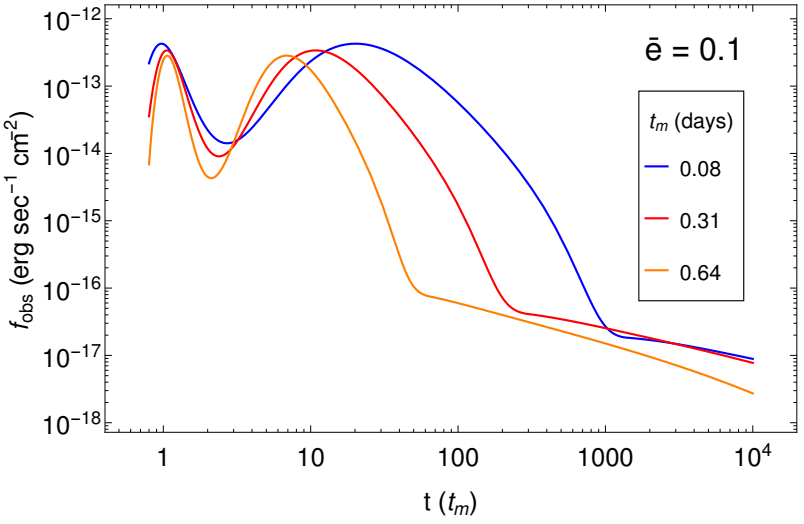

(b)

FIGURE 5.19: The observed flux $f_{\rm obs}$ (Equation (5.78)) in the optical g band for $M_6 = 1$, $m = 1$, redshift $z = 0.1$, and ℓ= 0.6 (blue), 0.8 (red), 1.0 (orange). The peak flux decreases with ℓ and the light curve profile gets widened with a decrease in ℓ. The initial dip in the flux is due to the outflowing wind. The time is scaled with t_m (in days), which is the orbital period of inner-most bound debris that decreases with ℓ due to the increase in the energy of the disrupted debris.

$\propto r_{\rm ph}^2 B(T_{\rm ph})$ and decreases with $\dot{M}_p$ if the decline in $B(T_{\rm ph})$ is higher than the rise in $r_{\rm ph}$. Ulmer (1999) predicted that the minimum value of $n_{\rm orb}$ for the disrupted debris to get circularized is $\sim$ 2–3 and thus we have utilized the $f_{\rm obs}$ starting from the time $\tau = 3$ to generate a digitized signal and calculate the duration of the detection.

5.6 Event rate calculation

For any transient survey, the net detectable TDE rate depends on the number density of non-active galaxies, the theoretical capture rate per galaxy (see Section 5.2), the luminosity distance of galaxies, the sensitivity of the detector, and the duration of flare detection. In this section, we will carry out the detailed calculation of each quantity separately and then combine them in Section 5.6.3.

5.6.1 Number density of non active galaxies

The number density of quasars is a function of redshift and luminosity, where quasars emitting radiation of low intensity ($L < 10^{40}\,{\rm erg\,sec^{-1}}$) are non-active galaxies as compared to the normal quasars ($L \gg 10^{45} - 10^{46}\,{\rm erg\,sec^{-1}}$). According to the Soltan (1982) argument, if quasars were powered by accretion onto a SMBH, then such SMBH must exist in our local universe as "dead" quasars or non-active galaxies. The number density of galaxies (quasars) can be obtained by using the quasar luminosity function (QLF; Hopkins *et al.* (2007)),

$$\frac{{\rm d}\psi}{{\rm d}\log L} = \frac{\psi_*}{(\frac{L}{L_*})^{\gamma_1} + (\frac{L}{L_*})^{\gamma_2}}, \tag{5.80}$$

where ψ_*, L_*, γ_1, γ_2 are a function of redshift z. As TDEs are the main observational signatures of quiescent galaxies, we need to determine the number density of quiescent galaxies at any redshift z. Chen *et al.* (2007) used the QLF to obtain the duty cycle $\delta(z) = 10^{-3}\,(z/0.1)^{2.5}$ where $\delta(z)$ is defined as the ratio of the number of active galaxies to the total number of galaxies. Thus, the BH mass function of quiescent galaxies is given by

$$\frac{\mathrm{d}\psi}{\mathrm{d}M_\bullet} = (1-\delta(z))\frac{\mathrm{d}\psi}{\mathrm{d}\log L}\left|\frac{\mathrm{d}\log L}{\mathrm{d}M_\bullet}\right| \tag{5.81}$$

where L is the luminosity of the quasars, which is taken to be $L = \eta L_E = \eta 4\pi G M_\bullet c/\kappa$ where L_E is the Eddington luminosity, η is taken to be 0.1, and κ is the opacity due to Thompson scattering. This gives the number density of quiescent galaxies as a function of BH mass $M_\bullet$ and redshift z as

$$\frac{\mathrm{d}\psi}{\mathrm{d}M_\bullet}(M_\bullet,\, z) = (1-\delta(z))\frac{1}{M_\bullet}\frac{\mathrm{d}\psi}{\mathrm{d}\log L} \tag{5.82}$$

5.6.2 Luminosity Distance

We assume ΛCDM cosmology with $\Omega_m = 0.315, \Omega_\Lambda = 0.685$,
$H_o = 67.3\,\mathrm{Km\,sec^{-1}\,Mpc^{-1}}$ (Planck Collaboration *et al.* 2013). The luminosity distance as a function of redshift z is given as

$$\mathrm{d}_L(z) = (1+z)\frac{c}{H_o}\int_0^z \frac{1}{((1+z')^3\Omega_m + \Omega_\Lambda)^{0.5}}\,\mathrm{d}z'. \tag{5.83}$$

Consider now a small volume of the universe at redshift z with radial width $\mathrm{d}z$

covering an opening angle ω on the observer's sky (Khabibullin *et al.* 2014). The comoving volume of the slice is

$$\mathrm{d}V_c = \omega d_H^3 \frac{I^2(z)}{W(z)} \mathrm{d}z \tag{5.84}$$

where $\omega = 4\pi f_s,\ d_H = c/H_o,\ W(z) = ((1+z)^3\Omega_m + \Omega_\Lambda)^{0.5}$,

$$I(z) = \int_0^z \frac{1}{((1+z')^3\Omega_m + \Omega_\Lambda)^{0.5}}\, \mathrm{d}z' \tag{5.85}$$

and f_s is the fraction of sky observed.

5.6.3 Probability of flare detection

We generate the spectrum in the form of digital signal using Equation (5.79), and the width of the digital signal provides the duration of flare detection $\delta t_f(\bar{e},\ \ell,\ M_\bullet,\ m,\ z)$. If $t_{\rm cad}$ and $t_{\rm int}$ are the cadence and integration time of the detector, then the probability of detection of an event is given by

$$P(\bar{e},\ \ell,\ M_\bullet,\ m,\ z) = \mathrm{Min}\left[1,\ \frac{\delta t_f(\bar{e},\ \ell,\ M_\bullet,\ m,\ z)}{t_{\rm cad} + t_{\rm int}}\right] \tag{5.86}$$

Using Equations (5.26), (5.46), (5.82), (7.13) and (5.86), the net detectable event rate by the detector is given by

$$\frac{\mathrm{d}^5\dot{N}_D(\gamma,\bar{e},\ell,M_\bullet,m,z)}{\mathrm{d}M_\bullet \mathrm{d}m\mathrm{d}\bar{e}\mathrm{d}\ell\mathrm{d}z} = \omega d_H^3 \left(\frac{\mathrm{d}\Psi}{\mathrm{d}M_\bullet}\right) \frac{\mathrm{d}^2\dot{N}_t}{\mathrm{d}\bar{e}\mathrm{d}\ell\mathrm{d}m}(\gamma,\bar{e},\ell,M_\bullet,m)\frac{I^2(z)}{W(z)} \cdot P(\bar{e},\ell,M_\bullet,m,z) \quad (5.87)$$

With the given initial parameters $M_\bullet,\ m,\ \bar{e},\ \ell$ and z, we generate the light curves using Equation (5.77) in the optical g and soft X-ray bands. The generated spectrum is compared with the sensitivity of the detector f_l to generate a digital signal using Equation (5.79), and the width of the digital signal gives the duration of flare detection. The range of initial parameters in the calculation are taken to be $M_6 = M_\bullet/10^6 M_\odot = 1-100,\ m = 0.8-150,\ \bar{e} = \bar{e}_h - 1,\ \ell = 0-1$ and $z = 0 - z_s$, where $z_s(M_\bullet,\ m,\ \bar{e},\ \ell)$ is the detection limit of the survey. Then, using Equation (5.87), we calculated the net detectable rate by integrating in steps over redshift $z,\ \ell,\ \bar{e},\ m$, and finally over $M_\bullet$ such that

$$\dot{N}_D = \int_1^{100} \mathrm{d}M_6 \int_{0.8}^{150} \mathrm{d}m \int_{\bar{e}_h}^1 \mathrm{d}\bar{e} \int_0^1 \mathrm{d}\ell \int_0^{z_s} \mathrm{d}z\ \frac{\mathrm{d}^5\dot{N}_D(\gamma,\bar{e},\ell,M_6,m,z)}{\mathrm{d}M_6\mathrm{d}m\mathrm{d}\bar{e}\mathrm{d}\ell\mathrm{d}z}. \quad (5.88)$$

The detectable rate per M_6 integrated over z, $\bar{e}$, ℓ and m for various γ is shown in Figure 5.20 for LSST and Pan-STARRS 3π detectors parameters. As the $\dot{N}_t$ and BH mass function decreases with M_6, the $\mathrm{d}\dot{N}_D/\mathrm{d}M_6$ decreases with M_6. The net $\dot{N}_D$ integrated over $\bar{e}$, ℓ, m and M_6 is plotted as a function of γ in Figure 5.21 for various missions. The resulting $\dot{N}_D \propto \gamma^\Delta$ where Δ is given in Table 5.2.

Using Equation (5.26), (5.34), (5.82) and (7.13), the occurrence rate of TDE is given by

$$\dot{N}_o = \int_1^{100} \mathrm{d}M_6 \int_{0.8}^{150} \mathrm{d}m \int_{\bar{e}_h}^1 \mathrm{d}\bar{e} \int_0^1 \mathrm{d}\ell \int_0^{z_s} \mathrm{d}z \; \omega d_H^3 \left(\frac{\mathrm{d}\Psi}{\mathrm{d}M_6}\right) \cdot \frac{\mathrm{d}^3\dot{N}_t}{\mathrm{d}\bar{e}\mathrm{d}\ell\mathrm{d}m}(\gamma, \bar{e}, \ell, M_6, m)\frac{I^2(z)}{W(z)} \quad (5.89)$$

where integration limits are same as those taken for Equation (7.21). We define the detection efficiency of TDE for a detector to be

$$\Upsilon = \frac{\dot{N}_D}{\dot{N}_o} \quad (5.90)$$

The $\dot{N}_D$ calculated for LSST, Pan-STARRS 3π, Pan-STARRS MDS, and eROSITA mission along with their detection efficiency are given in Table 5.2. van Velzen *et al.* (2011) estimated the event rates on the basis of observational studies in the optical bands for the Sloan Digital Sky survey (SDSS) and scaled the result of SDSS to the other missions using the relation $\dot{N} \propto f_s f_l^{-3/2}$ (Gezari *et al.* 2009). This relation is valid only if we assume all other parameters, such as cadence and integration time of the detector, to be same and Table 5.2 shows the estimated rates by van Velzen *et al.* (2011) $\dot{N}_{obs}$ (column with c notation) and our predicted rates $\dot{N}_D$ (column with a notation). The value of γ from the observed density profile is in the range $\sim$ 0.5-1.2(Wang and Merritt 2004; Stone and Metzger 2016). Our results are in reasonable agreement with their results. Khabibullin *et al.* (2014) calculated the number of events N detectable at any moment in the X-ray band for the eROSITA mission assuming a constant theoretical rate for $M_6 \sim$ 1–10 and light curve profile to follow the $t^{-5/3}$ law, whereas we have followed a more rigorous calculation to obtain $\dot{N}_D$. Our prediction for eROSITA does not include the limitations in Khabibullin *et al.* (2014), but are more precise and in agreement with their rough estimate.

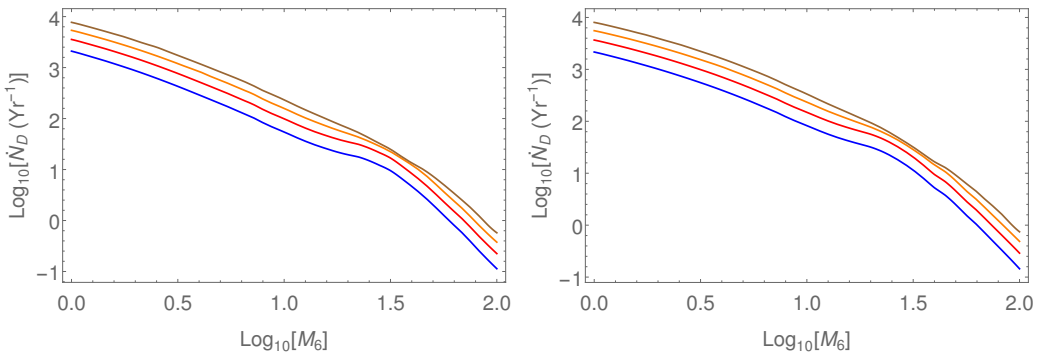

(a) (b)

FIGURE 5.20: The detectable rate, $\dot{N}_D$ per M_6 obtained by integrating Equation (5.87) in steps over z, ℓ, $\bar{e}$ and m for various γ for (a) LSST survey and (b) Pan-STARRS 3π survey for γ =0.6 (blue), 0.8 (red), 1.0 (orange), and 1.2 (brown). With increase in γ, the detectable rate increases due to the increase in $\dot{N}_t$.

The values of γ for which our predictions of $\dot{N}_D$ match with the scaled-up values in van Velzen *et al.* (2011) are shown as γ_s in Table 5.2. The only free parameter in our estimate is γ and this is likely to vary from source to source. Not knowing the expected distribution of γ as a function of say redshift, we have calculated the error in our estimation of $\dot{N}_D$ by taking a fiduciary range in the observed median of $\gamma = 0.7 \pm 0.1$, as is shown in Table 5.2.

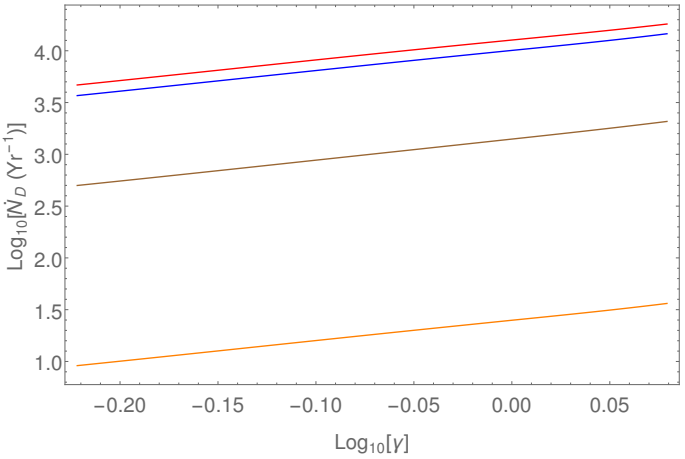

FIGURE 5.21: The detectable rate, $\dot{N}_D$ (Equation (7.21)), as a function of γ for LSST (blue), Pan-STARRS 3π (red), Pan-STARRS MDS (orange), and eROSITA (brown). It is seen that $\dot{N}_D \propto \gamma^{\Delta}$ where Δ is the slope given in Table 5.2.

Survey	Band	f_s	Sensitivity/flux	Cadence time (s)	Integration time (s)	$\dot{N}_D$ $(\mathrm{yr}^{-1})^a$ $\gamma = 0.7 \pm 0.1$	γ_s^b	$\dot{N}_{obs}$ $(\mathrm{yr}^{-1})^c$	Υ^d	Δ^e
LSST	Optical	0.5	24.5 AB mag (g band)	2.6×10^5	10	5003 ± 1421	0.63	4131	0.91	1.97
Pan-STARRS (MDS)	Optical	0.0012	24.8 AB mag (g band)	3.46×10^5	30	12.3 ± 3.5	0.77	15	0.92	1.98
Pan-STARRS 3π	Optical	0.75	24 AB mag (g band)	6.05×10^5	30	6337 ± 1800	0.48	3106	0.85	1.94
eROSITA	X-ray	1	$2.4{\times}10^{-14}(\mathrm{erg\ sec}^{-1}\ \mathrm{cm}^{-2})$	1.58×10^7	1.6×10^3	679.5 ± 195	–	–	0.7	2.06

TABLE 5.2: Mission instrument parameters and predicted rate of the surveys

The parameters of the survey are taken from (1) LSST (Strubbe and Quataert (2009) & `http://www.lsst.org/lsst/overview/`),

(2) Pan-STARRS (MDS; Medium Deep survey; van Velzen *et al.* (2011)),

(3) Pan-STARRS 3π (Strubbe and Quataert (2009) & `http://pan-starrs.ifa.hawaii.edu/public/`),

(4) eROSITA (SRG; Khabibullin *et al.* (2014) & `http://www.mpe.mpg.de/eROSITA`)

[a] Our predicted values along with the error estimates for an assumed range of $\Delta\gamma = 0.1$ around a typically observed median of $\gamma = 0.7$.

[b] $\dot{N}_D(\gamma_s) = \dot{N}_D$ estimated by van Velzen *et al.* (2011).

[c] Results from van Velzen *et al.* (2011).

[d] Detection efficiency of the detector given by Equation (5.90).

[e] Detectable rate $\dot{N}_D \propto \gamma^{\Delta}$.

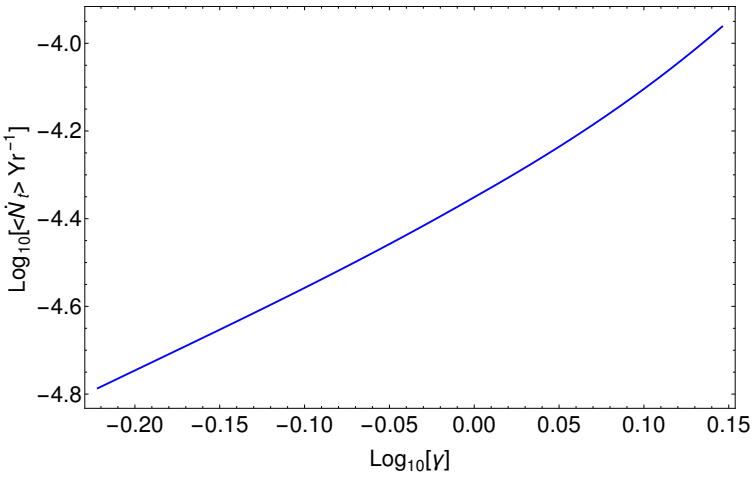

FIGURE 5.22: The galaxy averaged $\dot{N}_t$ (Equation (5.91)) increases with γ and for $\gamma \leq 1.2$, $\left\langle \dot{N}_t \right\rangle \approx \gamma^2$.

5.7 Discussion of the results

The star's initial orbital parameters E and J have significant effects on both stellar and accretion dynamics. We have seen that the effect of J which has not been included previously, plays a crucial role in constructing the shape of light curve profiles.

We have employed a single power density model because most of the galaxies given in Wang and Merritt (2004) and Stone and Metzger (2016) have a break radius $r_b > r_h$ and we calculated the $\dot{N}_t \sim 10^{-5} - 10^{-4}$ Yr^{-1}, which shows a nonlinear dependence with $M_\bullet$ as shown by Wang and Merritt (2004) for single stellar mass distribution with a Nuker profile. Using Equations (5.26), (5.47), (5.82) and (7.13), the galaxy average $\dot{N}_t$ is given by

$$\left\langle \dot{N}_t \right\rangle (\gamma) = \frac{\int_{10^6 M_\odot}^{10^8 M_\odot} \mathrm{d}M_\bullet \int_0^1 \mathrm{d}z \ \left(\frac{\mathrm{d}\psi}{\mathrm{d}M_\bullet}\right) \frac{I^2(z)}{W(z)} \dot{N}_t(\gamma,\ M_\bullet)}{\int_{10^6 M_\odot}^{10^8 M_\odot} \mathrm{d}M_\bullet \int_0^1 \mathrm{d}z \ \left(\frac{\mathrm{d}\psi}{\mathrm{d}M_\bullet}\right) \frac{I^2(z)}{W(z)}} \tag{5.91}$$

and is shown in Figure 5.22. For $\gamma = 0.7$, $\left\langle \dot{N}_t \right\rangle \sim 6.8 \times 10^{-5}$ yr^{-1} which is close to the observational inferred value $\sim 10^{-5}$ yr^{-1} and $\left\langle \dot{N}_t \right\rangle \approx \gamma^2$ for $\gamma \leq 1.2$. The sample of galaxies taken by Stone and Metzger (2016) have γ varying over all ranges upto $\gamma = 1.2$, which implies that their $< \dot{N}_t >$ is γ independent, whereas we have calculated the $< \dot{N}_t >$ assuming that all galaxies to have the same γ. The discrepancy in theory and observation is smaller in our model for $\gamma \leq 1$ compared with Stone and Metzger (2016) who have predicted $< \dot{N}_t > \sim$ few $\times 10^{-4}$ yr^{-1} by taking into account the Schechter BH mass function and a Nuker profile. The γ averaged $\left\langle \dot{N}_t \right\rangle$ integrated over the range $0.6 \leq \gamma \leq 1.2$ is $\sim 1.3 \times 10^{-4}$ yr^{-1}.

Rees (1988) and others have considered the stellar orbit to be nearly parabolic. We have included the angular momentum J in the calculation and studied the effect of J on accretion dynamics. We have modified the dimensionless quantities given in Lodato *et al.* (2009) and for the low eccentric orbits, which results in an increase in peak accretion rate. Strubbe and Quataert (2009) and Lodato and Rossi (2011) have calculated the spectral profile for a parabolic orbit that does not have any dip in their luminosity profile. The inclusion of J induces a dip in the light curve profile, which gets deeper with increased energy. We can also see that our results in the optical band match with the result of Lodato and Rossi (2011) for $\bar{e} \ll 1$.

In general, the accretion of matter into the BH is non-steady because the mass at the outer radii are higher than the mass at inner radii. Montesinos Armijo and de Freitas Pacheco (2011) evaluated the surface density and temperature profile assuming the accretion disk to be thin and the accretion rate $\propto t^{-5/3}$. A model for a non-steady accretion mechanism that includes both super- and sub-Eddington phase is required to better understand the evolution and emission from the disk. The α viscosity prescription used by Strubbe and Quataert (2009) is not applicable in the super-Eddington phase due to low efficiency and high opacity of the disk, so a general viscosity prescription, such as $\nu \propto \Sigma^d(r) r^e$ where d and e are constants,

can be used to evaluate the accretion disk, where $\Sigma(r)$ is surface density profile (Mangalam 2001; Shen and Matzner 2014).

Strubbe and Quataert (2009) have predicted $\dot{N}_D$ assuming a constant capture rate, stellar orbits to be parabolic, and the flare duration to be the duration of Eddington phase, which is obtained assuming $\mathrm{d}M/\mathrm{d}E_d$ as a constant. Gezari *et al.* (2008) and van Velzen *et al.* (2011) have used the observed detectable rate for the GALEX mission in the Near Ultra Violet (NUV) and SDSS in optical band respectively and scaled it to the other missions assuming survey parameters such as cadence and integration time to be same. van Velzen *et al.* (2011) have observationally estimated higher rates compared to the estimation by Gezari *et al.* (2008) due to low sample size. We have performed a detailed calculation, taking into account the both stellar and accretion dynamics, and predicted the detectable rates that are in agreement with the prediction by van Velzen *et al.* (2011). We have not included the filter transmission in generating the spectrum. As the filter transmission varies over the wavelength in the given spectral band, and is less than unity, the simulated flux gets reduced, which results in the reduction in the δt_f and hence the detectable rate $\dot{N}_D$.

India's space mission ASTROSAT that was launched recently, has a payload SSM (Sky Scanning Monitor) to follow up the transient universe in the X-ray band by nearly scanning half the sky in about 6 hours duration for a continued same stellar pointing of the spacecraft (`http://astrosat.iucaa.in/?q=node/13`). The sensitivity of the instrument is $\sim 7.2 \times 10^{-10}$ erg sec^{-1} cm^{-2} with the integration time of the detector to be 10 min. With these parameters, the detectable rate for ASTROSAT is expected to be less than ~ 1 yr^{-1}. For the optical surveys in the g-band, namely LSST and PAN-STARRS, the TDE may not be resolved and the rates corresponding predicted could be an over estimate by a factor of a few.

5.8 Summary and conclusions

We studied in detail, the model of the TDE, taking into account the both stellar dynamical and gas dynamical inputs. The overall system parameters include BH mass $M_\bullet$, specific orbital energy E and angular momentum J, star mass $M_\star$ and radius $R_\star$ and pericenter of the star orbit $r_p(E,\ J,\ M_\bullet)$. We solved the steady state FP equation using the standard loss cone theory for the galactic density profile $\rho(r) \propto r^{-\gamma}$ and stellar mass function $\xi(m)$, where $m = M_\star/M_\odot$ and obtained the feeding rate of stars to the BH $\dot{N}(E,\ J,\ m,\ \gamma)$ that it is an increasing function of J and γ, but a decreasing function of E and m. Because the stars evolve along their orbits toward the BH, we compared the lifetime of main sequence star to the radial period of its orbit and calculated the probability $f_\star$ for a star to be captured as a main sequence given by Equation (5.45). Using this we model the in-fall rate of the disrupted debris, $\dot{M}(E,\ J,\ m,\ t)$, and discuss the conditions for the formation of an accretion disk considering accretion, viscous, ring formation, and radiation timescales. We find that the accretion disk is almost always formed for the fiduciary range of the physical parameters. By equating the peak of $\dot{M}(E,\ J,\ m,\ t)$ to the Eddington rate, we derive the critical black mass $M_c(E, J,\ m)$. We simulated the light curve profiles in relevant optical g band and soft X-rays for both super- and sub-Eddington accretion disks as a function of $\dot{M}(E,\ J,\ m,\ t)$, taking typical stellar system parameters. Specifically, we have found the following key results:

1. In Section 5.2.1, we have approximated the radial period of an orbit with Equation (5.44) and the $M_\bullet - \sigma$ relation. The radial period of an orbit in Keplerian potential is $T_r \propto M_\bullet^{-0.38}\mathcal{E}^{-3/2}$. The capture rate $\dot{N}_t = \int (N_{lc}(\mathcal{E})/T_r)\,\mathrm{d}\mathcal{E} \propto M_\bullet^{-0.38}$.

2. The applicable ranges of dimensionless energy $\bar{e}$ and angular momentum ℓ are given by $\{\bar{e}_h < \bar{e} < 1,\ 0 < \ell < 1\}$ where $\bar{e}_h = s_t = r_t/r_h$.

3. We solved the steady state FP equation in Section 5.2.1 and obtained the capture rate using Equation (5.47). We found that the capture rate $\dot{N}_t$ does not show a power law dependence with $M_\bullet$ and it increases with γ. Even though the increase in $\dot{N}_t$ with γ is non linear, an approximate fit gives $\dot{N}_t \propto \gamma^p$, where $p \sim 2.1$ (see Figure 5.13). For $M_6 > 10$, $\dot{N}_t \propto M_6^{-\beta}$ and $\beta \sim 0.3 \pm 0.01$ (see Figure 5.12).

4. In Section 5.3, we show that the fractional radius from the star center $x_l(\bar{e},\, \ell,\, M_\bullet,\, m)$ to the point where the debris is bound to the BH increases with $\bar{e}$ and ℓ (see Figure 5.14). The increase with ℓ is significant only for high energy orbits. The peak accretion rate increases with x_l. The decline to later $t^{-5/3}$ law is steeper if the energy of the initial orbit is higher, as shown in Figure 5.15 .

5. In Section 5.5, by equating $\dot{M}_p$ and $\dot{M}_E$, the critical BH mass $M_c(\bar{e},\, \ell,\, m)$ is found to increase with $\bar{e}$ and decrease with ℓ and m (see Figure 5.18). With the decrease in ℓ, the r_p decreases and thus $\dot{M}$ increases, which results in an increase in $\dot{M}_p$. For higher $\bar{e}$ and lower ℓ, $M_c(\bar{e},\, \ell,\, m)$ can exceed the BH mass limit for TDE to occur (i.e, $\sim 3 \times 10^8 M_\odot$).

6. In Section 5.4, we found that Max$[\mathcal{T}_r(\, 10^{-6} \leq \bar{e} \leq 1,\, 0 \leq \ell \leq 1, 1 \leq M_6 \leq 100)]< 1$, which implies that the debris will form an accretion disk (see Figure 5.16). The ratio $\mathcal{T}_v < 1$ for $M_6 \leq 31.6$ which implies that the accretion disk formed is a slim disk. The $\mathcal{T}_v$ increases with M_6 and decreases with $\bar{e}$ as shown in Figure 5.17. The higher mass SMBHs form a thin disk from the disrupted debris of a star on low energy orbit and $\ell \sim 1$ and a thick disk for a star on a high energy orbit.

7. In Section 5.5.2, we derive the observed flux as a function of $\bar{e}$ and ℓ. Figure 5.19 shows the observed fluxes $f_{\rm obs}$ in the optical g band and the peak observed flux increases with a decrease in ℓ. The decline of the light curve profile to the later stage gets steeper with increasing ℓ.

8. In Section 5.6, the net detectable rate $\dot{N}_D$ is calculated for the various missions observing in optical and X-ray bands. Using standard cosmological parameters and mission instrument details, we predict the detectable tidal disruption rates for $\gamma = 0.7$ for LSST to be ~ 5003 yr^{-1}; Pan-STARRS in the optical g band performing in either all-sky survey (ASS) mode or the deep imaging survey (DIS) mode were predicted to be ~ 6337 yr^{-1} for operation in 3 π mode and ~ 12.3 yr^{-1} in the MDS mode, which are in reasonable agreement with scaled-up values based on Sloan Digital Sky Survey (SDSS) detection. Our prediction for eROSITA in the soft X-ray band is about ~ 679.5 yr^{-1}, which is consistent with Khabibullin *et al.* (2014). The values of γ for which our predictions of $\dot{N}_D$ match with the scaled-up values in van Velzen *et al.* (2011) are shown as γ_s in Table 5.2. We have also estimated the error in $\dot{N}_D$ for an error in fit to γ which is taken to be 0.1 and is also shown in Table 5.2.

9. Our results are in reasonable agreement with the scaled-up values from the SDSS observations (van Velzen *et al.* 2011), as given in Table 5.2 along with the detection efficiency of the detector Υ. The Υ is lowest for the eROSITA mission due to the high cadence of half year and is highest for Pan-STARRS MDS due to very high sensitivity. The $\dot{N}_D \propto \gamma^{\Delta}$, where $\Delta \sim 1.95$ in optical band is shown in Figure 5.21.

Chapter 6

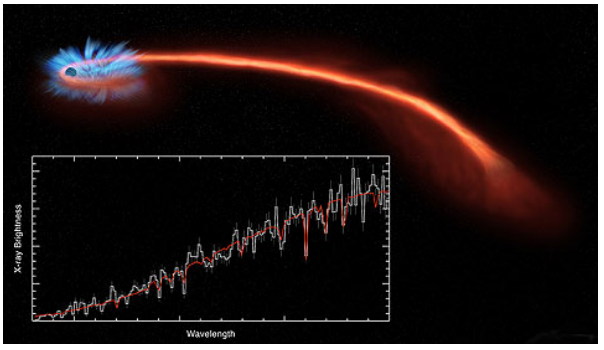

Image: ASAS-AN 14li
NASA/CXC/U. Michigan/J. Miller et al

Accretion and wind dynamics in TDEs

6.1 Introduction

In chapter 4, we have discussed the viscous transport dynamics and the accretion disk model of the thin disk and slim disks with an outflowing wind. We have studied the steady and time-dependent model of the thin disk and derived the self-similar model of thin disks. The existing TDE disk models are shown in Table 4.3. In this chapter, we construct the self-similar models of time-dependent and non-relativistic accretion disk for both sub-Eddington (model A) and super-Eddington disks (model B) with an outflowing wind with a general viscosity prescription. We consider the pressure to be dominated by gas pressure for the sub-Eddington disk and radiation pressure for the super-Eddington disk and obtained the constants b

and d. In our case, the total angular momentum of the disk is a function of time due to the introduction of the fallback and thus our TDE solutions differ from the solution obtained by Mangalam (2001). We construct the super-Eddington model for a radiative slim disk whereas Shen and Matzner (2014) have constructed the model of TDE disk with and without fallback from disrupted debris by developing a self-similar structure of a non-radiative, advective disk with an outflowing wind and using the self-similar solution of Cannizzo *et al.* (1990) for a radiative thin disk with total angular momentum constant. In this work, we calculate the structure of outflowing wind using vertical momentum equation and obtained a relation between mass out flowing rate $\dot{M}_w$ and $\dot{M}_a$, which is different from Dotan and Shaviv (2011).

Table 4.3 shows the various accretion models with their assumptions and assumed viscosity prescriptions for the accretion disk structures shown in Fig 6.1. The Table 6.1 shows a glossary of symbols we use in this paper. Table 6.2 shows various accretion models constructed by us.

6.2 Physics of TDEs

The tidally captured star is disrupted and debris falls back towards the pericenter and circularizes to form a seed accretion disk which evolves due to accretion by the black hole, wind outflow and continuous supply of mass from the fallback debris. The vertically integrated time-dependent equations of an axially symmetric disk

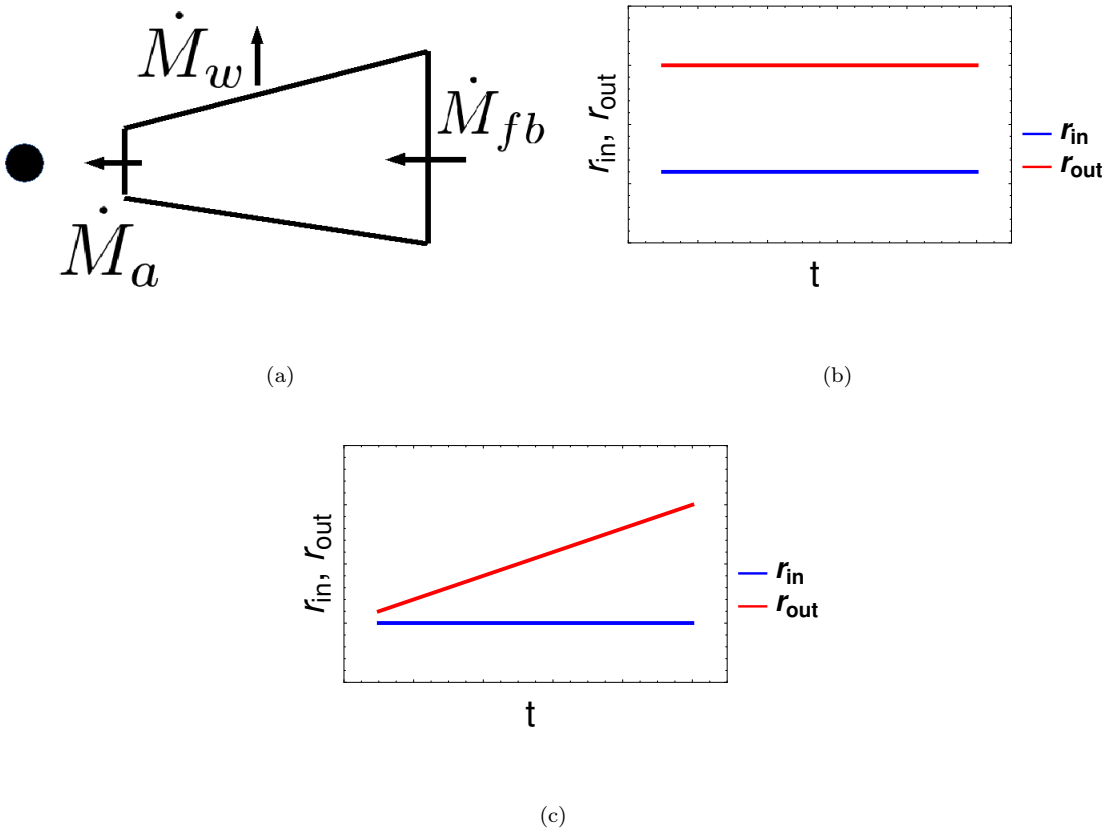

FIGURE 6.1: (a) A schematic structure of accretion disk showing the accretion rate, $\dot{M}_a$, mass fallback rate, $\dot{M}_{fb}$, and mass outflow rate, $\dot{M}_w$. The evolution of the disk inner radius r_{in} (blue) and outer radius r_{out} (red) are shown in (b) and (c).

are given by

$$\frac{\partial}{\partial t}\Sigma_d = -\frac{1}{r}\frac{\partial}{\partial r}(r v_r \Sigma_d) - \dot{\Sigma}_w + \dot{\Sigma}_f \tag{6.1a}$$

$$v_r \Sigma_d \frac{\partial}{\partial r}(r^2\omega(r)) + \dot{\Sigma}_w r^2 \omega(r) = -\frac{1}{r}\frac{\partial}{\partial r}(r^2 \Pi_{r\phi}) + \dot{j}_f, \tag{6.1b}$$

where $\omega(r)$ is the rotational velocity, $\dot{\Sigma}_w$ is the mass loss rate per unit area due to the outflowing wind and $\dot{\Sigma}_f$ and $\dot{j}_f$ are the rates of mass and angular momentum

Dynamical input parameters			
$M_\bullet$	black hole mass	M_6	$M_\bullet/10^6 M_\odot$
$M_\star$	star mass	m	$M_\star/M_\odot$
E	orbital energy of star	$\bar{\epsilon}$	$GM_\bullet/r_t$
J	orbital angular momentum	ℓ	J/J_{lc}
r_t	tidal radius	J_{lc}	loss cone angular momentum
$R_\star$	radius of star	j	black hole spin
r_{ISCO}	radius of innermost stable circular orbit		
Disk structure parameters			
ρ	density of disk	κ	opacity taken to be Thompson opacity
Σ_d	surface density of disk	H	disk height
M_d	disk mass	J_d	disk angular momentum
r_{out}	outer radius of disk	r_{in}	inner radius of disk
P_r	radiation pressure	P_g	gas pressure
$\mathcal{K}$	Constant of equation of state	$\dot{M}_a$	accretion rate
Wind parameters			
$c_1(r)$	Bernoulli parameter	c_2	$(c_1(r)\sqrt{r^2+z_{ph}^2})/(GM_\bullet)$
$\dot{\Sigma}_w$	rate of surface density of wind	$\dot{M}_w$	mass loss rate due to wind
f_{out}	$\dot{M}_f/\dot{M}_a$	z_{ph}	photosphere height
Accretion parameters			
R_l	maximum radius from star center to bound debris	x_l	$R_l/R_\star$
ε	E_d/E_{dm}	$E_{\rm dm}$	energy of inner-most bound debris
μ	$M/M_\star$	M	debris mass with energy E_d
$\dot{M}_{fb}$	fallback rate of debris		
Viscosity parameters			
$\Pi_{r\phi}$	viscous stress	ω	angular frequency
b	power index of Σ_d	d	power index of r
Self similar quantities			
t_0	self similar time constant	r_0	self similar radius taken to be outer radius at t_0
Σ_0	self similar surface density at t_0	β and α	self similar constants
ξ	$(r/r_0)(t/t_0)^{-\alpha}$	v_r	radial velocity
ξ_{out}	$(r_{out}/r_0)(t/t_0)^{-\alpha}$	ξ_{in}	$(r_{in}/r_0)(t/t_0)^{-\alpha}$
Thermodynamical quantities			
T_e	effective temperature of disk	L_b	bolometric luminosity
T_h	hydrostatic temperature	T_{ph}	photosphere temperature
T_E	Eddington temperature	L_E	Eddington luminosity
Q^+	viscous heating rate per unit area	Q^-_{rad}	radiative loss rate per unit area
Q^-_{adv}	energy loss rate per unit area due to advection	L_ν	luminosity in spectral band

TABLE 6.1: Glossary of symbols used in our calculations.

per unit area added to disk by the fallback debris respectively.

Using eqn (6.1), the reduced disk equation is given by

$$\dot{\Sigma}_d = \frac{1}{r}\frac{\partial}{\partial r}\left[\frac{\partial_r(r^2\Pi_{r\phi})}{\partial_r(r^2\omega(r))}\right] + \omega(r)r\frac{\partial}{\partial r}\left[\frac{\dot{\Sigma}_w r}{\partial_r(r^2\omega(r))}\right] + S(r, \quad t) \quad (6.2)$$

where

$$S(r,\ t) = \dot{\Sigma}_f - \frac{1}{r}\frac{\partial}{\partial r}\left(\frac{\dot{j}_f r}{\partial_r(r^2\omega(r))}\right). \tag{6.3}$$

The viscous stress $\Pi_{r\phi}$ has a self-similar form given by

$$\Pi_{r\phi} = K\Sigma_d^b r^d, \tag{6.4}$$

where K is a constant and

$$\Sigma_d = \Sigma_0 \left(\frac{t}{t_0}\right)^{\beta} g(\xi), \quad \xi = \frac{r}{r_0}\left(\frac{t}{t_0}\right)^{\alpha}. \tag{6.5}$$

where $\Sigma_0,\ r_0$ and t_0 are the constants. We describe a general time-dependent accretion disk whose dynamics and evolution depends on the mass fallback rate, the viscous stress and the wind outflow rate in the following sections.

The inner radius is taken to be the ISCO given by $r_{ISCO} = R_s Z(j)/2$, where $R_s = 2GM_\bullet/c^2$ is the Schwarzschild radius, j is the black hole spin and $Z(j)$ is given by (Bardeen *et al.* 1972)

$$Z_1(j) = 1 + (1-j^2)^{\frac{1}{3}}\left[(1+j)^{\frac{1}{3}} + (1-j)^{\frac{1}{3}}\right] \tag{6.6a}$$

$$Z_2(j) = \sqrt{3j^2 + Z_1(j)^2} \tag{6.6b}$$

$$Z(j) = 3 + Z_2(j) - \sqrt{(3-Z_1(j))(3+Z_1(j)+2Z_2(j))}, \tag{6.6c}$$

and outer radius $r_{out} = r_t f(\bar{e},\ \ell)$ to be the circularization radius where $f(\bar{e},\ \ell)$ obtained using eqn (5.65) is given by

$$f(\bar{e},\ \ell) = \frac{4\ell^2(1-\bar{e})}{1+\sqrt{1-4\ell^2\bar{e}(1-\bar{e})}}\left[1 - \frac{2\ell^2\bar{e}(1-\bar{e})}{1+\sqrt{1-4\ell^2\bar{e}(1-\bar{e})}}\right], \tag{6.7}$$

and $R_\star = R_\odot m^{0.8}$ where $m = M_\star/M_\odot$ (Kippenhahn and Weigert 1994).

6.2.1 Disk structure

The accretion disks we consider here are sub-Eddington with a vertical structure similar to standard thin disk and super-Eddington disks with an extended vertical structure. We first derive the structure of these disks and then obtain the forms of viscous stress based on nature of pressure dominating in the disk.

6.2.1.1 Sub-Eddington disk structure

The sub-Eddington disk structure is discussed in §4.7 and we saw that the scale height is given by

$$H^2\frac{GM_\bullet}{r^3} = c_s^2 = \left|\frac{\partial P}{\partial \rho}\right|_{z=0}, \tag{6.8}$$

and the angular velocity is

$$\omega = \sqrt{\frac{GM_\bullet}{r^3}}. \tag{6.9}$$

The total pressure is $P = P_r + P_g$ with gas pressure $P_g = \rho k_B T_c/\mu m_p$ and radiation pressure $P_r = aT_c^4/3$, where $\rho = \Sigma_d/(2H)$, T_c is the mid-plane temperature of the disk, m_p is the mass of the proton and μ is the mean molecular weight taken to be of solar metallicity equal to 0.65.

6.2.1.2 Super-Eddington disk structure

In the case of a super-Eddington disk, the pressure is dominated by radiation pressure which gives strong radiative outflows. The vertical momentum equation is given by

$$\frac{1}{2}\frac{\partial}{\partial z}v_z^2 = -\frac{1}{\rho}\frac{\partial}{\partial z}P - \frac{\partial}{\partial z}\Phi(r,z), \tag{6.10}$$

where P is the total pressure and $\Phi(r,\ z) = -GM_\bullet/\sqrt{r^2+z^2}$. A radiation dominated disk is radiatively inefficient and the strong radiative pressure leads to an extended disk geometry, whose vertical structure is in hydrostatic equilibrium up to a height z_{ph}, from where the wind is launched. We consider a polytropic relation in which the total pressure is given by $P = \mathcal{K}\rho^\gamma$ where $\mathcal{K}$ is a constant that is set by the entropy of the gas; this is a more general assumption than adiabaticity (Chandrasekhar 1939, p86) as it results in the energy transport in the disk leading to radiation. Using this, eqn (6.10) gives

$$\frac{v_z^2}{2} + \frac{\gamma}{\gamma-1}\mathcal{K}\rho^{\gamma-1} + \Phi(r,\ z) = c_1(r), \tag{6.11}$$

where $c_1(r)$ is constant of integration taken to be zero in the hydrostatic equilibrium regime and non-zero at the photosphere z_{ph}. The hydrostatic regime ($v_z = 0$)

gives the hydrostatic density to be

$$\rho(r,\ z) = \rho_0 \left[\frac{r}{\sqrt{r^2+z^2}}\right]^{\frac{1}{\gamma-1}}, \tag{6.12}$$

where $\rho_0 = Br^{-1/(\gamma-1)}$, and B is given by

$$B = \left[\frac{\gamma-1}{\gamma}\right]^{\frac{1}{\gamma-1}} \mathcal{K}^{-\frac{1}{\gamma-1}} (GM_\bullet)^{\frac{1}{\gamma-1}}. \tag{6.13}$$

The total pressure is given by

$$P = P_r + P_g = \frac{1}{3}aT^4 + \frac{k_B}{\mu m_p}\rho T, \tag{6.14}$$

where a is the radiation constant. We consider $P_g = \beta_g P$ (Chandrasekhar 1939), which gives the temperature

$$T = \left[\frac{3}{a}\frac{k_B}{\mu m_p}\right]^{\frac{1}{3}} \left[\frac{1-\beta_g}{\beta_g}\right]^{\frac{1}{3}} \rho^{\frac{1}{3}}. \tag{6.15}$$

Using eqn (6.14) and (6.15), we obtain $\gamma = 4/3$ and $\mathcal{K}$ given by

$$\mathcal{K} = \left[\frac{3}{a}\right]^{\frac{1}{3}} \left[\frac{k_B}{\mu m_p}\right]^{\frac{4}{3}} (1-\beta_g)^{\frac{1}{3}} \beta_g^{-\frac{4}{3}}. \tag{6.16}$$

Using eqn (6.12) and (6.15), the hydrostatic temperature is given by

$$T_h(r,\ z) = \left[\frac{3}{a}\frac{k_B}{\mu m_p}\right]^{\frac{1}{3}} \left[\frac{1-\beta_g}{\beta_g}\right]^{\frac{1}{3}} B^{\frac{1}{3}} r^{-1} \left[\frac{r}{\sqrt{r^2+z^2}}\right]. \tag{6.17}$$

The height of the disk H using eqn (6.12) and

$$\Sigma_d = 2\int_0^H \rho(r,z)\,\mathrm{d}z = 2\frac{B}{r^2}\frac{y_h}{\sqrt{1+y_h^2}} \tag{6.18}$$

where $y_h = H/r$; in the limit $y_h \ll 1$ which is justified a posteriori, we obtain

$$y_h = \frac{1}{2B}\Sigma_d r^2. \tag{6.19}$$

6.2.1.3 Wind structure

The outflowing wind is launched from the photospheric height z_{ph}. Considering a plane parallel atmosphere, the temperature using Eddington approximation is given by

$$T^4(\tau) = \frac{3}{4}T_e^4\left(\tau + \frac{2}{3}\right), \tag{6.20}$$

where τ is the optical depth measured from the top of the atmosphere. Thus, the photosphere temperature is given by

$$T_{ph}^4 = T_0^4\ \frac{4}{3}\ \frac{1}{\tau_{ph}+\frac{4}{3}}, \tag{6.21}$$

where τ_{ph} is the optical depth at the photosphere measured from the mid-plane of the disk. Using eqn (6.17), we obtain

$$T_{ph}^4 = T_0^4(1 + y_{ph}^2)^{-2} \tag{6.22}$$

where $y_{ph} = z_{ph}/r$. Now τ_{ph} is given by

$$\tau_{ph} = \int_0^{z_{ph}} \rho\kappa \, \mathrm{d}z = \rho_0 \ \kappa \ r \ \frac{y_{ph}}{\sqrt{1 + y_{ph}^2}}, \tag{6.23}$$

where κ is the opacity due to Thompson scattering; using eqn (6.21), (6.22) and (6.23), we find

$$y_{ph}(2 + y_{ph}^2)\sqrt{1 + y_{ph}^2} = \frac{3}{4}\rho_0\kappa r, \tag{6.24}$$

whose limiting solutions are

$$y_{ph} \approx \begin{cases} \left(\frac{3B\kappa}{4}\right)^{\frac{1}{4}} r^{-\frac{1}{2}}, & y_{ph} \gg 1 \\ \\ \frac{3B\kappa}{4}\frac{1}{r^2}, & y_{ph} \ll 1 \end{cases} \tag{6.25}$$

The outflowing wind is launched at $z = z_{ph}$ and the velocity of the wind decreases for $z > z_{ph}$ due to gravity, thus $\mathrm{d}v_z^2/\mathrm{d}z|_{z_{ph}} < 0$, so that the eqn (6.10) reduces to

$$v_z^2(z_{ph}) = \frac{8}{\beta_g}\left[\frac{k_B}{\mu m_p}\right](T_{ph} - T_E) + 2c_1(r), \tag{6.26}$$

where T_E is the Eddington temperature given by eqn (6.17) at the photosphere. Due to strong radiative pressure, the photospheric height $z_{ph}/r = y_{ph} \gg 1$ and thus using eqn (6.25), the Eddington temperature is given by

$$T_E = \left[\frac{GM_\bullet}{a\kappa}\right]^{\frac{1}{4}}(1-\beta_g)^{\frac{1}{4}} r^{-\frac{1}{2}}. \tag{6.27}$$

Hence using eqn (6.26),

$$v_z^2(z_{ph}) = \frac{8k_B}{\mu m_p}\left(\frac{GM_\bullet}{a\kappa}\right)^{\frac{1}{4}}(1-\beta_g)^{\frac{1}{4}}\beta_g^{-1} r^{-\frac{1}{2}}\left[\frac{T_{ph}}{T_E} - 1 + c_2\right], \tag{6.28}$$

where $c_2 = c_1(r)/(2\Phi(r,\ z_{ph}))$ is taken to be a constant. This simplifying assumption ensures the existence of the wind as decided by

$$\frac{T_{ph}}{T_E} - 1 + c_2 \geq 0, \tag{6.29}$$

which is taken to be only a function of time and independent of radius. The rate of surface density of the out flowing wind $\dot{\Sigma}_w^2 = \rho^2(z_{ph})v_z^2(z_{ph})$ with $\rho(z_{ph})$ given in eqn (6.12), is given by

$$\dot{\Sigma}_w = \frac{\sqrt{8}}{3}\left(\frac{\mu m_p}{k_B}\right)^{\frac{1}{2}}(GM_\bullet)^{\frac{7}{8}}a^{\frac{1}{8}}\kappa^{-\frac{7}{8}}\beta_g^{\frac{1}{2}}(1-\beta_g)^{-\frac{1}{8}}r^{-\frac{7}{4}} \cdot\sqrt{\frac{T_{ph}}{T_E}-1+c_2}. \quad (6.30)$$

For a TDE disk, the viscous heating decreases with time after the wind is switched on which results in a decrease in the radiative pressure and thus a decrease in mass outflow rate. Since mass outflow rate decreases, $\dot{\Sigma}_w$ decreases, so we assume

$$\sqrt{\frac{T_{ph}}{T_E}-1+c_2} = \mathcal{W}\left(\frac{t}{t_0}\right)^{\delta}, \quad (6.31)$$

such that $\dot{\Sigma}_w$ is given by

$$\dot{\Sigma}_w = Wr^{-\frac{7}{4}}\left(\frac{t}{t_0}\right)^{\delta}, \quad (6.32)$$

where

$$W = \frac{\sqrt{8}}{3}\left(\frac{\mu m_p}{k_B}\right)^{\frac{1}{2}}(GM_\bullet)^{\frac{7}{8}}a^{\frac{1}{8}}\kappa^{-\frac{7}{8}}\beta_g^{\frac{1}{2}}(1-\beta_g)^{-\frac{1}{8}}\mathcal{W}. \quad (6.33)$$

So eqn (6.31) results in T_{ph}/T_E being purely a function of time and independent of the radius and along with the assumption of constant c_2, this ensures that the entire disk is super-Eddington with wind outflow at all radii, provided eqn (6.29) is satisfied.

The rotational velocity of the gas in a super-Eddington disk is non-Keplerian as the radiation pressure is significant. We adopt a solution of a thick disk along the lines of [Loeb and Laor (1992); see the appendix] for a radiative viscosity $\eta = 8\epsilon_{ph}/(27 n_e \sigma_T)$ (Misner 1968; Weinberg 1971), where ϵ_{ph} is the photon energy density, n_e is electron density and σ_T is Thompson scattering coefficient, the velocity $v_\phi(r)$ depends on the ratio $\delta_p = \epsilon_{ph}/(\rho c^2)$ which is taken to be $\delta_p = (27/8)\delta_0 \left(c^2 r/GM_\bullet\right)^{-s}$.

The radial and vertical momentum equations for $v_r,\ v_z \ll v_\phi$, are given by

$$v_\phi^2 = \frac{1}{r}\frac{\partial P}{\partial r} + \frac{GM_\bullet r}{(r^2+z^2)^{3/2}} \tag{6.34a}$$

$$\frac{1}{r}\frac{\partial P}{\partial r} = -\frac{GM_\bullet r}{(r^2+z^2)^{3/2}}. \tag{6.34b}$$

Loeb and Laor (1992) used a radiative viscosity $\eta = (8/27)\epsilon_{ph} m_p/(\rho c \sigma_t)$ and obtained the corresponding conservation equation that is given by

$$\eta\left[\left(\frac{\partial v_\phi}{\partial r} - \frac{v_\phi}{r}\right)^2 + \left(\frac{\partial v_\phi}{\partial z}\right)^2\right] = \boldsymbol{\nabla}\cdot\boldsymbol{F}, \tag{6.35}$$

where radiative heat flux $\boldsymbol{F}$ for Thomson scattering is given by

$$F = -\frac{c}{n_e\sigma_T}\boldsymbol{\nabla}P = -\frac{m_p c}{\sigma_T}\frac{1}{\rho}\boldsymbol{\nabla}P. \tag{6.36}$$

Using the Euler equation given by

$$\frac{\partial \boldsymbol{v}}{\partial t} + v \cdot \nabla v - \frac{v_\phi^2}{r}\hat{r} = -\frac{1}{\rho}\boldsymbol{\nabla} P + \boldsymbol{g}, \tag{6.37}$$

and the divergence of eqn (6.36) is given by

$$\boldsymbol{\nabla} \cdot \boldsymbol{F} = \frac{m_p c}{\sigma_T}\frac{1}{r}\frac{\partial v_\phi^2}{\partial r}, \tag{6.38}$$

for a space dependent velocity field. Thus, assuming $\boldsymbol{v} \cdot \boldsymbol{\nabla} \boldsymbol{v} = (v_r \partial_r + v_\phi \partial_\phi + v_z \partial_z)\boldsymbol{v}$, where v_r and v_z are small and $\partial_\phi = 0$, the energy conservation equation is given by

$$\eta \left[\left(\frac{\partial v_\phi}{\partial r} - \frac{v_\phi}{r} \right)^2 + \left(\frac{\partial v_\phi}{\partial z} \right)^2 \right] = \frac{m_p c}{\sigma_T}\frac{1}{r}\frac{\partial v_\phi^2}{\partial r}. \tag{6.39}$$

Using the density structure given in eqn (6.12) that is obtained using the pressure $P = \mathcal{K}\rho^\gamma$, the $\delta_p = \epsilon_{ph}/(\rho c^2)$ for $\gamma = 4/3$ is given by

$$\delta_p(r) = \frac{3}{8}\frac{1-\beta_g}{Z(j)}\left(\frac{r}{r_{ISCO}}\right)^{-1}, \tag{6.40}$$

which is in the range $0.0625 - 0.375$ for $j = 0 - 1$ and decreases with radius. The disk extent is few times r_{ISCO} initially and the variation in δ_p is small.

Using $\eta = (8/27)(m_p c/\sigma_T)\delta_p(r)$, eqn (6.39) is given by

$$\frac{8}{27}\delta_p(r) \left[\left(\frac{\partial v_\phi}{\partial r} - \frac{v_\phi}{r} \right)^2 + \left(\frac{\partial v_\phi}{\partial z} \right)^2 \right] = \frac{1}{r}\frac{\partial v_\phi^2}{\partial r}. \tag{6.41}$$

We consider the solution of eqn (6.41) for $v_\phi = v_0(r/r_0)^{-f}$ with $f > 0$, assuming the variation in δ_p to be small which leads to

$$f(r) = -1 + \frac{27}{8\delta_p(r)} \pm \frac{27}{8\delta_p(r)}\sqrt{1 - \frac{16\delta_p(r)}{27}}. \tag{6.42}$$

Assuming that the $\delta_p(r) \ll 1$ and neglecting $\mathcal{O}(\delta_p^3)$, we obtain

$$f(r) = -1 \mp 1 + \frac{27}{8\delta_p(r)}\,(1 \pm 1) \mp \frac{4\delta_p(r)}{27} \tag{6.43}$$

which gives $f(r) = -2 - 4/(27\delta_p(r)) + (27/4)\delta_p(r)$ or $f(r) = 4\delta_p(r)/27$. The first solution of $f(r)$ is very high and negative for small $\delta_p(r)$; so we take the second solution $f = 4\delta_p(r)/27$. This solution produces f in the range of 0.01 to 0.05 so that v_0 is nearly constant. Following Loeb and Laor (1992), who assumed $\delta_p = (27/8)\delta_0(c^2 r/(GM_\bullet))^{-s}$, where δ_0 is a constant and applying the radial momentum equation given in eqn (6.34) at the mid-plane plane, we integrate it to obtain the density structure

$$\ln\left(\frac{\rho}{\rho_0}\right) = \begin{cases} s \neq 1: \\ \\ \frac{8}{9\delta_0 c^2}\left(\frac{c^2 r_0}{GM_\bullet}\right)^s \left[\frac{v_0^2}{s-2f}\left\{\left(\frac{r}{r_0}\right)^{s-2f} - 1\right\} - \right. \\ \left. \frac{1}{s-1}\frac{GM_\bullet}{r_0}\left\{\left(\frac{r}{r_0}\right)^{s-1} - 1\right\}\right] + s\ln\left(\frac{r}{r_0}\right) \\ \\ s = 1: \\ \\ \frac{8}{9\delta_0 c^2}\left(\frac{c^2 r_0}{GM_\bullet}\right)\left[\frac{v_0^2}{1-2f}\left\{\left(\frac{r}{r_0}\right)^{1-2f} - 1\right\} - \right. \\ \left. \frac{GM_\bullet}{r_0}\ln\left(\frac{r}{r_0}\right)\right] + \ln\left(\frac{r}{r_0}\right) \end{cases} \tag{6.44}$$

Since v_0 is independent of radius, we take $r_0 = r_{ISCO} = (GM_\bullet/c^2)Z(j)$ and we assume that $\rho(r_q) = \rho_0$ where $r_q = qr_0$, so that v_0 is given by

$$v_0^2 = \begin{cases} s \neq 1: \\ \\ \frac{s-2f}{q^{s-2f}-1}\left[\frac{1}{s-1}\frac{GM_\bullet}{r_0}(q^{s-1} - 1) - \frac{9\delta_0 c^2}{8} s\left(\frac{GM_\bullet}{c^2 r_0}\right)^s\right], \\ \\ s = 1: \\ \\ \left(1 - \frac{9\delta_0}{8}\right)\frac{(1-2f)\ln q}{q^{1-2f}-1}\frac{GM_\bullet}{r_0}, \end{cases} \tag{6.45}$$

The azimuthal velocity, $v_\phi(r)$, is nearly constant if $\delta_p \ll 1$ which is valid in TDE disks for $r/(GM_\bullet) < (1/c^2)(v_0/c)^{-2/(1-\delta_0)}$. The TDE disks are evolving from the initial radii ratio $q = r_{out}/r_{in}$, which is slightly higher than the unity. The range of $\delta_0 = (8/27)\delta_p$ is $0.018 - 0.11$ and the range of $f(r) = (4/27)\delta_p$ is $0.01 - 0.05$. Thus, we neglect the variation of $v_\phi \propto r^{-f(r)}$ in radius and consider it to be a constant. We take $v_\phi = \omega(r)r = v_0(r/r_0)^{-f}$, where $f = \delta_0/2$, $\delta_0 = 0.05$ and $\omega = \chi r^{-e}$, where

$$\chi = v_0 r_0^{\delta_0/2} \quad \text{and} \quad e = 1 + \frac{\delta_0}{2}. \tag{6.46}$$

We assume the angular frequency to be $\omega = \chi r^{-e}$, where r_0 is taken to be ISCO radius, for the super-Eddington thick disk. Here, we consider δ_0 as a free parameter in the range $0.018-0.11$. While this parameterization is justified within the context of a thick disk (with properties averaged for the mid-plane) as proposed by Loeb and Laor (1992), a full quasi-spherical model will be presented in a subsequent paper.

6.2.2 Viscous stress

The viscous stress results in the exchange of angular momentum and viscous heating in the disk. The heat generated due to viscous heating is emitted in the form of radiation in the sub-Eddington disk, whereas in a case of super-Eddington disk, some fraction of heat is advected to the black hole and the remaining is radiated. The heating flux in the disk is given by (see eqn 6.47)

$$Q^+ = \frac{3}{8}\omega\Pi_{r\phi} \tag{6.47}$$

which results in the flux radiated from the disk given by

$$Q^-_{rad} = Q^+, \tag{6.48}$$

and the luminosity to be

$$L = \int_{r_{in}}^{r_{out}} Q^{-}_{rad}\, 2\pi r\, \mathrm{d}r, \tag{6.49}$$

where r_{in} and r_{out} are inner and outer radius of the disk. We now derive the form of viscous stress for a sub and super-Eddington disk with viscosity driven by α, radiation, and gravitational instabilities. We then compare these viscous stresses based on their luminosity and accretion time-scales to obtain the most viable and dominant viscous stress in the typical regime of the physical parameter space.

In this paper, we consider the opacity to be Thompson opacity $\kappa = 0.34$ and mean molecular weight $\mu = 0.65$ which is the mean molecular weight of the ionized solar atmosphere.

6.2.3 α viscous stress: sub-Eddington disk

The accretion disk in sub-Eddington phase is gas pressure dominated and the viscous stress as given by (Shakura and Sunyaev 1973)

$$\Pi_{\phi r} = \alpha_s P H, \tag{6.50}$$

where α_s is the constant, H is the scale height and $P = P_r/(1-\beta_g)$. Using eqn (6.47) and the radiative loss given by $Q^{-} = \sigma T_e^4 = (4ac/3\kappa)(T_c^4/\Sigma_d)$, the energy conservation equation gives

$$\frac{3}{8}\omega\Pi_{\phi r} = \frac{4ac}{3\kappa}\frac{T_c^4}{\Sigma_d} = \frac{4c}{\kappa}\frac{P_r}{\Sigma_d}, \tag{6.51}$$

which together with eqn. (6.50) gives $\Pi_{\phi r} = K\Sigma_d^b r^d$ where $b = -1$, $d = 0$ and K is given by

$$K = \frac{512}{9}\frac{(1-\beta_g)^2}{\alpha_s}\frac{c^2}{\kappa^2}. \tag{6.52}$$

The accretion timescale for a steady flow is given by (Mangalam 2001)

$$t_a \simeq \frac{M_d\omega}{2\pi\Pi_{r\phi}} \tag{6.53}$$

where M_d is the disk mass. Using eqns (6.53), (6.48) and (6.49), the accretion time, heating flux and the luminosity are estimated to be

$$t_\alpha^{sub} = 8.2\times10^6 \text{ yr}\left(\frac{\alpha_s}{0.1}\right)^{-1} M_6^{-1}\left(\frac{M_d}{M_\odot}\right)\left(\frac{\Sigma_d}{10^6 \text{ g cm}^{-2}}\right) \cdot \left(\frac{r}{R_s}\right)^{-\frac{3}{2}}(1-\beta_g)^{-2} \tag{6.54}$$

$$Q^+ = 1.2\times10^{17}\left(\frac{\alpha_s}{0.1}\right)^{-1}\left(\frac{\Sigma_d}{10^6 \text{ g cm}^{-2}}\right)^{-1}\left(\frac{r}{R_s}\right)^{-\frac{3}{2}} M_6^{-1} (1-\beta_g)^2 \text{ erg sec}^{-1}\text{ cm}^{-2} \tag{6.55}$$

$$L_{\alpha}^{sub} = 1.3 \times 10^{40} \left(\frac{\alpha_s}{0.1}\right)^{-1} \left(\frac{\Sigma_d}{10^6 \text{ g cm}^{-2}}\right)^{-1} M_6 (1-\beta_g)^2 \cdot \left(\left(\frac{r_{out}}{R_s}\right)^{\frac{1}{2}} - \left(\frac{r_{in}}{R_s}\right)^{\frac{1}{2}}\right) \text{ erg sec}^{-1} \quad (6.56)$$

6.2.4 α viscous stress: super-Eddington disk

The α viscous stress for a gas pressure dominated disk is given by

$$\Pi_{r\phi} = \alpha_s P H. \quad (6.57)$$

The H is given by eqn (6.19) and $P = \mathcal{K}\rho_0^{4/3}$ with $\mathcal{K}$ given is by eqn (6.16) and density $\rho_0 = B/r^3$ where B is given by eqn (6.13). Thus the viscous stress $\Pi_{\phi r} = K\Sigma_d^b r^d$ where $b = 1$, $d = -1$ and K is given by

$$K = \frac{\alpha_s}{8} G M_{\bullet}. \quad (6.58)$$

Taking $\delta_0 = 0.01$, eqns (6.53), (6.48) and (6.49), the accretion time, heating flux and luminosity are estimated to be

$$t_{\alpha}^{sup} = 0.018 \text{ yr } \left(\frac{M_d}{M_{\odot}}\right) M_6^{-1} \left(\frac{\Sigma_d}{10^6 \text{ g cm}^{-2}}\right)^{-1} \left(\frac{\alpha_s}{0.1}\right)^{-1} \left(\frac{r}{R_s}\right)^{-0.005} Z(j)^{-\frac{1}{2}} \quad (6.59)$$

$$Q^{+} = 2.1 \times 10^{23} \left(\frac{\Sigma_d}{10^6 \text{ g cm}^{-2}}\right) \left(\frac{\alpha_s}{0.1}\right) M_6^{-1} \left(\frac{r}{R_s}\right)^{-2.005} Z(j)^{-\frac{1}{2}} \text{ erg sec}^{-1} \text{ cm}^{-2} \quad (6.60)$$

$$L_{\alpha}^{sup} = 2.35 \times 10^{48} \left(\frac{\alpha_s}{0.1}\right) \left(\frac{\Sigma_d}{10^6 \text{ g cm}^{-2}}\right) M_6 Z(j)^{-\frac{1}{2}} \left[\left(\frac{r_{in}}{R_s}\right)^{-0.005} - \left(\frac{r_{out}}{R_s}\right)^{-0.005}\right] \text{ erg sec}^{-1}, \quad (6.61)$$

6.2.5 Radiative viscous stress: super-Eddington disk

The radiative viscous stress is given by (Misner 1968; Weinberg 1971; Mangalam 2003)

$$\Pi_{r\phi} = \eta_{\gamma} r H \left|\frac{\mathrm{d}\omega}{\mathrm{d}r}\right| \quad (6.62)$$

where $\eta_{\gamma} = (8/27)(\epsilon_{\gamma}/\sigma_T n_e c)$. Following Loeb and Laor (1992),
the $\eta = (m_p c/\sigma_T)(c^2/(GM_{\bullet}))^s \delta_0 r^{-s}$, $\omega = \chi r^{-e}$ and H given by eqn (6.19), the viscous stress is given by

$$\Pi_{r\phi} = K \Sigma_d^b r^d \quad (6.63)$$

where $b = 1,\ d = 2 - e - s$ and

$$K = \frac{96e}{a}\frac{m_p}{\sigma_T c}\delta_0 \left(\frac{c^2}{GM_\bullet}\right)^{-s} \left[\frac{k_B}{\mu m_p}\right]^4 (GM_\bullet)^{-3}\chi(1-\beta_g)\beta_g^{-4}. \tag{6.64}$$

Here we take a radiation pressure dominated disk ($\boldsymbol{\beta_g \ll 1}$) which is justified later. Using $\omega = \chi r^{-e}$ with $s = 1$, eqns (6.53), (6.48) and (6.49), the accretion time, the heating flux and the luminosity are estimated to be

$$t_R^{sup} = 0.143 \text{ yr} \left(\frac{M_d}{M_\odot}\right)\left(\frac{r}{R_s}\right)^{-2}\left(\frac{\Sigma_d}{10^6 \text{ g cm}^{-2}}\right)^{-1} \cdot \left(\frac{\beta_g}{10^{-6}}\right)^4 (1-\beta_g)^{-2}, \tag{6.65}$$

$$Q^+ = 1.16\times 10^{24}\left(\frac{\Sigma_d}{10^6 \text{ g cm}^{-2}}\right) M_6^{-2}(1-\beta_g)^2\left(\frac{\beta_g}{10^{-6}}\right)^{-4} Z(j)^{-0.99}\left(\frac{r}{R_s}\right)^{-0.01} \text{ erg sec}^{-1} \text{ cm}^{-2}, \tag{6.66}$$

$$L_R^{sup} = 3.24\times 10^{45}\left(\frac{\Sigma_d}{10^6 \text{ g cm}^{-2}}\right)(1-\beta_g)^2\left(\frac{\beta_g}{10^{-6}}\right)^{-4} Z(j)^{-0.99}\left[\left(\frac{r_{out}}{R_s}\right)^{0.99} - \left(\frac{r_{in}}{R_s}\right)^{0.99}\right] \text{ erg sec}^{-1}. \tag{6.67}$$

6.2.6 Radiative viscous stress: sub-Eddington disk

Using eqn (6.62), $\rho = \Sigma_d/(2H)$, $\omega = \sqrt{GM_\bullet/r^3}$, $H^2\omega^2 = \partial P/\partial\rho|_{z=0}$ where $P = P_r/(1-\beta_g)$ and using eqn (6.51), we obtain $\Pi_{\phi r} = K\Sigma_d^b r^d$ where $b = 0$, $d = 0$ and K is given by

$$K = \sqrt{\frac{1028}{9}}\sqrt{\frac{\sigma_T c}{m_p}}\left(\frac{c}{\kappa}\right)^{\frac{3}{2}}(1-\beta_g). \tag{6.68}$$

Using eqns (6.53), (6.48) and (6.49), the accretion time, heating flux and the luminosity are estimated to be

$$t_R^{sub} = 23.6 \text{ yr}\left(\frac{M_d}{M_\odot}\right) M_6^{-1}(1-\beta_g)^{-1}\left(\frac{r}{R_s}\right)^{-\frac{3}{2}}, \tag{6.69}$$

$$Q^+ = 8.2\times10^{21}\left(\frac{r}{R_s}\right)^{-\frac{3}{2}} M_6^{-1}(1-\beta_g) \text{ erg sec}^{-1}\text{ cm}^{-2} \tag{6.70}$$

$$L_R^{sub} = 9.1\times10^{44} M_6(1-\beta_g)\left[\left(\frac{r_{out}}{R_s}\right)^{\frac{1}{2}} - \left(\frac{r_{in}}{R_s}\right)^{\frac{1}{2}}\right] \text{ erg sec}^{-1} \tag{6.71}$$

From eqns (6.54), (6.69), (6.59) and (6.65), we can see that

$$t_\alpha^{sup}(\beta_g) < t_R^{sup}(\beta_g) < t_R^{sub}(\beta_g) < t_\alpha^{sub}(\beta_g), \tag{6.72}$$

and using eqns (6.56), (6.61), (6.67) and (6.71), we find

$$L_\alpha^{sub}(\beta_g) < L_R^{sub} < L_R^{sup}(\beta_g) < L_\alpha^{sup}(\beta_g). \tag{6.73}$$

The time scales and the luminosity of the radiative super-Eddington, the α super-Eddington and the radiative sub-Eddington disks depend on β_g. The smaller the value of β_g, the higher is the dominance of radiation pressure and the luminosity which implies that the radiation pressure dominated disk is more luminous compared to gas pressure dominated disk.

The self-gravity in a disk dominates if the density is sufficiently high. Since the tidally disrupted star has a mass much lower than the black hole, the instabilities due to the self-gravity of the disk are negligible. So we are left with four cases, a sub-Eddington disk with α or radiative viscosity and super-Eddington disk with α or radiative viscosity.

6.3 Self similar disk solution

Using eqns (6.2), (6.5) and $\Pi_{r\phi} = K\Sigma_d^b r^d (t/t_0)^{\delta_1}$, we obtain

$$\beta g(\xi) - \alpha\xi \mathrm{d}_\xi g(\xi) - \frac{1}{2-e}\frac{1}{\xi}\mathrm{d}_\xi(\xi^{e-1}\mathrm{d}_\xi(\xi^{2+d}g^b(\xi))) - \frac{e-7/4}{2-e}\xi^{-7/4} = S(r,\ t)\frac{t_0}{\Sigma_0}\left(\frac{t}{t_0}\right)^{1-\beta}, \quad (6.74)$$

$$\frac{K}{\chi}\Sigma_0^{b-1} r_0^{d+e-2} t_0 = 1, \qquad \delta_1 + \beta(b-1) + \alpha(d+e-2) + 1 = 0, \quad (6.75)$$

$$\frac{W r_0^{-7/4} t_0}{\Sigma_0} = 1, \qquad \text{and} \qquad \delta - \frac{7}{4}\alpha + 1 - \beta = 0. \quad (6.76)$$

We consider a power law solution $g(\xi) = A\xi^p$ so that the eqn (6.74) reduces to

$$(\beta - \alpha p)A - \frac{A^b}{2-e}(p\ b + d + 2)(p\ b + d + e)\xi^{p\ (b-1)+d+e-2} - \frac{e - 7/4}{2-e}\xi^{-7/4-p} = S(r,\ t)\frac{t_0}{\Sigma_0}\left(\frac{t}{t_0}\right)^{1-\beta}\xi^{-p}, \quad (6.77)$$

and we assume

$$S(r,\ t)\frac{t_0}{\Sigma_0}\left(\frac{t}{t_0}\right)^{1-\beta}\xi^{-p} = s_c, \quad (6.78)$$

where s_c is a constant and using eqn (6.5), $S(r,\ t) = (s_c/A)\Sigma_d/t$.

The matter added to the disk at outer radius r_{out} results in a jump in the density at outer radius so that the eqn (6.2) is given by

$$\frac{\partial}{\partial t}(\Sigma_d(r^+_{out},\ t) - \Sigma_d(r^-_{out},\ t)) = \frac{1}{r}\frac{\partial}{\partial r}\left[\frac{\partial_r(r^2\Pi_{r\phi})}{\partial_r(r^2\omega(r))}\right]_{r^-_{out}} + \omega(r)r\frac{\partial}{\partial r}\left[\frac{\dot{\Sigma}_w r}{\partial_r(r^2\omega(r))}\right]_{r^-_{out}} + S(r^+_{out},\ t). \quad (6.79)$$

In the r^-_{out} region, $S(r^-_{out},\ t) = 0$ and thus the equation reduces to

$$\frac{\partial}{\partial t}\Sigma_d(r^+_{out},\ t) = S(r^+_{out},\ t). \quad (6.80)$$

The infall mass rate at r_{out} can be written as $\dot{M}(r^+_{out},\ t) = 2\pi\Sigma_d(r^+_{out},\ t)r^+_{out}v_f(r^+_{out}) = \dot{M}_{fb}$, where $v_f(r^+_{out})$ is the infall velocity of the debris. Using eqn (6.78), the source function reduces to

$$S(r^+_{out},\ t) = \frac{s_c}{2\pi A}\frac{\dot{M}_{fb}}{t\ r^+_{out}\ v_f(r^+_{out})}\delta\left(\frac{r}{r_{out}} - 1\right); \tag{6.81}$$

further, if the infall velocity $v_f(r^+_{out})$ is constant and $\dot{M}_{fb} \propto t^{-5/3}$, the source function $S(r^+_{out},\ t) \propto t^{-8/3}$.

We neglect the jump in density at outer radius by assuming that the matter added is instantaneously (quickly compared to the disk evolution time) distributed on the disk so that the self-similar solution holds at all radii. For $r < r_{out}$, the eqn (6.77) reduces to

$$(\beta - \alpha p)A - \frac{A^b}{2-e}(p\ b + d + 2)(p\ b + d + e)\xi^{p\ (b-1)+d+e-2} - \frac{e - 7/4}{2-e}\xi^{-7/4-p} = 0, \tag{6.82}$$

and for the equation to be ξ independent, $p = (2 - e - d)/(b - 1)$ and $-7/4$. We consider a seed disk whose initial mass is $M_d(t_0)$, and the mass conservation equation is given by

$$\dot{M}_d = \dot{M}_{fb} - \dot{M}_a - \dot{M}_w, \tag{6.83}$$

where M_d is the disk mass, $\dot{M}_a$ is the accretion rate onto the black hole and $\dot{M}_w$ is

the mass outflow rate leaving the disk. The mass and angular momentum of the disk are

$$M_d(t) = \int_{r_{in}}^{r_{out}} 2\pi\Sigma_d r \, \mathrm{d}r \tag{6.84a}$$

$$= \frac{2\pi}{2+p} A\Sigma_0 r_0^2 \left(\frac{t}{t_0}\right)^{\beta+2\alpha} (\xi_{out}^{2+p}(t) - \xi_{in}^{2+p}(t)), \tag{6.84b}$$

$$J_d(t) = \int_{r_{in}}^{r_{out}} 2\pi\Sigma_d r\sqrt{GM_\bullet} \, \mathrm{d}r \tag{6.85a}$$

$$= \frac{2\pi A}{p+5/2}\sqrt{GM_\bullet}\Sigma_0 r_0^{\frac{5}{2}} \left(\frac{t}{t_0}\right)^{\beta+\frac{5}{2}\alpha} \left(\xi_{out}^{p+\frac{5}{2}} - \xi_{in}^{p+\frac{5}{2}}\right), \tag{6.85b}$$

The accretion rate to the black hole $\dot{M}_a = 2\pi r\Sigma_d v_r|_{r_{in}}$, and the mass outflow rate are given by

$$\dot{M}_a = 2\pi\frac{\Sigma_0 r_0^2}{t_0}\left(\frac{t}{t_0}\right)^{\beta+2\alpha-1} \begin{cases} \mathrm{sub-Eddington}: \\ \frac{A^b}{2-e}(p\ b+2+d)\xi_{in}^{p\ b+d+e}, \\ \\ \mathrm{super-Eddington}: \\ \frac{A^b}{2-e}(p\ b+2+d)\xi_{in}^{p\ b+d+e} + \frac{\xi_{in}^{1/4}}{2-e}, \end{cases} \tag{6.86}$$

$$\dot{M}_w = 2\pi \frac{\Sigma_0 r_0^2}{t_0} \left(\frac{t}{t_0}\right)^{\beta+2\alpha-1} \begin{cases} \text{sub} - \text{Eddington}: \\ 0, \\ \\ \text{super} - \text{Eddington}: \\ 4\left(\xi_{out}^{\frac{1}{4}} - \xi_{in}^{\frac{1}{4}}\right), \end{cases} \tag{6.87}$$

Differentiating eqn (6.84) and using eqn (6.83), (6.86) and (6.87), we obtain

$$\frac{A(\beta+2\alpha)}{2+p}\left[\xi_{out}^{2+p} - \xi_{in}^{2+p} + \frac{2+p}{\beta+2\alpha} t\left(\xi_{out}^{1+p}\dot{\xi}_{out} - \xi_{in}^{1+p}\dot{\xi}_{in}\right)\right] = \chi_m \frac{\mathrm{d}\mu}{\mathrm{d}\varepsilon}\left(\frac{t}{t_0}\right)^{-\frac{5}{3}-\beta-2\alpha+1} - \frac{t_0}{2\pi\Sigma_0 r_0^2}(\dot{M}_a + \dot{M}_w)\left(\frac{t}{t_0}\right)^{-\beta-2\alpha+1}. \tag{6.88}$$

where $\chi_m = (1/2\pi)(M_\star/\Sigma_0 r_0^2)(t_0/t_m)^{-2/3}$. As $\mathrm{d}\mu/\mathrm{d}\varepsilon$ is initially an increasing function of time (eqn 5.55) which attains a steady value at late times, we assume

$$\beta + 2\alpha = -\frac{2}{3} \tag{6.89}$$

so that $\dot{M}_d \propto t^{-5/3}$ at late times.

Using eqns (6.47) and (6.49), the effective temperature and the luminosity of the disk obtained to be

$$\sigma_{SB} T_e^4 = \frac{3}{8}\frac{\chi^2 \Sigma_0 r_0^{2-2e} A^b}{t_0} \xi^{p\ b+d-e} \left(\frac{t}{t_0}\right)^{\beta-2\alpha(e-1)-1}, \tag{6.90}$$

$$L_b^d = \frac{3\pi\chi^2}{4}\frac{\Sigma_0 r_0^{4-2e}}{t_0}\frac{A^b}{p\ b+d-e+2}\left(\frac{t}{t_0}\right)^{\beta-2\alpha(e-2)-1} \cdot \left[\xi_{out}^{p\ b+d-e+2} - \xi_{in}^{p\ b+d-e+2}\right], \quad (6.91)$$

where σ_{SB} is the Stefan-Boltzmann constant and $\chi = \sqrt{GM_\bullet}$ with $e = 3/2$ for sub-Eddington disk.

The out flowing wind starts from the photosphere z_{ph} and using eqns (6.31), (6.49) and (6.27), temperature of the photosphere, wind luminosity and Eddington luminosity are

$$T_{ph} = T_E\left(\mathcal{W}^2\left(\frac{t}{t_0}\right)^{2\delta} + 1 - c_2\right) \quad (6.92)$$

$$L_b^w = \left(\mathcal{W}^2\left(\frac{t}{t_0}\right)^{2\delta} + 1 - c_2\right)^4 L_E \quad (6.93)$$

$$L_E = \frac{\pi}{2}\frac{GM_\bullet c}{\kappa}(1-\beta_g)\ \mathrm{Log}\left(\frac{r_{out}(t)}{r_{in}}\right) \quad (6.94)$$

The luminosity in the given spectral band $\{\nu_l,\ \nu_h\}$, is given by

$$L_\nu(T) = \int_{\nu_l(1+z)}^{\nu_h(1+z)} \mathrm{d}\nu \int_{r_{in}}^{r_{out}} \mathrm{d}r\, 2\pi r B(T) \quad (6.95)$$

where $B(T)$ is the intensity of blackbody emission corresponding to temperature T and z is the redshift. The spectral luminosity is given by

$$L_\nu = \begin{cases} L_\nu(T_e), & \text{sub} - \text{Eddington} \\ \\ L_\nu(T_e) + L_\nu(T_{ph}), & \text{super} - \text{Eddington} \end{cases} \tag{6.96}$$

In the case of the sub-Eddington disk, the third term on LHS of eqn (6.82) is zero which results in $p = (2 - e - d)/(b - 1)$, which gives $p = -1/4$ for α viscosity and $p = -1/2$ for radiative viscosity. In the case of the super-Eddington disk with α viscosity, eqn (6.82) reduces to

$$(\beta - \alpha p)A = A\frac{(p+1)(p-1+e)}{2-e}\xi^{e-3} + \frac{e - 7/4}{2-e}\xi^{-7/4-p}, \tag{6.97}$$

whose solution for A is possible if $e = 3$ and $p = -7/4$ or $\beta - \alpha p = 0$ and $p = 5/4 - e$. In case $\beta - \alpha p = 0$, then $\Sigma_d \propto r^p$ which is independent of time and this is not possible, whereas for $e = 3$, the disk is super-Keplerian, which is not possible for a super-Eddington disk and thus there is no solution to eqn (6.100). Thus the TDE self-similar disks in the super-Eddington phase with wind are not α viscosity dominated. The scale height H for sub-Eddington disk with radiative viscosity is obtained using eqns (6.8) and (6.68), and given by

$$\frac{H}{r} = \frac{3}{16}\sqrt{\frac{1028}{9}}\sqrt{\frac{\sigma_T c}{m_p}}\sqrt{\frac{c}{\kappa}}\sqrt{\frac{r}{GM_\bullet}} = 3.06\left(\frac{r}{R_s}\right)^{\frac{1}{2}} > 1, \tag{6.98a}$$

Thus, we can conclude that the disk with radiative viscosity cannot be a sub-Eddington thin disk.

Hence we investigate the cases of accretion disks of TDEs that are sub-Eddington with α viscosity called model A and super-Eddington disk with radiative viscosity called model B.

The outer radius is $r_0 = r_{out} = r_t f(\bar{e},\ \ell)$ and $\Sigma_0 = \Sigma_d$ in the eqn (6.91) is taken to be the average surface density given by

$$\Sigma_d = \frac{M_d}{\pi(r_0^2 - r_{in}^2)} \simeq \frac{M_d}{\pi r_0^2}, \tag{6.99}$$

where the disk mass $M_d = f_s M_\star$, $f_s = \int_{-1}^{x_l}(1+x_l)\mathrm{d}\mu_m/\mathrm{d}x\ \mathrm{d}x$ is fraction of debris bound to the black hole where $\mathrm{d}\mu_m/\mathrm{d}x$ is given in eqn (5.55) and $r_0 \gg r_{in}$, so that the luminosity of accretion disk depends on $\bar{e},\ \ell,\ M_6,\ m,\ j$ and t_0. The observation time scale of accretion disk varies with spectral bands and is ~ 1 yr in the optical bands. The black hole and star mass range are taken to be $M_6 = 1 - 100$ and $m = 1 - 100$. We compare the luminosity from various models of viscous stress by comparing the region covered in $\{M_6,\ m\}$ and $\{L,\ t_0\}$ phase space taking the luminosity range $L = 10^{42} - 10^{48}$ erg sec^{-1} and $t_0 = 0.1 - 1$ yr based on estimates from observations.

For super-Eddington disk with radiative viscosity, the eqn (6.82) reduces to

$$(\beta - \alpha p)A = A\frac{(p+5-e-s)(p+3-s)}{2-e}\xi^{s-1} + \frac{e-7/4}{2-e}\xi^{-7/4-p}, \tag{6.100}$$

and the solution for A is possible if $s = 1$ and $p = -7/4$.

In the L, t_0, M_6 and m parameter ranges we have taken for comparison, we find that the sub-Eddington disks are low luminosity disks whereas high luminosity disks are super-Eddington radiative disks as shown in Fig 6.2.

Based on the range of luminosity and accretion timescale seen in the phase diagrams in Fig 6.2, we propose the following model of evolution. The luminosity of a TDE undergoes multiple phases with an initial rise and decline at late times. In the initial phase of accretion, the luminosity is low and the disk is expected to follow model A. Then the luminosity from the disk rises and if the peak luminosity is outside the applicable region of model B as shown in Fig 6.2, the disk entirely follows model A. If the luminosity lies in the model B regime, then the radiation pressure results in an extended disk from which the wind is launched. Then the disk follows model B and transits to model A later. The evolution of the disk through various phases depends on the physical parameters and the fitting will determine details of the transition times between phases.

The t_0 for model B given in Table 6.3 is solved numerically; this gives two values of t_0 whose difference is the duration of super-Eddington phase, τ_0. We find that the high mass black holes have a weak super-Eddington phase as the mass of the outflowing wind varies with $\mathcal{W}$. The given observed range of (L and τ_0) maps to the shaded region in the $\{L,\ t_0\}$ phase space of model B as shown in Fig 6.2 where the disk is super-Eddington and outside of which it is sub-Eddington. The disk structures for a sub and super-Eddington disks are shown in Fig 6.3.

The criteria for the existence and duration of the phases are based on the observed range of the physical parameters. Given the observed TDE light curves, we fit our TDE models (see §7.1) with the input physical parameters $\bar{e}$, ℓ, M_6, m and j and obtain the best fit physical parameters through the procedure explained in Fig 7.1. With the obtained parameters and the model, we derive the shape of light curve including transition through the phases.

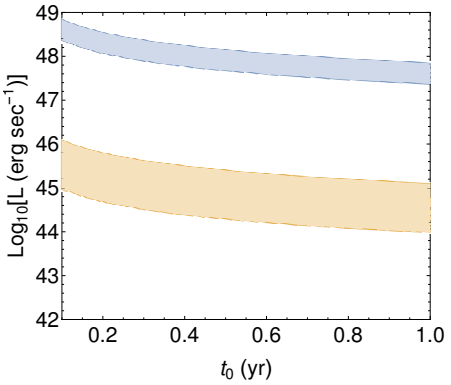

FIGURE 6.2: The shaded regions shows the applicable ranges of model A (orange) and model B (blue) for $\bar{e} = 0.01,\ \ell = 1,\ j = 0.5,\ \alpha = 0,\ \delta_0 = 0.05$. The low luminosity disks are sub-Eddington α disks and high luminosity disks are super-Eddington radiative disks.

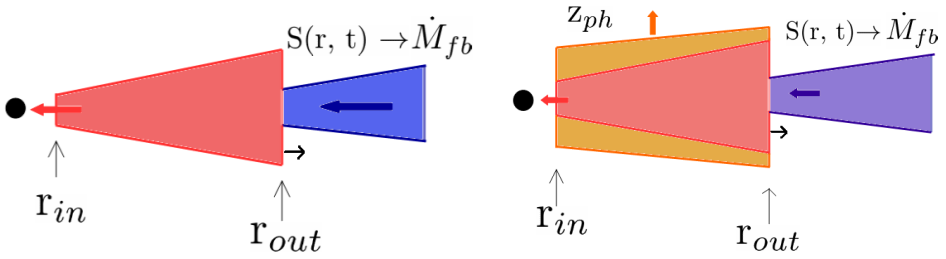

(a) Sub-Eddington (b) Super-Eddington

FIGURE 6.3: The schematic representation of the disk structure for sub-Eddington and super-Eddington phase is shown. The blue, red and orange shaded regions show the mass fallback of debris, the disk structure, and the wind structure respectively. The photospheric height of the wind outflows is z_{ph}. The thick black arrows show the evolution of outer radius.

Model	Dynamics	Disk	Viscous stress	$\dot{M}_{fb}$	Wind structure	Outer radius
A	Time dependent	Sub-Eddington	α viscosity	$\propto t^{-5/3}$	None	Evolving
B	Time dependent	Super-Eddington	Radiative viscosity	$\propto t^{-5/3}$	$\dot{\Sigma}_w = W(t/t_0)^{\delta} r^{-7/4}$	Evolving
C	Steady structure	Sub-Eddington	α viscosity	None	None	Static
D	Steady structure	Super-Eddington	α viscosity	None	$\dot{M}_w = f_{out}\dot{M}_a$	Static

TABLE 6.2: We consider various models of accretion disks. The first column identifies the model and the second column corresponds to the disk structure. The steady disk in C and D correspond to models of MM15 and is explained in Table 4.3. In all the models, the inner radius is taken to be fixed at ISCO radius.

6.4 Model A: sub-Eddington disk α viscous stress

Using eqns (6.8) and (6.50), H is given by

$$\frac{H}{r} = \frac{32}{3}\frac{c}{\alpha_s \kappa}\Sigma_d^{-1}\omega^{-1}r^{-1} \tag{6.101a}$$

$$= 1.1\times 10^{-4}\left(\frac{\alpha_s}{0.1}\right)^{-1}\left(\frac{\Sigma_0}{10^6 \text{ g cm}^{-2}}\right)^{-1}\left(\frac{r_0}{R_s}\right)^{\frac{1}{2}}\left(\frac{t}{t_0}\right)^{-1}\xi^{\frac{3}{4}}. \tag{6.101b}$$

The free parameters are $\bar{e}$, ℓ, M_6, m, α, e and β_g. We have solved the set of equations in Table 6.3 numerically to obtain t_0 and Σ_0 shown in Fig 6.4. The calculated values of Σ_0 and r_0 for each simulation set is given in Table 6.5. Using eqn (5.55) and (6.86), the ratio of accretion rate by the black hole and the mass fallback rate is given by

Model A: sub-Eddington disk with α viscosity

$b=-1,\ d=0,\ \beta=2/3,\ \alpha=-2/3,\ \delta_1=0,\ p=-1/4,\ A=\sqrt{63/4}$ and $\omega=\sqrt{GM_\bullet/r^3}$.

$\Sigma_0=\frac{2+p}{2\pi}\frac{1}{A}\frac{M_d(t_0)}{r_0^2}\frac{1}{\xi_{out}^{2+p}(t_0)-\xi_{in}^{2+p}(t_0)}$, $r_{out}(t_0)=r_0=qr_{in}$ and $r_{in}=r_{ISCO}$.

$M_d(t_0)\equiv M_d(\bar{e},\ \ell,\ M_6,\ m,\ t_0)=M_\star\int_1^{\frac{t_0}{t_m}}\frac{\mathrm{d}\mu_m}{\mathrm{d}\tau_m'}\mathrm{d}\tau_m'$, $\quad\frac{M_d(t_0)}{\sqrt{t_0}}=\frac{64\pi}{(2+p)\sqrt{18}}A\frac{r_0^{7/4}(1-q^{-2-p})}{(GM_\bullet)^{1/4}}\frac{1-\beta_g}{\sqrt{\alpha_s}}\frac{c}{\kappa}$.

$M_d(t)=\frac{2\pi}{2+p}A\Sigma_0 r_0^2\left(\frac{t}{t_0}\right)^{\beta+2\alpha}(\xi_{out}^{2+p}(t)-\xi_{in}^{2+p}(t))$, $\quad J_d(t)=\frac{2\pi A}{p+5/2}\sqrt{GM_\bullet}\Sigma_0 r_0^{\frac{5}{2}}\left(\frac{t}{t_0}\right)^{\beta+\frac{5}{2}\alpha}\left(\xi_{out}^{p+\frac{5}{2}}-\xi_{in}^{p+\frac{5}{2}}\right)$.

$\dot{M}_a=4\pi\frac{\Sigma_0 r_0^2}{t_0}\left(\frac{t}{t_0}\right)^{\beta+2\alpha-1}A^b(p\ b+2+d)\xi_{in}^{p\ b+d+3/2}$, $\quad L_b^d=\frac{3\pi GM_\bullet}{4}\frac{\Sigma_0 r_0}{t_0}\frac{A^b}{p\ b+d+1/2}\left(\frac{t}{t_0}\right)^{\beta+\alpha-1}\left[\xi_{out}^{p\ b+d+1/2}-\xi_{in}^{p\ b+d+1/2}\right]$.

Model B: super-Eddington disk with radiative viscosity

$b=1,\ d=2-e-s,\ \beta=-2/3-\alpha,\ \delta_1=-1,\ s=1,\ p=-7/4,\ A=\left(\frac{e-7/4}{2-e}\right)\left[\beta+\frac{7}{4}\alpha-\frac{1}{16}\frac{9-4e}{2-e}\right]^{-1}$ and $\omega=\chi r^{-e}$.

$\mathcal{W}=\frac{3}{\sqrt{8}}\left(\frac{k_B}{\mu m_p}\right)^{\frac{1}{2}}(GM_\bullet)^{-\frac{7}{8}}a^{-\frac{1}{8}}\kappa^{\frac{7}{8}}\frac{(1-\beta_g)^{1/8}}{\beta_g^{1/2}}\frac{r_0^{7/4}\Sigma_0}{t_0}$, $\quad\frac{\beta_g^4}{1-\beta_g}=\frac{96\epsilon}{a}\delta_0\frac{m_p}{\sigma_T c}\left(\frac{c^2}{GM_\bullet}\right)^{-1}\left(\frac{k_B}{\mu m_p}\right)^4(GM_\bullet)^{-3}t_0$.

$\Sigma_0=\frac{2+p}{2\pi}\frac{1}{A}\frac{M_d(t_0)}{r_0^2}\frac{1}{\xi_{out}^{2+p}(t_0)-\xi_{in}^{2+p}(t_0)}$, $r_{out}(t_0)=r_0=qr_{in}$ and $r_{in}=r_{ISCO}$.

$M_d(t)=\frac{2\pi}{2+p}A\Sigma_0 r_0^2\left(\frac{t}{t_0}\right)^{\beta+2\alpha}(\xi_{out}^{2+p}(t)-\xi_{in}^{2+p}(t))$, $\quad J_d(t)=\frac{2\pi A}{p+5/2}\sqrt{GM_\bullet}\Sigma_0 r_0^{\frac{5}{2}}\left(\frac{t}{t_0}\right)^{\beta+\frac{5}{2}\alpha}\left(\xi_{out}^{p+\frac{5}{2}}-\xi_{in}^{p+\frac{5}{2}}\right)$.

$\dot{M}_a=2\pi\frac{\Sigma_0 r_0^2}{t_0}\left(\frac{t}{t_0}\right)^{\beta+2\alpha-1}\left[\frac{A^b}{2-e}(p\ b+2+d)\xi_{in}^{p\ b+d+e}+\frac{\xi_{in}^{1/4}}{2-e}\right]$, $\quad\dot{M}_w=8\pi\frac{\Sigma_0 r_0^2}{t_0}\left(\frac{t}{t_0}\right)^{\beta+2\alpha-1}\left(\xi_{out}^{\frac{1}{4}}-\xi_{in}^{\frac{1}{4}}\right)$.

$L_b^d=\frac{3\pi\chi^2}{4}\frac{\Sigma_0 r_0^{4-2e}}{t_0}\frac{A^b}{p\ b+d-e+2}\left(\frac{t}{t_0}\right)^{\beta-2\alpha(e-2)-1}\left[\xi_{out}^{p\ b+d-e+2}-\xi_{in}^{p\ b+d-e+2}\right]$.

$L_b^w=\left(\mathcal{W}^2\left(\frac{t}{t_0}\right)^{2\delta}+1-c_2\right)^4 L_E$, $\quad L_E=\frac{\pi}{2}\frac{GM_\bullet c}{\kappa}(1-\beta_g)\ \mathrm{Log}\left(\frac{r_{out}(t)}{r_{in}}\right)$.

TABLE 6.3: Formulary for the various quantities calculated for models A and B. The Eddington luminosity L_E is given by eqn (6.94). The viscous stress is given by $\Pi_{r\phi}=-K\Sigma_d^b r^d(t/t_0)^{-\delta_1}$ where the self similar forms are $\Sigma_d=\Sigma_0(t/t_0)^\beta g(\xi)$ and $\xi=(r/r_0)(t/t_0)^\alpha$ with $g(\xi)=A\xi^p$. The parameters t_0 and Σ_0 are obtained by solving eqns (6.74, 6.75).

Set	$\bar{e}$	ℓ	M_6	m	j	q
I1	0.01	1	1	1	0	2
I2	0.01	1	1	10	0	2
I3	0.01	1	10	1	0	2
I4	0.01	1	1	1	0	2
I5	0.01	1	1	1	0.5	2
I6	0.01	1	1	10	0.5	2
I7	0.01	1	10	1	0.5	2
I8	0.01	1	1	1	0.5	2

TABLE 6.4: The parameter sets used for simulations in our sub and super-Eddington models A and B.

$$\frac{\dot{M}_a}{\dot{M}_{fb}} = 1.9\frac{q^{-\frac{7}{4}}}{1-q^{-\frac{7}{4}}}\left(\frac{M_d(t_0)}{M_\odot}\right)\left(\frac{M_\star}{M_\odot}\right)^{-1}\left(\frac{t_0}{t_m}\right)^{\frac{2}{3}} \cdot \left[\frac{\mathrm{d}\mu_m}{\mathrm{d}\varepsilon}(t)\right]^{-1}\left(\frac{t}{t_0}\right)^{\frac{7}{6}} \quad (6.102)$$

where $\mathrm{d}\mu_m/\mathrm{d}\varepsilon$ is given by eqn (5.55). Since we assume that the matter added by the fallback debris is instantaneously distributed in the disk such that the self-similar structure remains same, the outer radius of the disk expands initially as the mass fallback is higher than the accretion and decreases at late time as accretion dominates over fallback as shown in Fig 6.5 obtained using eqn (6.88). Since t_0 is smaller, the accretion dynamics is faster for high spin BHs which implies that the

Set	t_0 (days)	$\Sigma_0(10^3 \text{g cm}^{-2})$	$r_0(R_s)$
I1	2.47	7.76	6
I2	4.22	10.1	6
I3	7.70	4.3	6
I4	2.47	7.76	6
I5	2.42	8.4	4.23
I6	4.17	10.9	4.23
I7	7.26	4.6	4.23
I8	2.42	8.4	4.23

TABLE 6.5: The values of t_0, Σ_0 and r_0 in units of $R_s = 2.9 \times 10^{11} M_6$ in cm with $M_6 = 1$ obtained using equations given in Table 6.3 for the sub-Eddington α disk and $\beta_g = 0.01$.

fallback rate is high and hence more mass is added to the disk which causes the outer radius to move outward more.

From eqn (6.102) and Fig 6.6, we see that the rate of mass loss by the disk due to accretion is higher than the mass gain by the addition of fallback debris at late times which results in the decline in the disk mass as shown in Fig 6.7. The overall angular momentum of the disk including the angular momentum loss due to accretion and the addition by fallback debris is shown in Fig 6.7.

The bolometric luminosity is given by eqn (6.91) and the spectral luminosity is given by eqn (6.96).

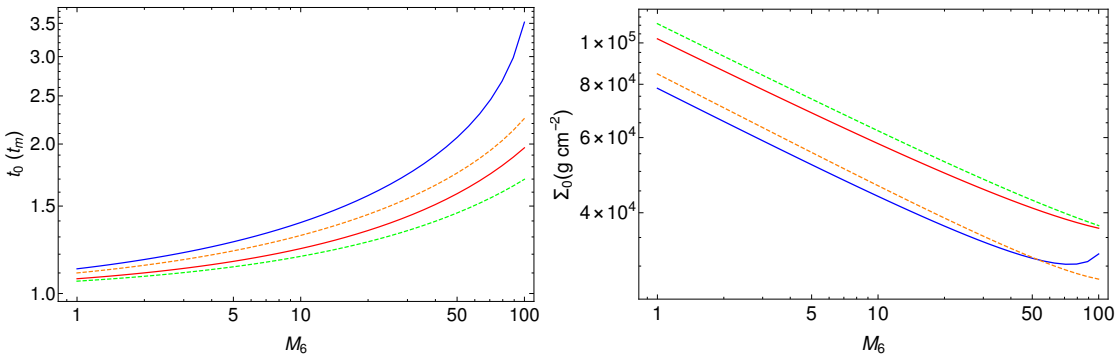

(a) (b)

FIGURE 6.4: (a) The self similar parameters $t_0(t_m)$ and (b) Σ_0 g cm^{-2} as a function of black hole mass M_6 for parameter set I1 (blue), I2 (red), I5 (orange) and I6 (green).

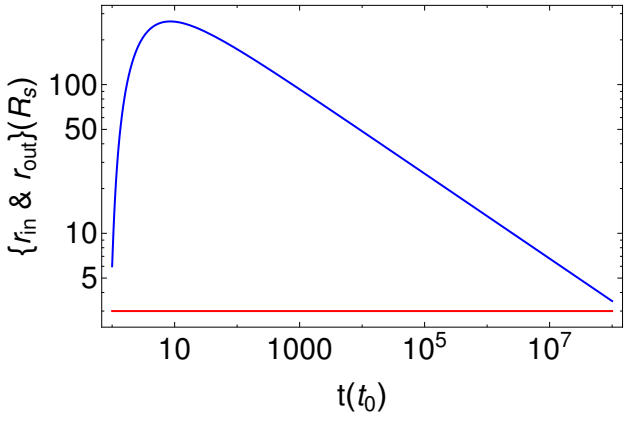

(a)

FIGURE 6.5: (a) The values of r_{in} (red) and r_{out} (blue) in terms of r_0 for the parameter set I1.

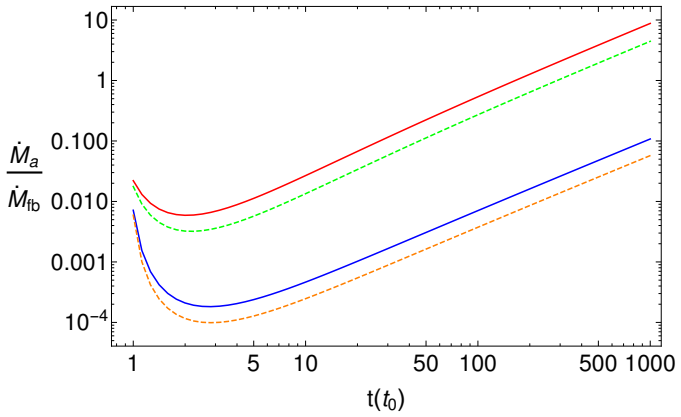

FIGURE 6.6: The ratio of accretion rate to mass fallback rate from the disrupted debris is shown for the parameter set I1 (blue), I3 (red), I5 (green dashed) and I7 (red dashed). The increase in the ratio results in a decrease in the disk mass.

The Fig 6.8, shows the bolometric luminosity as a function of t. From eqn (5.55), we can see that the mass fallback rate causes an enhancement in surface density, viscous heating, effective disk temperature and luminosity. The spectral luminosity simulated in various spectral bands for the set I1 are also shown.

6.5 Model B: super-Eddington radiative viscous stress dominated thick disk

We have numerically solved the eqns given in Table 6.3 to obtain the maximum value of $\mathcal{W}$ denoted by $\mathcal{W}_{max}$ as shown in Fig 6.9 and normalized the $\mathcal{W}$ with respect to its maximum given by $\mathcal{W}_n = \mathcal{W}/\mathcal{W}_{max}$. The $\mathcal{W}_n$ is taken to be a free parameter and is used to obtain t_0 and then Σ_0 is given by eqn (6.84) at $t = t_0$. For a given value of $\mathcal{W}_n$, there are two values of t_0 and we have considered the smaller value because the super-Eddington phase dominates early. The free parameters are $\bar{e},\ \ell,\ M_6,\ m,\ \alpha$ and $\mathcal{W}_n$. The value for δ_0 is taken to be 0.05 which is typically the mid-value in the range of δ_0.

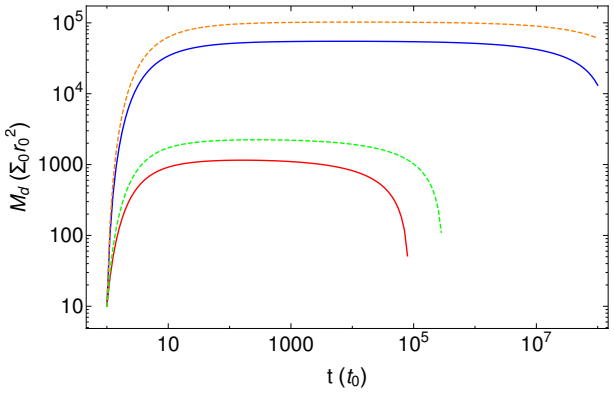

(a)

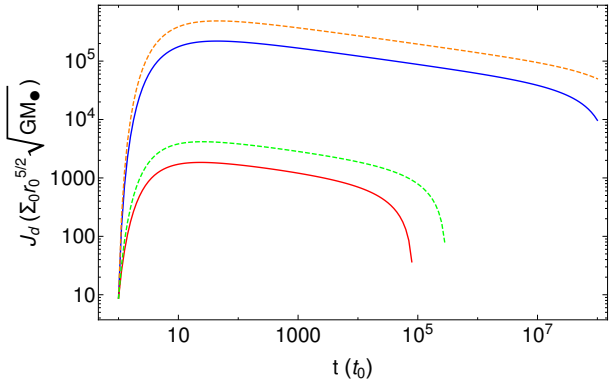

(b)

FIGURE 6.7: (a) The evolution of the mass of disk and (b) the angular momentum is shown for the parameter set I1 (blue), I3 (red), I5 (orange) and I7 (green) with the Σ_0 and r_0 values given in Table 6.5.

The ratio of mass outflow to the accretion by the black hole using eqns (6.86) and (6.87) is given by

$$f_{out} = \frac{\dot{M}_w}{\dot{M}_a} = \frac{4(\xi_{out}^{1/4} - \xi_{in}^{1/4})}{\frac{A}{2-e}(p+4-e)\xi_{in}^{p+4-e} + \frac{\xi_{in}^{1/4}}{2-e}}, \tag{6.103}$$

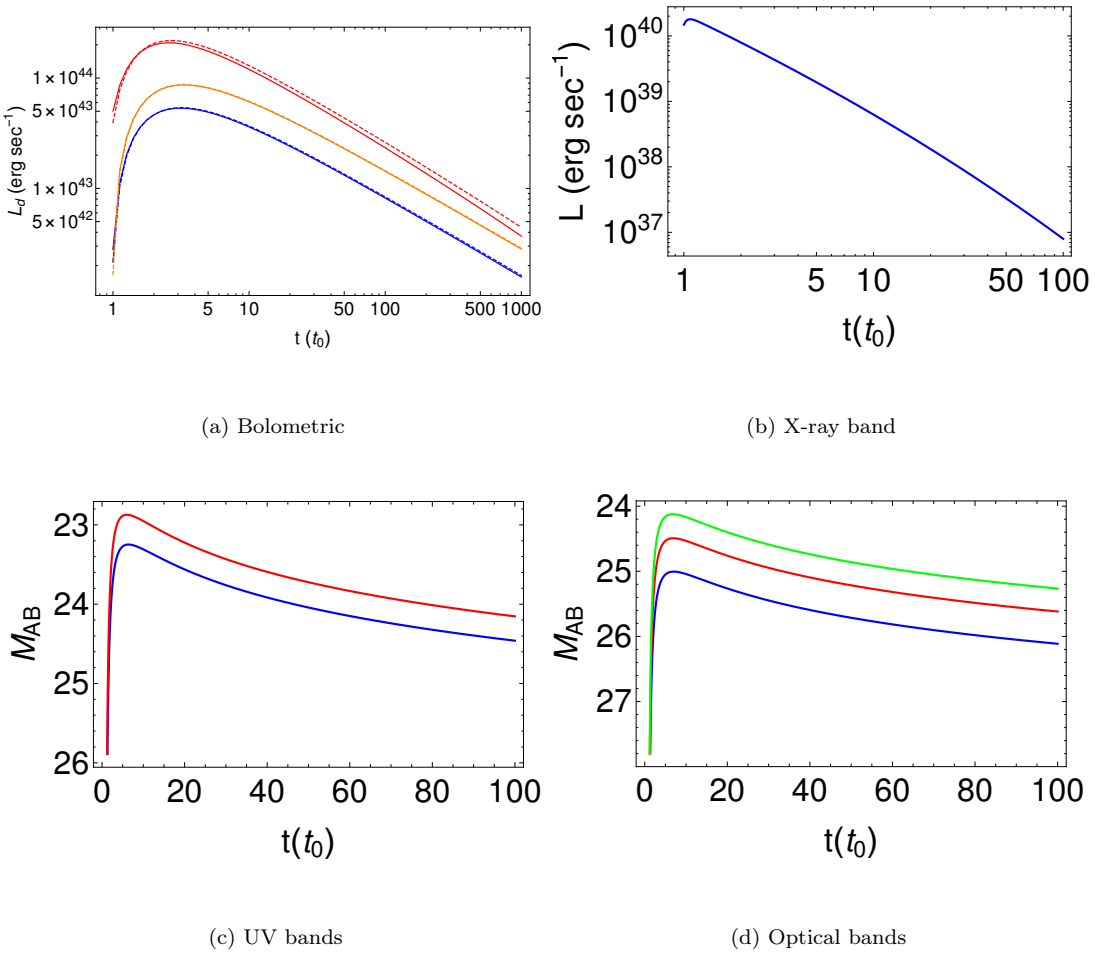

(a) Bolometric

(b) X-ray band

(c) UV bands

(d) Optical bands

FIGURE 6.8: (a) The bolometric luminosity (eqn 6.91) as a function of t for the set I1 (blue), I2 (orange), I3 (red), I5 (blue dashed), I6 (orange dashed) and I7 (red dashed). It is found that I1 is overlapping with I5 and I2 is overlapping with I6. The spectral luminosity simulated in various bands for the run I1 and redshift $z = 0.1$ for soft X-ray in (b), UV where Swift UVM2 (1800-3000 $A°$) (blue) and UVW2 (1500-2500 $A°$) (red) in (c) and optical in (d) where the curves for V band (blue), B Band (red) and U Band (green) are indicated.

Run	$\mathcal{W}_n$	t_0 (days)	$\Sigma_0(10^3$ g cm$^{-2})$	$r_0(R_s)$
I1	0.01	2.62	101.66	6
I2	0.01	4.68	797.94	6
I3	0.01	6.55	1.57	6
I4	0.1	3.21	1279.2	6
I5	0.01	2.62	204.25	4.23
I6	0.01	4.69	1603.2	4.23
I7	0.01	6.55	3.16	4.23
I8	0.1	3.21	2570.1	4.23

TABLE 6.6: The values of t_0, Σ_0 and r_0 for $\alpha = 0$ and $\delta_0 = 0.05$, obtained using equations given in Table 6.3 in units of $R_s = 2.9 \times 10^{11} M_6$ cm with $M_6 = 1$ for the super-Eddington radiative disk are given above.

which shows that the mass outflow rate dominates on the accretion by black hole which results in the decrease in disk mass.

The t_0 and Σ_0 values are shown in Fig 6.10 for model B. For higher m, the fallback rate of the debris is higher which results in the growth of the mass of the disk, enhanced surface density and viscous stress shortening t_0. The pressure in the disk is dominated by radiation because of the small value of β_g as shown in Fig 6.11. The Fig 6.12 shows the evolution of outer and inner radius obtained using eqn (6.88) and the radius decreases with j and α. The Fig 6.13 shows the evolution of $\dot{M}_a$, $\dot{M}_w$ and $\dot{M}_{fb}$. In the initial stages, the mass fallback rate dominates and as the time progresses, the mass loss due to wind dominates over accretion and fallback which results in the reduction in the mass of the disk as shown in Fig 6.14.

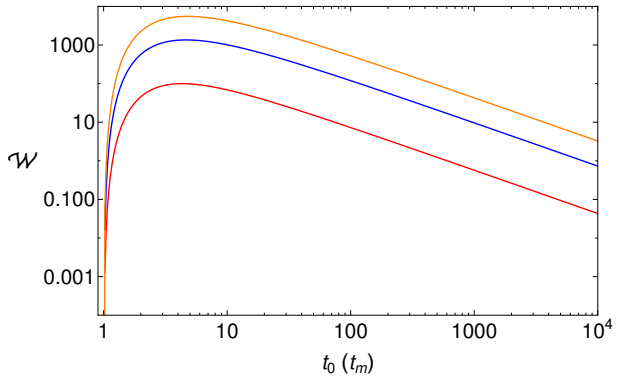

FIGURE 6.9: The $\mathcal{W}$ as a function of parameter t_0 in terms of t_m for the set I1 (blue), I2 (red) and I3 (orange) given in Table 6.4.

The outflowing wind also carries the angular momentum from the disk and the dominance of mass loss rate due to the wind later stages results in the reduction of disk angular momentum as shown in Fig 6.15.

In previous studies by Strubbe and Quataert (2009) and MM15, a spherical Eddington luminosity was assumed with Thompson opacity given by $L_E^s = 4\pi G M_\bullet c/\kappa = 1.48 \times 10^{44}\ M_6$ erg sec^{-1}, whereas we have considered a cylindrical geometry given by eqn (6.94) and L_E/L_E^s shown in Fig 6.16. The wind luminosity given by eqn (6.93) is shown in Fig 6.17 for various values of c_2 and it shows a cutoff for higher value of c_2, as expected.

The Fig 6.18 shows the bolometric luminosity obtained using eqn (6.91) and spectral luminosity in various spectral bands using eqn (6.96).

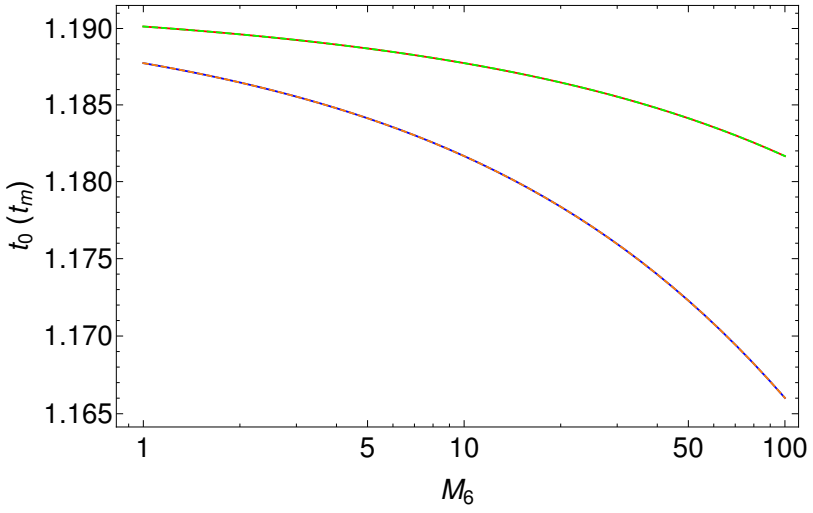

(a)

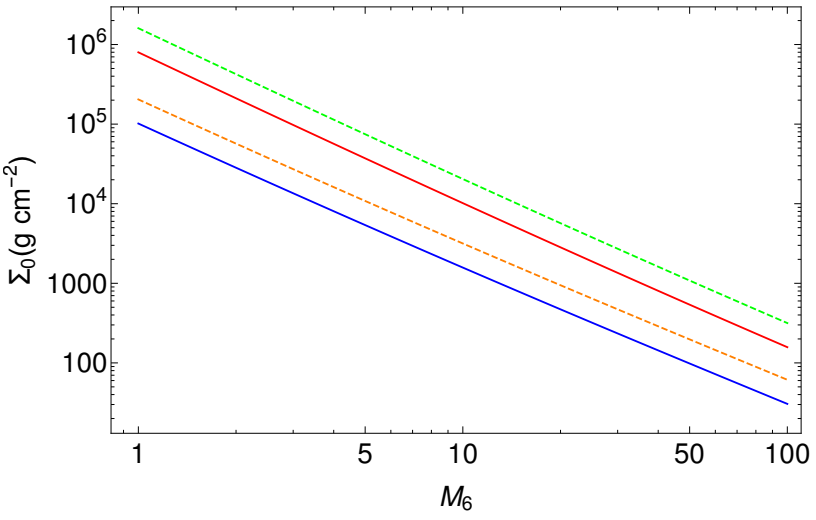

(b)

FIGURE 6.10: (a) The parameters t_0 in units of t_m and (b) Σ_0 as a function of M_6 with other parameters given in set I1 (blue), I2 (red), I5 (orange dashed) and I6 (green dashed). It is found that I1 is overlapping with I5 and I2 is overlapping with I6.

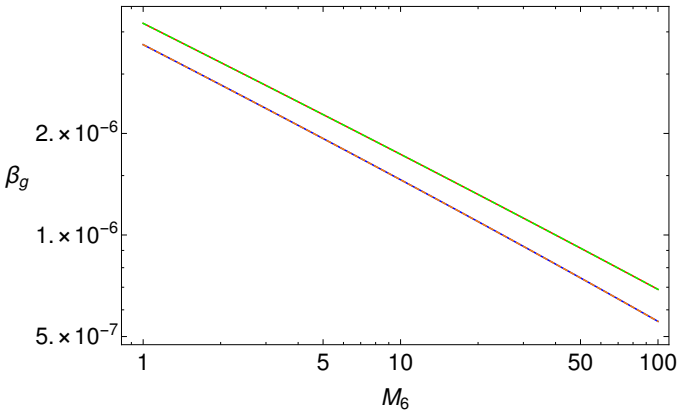

FIGURE 6.11: The value of β_g given in Table 6.3 is shown as a function of M_6 for the parameter sets I1 (blue), I2 (red), I5 (orange dashed) and I6 (green dashed) given in Table 6.4. It is found that I1 is overlapping with I5 and I2 is overlapping with I6.

6.6 Model T: Transition from super-Eddington radiative disk with wind to without wind

The luminosity in model B decreases with time and goes below the Eddington limit after a certain time when the wind shuts off. Since the wind shut off cannot be instantaneous, we consider that the disk transits from super-Eddington disk with wind to without wind when the wind luminosity $L_b^w = uL_b^d$, where u is the unknown parameter fixed through boundary conditions.

In case of the super-Eddington radiative disk without wind, the self similar solution is obtained by solving eqn (6.1) with $\dot{\Sigma}_w = 0$, so that the third term on LHS of eqn (6.82) is zero and $p(b-1)+d+e-2=0$ which gives

$$(\beta - \alpha p) - \frac{(p\ b + d + 2)(p\ b + d + e)}{2 - e} = 0, \tag{6.104}$$

and p can be obtained for a given β and α. From mass conservation given by eqn

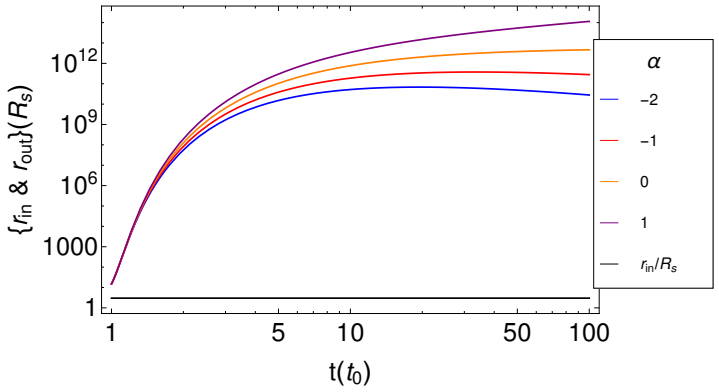

(a)

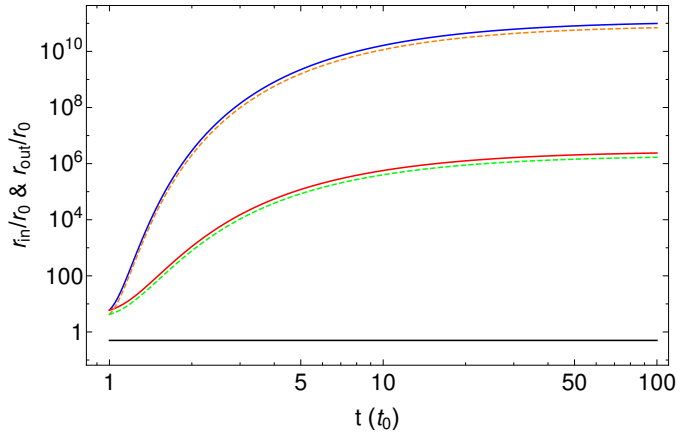

(b)

FIGURE 6.12: (a) The evolution of outer radius for set I1 with $e = 1$ and various values of α. (b) The evolution of outer radius with time for the set I1 (blue), I4 (red), I5 (orange dashed) and I8 (green dashed).

(6.88), we have $\beta + 2\alpha = -2/3$ and we take α as a free parameter to obtain β and p. The evolution of outer radius is given by eqn (6.88) with $\dot{M}_a$ given by eqn (6.86) and $\dot{M}_w$ given by eqn (6.87).

At the time of transition, the mass, bolometric luminosity and the derivative of the luminosity remain same. We denote the model B parameters as it is and the model T parameters with 1 as a subscript. The transition time is denoted by t_r for

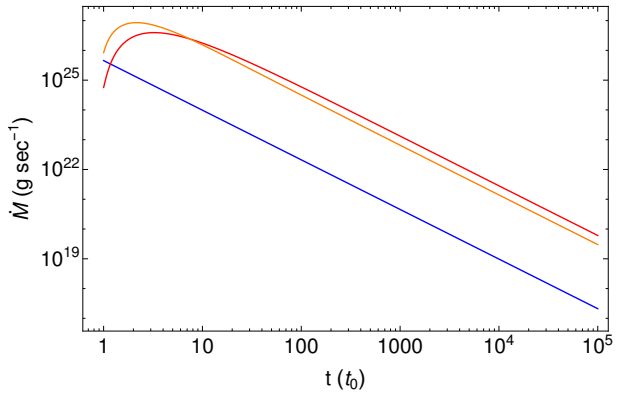

FIGURE 6.13: The accretion rate $\dot{M}_a$ (blue), mass fallback rate $\dot{M}_{fb}$ (orange) and wind outflow rate $\dot{M}_w$ (red) for super-Eddington disk with time for the run I1. At the late stage, the wind loss rate dominates over fallback rate and accretion rate which implies that the disk mass will decrease at late stages.

model B and $t_{r,1}$ for model T. The bolometric luminosity is below the Eddington luminosity for $t > t_r$.

We consider the edge radius r_{out} and r_{in} to be same during the transition and using eqn (6.84) for disk mass matching at the transition, we obtain

$$A_1 \frac{\Sigma_{0,1}}{r_{0,1}^{p_1}} \left(\frac{t_{r,1}}{t_{0,1}}\right)^{\beta_1-\alpha_1 p_1} = \frac{2+p_1}{2+p} A \frac{\Sigma_0}{r_0^p} \left(\frac{t_r}{t_0}\right)^{\beta-\alpha p} \left[\frac{r_{out}^{2+p} - r_{in}^{2+p}}{r_{out}^{2+p_1} - r_{in}^{2+p_1}}\right]. \tag{6.105}$$

The luminosity in model T is given by

$$L_{b,1} = A_1 \frac{\Sigma_{0,1}}{r_{0,1}^{p_1}} \left(\frac{t_{r,1}}{t_{0,1}}\right)^{\beta_1-\alpha_1 p_1} \frac{\Delta}{t_{r,1}}, \tag{6.106}$$

where Δ is given by

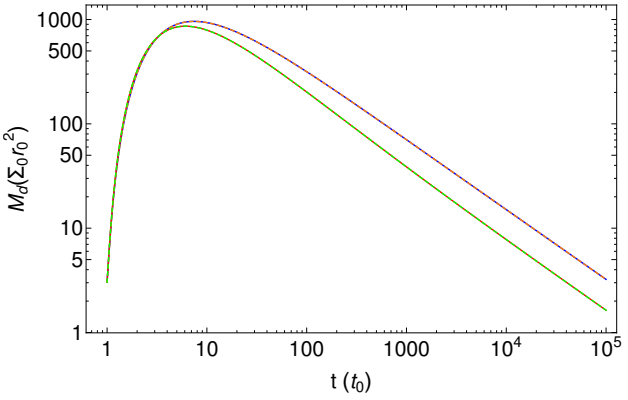

(a)

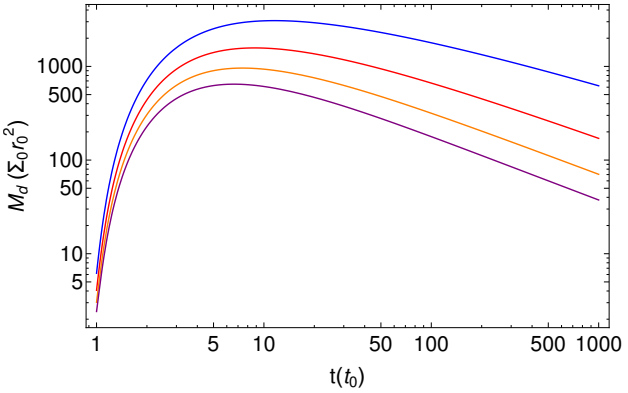

(b)

FIGURE 6.14: The mass evolution of super-Eddington disk with time for the set I1 (blue), I4 (red), I5 (orange dashed) and I8 (green dashed) in (a) and for various values of α= -2 (blue), -1 (red), 0 (orange) and 1 (purple) with $\delta_0 = 0.01$ for set I1 in (b) and the derived values of Σ_0 and r_0 are given in Table 6.6. It is found in (a) that I1 is overlapping with I5 and I4 is overlapping with I8. The mass decreases at late stages because the mass loss rate due to outflowing wind dominates over the mass fallback rate.

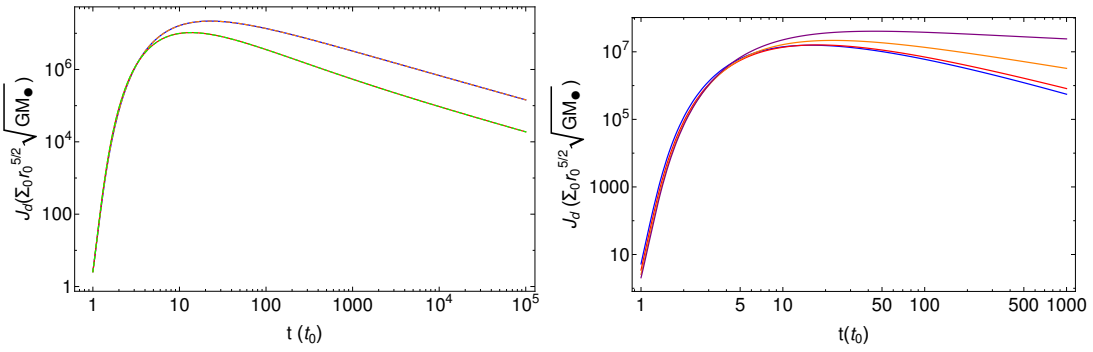

(a) (b)

FIGURE 6.15: The angular momentum evolution of super-Eddington disk for the set I1 (blue), I4 (red), I5 (orange dashed) and I8 (green dashed) in (a) and for various values of α= -2 (blue), -1 (red), 0 (orange) and 1 (purple) with $\delta_0 = 0.01$ for set I1 in (b) and the derived values of Σ_0 and r_0 are given in Table 6.6. It is found in (a) that I1 is overlapping with I5 and I4 is overlapping with I8.

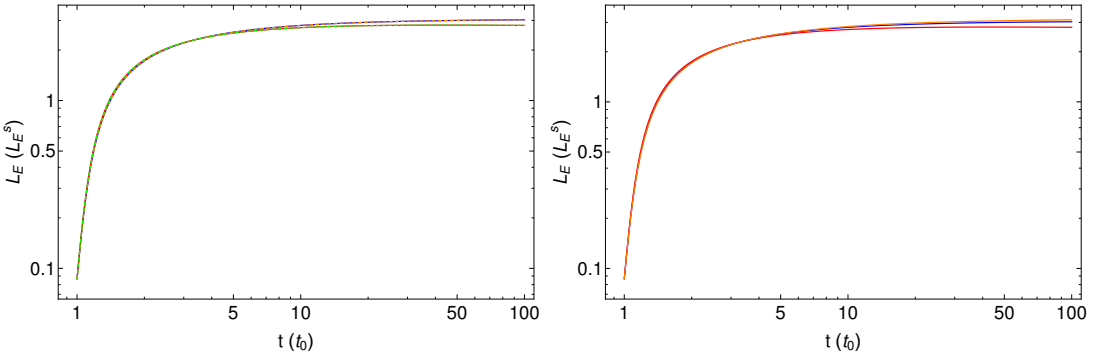

(a) (b)

FIGURE 6.16: The ratio of Eddington luminosity to the Eddington luminosity for spherical geometry $L_E^S = 1.48 \times 10^{44}\ M_6$ erg sec^{-1} for the set I1 (blue), I4 (red), I5 (orange dashed) and I7 (green dashed) in (a) and I1 (blue), I2 (red) and I3 (orange) in (b). It is found in (a) that I1 is overlapping with I5 and I4 is overlapping with I7.

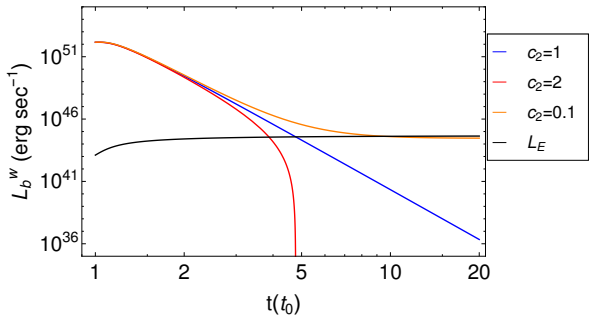

FIGURE 6.17: The wind luminosity as a function of time for the simulation I1 with various values of c_2.

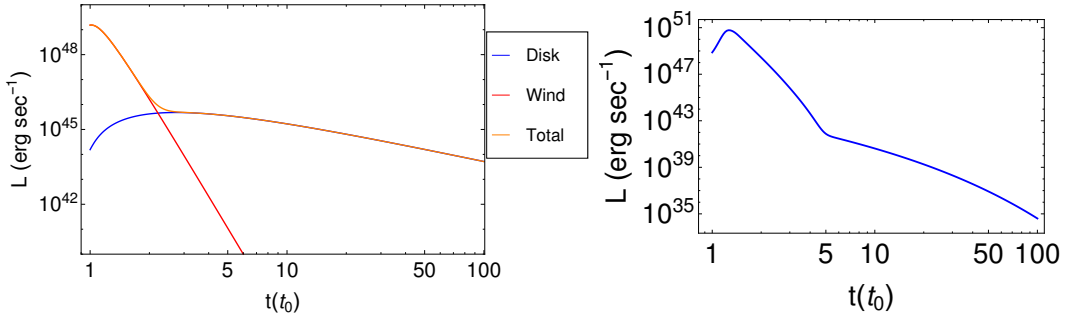

(a) Bolometric

(b) X-ray band

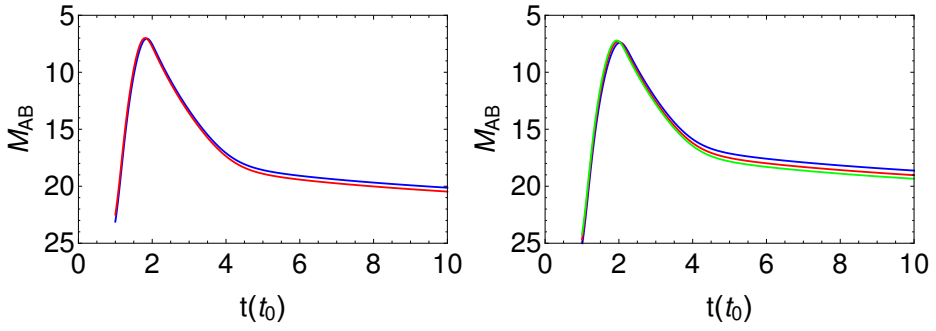

(c) UV bands

(d) Optical bands

FIGURE 6.18: (a) The bolometric disk luminosity, wind luminosity and total luminosity of super-Eddington disk are shown for the run I1, $c_2 = 1$ and $\chi = 10^9$. The spectral luminosity in various bands for redshift $z = 0.1$ for soft X-ray in (b), UV where Swift UVM2 (1800-3000 $A°$) (blue) and UVW2 (1500-2500 $A°$) (red) in (c) and optical in (d) where the curves for V band (blue), B Band (red) and U Band (green) are indicated.

$$\Delta = \frac{3\pi\chi_1^2}{4}\frac{r_{out}^{p_1-2(e_1-2)} - r_{in}^{p_1-2(e_1-2)}}{p_1 - 2(e_1-2)} - \frac{2\pi G M_\bullet}{2-e_1}\frac{p_1+4-e_1}{p_1+1}\left(r_{out}^{p_1+1} - r_{in}^{p_1+1}\right). \quad (6.107)$$

with $e_1 = 1 + \delta_{0,1}/2$. By matching the luminosity of the disk at the time of transition using eqn (6.91), we obtain

$$t_{r,1} = A_1 \frac{\Sigma_{0,1}}{r_{0,1}^{p_1}} \left(\frac{t_{r,1}}{t_{0,1}}\right)^{\beta_1 - \alpha_1 p_1} \frac{\Delta}{L_b}, \quad (6.108)$$

where L_b is given by eqn (6.91) for model B. In model B, the time is given by

$$\frac{t}{t_0} = \frac{t_0 + t_d}{t_0} = 1 + \frac{t_d}{t_0}, \quad (6.109)$$

where t_d is the time parameter assuming that the dynamics of accretion disk starts at t_0, whereas for super-Eddington disk without wind, the time is given by

$$\frac{t_1}{t_{0,1}} = \frac{t_{0,1} + t_{d,1}}{t_{0,1}} = 1 + \frac{t_{d,1}}{t_{0,1}}. \quad (6.110)$$

The difference in the timescale of both disks is given by $\Delta t = t_0 + t_d - t_{0,1} - t_{d,1}$ which reduces to $t_{0,1} + t_{d,1} = t_0 + t_d - \Delta t$ where $\Delta t = t_r - t_{r,1}$. Thus the time in model T is given by

$$\frac{t_1}{t_{0,1}} = \left(1 + \frac{t_d - \Delta t}{t_0}\right) \frac{t_0}{t_{0,1}}. \tag{6.111}$$

We find the net luminosity of the disk to be given by

$$L_b = \begin{cases} L_b^B(x_d) & x_d \leq x_r - 1 \\ L_b^T \left(\left(1 + \frac{x_d t_0 - \Delta t}{t_0}\right) \frac{t_0}{t_{0,1}}\right) & x_d > x_r - 1 \end{cases} \tag{6.112}$$

where $x_d = t_d/t_0$, L_b^B and L_b^T are given by eqn (6.91) for model B and model T respectively.

The Fig 6.19 shows the evolution of the disk mass and outer radius including both model B and model T. The transition time is decided by the parameter $u = L_w/L_d$ and increases with u. It can be seen that the transition is smoother for a smaller value of u because the luminosity is dominated by the disk. The derivative of the bolometric luminosity with respect to t_d is matched at the transition to obtain the parameter u which is then used to obtain the net luminosity profile.

The Fig 6.20 shows the bolometric luminosity and spectral luminosity in various bands. In the next sections, we discuss the fits of our accretion model to the observations.

6.7 Discussion

We have constructed a self-similar model of the time-dependent and nonrelativistic accretion disk with fallback from disrupted debris and viscosity prescription $\Pi_{r\phi} = K\Sigma_d^b r^d$ and derived b and d for an assumed pressure and density structure of

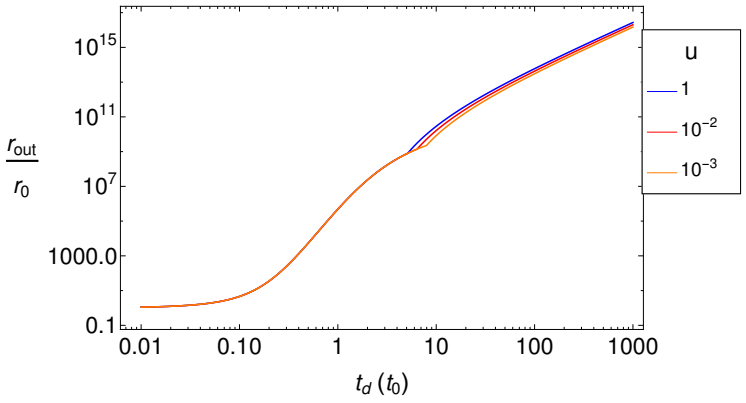

(a)

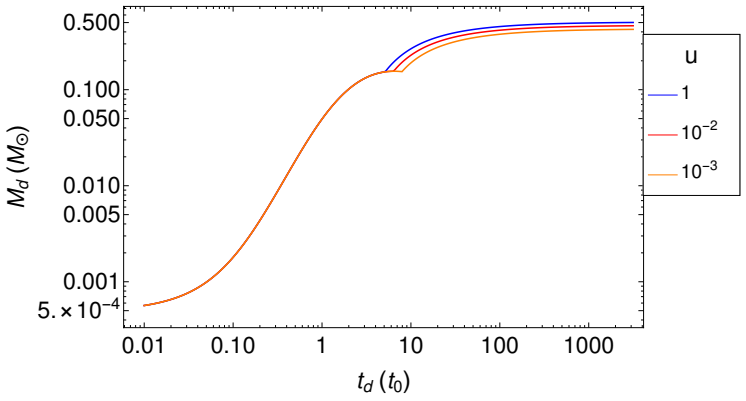

(b)

FIGURE 6.19: The outer radius (a) and the mass (b) are shown as a function of time for set I1, $c_2 = 1$, $\alpha = \alpha_1 = 0$ and $\delta_0 = \delta_{0,1} = 0.05$ where r_0 and t_0 are parameters for model B. The transition time decreases with $u = L_w/L_d$ and transition is smoother for lower value of u.

the disk. We have considered four models which include the α viscosity sub-Eddington, the radiative viscosity sub-Eddington, the α viscosity super-Eddington and the radiative viscosity super-Eddington. The sub-Eddington radiative disk has a strong radiative pressure which results in an extended disk and the thin disk approximation is no longer valid, but our disk structure for super-Eddington disk holds instead. We further found that the super-Eddington α disk does not have consistent solutions and thus we are left with two types of accretion disks which

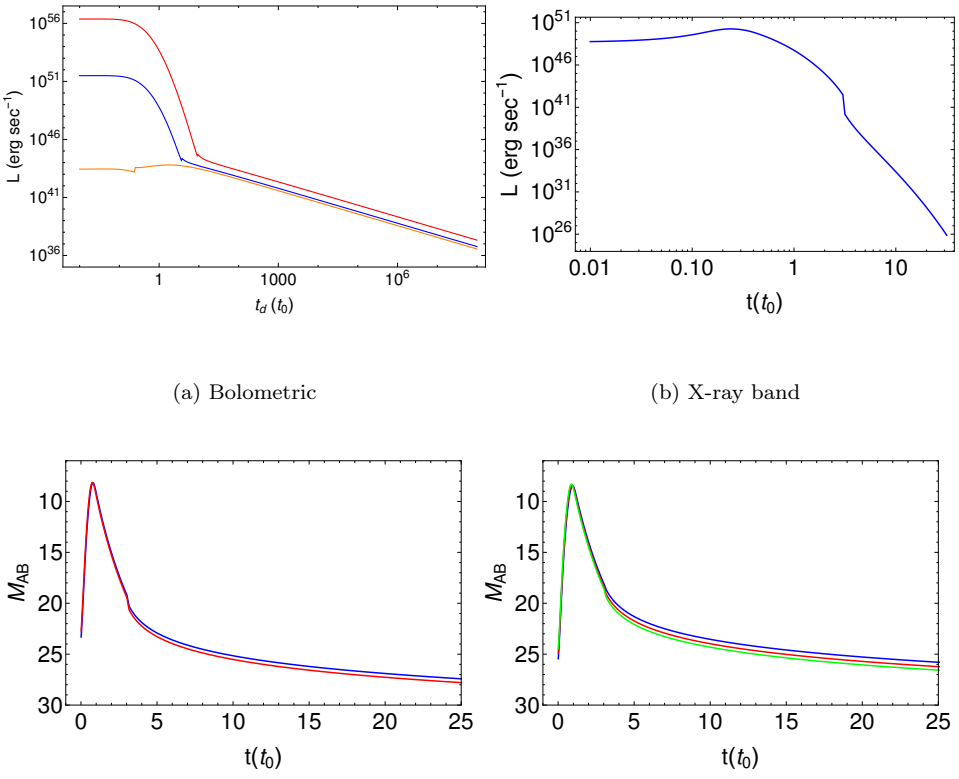

(a) Bolometric

(b) X-ray band

(c) UV bands

(d) Optical bands

FIGURE 6.20: (a) The bolometric disk luminosity for set I1 (blue), I2 (red) and I3 (orange) for $\alpha = \alpha_1 = 0$ and $\delta_0 = \delta_{0,1} = 0.05$. For I1, the spectral luminosity simulated in soft X-ray in (b), UV where Swift UVM2 (1800-3000 $A°$) (blue) and UVW2 (1500-2500 $A°$) (red) in (c) and optical in (d) where the curves for V band (blue), B Band (red) and U Band (green) are indicated.

are α viscosity sub-Eddington (model A) and radiative viscosity super-Eddington with wind (model B). When the luminosity in model B goes below the Eddington luminosity, the disk should transit from model B to model A and the viscosity transits from radiative to α which has a lower Q^+. Thus we conclude that the model B transits to model T and then to model A at late times. The evolutionary track of a super-Eddington disk is given in Fig 6.21.

Shen and Matzner (2014) considered the surface density of out flowing wind $\dot{\Sigma}_w \propto \Sigma_d\ \nu/r^2 \propto \Sigma_d\ r^{-3/2}$, which is derived on the basis that for non-radiative

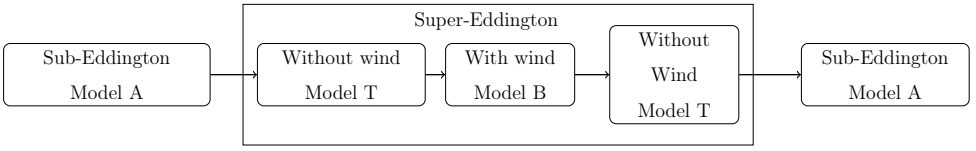

FIGURE 6.21: The evolutionary track of super-Eddington TDEs. The sub-Eddington TDEs will have a single phase which can be fit by model A. The dynamics in the individual phases and the transition between them decide the light curve profiles.

advective disks the steady accretion rate is $\dot{M}_a \propto r^s$, where s is constant. We have modeled the super-Eddington disk (model B) with the radiative structure and following vertical momentum equation obtained the surface density of the wind $\dot{\Sigma}_w \propto r^{-7/4}(t/t_0)^\delta$ where $\delta = -5/3$. Strubbe and Quataert (2009) have developed the wind structure using spherical geometry and fraction of out flowing mass constant. Dotan and Shaviv (2011) using their porous model with steady accretion disk obtained the fraction of outflow $f_{out} = \dot{M}_w/\dot{M}_a$, numerically which is approximated by a formula in MM15 of the form $f_{out} = (2/\pi)\arctan\left[(1/4.5)(\dot{M}_a/\dot{M}_E - 1)\right]$ where $\dot{M}_E$ is the Eddington mass accretion rate given by $L_E^S/(\eta c^2)$ and η is radiative efficiency. In model B, the f_{out} is the function of edge radius ξ_{out} and ξ_{in} as shown in eqn (6.103) and grows as $\xi_{out}/\xi_{in} = r_{out}/r_{in}$ evolves. Thus the mass loss rate by outflows is higher than that of accretion and is even higher than the fallback rate as shown in Fig 6.13 which results in reduction in disk mass at late times as shown in Fig 6.14.

For a system with radiation $P_r = (1/3)aT^4$ and gas pressure $P_g = (R/V)T$, where R is the gas constant, V is the volume and T is the temperature, the first law of thermodynamics gives (Chandrasekhar 1939)

$$\mathrm{d}Q = \frac{V}{T}\left(12P_r + \frac{1}{\Gamma - 1}\right)\mathrm{d}T + (4P_r + P_g)\,\mathrm{d}V, \tag{6.113}$$

where $\Gamma = c_p/c_v$, $c_v = \mathrm{d}Q/\mathrm{d}T|_{\text{constant V}}$ and $c_p = \mathrm{d}Q/\mathrm{d}T|_{\text{constant P}}$ with $P = P_r + P_g$ as total pressure. Following our assumption $P_g = \beta_g P$ with constant β_g and using eqn (6.113), we obtained $P \propto \rho^\gamma$ where γ is given by (Chandrasekhar 1939)

$$\gamma = \frac{\beta_g(\frac{C}{R} - \frac{\Gamma}{\Gamma-1}) - 16(1-\beta_g)}{\beta_g(\frac{C}{R} - \frac{1}{\Gamma-1}) - 12(1-\beta_g)}, \tag{6.114}$$

where $C = \mathrm{d}Q/\mathrm{d}T$ is constant. For $\beta_g \ll 1$ (which is true in our radiation dominated model B; see Fig 6.11), $\gamma \approx 4/3$ ($\lim_{\beta_g \to 0} \gamma = 4/3$) which validates our assumption.

Strubbe and Quataert (2009) have taken the edge radius of the disk to be steady with an inner radius as r_{ISCO} and outer radius to be circularization radius $\sim 2\ r_p$. The self-similar model by Mangalam (2001) and Cannizzo *et al.* (1990) for sub-Eddington disks have shown that the outer radius increases with time as $r_{out} \propto t^{3/8}$. We have used the mass conservation to derive the evolution of outer radius r_{out} which increases with time for both super and sub-Eddington disks. The evolution of outer radius is faster for model B due to a smaller timescale of accretion t_0.

The mass and angular momentum of the disk in Model A enhances at late stages whereas it diminishes for model B because of the wind outflow rate which dominates at late times. The previous studies have taken the spherical Eddington luminosity $L_E^S = 1.48 \times 10^{44}\ M_6$ erg sec^{-1} and the disk is considered to be sub-Eddington if the luminosity is less than the L_E^S. The wind is launched if photosphere temperature is higher than the Eddington temperature which is derived using vertical momentum equation given by eqn (6.26) and the Eddington luminosity can exceed the spherical Eddington value at late times. Therefore Eddington temperature is useful in defining the wind structure locally and we have assumed the ratio T_{ph}/T_E to be the function of time alone so that the entire disk is super-Eddington with wind as seen in eqn (6.31).

We have considered that the fallback debris forms a seed disk which evolves due to mass loss due to accretion by the black hole and the out flowing wind and mass gain through fallback debris assuming that the self-similar structure of accretion disk remains same. If the matter enters at the outer radius, this induces a high density at the outer radius which results in a jump in the self-similar structure at the outer radius. We have assumed that the added matter is quickly distributed in the disk since the disk evolutionary time scale is longer than the accretion time scale.

The bolometric luminosity of the model A is given by $L_b \propto t^{-1}(\xi_{out}^{3/4} - \xi_{in}^{3/4})$ (see eqn 6.91) and the net bolometric luminosity at late time is found to be $L_b \propto t^{-0.7}$. Cannizzo *et al.* (1990) obtained the bolometric luminosity of the sub-Eddington accretion disk without fallback and constant edges radius to be $L_b \propto t^{-1.9}$ which is similar to our result if we consider the ξ_{out} and ξ_{in} to be constant. Strubbe and Quataert (2009) and Lodato and Rossi (2011) have assumed the accretion rate to be $\dot{M} \propto t^{-5/3}$ and for sub-Eddington disk without fallback and constant outer edge radius, they found $L_b \propto \dot{M} \propto t^{-5/3}$ and for super-Eddington disk with slim disk structure, they obtained the bolometric luminosity from out flowing wind as $L_b \propto t^{-5/9}$ and from the disk as $L_b \propto t^{-5/3}$. Montesinos Armijo and de Freitas Pacheco (2011) performed the numerical simulation of an accretion disk without wind with edge radius constant and showed that the bolometric luminosity evolves as $L_b \propto t^{-5/3}$ at late stages.

The bolometric disk luminosity for model B is $L_b^d \propto t^{-5/3+(3-2e)\alpha}(\xi_{out}^{9/4-2e} - \xi_{in}^{9/4-2e})$ and the outflow luminosity $L_b^w \propto (\mathcal{W}^2(t/t_0)^{(-10/3-\alpha/2)}+1-c_2)^4 \ln(r_{out}/r_{in})$ where α, e and c_2 are considered to be a free parameters. From Fig 6.18, we can see that the bolometric luminosity decreases with time and we found that if the disk transits from model B to model A, there is a huge drop in the luminosity of the disk. This is because a radiation pressure dominated disk with wind cannot instantaneously change to a gas pressure dominated disk with no outflow.

The super-Eddington model B is two-dimensional as the density and the temperature of the disk are functions of r and z. We have also used the vertical momentum equation to obtain the velocity of the outflow that occurs at the photosphere z_{ph}, where the luminosity is calculated. Our simplistic semi-analytic model of the super-Eddington disk which includes the fallback $\dot{M}_{fb}$, accretion $\dot{M}_a$, and outflow $\dot{M}_w$, is able to produce reasonable fits to the observations as compared to earlier steady accretion models. A more general multi-dimensional model with a detailed radiative transfer which entails intensive high-performance computing will be taken up in the future. However, we expect a multi-dimensional model of the disk to have a structure similar to our models.

6.8 Summary

We have constructed the self-similar models of the time-dependent and non-relativistic accretion disk in both sub and super-Eddington disk with fallback from disrupted debris. We have obtained the following results.

- The self similar parameters $\{\beta,\ \alpha,\ p,\ \Sigma_0,\ t_0,\ r_0\}$ obtained for models A and B are given in Table 6.3.
- The parameter t_0 is smaller in model B (Fig 6.4) compared to model A (Fig 6.10). This implies that the accretion process starts earlier in a super-Eddington disk.
- Using the mass conservation equation, we have found that the outer radius increases for a super-Eddington model (model B) as both the accretion rate and the wind outflow decreases with time whereas the outer radius increases initially and then decreases for the sub-Eddington disk (model A) as the accretion rate increases and dominates over fallback at late times.

- The disk mass in models A and B increases initially and decreases as accretion rate dominates over the mass fallback rate at late times in model A, whereas the mass outflow rate dominates over the fallback rate in model B.

- The angular momentum as shown in Fig 6.7 for model A and in Fig 6.15 for model B increases initially and decreases at late stages due to the dominance of outflow rate.

- The bolometric luminosity of the model A is given by $L_b \propto t^{-1}(\xi_{out}^{3/4} - \xi_{in}^{3/4})$ (see eqn 6.91) and the net bolometric luminosity at late time is found to be $L_b \propto t^{-0.7}$. The bolometric disk luminosity for model B is $L_b^d \propto t^{-5/3+(3-2e)\alpha}(\xi_{out}^{9/4-2e} - \xi_{in}^{9/4-2e})$ and the outflow luminosity
$L_b^w \propto (\mathcal{W}^2(t/t_0)^{(-10/3-\alpha/2)} + 1 - c_2)^4 \ln(r_{out}/r_{in})$ where α, e and c_2 are considered to be a free parameters which are obtained by fit to the observations.

- We found that there is a huge drop in the luminosity if the disk transits from model B to model A and this is because the viscosity transits from radiative to α viscosity; we model transition from model B to model T by taking $L_b^w = uL_b^d$ and then to model A at later time.

- We have fit our time-dependent accretion model to the X-ray observations of XMMSL1 J061927.1-655311 and SDSS J120136.02+300305.5 as shown in Fig 7.2, in optical and UV observations of PS1-10jh as shown in Fig 7.3 and X-ray observations of Swift J1644+57 in Fig 7.4. We have also compared our time-dependent accretion models A and B with steady accretion models C and D of MM15 and found that the models A and B give a good fit to the observations. The best fit physical parameters to the observations are shown in Table 7.1 and 7.2.

6.9 Conclusions

We have been able to construct TDE light curves in both super-Eddington and sub-Eddington regimes by demonstrating that our models A and B are viable.

1. There is likely to be an α viscous sub-Eddington disk which would be operative during the rising phase. The typical time scale of this phase will be given by either the typical rise time in the $\dot{M}$ profile or the time taken to reach the Eddington luminosity.

2. If there is a super-Eddington phase to follow as determined by eqn (6.10), then the typical time scale would be given by eqn (6.65). The super-Eddington disk will be effected by radiative viscosity with a wind launched from the photosphere. During the onset and the decline of this super-Eddington phase, the wind is rendered weak in our models and we have illustrated in §6.6 a method of calculating this transition through model T so that the light curves smoothly connect to the sub-Eddington regimes.

3. The TDE physics we have employed includes all the essentials of accretion, fall back, and the wind; we have presented hydrodynamic criteria for the operation of the wind with $v_z^2 \propto (T - T_E)$ given by eqn (6.26). We have demonstrated in §6.2 that the timescales of evolution and magnitude of the bolometric luminosity are in good agreement with typical observed values.

4. While our time-dependent models are reasonably successful in producing fits to the four diverse TDE sources chosen here, we plan on producing fits to a larger sample of light curves available in the literature with a higher resolution search in parameter space. In the fits produced thus far, we have been able to extract the mass of the star and its orbital elements, the black hole

mass, and the initial accretion disk radius. The parameter search was limited by numerical resources; in the future, we plan on doing more extensive simulations.

5. The basic paradigm is sufficiently elaborate in terms of essential physics; it also transparently and adequately demonstrates the existence of two different phases with a transition model that produces reasonably good fits. In the future, we plan to add an atmosphere to predict the details of the spectrum.

6. One can with a large statistics of detection that will soon become available, infer the basic parameters using our models and study the demographics of the black hole mass and stellar properties such as mass and evolutionary state as a function of redshift (Kochanek 2016,Stone and Metzger 2016).

7. It is also desirable and possible in the future to add black hole spin and mass evolution to predict the jet phase.

Chapter 7

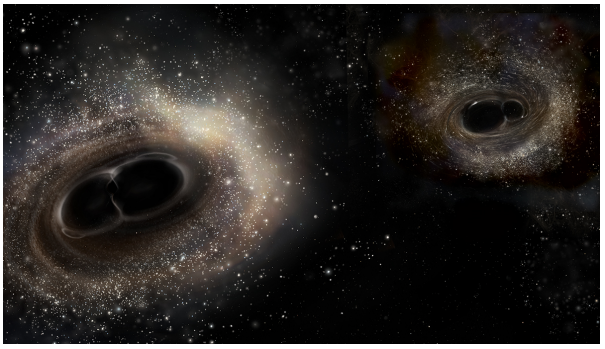

Image: LIGO/A. Simonnet.

Demographics of black holes derived from TDE model fits to observations

7.1 Fit to observations

In this chapter, we have fit the time-dependent accretion models A and B developed in chapter 6 to the observed TDEs and derive the physical parameters such as dimensionless orbital energy $\bar{e}$ and angular momentum ℓ, star mass m, black hole mass M_6, q and δt, where δt is the shift in time t to the light curves considering the starting time of accretion to be $t = t_0$. We first fit model A to the observations to obtain the physical parameters and then compare the bolometric luminosity obtained using the derived physical parameters with the Eddington luminosity. If the bolometric luminosity is less than the Eddington luminosity, the disk is sub-Eddington and we obtain the required parameters. If not, we fit

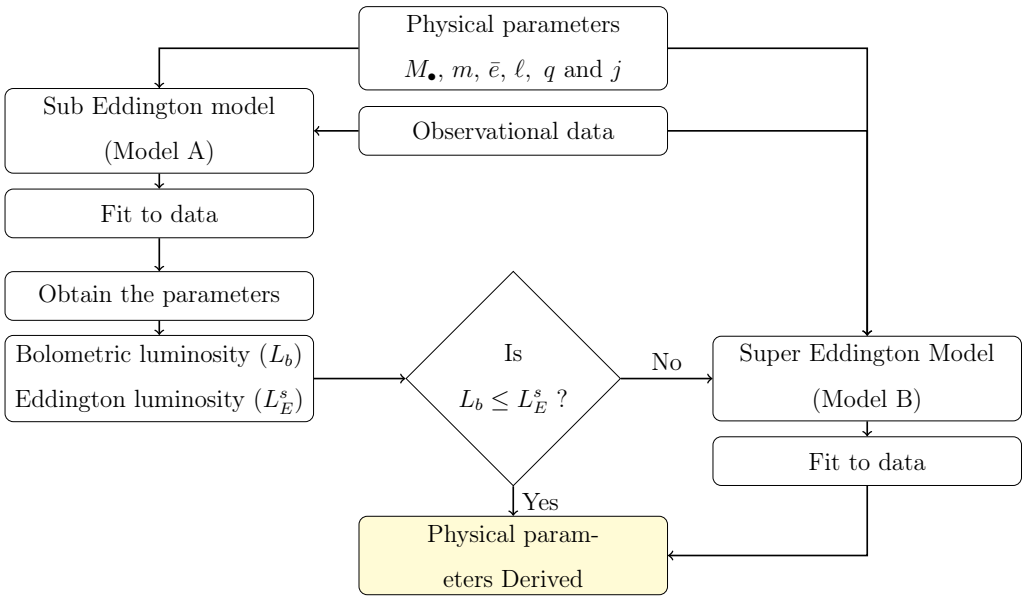

FIGURE 7.1: The flow chart of the procedure we have adopted in fitting the model to the observations.

model B to obtain the physical parameters. The Fig 7.1 shows the flowchart of the procedure adopted in fitting the model to the observational data.

In MM15, we have developed a steady accretion model with edge radii constant and this model is based on a slim disk model given in Strubbe and Quataert (2009) with accretion rate following the eqn (5.55) as shown in Table 4.3. We have compared the fits given by models C and D with that of our time-dependent accretion models given by models A and B as shown in Table 6.2.

The Fig 7.2 shows models B and C fit to the X-ray observations of XMMSL1 J061927.1-655311 and SDSS J120136.02+300305.5 whereas Fig 7.3 and Fig 7.4 show the model B and D fit to the PS1-10jh observations in optical and UV bands and Swift J1644+57 observations in X-ray band. Our time-dependent model gives a better fit to the observations as compared to the steady accretion models. The physical parameters obtained through the best fits are α, δ_0, $\bar{e}$, ℓ, M_6, m, q, $\mathcal{W}_n$ and δt. They are shown in Table 7.1 for model B and C fits to the X-ray observations of XMMSL1 J061927.1-655311 and SDSS J120136.02+300305.5 and in

Model	Observation	Band	α	$\bar{e}$	ℓ	M_6	m	q	j	w_n	c_2	δt (days)	χ_s
B	XMMSL1 J061927.1-655311	X-ray	0	0.001	1	8	8.3	5	0.5	0.44	0.1	200	1.6
C	XMMSL1 J061927.1-655311	X-ray	–	0.00001	1	2.5	1	–	0.4	–	–	20	2.8
B	SDSS J120136.02+300305.5	X-ray	0	0.001	1	7	8.3	5	0.6	0.425	0.1	180	1.94
C	SDSS J120136.02+300305.5	X-ray	–	0.00021	1	6.8	2.15	–	0.5	–	–	5	2.93

TABLE 7.1: The physical parameters obtained from reduced chi-square χ^2_s fit of models B and C to the observations with a time shift of δt, mass of star m, star's initial dimensionless energy $\bar{e}$, angular momentum ℓ, and black hole mass M_6 and spin j along with the χ_s values are shown.

Table, 7.2 for model B and D fit to the PS1-10jh observations in optical and UV and Swift J1644+57 observations in X-rays.

Fig 7.11 show the distribution of black hole mass and star mass in redshift obtained from the time-dependent model fit to the observations. The TDEs are dominated by the disruption of a low mass star by low mass supermassive black holes.

For disruption of a solar mass star, the energy released $E_{rad} \propto M_\bullet^{-0.4}$ obtained using thin disk model and is shown in Fig 7.12. The capture of TDEs in the initial phase is crucial to understand the initial dynamics of TDEs and the bolometric peak luminosity is a function of black hole mass and star mass. From §5.3, the mass fallback rate is approximated by

$$\dot{M}_{fb} = \frac{2}{3}\frac{M_\star}{t_m}(1+x_\ell)(-0.0175\ x^2 + 0.0175\ \mathrm{Exp}[-4.216(x^2-1)])\tau^{-\frac{5}{3}}, \qquad (7.1)$$

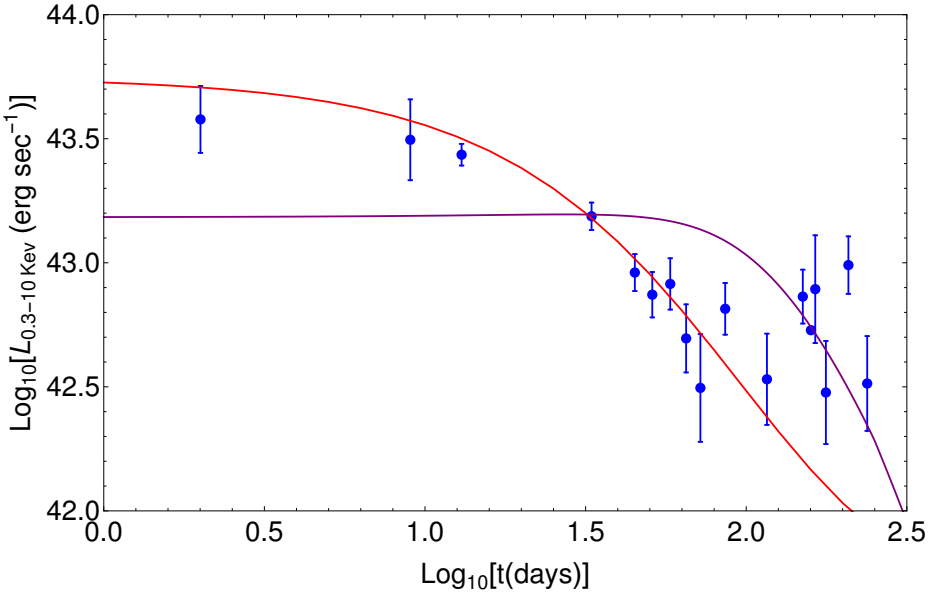

(a)

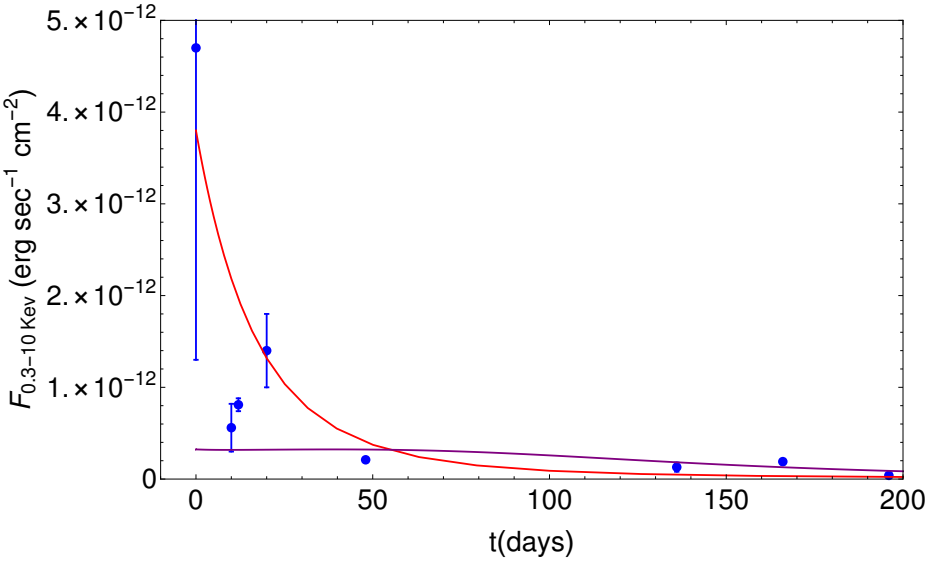

(b)

FIGURE 7.2: The model B (red) without transition and model C (purple) fits to the X-ray observations of XMMSL1 J061927.1-655311 (top) Saxton *et al.* (2014) and SDSS J120136.02+300305.5 (bottom) Saxton *et al.* (2012). The derived parameters are given in Table 7.1.

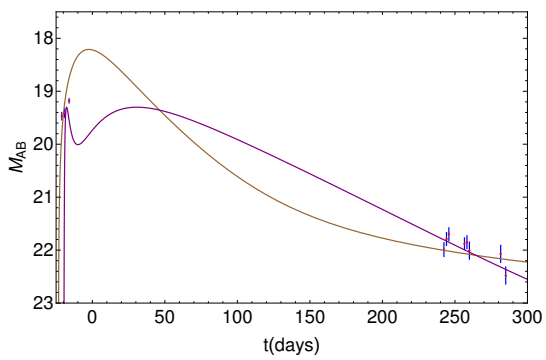

(a) Nuv band

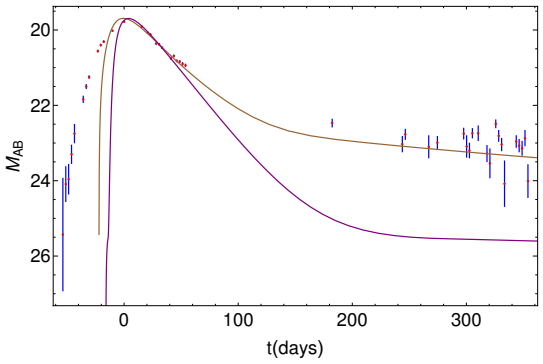

(b) g band

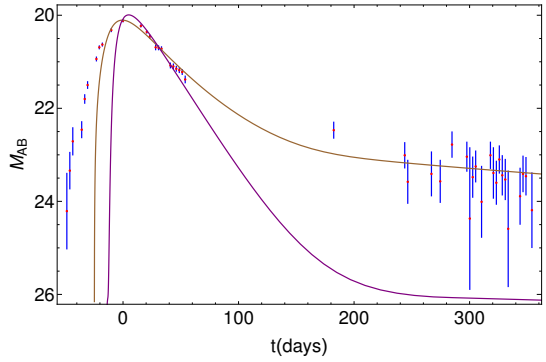

(c) r band

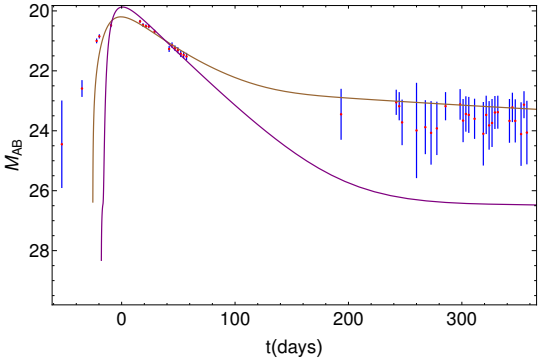

(d) i band

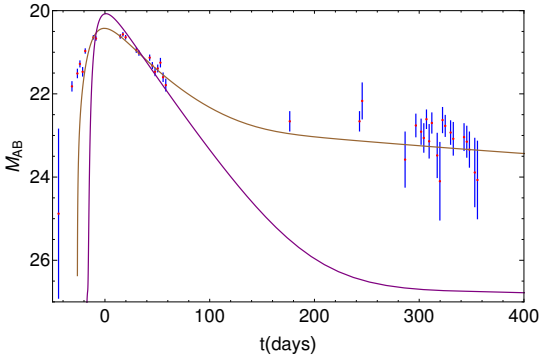

(e) z band

FIGURE 7.3: The model B (brown) without transition and model D (purple) fit to the PS1-10jh observations (Gezari *et al.* 2012) and the deduced parameters are given in Table 7.2.

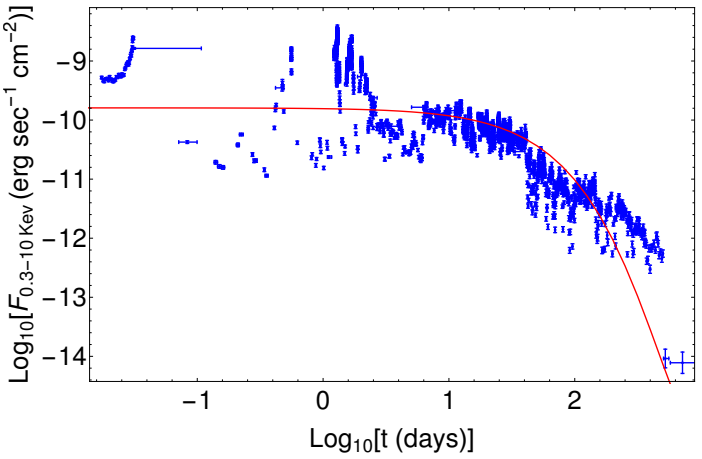

FIGURE 7.4: The model B without transition fit to the X-ray observation of Swift J1644+57 (Burrows *et al.* 2011) and model D is not able to fit the observation.

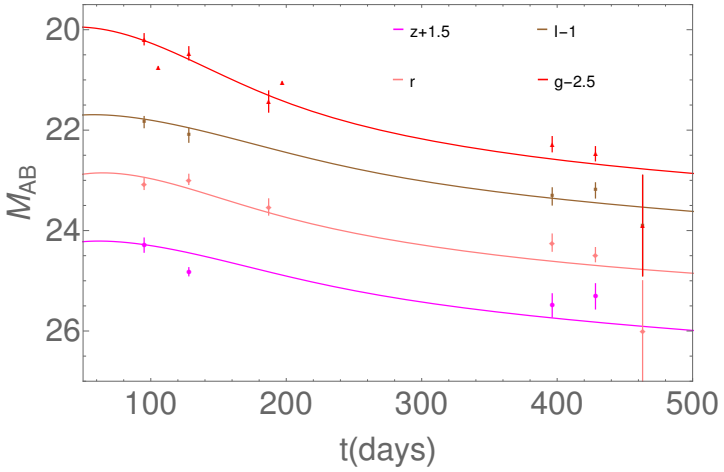

FIGURE 7.5: The time-dependent model fit to the observations Swift J2058+0516 in X-ray band.

where $\tau = t/t_m$, $x = x_\ell - \tau^{-2/3}(1+x_\ell)$ and t_m is time period of inner bound debris given by

$$t_m = 0.041 \text{ days } \; m^{0.7}\bar{e}^{-\frac{3}{2}}\left[1+\frac{1}{x_\ell}\right]^{-\frac{3}{2}}, \tag{7.2}$$

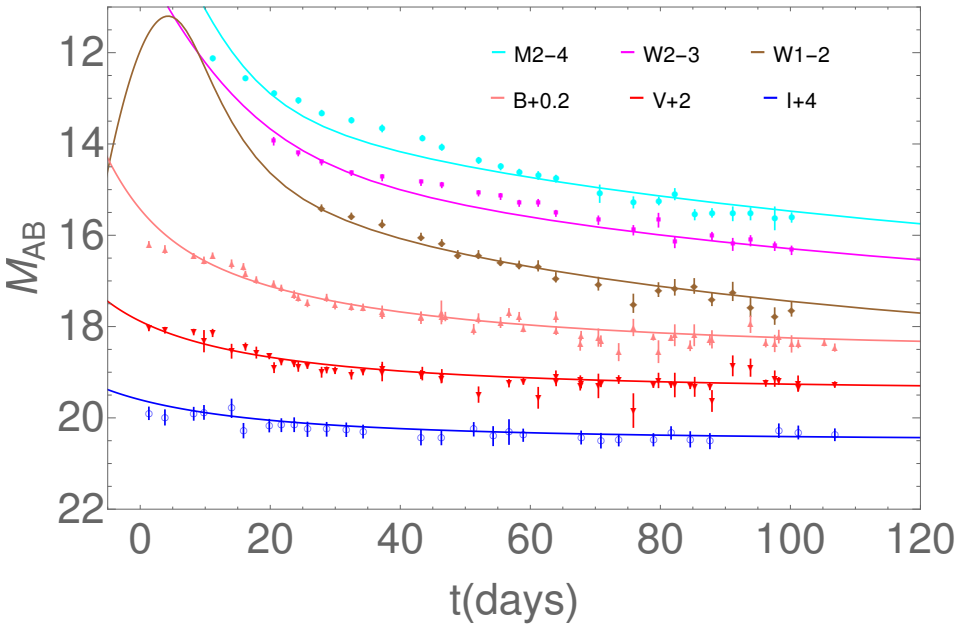

(a) ASAS-SN 15oi

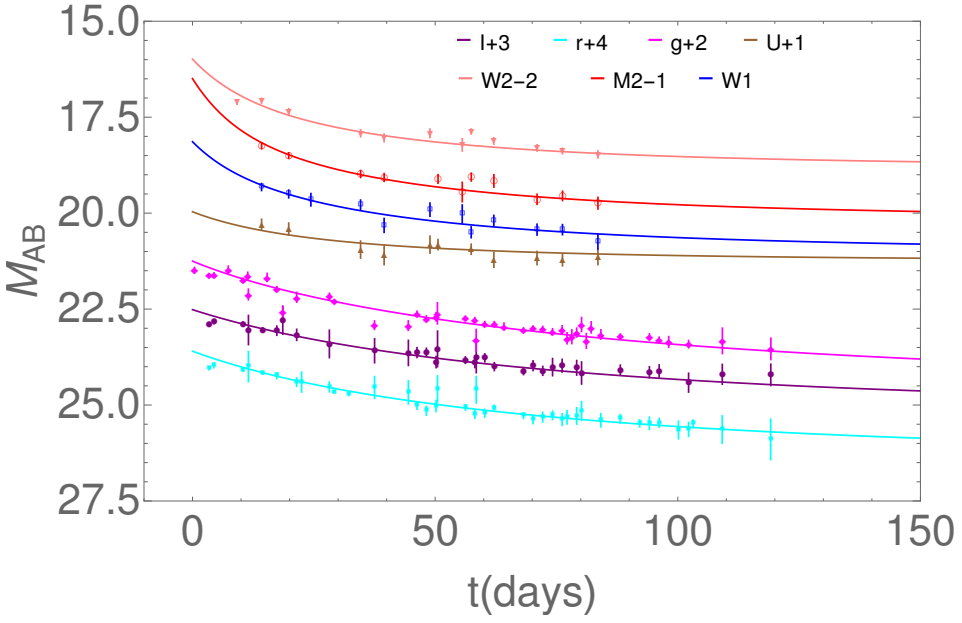

(b) iPTF16axa

FIGURE 7.6: The time-dependent model fit to the observations ASAS-SN 15oi (top) and iPTF16axa (bottom).

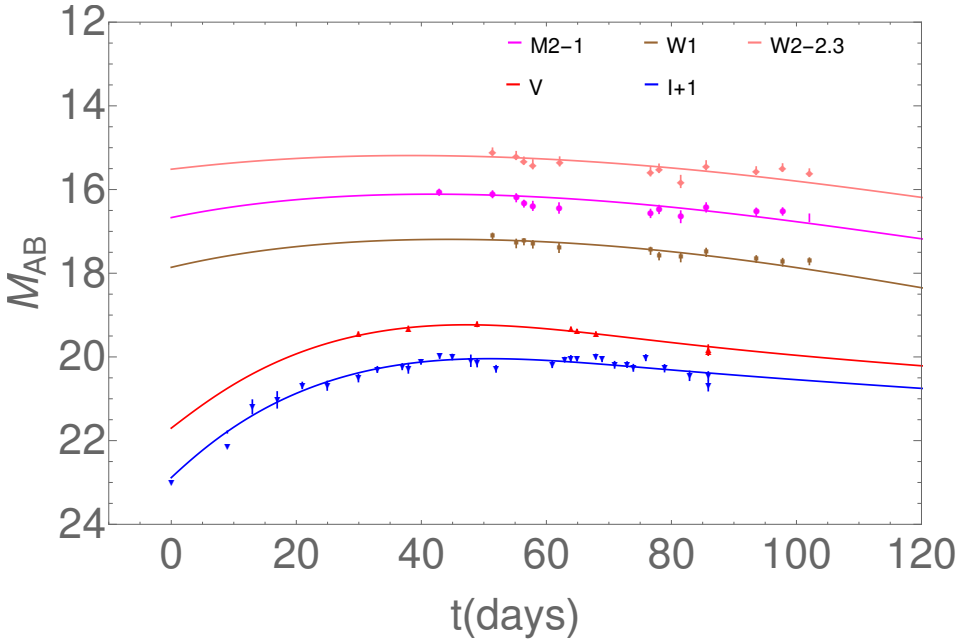

(a) OGLE16aaa

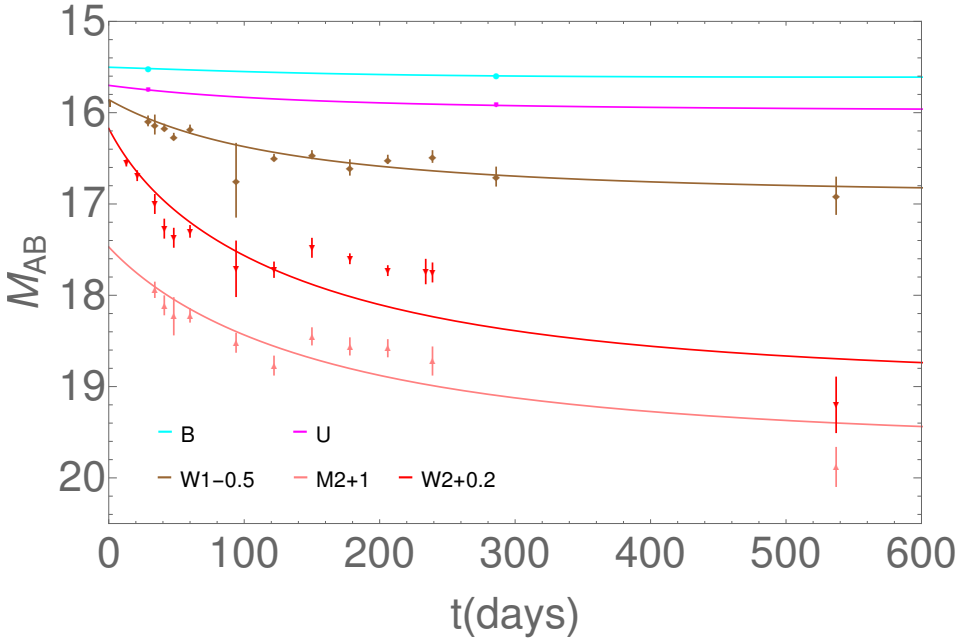

(b) XMMSL1 J074008.2-853927

FIGURE 7.7: The time-dependent model fit to the observations OGLE16aaa (top) and XMMSL1 J074008.2-853927 (bottom).

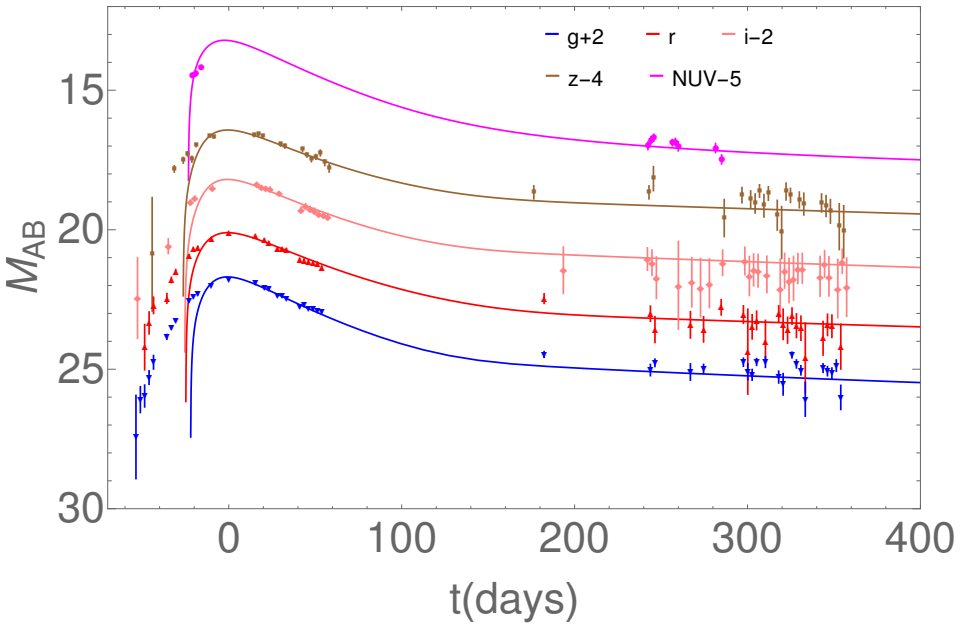

(a) Ps1-10jh

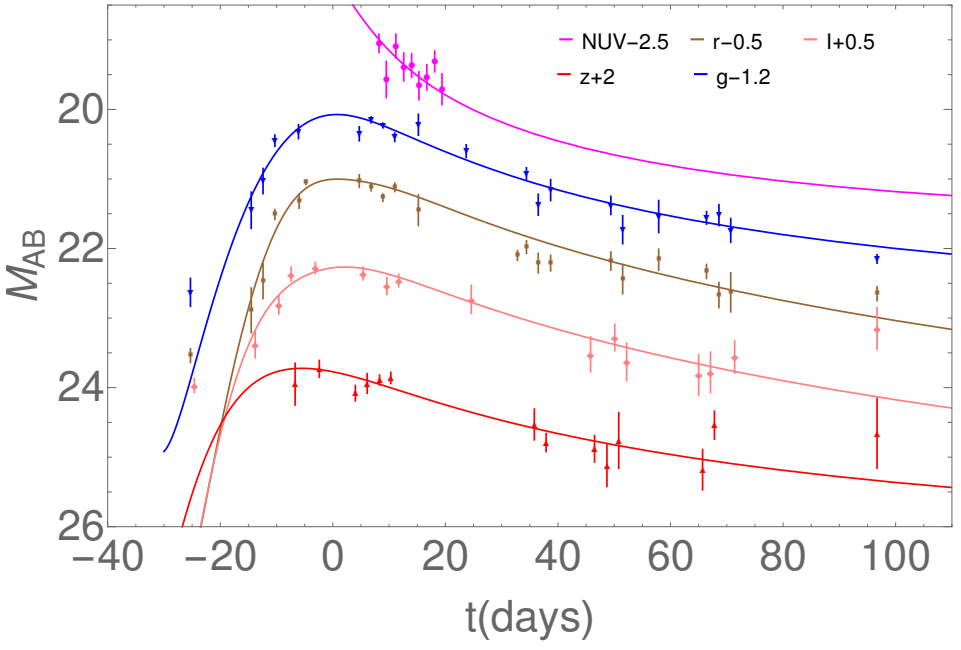

(b) PS-11af

FIGURE 7.8: The time-dependent model fit to the observations PS1-10jh (top) and PS-11af (bottom).

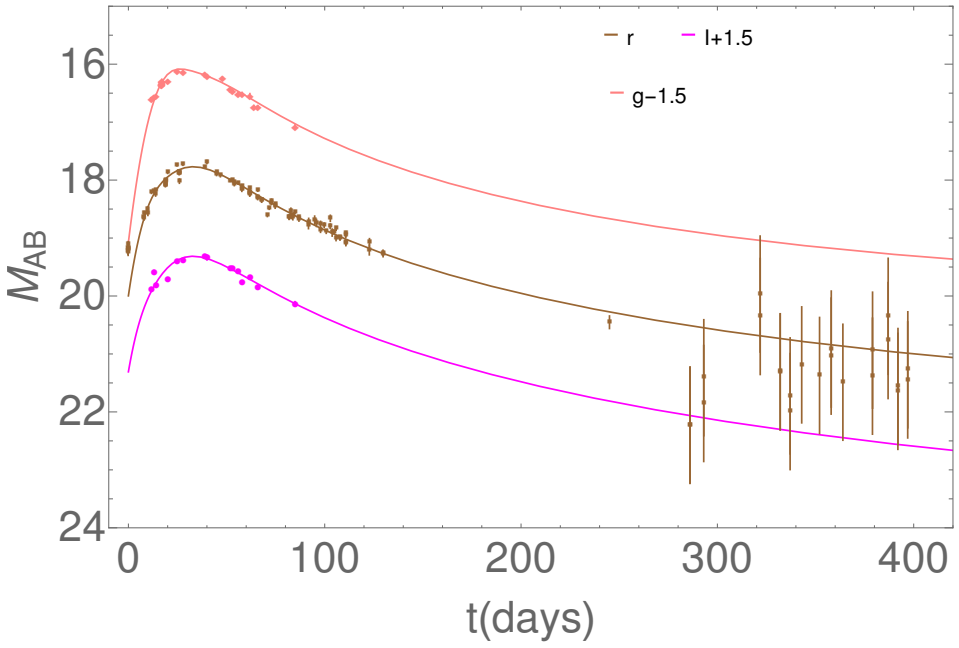

(a) PTF09ge

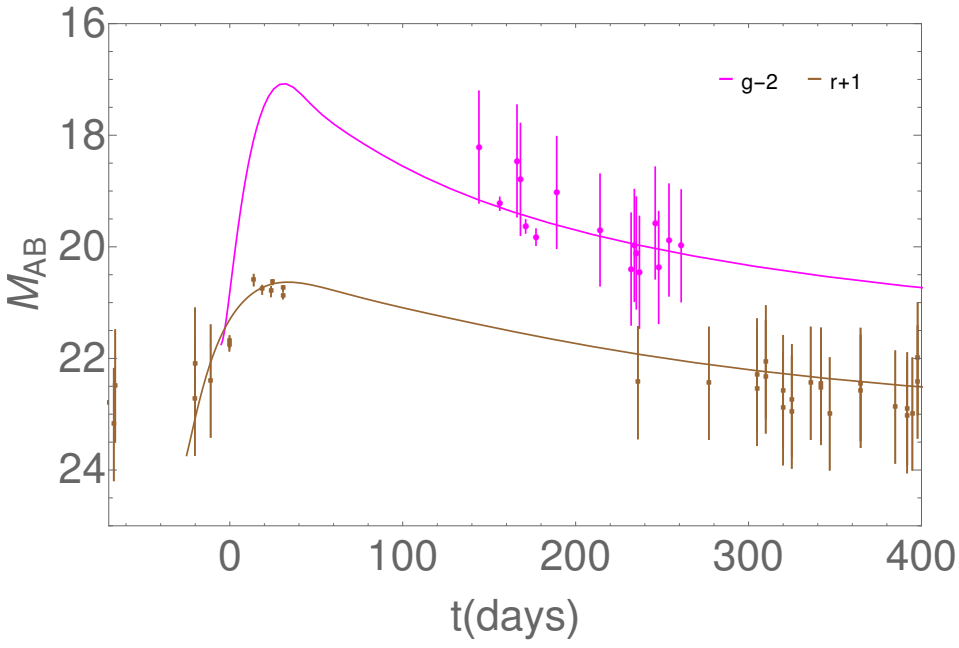

(b) PTF09djl

FIGURE 7.9: The time-dependent model fit to the observations PTF09ge (top) and PTF09djl (bottom).

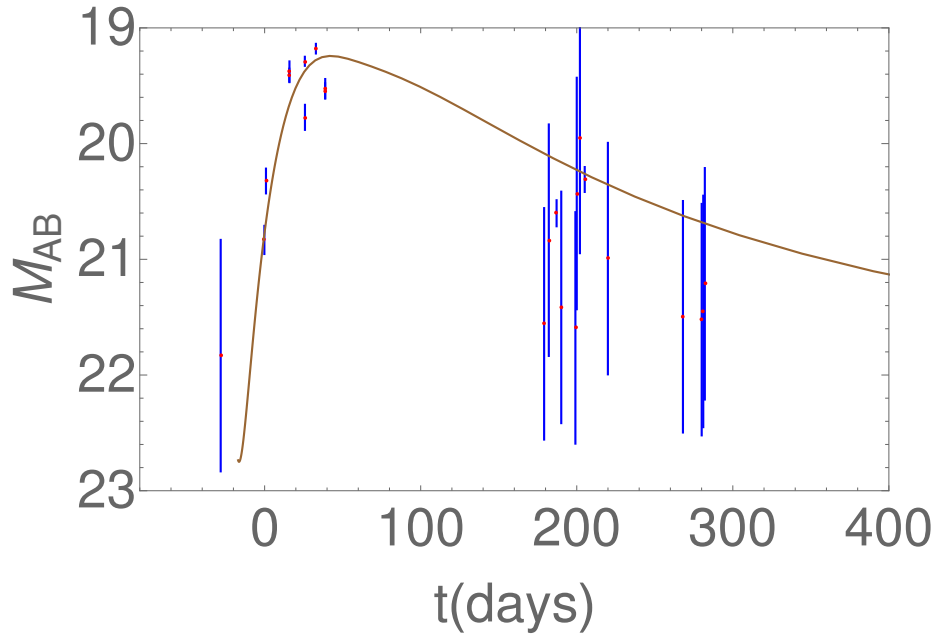

(a) PTF09axc

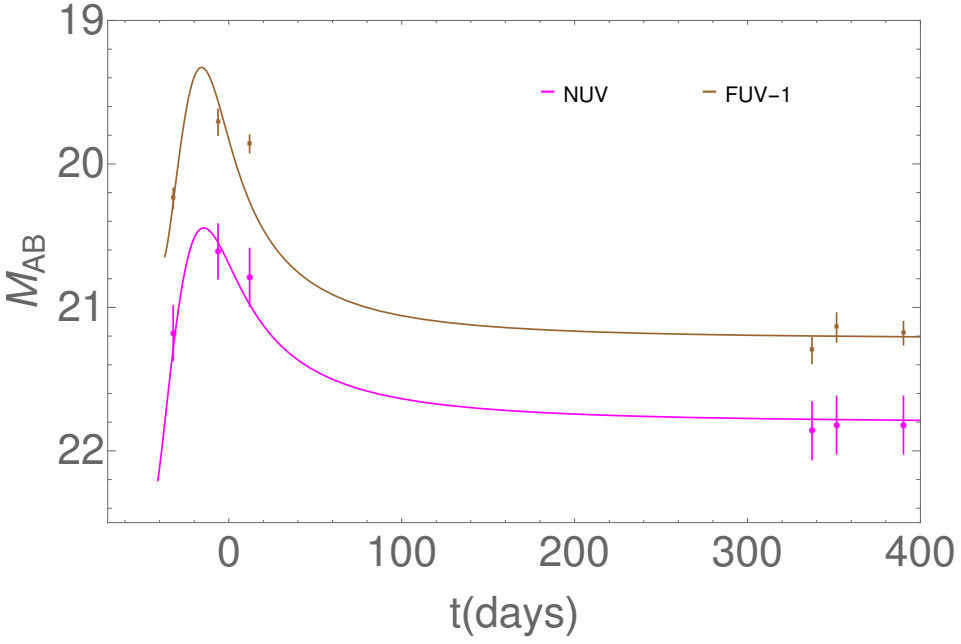

(b) D23H-1

FIGURE 7.10: The time-dependent model fit to the observations PTF09axc in r band (top) and D23H-1 (bottom).

Model	Observation	Band	α	$\bar{e}$	ℓ	M_6	m	q	j	w_n	c_2	δt (days)	χ
B	PS1-10jh	g band	0	0.01	1	6.8	1.0	1.119	0.4	0.101	1	225	4.1
D		g band	–	0.00001	1	12	3	–	0.4	–	–	16	23.3
B	PS1-10jh	r band	0	0.01	1	6.8	1.25	1.119	0.4	0.1	1	28	3.66
D		r band	–	0.001	1	13	3.16	–	0.6	–	–	15	11.97
B	PS1-10jh	i band	0	0.01	1	6.8	1.1	1.119	0.4	0.091	1	28	3.78
D		i band	–	0.001	1	11	3.5	–	0.6	–	–	18	4.22
B	PS1-10jh	z band	0	0.01	1	6.8	1.19	1.119	0.4	0.091	1	29	2.1
D		z band	–	0.001	1	11	3.6	–	0.6	–	–	18	8.67
B	PS1-10jh	nuv band	0	0.01	1	6.8	1.15	1.119	0.4	0.11	0.61	27	3.8
D		nuv band	–	0.01	1	3.98	5.8	–	0	–	–	20	4.78
B	Swift J1644+57	X-ray	0	0.01	1	1	21	1.29	0.4	0.09	0.1	400	3.8
D		X-ray	–	–	–	–	–	–	–	–	–	–	–

TABLE 7.2: The physical parameters obtained from reduced chi-square χ^2 fit with models B and D to the observations with a time shift of δt, mass of star m, star's initial dimensionless energy $\bar{e}$, angular momentum ℓ and black hole mass M_6 and spin j along with the χ_s values are shown above.

where $m = M_\star/M_\odot$ and $R_\star = R_\odot m^{0.8}$. The peak mass fallback rate and the corresponding rise time are approximated by

Observation	Band	$\bar{e}$	α	ℓ	M_6	m	q	j	$\mathcal{W}_n$	c_2	δt (days)	χ
ASAS-SN 15oi	i band	0	0.001	1	7	1.3	3	0.5	0.09	0.3	35	0.9
	V band	0	0.004	1	7	1.2	3	0.5	0.09	0.38	30	1.46
	b band	0	0.01	1	6.5	1.0	3	0.5	0.1	0.46	27	2.23
	W1 band	0	0.001	1	6.5	1.51	2.9	0.5	0.13	0.7	10	1.41
	W2 band	0	0.01	1	7	1.5	3	0.5	0.18	0.7	35	3.37
	M2 band	0	0.001	1	6.5	2	3	0.5	0.15	0.8	20	1.6
iPTF16axa	W1 band	0	0.0001	1	5	1.1	3	0.4	0.15	0.3	30	1.06
	M2 band	0	0.0001	1	5	1.1	3	0.4	0.15	0.46	25	1.45
	W2 band	0	0.0001	1	5	1.1	3	0.4	0.17	0.40	32	2.45
	U band	0	0.0001	1	5	1.0	3	0.4	0.1	0.40	33	0.88
	g band	0	0.0001	1	5	1.0	3	0.4	0.1	0.68	33	1.94
	r band	0	0.0001	1	5	0.8	3	0.4	0.07	0.69	33	1.80
	i band	0	0.0001	1	5	0.8	3	0.4	0.07	0.69	38	1.29
OGLE16aaa	I band	0	0.0001	1	11	2.2	3	0.5	0.33	0.70	12	1.63
	V band	0	0.0001	1	11	1.9	3	0.5	0.37	0.7	10	1.13
	W2 band	0	0.00005	1	10.5	3.8	3	0.5	0.55	0.50	25	1.72
	W1 band	0	0.0001	1	10	4.5	3	0.5	0.46	0.60	30	1.19
	M2 band	0	0.0001	1	10	4.1	3	0.5	0.48	0.4	30	1.62
PS1-10jh	g band	0	0.01	1	6.8	1	1.119	0.4	0.101	1	25	6.0
	r band	0	0.01	1	6.8	1.25	1.119	0.4	0.100	1	28	3.66
	i band	0	0.01	1	6.8	1.1	1.119	0.4	0.091	1	28	3.78
	z band	0	0.01	1	6.8	1.19	1.119	0.4	0.091	1	29	2.11
	nuv band	0	0.01	1	6.8	1.15	1.119	0.4	0.11	0.61	27	3.88
PS1-11af	g band	0	0.0001	1	10	1	3	0.45	0.26	0.63	40	4.3
	z band	0	0.0001	1	11	0.8	4	0.45	0.25	0.7	38	1.22
	i band	0	0.0001	1	11	0.8	2.5	0.45	0.17	0.8	31	1.16
	r band	0	0.0001	1	11	1.1	2.5	0.45	0.17	0.8	27	2.04
	nuv band	0	0.0001	1	11	1.5	2.5	0.45	0.17	0.57	27	1.13

TABLE 7.3: The physical parameters obtained from reduced χ^2 fit of time-dependent model to the observations with a time shift of δt, mass of the star m, star's initial dimensionless energy $\bar{e}$, angular momentum ℓ and black hole mass M_6 and spin j along with the χ values are shown above. The model fits to light curves are shown in Figs 7.6, 7.7 and 7.8.

Observation	Band	$\bar{e}$	α	ℓ	M_6	m	q	j	$\mathcal{W}_n$	c_2	δt (days)	χ
PTF09axc	r band	0	0.0001	1	7.3	1	3.3	0.50	0.4	0.7	17	2.28
PTF09ge	g band	0	0.0001	1	9.0	0.8	2	0.6	0.2	0.75	9	4.9
	r band	0	0.0001	1	9.4	0.65	2	0.6	0.185	0.8	14	3.38
	i band	0	0.0001	1	9.4	0.55	2	0.6	0.18	0.83	16.5	5.2
PTF09djl	r band	0	0.0001	1	7.0	1.5	3.3	0.50	0.40	0.63	30	1.45
	g band	0	0.0001	1	8.0	1.2	3.22	0.7	0.3	0.73	5	0.84
D23H-1	FUV band	0	0.0001	1	21	1	3	0.4	0.35	0.56	39	2.35
	NUV band	0	0.0001	1	21	1	3	0.4	0.35	0.56	45	0.41
Swift J1644+57	X-ray	0	0.01	1	1	21	1.29	0.4	0.09	0.1	400	3.86
Swift J2058+0516	g band	0	0.0001	1	3.8	1.15	3.3	0.65	0.47	0.4	45	4.5
	r band	0	0.0001	1	3.8	1.12	3.3	0.65	0.45	0.35	35	1.49
	i band	0	0.0001	1	3.3	1.5	3.3	0.65	0.46	0.40	45	0.84
	z band	0	0.0001	1	3.3	1.5	3.3	0.65	0.44	0.4	45	2.37
XMMSL1-	W2 band	0	0.005	1	10.5	1.1	3	0.3	0.4	0.69	100	3.9
J074008.2-853927	M2 band	0	0.005	1	10.5	1.1	3	0.3	0.4	0.69	130	2.02
	W1 band	0	0.005	1	10.5	1.1	3	0.3	0.4	0.6	170	1.50
	U band	0	0.005	1	10.5	1.0	3	0.3	0.5	0.485	210	0.05
	B band	0	0.0001	1	10.5	1.5	3	0.3	0.535	0.455	210	0.33

TABLE 7.4: The physical parameters obtained from reduced χ^2 fit of time-dependent model to the observations with a time shift of δt, mass of the star m, star's initial dimensionless energy $\bar{e}$, angular momentum ℓ and black hole mass M_6 and spin j along with the χ values are shown above. The model fits to light curves are shown in Figs 7.5, 7.9 and 7.10.

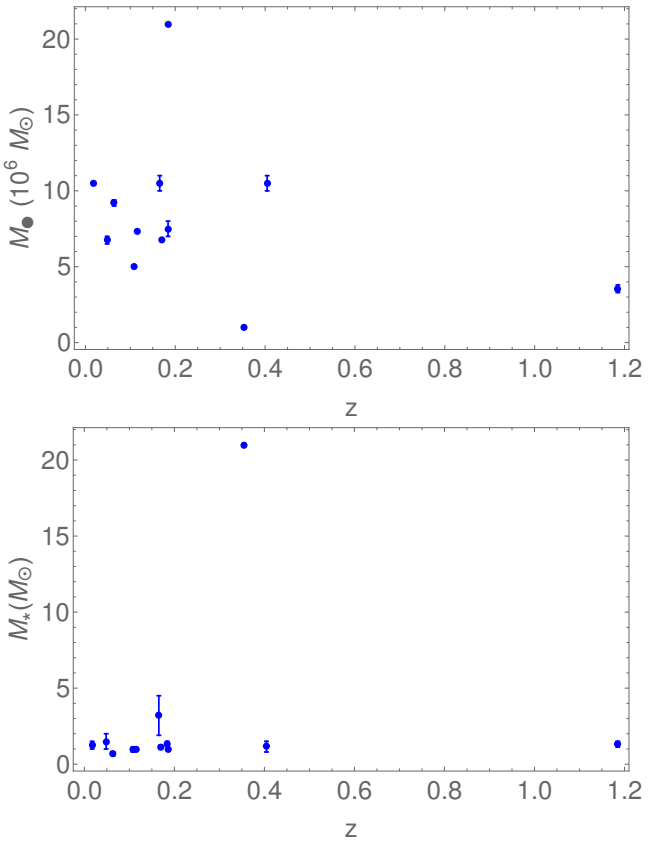

FIGURE 7.11: The black hole mass (top) and star mass (bottom) as a function of redshift obtained by time-dependent model fit to the various TDE sources given in Table 2.1. The TDE observations are dominated by low star mass.

$$\dot{M}_p = 5.6 \times 10^{29} \text{g sec}^{-1} \quad \left[m^{0.3} \bar{e}^{\frac{3}{2}} \left[1 + \frac{1}{x_\ell} \right]^{\frac{3}{2}} (0.05 + 0.16 x_\ell + 0.197 x_\ell^2 - 0.026 x_\ell^3) \right], \tag{7.3}$$

$$t_p = 0.041 \text{ days} \quad \left[m^{0.7} \bar{e}^{-\frac{3}{2}} \left[1 + \frac{1}{x_\ell} \right]^{-\frac{3}{2}} (2.66 - 0.625 x_\ell - 0.177 x_\ell^2 + 0.164 x_\ell^3) \right]. \tag{7.4}$$

For a standard thin model with constant radii, the peak bolometric luminosity is given by

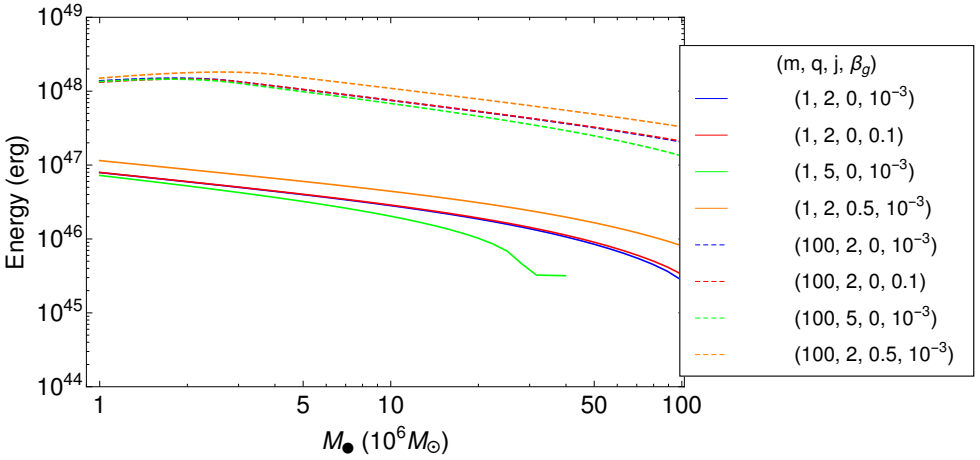

FIGURE 7.12: The total energy released from a time-dependent sub-Eddington accretion model for the various physical parameters.

$$L_b^{peak} = 5.1\times10^{49}\text{erg sec}^{-1}\frac{m^{0.3}\bar{e}^{\frac{3}{2}}}{Z(j)}\left[1+\frac{1}{x_\ell}\right]^{\frac{3}{2}}(0.05+0.16x_\ell+0.197x_\ell^2-0.026x_\ell^3)\left[1-\frac{r_{ISCO}}{r_{out}}-\frac{2}{3}\left(1-\left(\frac{r_{ISCO}}{r_{out}}\right)^{\frac{3}{2}}\right)\right]. \quad (7.5)$$

Thus, keeping the leading term, we find

$$t_p = 0.11 \text{ days } m^{0.7}\bar{e}^{-\frac{3}{2}}\left[1+\frac{1}{x_\ell}\right]^{-\frac{3}{2}} \quad (7.6)$$

$$L_p = 5.1\times10^{49} \text{ erg sec}^{-1} m^{0.3}\bar{e}^{\frac{3}{2}}\left[1+\frac{1}{x_\ell}\right]^{\frac{3}{2}} \quad (7.7)$$

$$\dot{M}_p = 2.8\times10^{28}\text{g sec}^{-1} m^{0.3}\bar{e}^{\frac{3}{2}}\left[1+\frac{1}{x_\ell}\right]^{\frac{3}{2}} \quad (7.8)$$

$$\dot{M} = \frac{(2\pi)^{2/3}}{3}\frac{1}{k}\frac{1}{G^{1/3}}M_\bullet^{\frac{1}{3}}M_\star^{\frac{1}{3}}R_\star t^{-\frac{5}{3}}, \quad (7.9)$$

If the coefficients of eqn (7.9) are measured, then it is possible to obtain the black hole mass, star mass, and star radius.

7.2 The supermassive black hole mass function

The black hole mass function (BHMF) for $10^5 < M_\bullet/M_\odot < 10^9$, shows an evolution of the distribution of SMBH mass and is crucial to trace the growth of black holes. The surveys for estimating the BHMF are constrained by the luminosity criteria: the luminosity from galactic nuclei is to be above a limiting value that depends on the star luminosity that is subject to the detectors sensitivity and a theoretical model of emission. The black hole mass is related to the host galaxy properties such as black hole-bulge mass relation (Häring and Rix 2004) and black hole-stellar velocity dispersion (Ferrarese and Merritt 2000; Ferrarese and Ford 2005; McConnell and Ma 2013). The black hole mass can be estimated by either measuring the velocity dispersion of the stars or the luminosity from the nuclei. The method of mass estimation through velocity dispersion is useful for non-active nuclei but is constrained by the resolution of the stars and their spectrum at high redshift whereas the mass estimation through luminosity is used for high redshift galaxies.

The tidal disruption events (TDEs) where a star is captured by the black hole in the galactic nuclei depends on the host galaxy properties and the emission from the accretion of the debris is a primary tool to measure the black hole mass of the non-active galaxies. The detection rate of TDEs depends on the theoretical capture rate, duration of the TDE observation, BHMF of non-active galaxies and instrumental parameters such as sensitivity, cadence and integration time. The observed detection rate for various missions can be used to measure the LF of non-active galaxies. Milosavljević *et al.* (2006) obtained a luminosity function of X-ray

LF for TDEs assuming a Schechter LF with X-ray luminosity assumed to follow the bolometric luminosity. They found that TDEs makes a negligible contribution to the higher luminosities and black hole mass $M_\bullet > 10^7$ mostly grow by accreting nonstellar material. Their measurement is limited by the low sample size. The detection rate of TDEs for various surveys are calculated by Strubbe and Quataert (2009) and Mageshwaran and Mangalam (2015) (hereafter MM15) using the QLF of Hopkins *et al.* (2007) with MM15 including the duty cycle given by Chen *et al.* (2007) to obtain LF of non-active galaxies.

In this chapter, we fit the time-dependent accretion model (Mageshwaran & Mangalam 2017) to various multiwavelength observations to obtain the physical parameters such as $M_\bullet$, $M_\star$, E and J and study the demographics of the black hole mass and star mass. We will use the Schechter luminosity function with Faber-Jackson law and the $M_\bullet - \sigma$ relation, where σ is the velocity dispersion, to obtain the black hole mass function which is then used to calculate the detection rate of TDEs for various surveys and from the detected number of TDEs by the surveys, we will derive the Schechter parameters. The Fig 2.5 shows the distribution for TDE sources in redshift given in Table 2.1. Most of the TDEs are at low redshift which may be attributed to a low occurrence rate of TDEs, detectors sensitivity, sky coverage, cadence and black hole mass function.

The detection rate of TDEs depends on the theoretical capture rate of stars by black hole, the probability of detection and the black hole mass function (BHMF) of the galaxies $\Phi(M_\bullet,\ z)$. We consider a separable form of black hole mass function $\Phi(M_\bullet,\ z) = \mu(M_\bullet)Z(z)$, where $Z(z) = 1 - \delta(z)$ with duty cycle $\delta(z) = 10^{-3}(z/0.1)^{2.5}$ (Chen *et al.* 2007) and $\mu(M_\bullet)$ obtained using Schechter function given by (Schechter 1976)

$$\Phi(L_R)\mathrm{d}L_R = \frac{\Phi_\star}{L_\star}\left(\frac{L_R}{L_\star}\right)^{-\alpha}\exp(-L_R/L_\star)\mathrm{d}L_R, \tag{7.10}$$

where L_R is the R-band luminosity and $\alpha = 1.1$. Brown *et al.* (2001) obtained the Schechter parameters $\Phi_\star = 4.9 \times 10^{-3} h_7^3$ Mpc^{-3} and $L_\star = 2.9 \times 10^{10} h_7^{-2} L_\odot$ where $L_\odot$ is the solar luminosity and $h_7 = H_0/(70$ Km sec^{-1} Mpc$^{-1})$. Combining the Faber-Jackson law which gives the velocity dispersion $\sigma \propto L_R^{1/n}$ and the $M_\bullet - \sigma$ relation which gives $\sigma \propto M_\bullet^{\frac{1}{\lambda}}$, we obtain $L_R \propto M_\bullet^{n/\lambda}$. Then $\mu(M_\bullet)$ is given by (Aller and Richstone 2002)

$$\mu(M_\bullet) = \frac{\Phi_\star \epsilon}{M_s} \left(\frac{M_\bullet}{M_s}\right)^\beta \exp(-(M_\bullet/M_s)^\epsilon), \tag{7.11}$$

where $M_s \propto L_\star^{\lambda/n}$, $\beta = \epsilon(1-\alpha) - 1$ and $\epsilon = n/\lambda$.

We assume ΛCDM cosmology with $\Omega_m = 0.308, \Omega_\Lambda = 0.692$, $H_o = 67.8$ Km sec^{-1} Mpc^{-1} (Planck Collaboration *et al.* 2016). The luminosity distance as a function of redshift z is given by

$$\mathrm{d}_L(z) = (1+z)\frac{c}{H_o}\int_0^z \frac{1}{((1+z')^3\Omega_m + \Omega_\Lambda)^{0.5}}\,\mathrm{d}z'. \tag{7.12}$$

Consider now a small volume of the Universe at redshift z with radial width dz covering an opening angle ω on the observer's sky (Khabibullin *et al.* 2014). The comoving volume of the slice is

$$\mathrm{d}V_c = \omega d_H^3 \frac{I^2(z)}{W(z)}\mathrm{d}z \tag{7.13}$$

where $\omega = 4\pi f_s$, f_s is the fraction of sky observed, $d_H = c/H_o$, $W(z) = ((1+z)^3\Omega_m + \Omega_\Lambda)^{0.5}$, and

$$I(z) = \int_0^z \frac{1}{((1+z')^3\Omega_m + \Omega_\Lambda)^{0.5}}\,\mathrm{d}z', \tag{7.14}$$

whose integral is given by

$$I(z) = \frac{1}{\sqrt{\Omega_m}}\frac{1}{3^{1/4}\omega^{1/6}}\left[F\left\{\mathrm{Cos}^{-1}\left(\frac{-(-1+\sqrt{3})\omega^{1/3}+1}{(1+\sqrt{3})\omega^{1/3}+1}\right), \frac{2+\sqrt{3}}{4}\right\} - F\left\{\mathrm{Cos}^{-1}\left(\frac{-(-1+\sqrt{3})\omega^{1/3}+1+z}{(1+\sqrt{3})\omega^{1/3}+1+z}\right), \frac{2+\sqrt{3}}{4}\right\}\right], \tag{7.15}$$

where F is Elliptic integral of first kind and $\omega = \Omega_\Lambda/\Omega_m$. Thus the luminosity distance is given by $d_L(z) = (c/H_0)(1+z)I(z)$.

The probability of event detection depends on the peak luminosity and the detectors parameters such as sensitivity of the detector f_l, cadence t_{cad}, and integration time t_{int}. We consider the steady accretion disk model with time varying accretion rate of MM15 for parabolic orbit with $r_p = r_t$, to calculate the peak luminosity $L_p(M_\bullet,\ M_\star,\ z)$ in the given spectral bands with the corresponding time $t_p(M_\bullet,\ M_\star,\ z)$. Assuming the luminosity decline from the peak to be

$$L = L_p(M_\bullet,\ M_\star,\ z)\left(\frac{t_p(M_\bullet,\ M_\star,\ z)+\delta t}{t_p(M_\bullet,\ M_\star,\ z)}\right)^{-\frac{5}{3}}, \tag{7.16}$$

where δt is the time after the peak and comparing it with the sensitivity of the detector f_l, we obtained the duration of flare detection given by

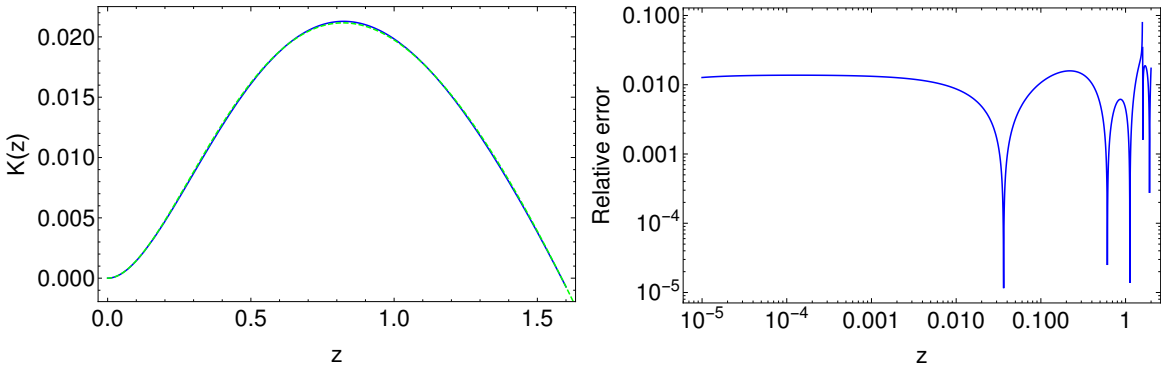

FIGURE 7.13: (Left:) The model given by eqn (7.23) is shown in green dashed line and the numerically obtained result is shown in blue. (Right:) The relative error= Abs[(fit-numerical)/numerical] of the fit to the numerical results.

$$\delta t_f(M_\bullet,\ M_\star,\ z) = t_p(M_\bullet,\ M_\star,\ z)\left[\left(\frac{L_p(M_\bullet,\ M_\star,\ z)}{4\pi f_l d_L^2(z)}\right)^{\frac{3}{5}} - 1\right]. \tag{7.17}$$

The probability of detection is given by (MM15)

$$P(M_\bullet,\ M_\star,\ z) = \text{Min}\left[1, \frac{\delta t_f(M_\bullet,\ M_\star,\ z)}{t_{cad} + t_{int}}\right], \tag{7.18}$$

and we assume in our calculation that $\delta t_f(M_\bullet,\ M_\star,\ z) \geq t_{cad} + t_{int}$ which implies that $P(M_\bullet,\ M_\star,\ z) = 1$; by taking the limiting value $\delta t_f(M_\bullet,\ M_\star,\ z) = t_{cad} + t_{int}$, the maximum detectable redshift is $z_m(M_\bullet,\ M_\star)$ which is obtained by solving

$$d_L^2(z_m) = \frac{L_p(M_\bullet,\ M_\star,\ z_m)}{4\pi f_l}\left(\frac{t_p(M_\bullet,\ M_\star,\ z_m) + t_{cad} + t_{int}}{t_p(M_\bullet,\ M_\star,\ z_m)}\right)^{-\frac{5}{3}}. \tag{7.19}$$

Thus, the detection rate of TDEs for a given survey is given by

$$\dot{N}_D = \int\int\int \Phi(M_\bullet,\ z)\mathrm{d}M_\bullet \frac{\mathrm{d}\dot{N}_t(\gamma,\ M_\bullet,\ M_\star)}{\mathrm{d}M_\star}\mathrm{d}M_\star \frac{\mathrm{d}V_c}{1+z}, \tag{7.20}$$

where $\mathrm{d}\dot{N}_t(\gamma,\ M_\bullet,\ M_\star)/\mathrm{d}M_\star$ is obtained using eqn (5.47), and using eqn (7.11) and (7.13), $\dot{N}_D$ is given by

$$\dot{N}_D = 4\pi f_s d_H^3 \int \mathrm{d}M_\bullet \mu(M_\bullet) \int \mathrm{d}M_\star \frac{\mathrm{d}\dot{N}_t(\gamma,\ M_\bullet,\ M_\star)}{\mathrm{d}M_\star} \int_0^{z_m(M_\bullet,\ M_\star)} \mathrm{d}z \quad K(z), \tag{7.21}$$

where $K(z)$ is given by

$$K(z) = \frac{Z(z)}{1+z}\frac{I^2(z)}{W(z)}, \tag{7.22}$$

and $1+z$ is due to the time dilation. Then $K(z)$ is solved numerically and the best fit model is given by

$$K(z) = 0.179z^2 - 0.477z^3 + 0.427z^{3.5} - 0.11z^4, \tag{7.23}$$

as shown in Fig 7.13, which results in the detection rate given by

$$\dot{N}_D = 4\pi f_s d_H^3 \int \mathrm{d}M_\bullet \mu(M_\bullet)\chi(M_\bullet), \tag{7.24}$$

where $\chi(M_\bullet)$ given by

$$\chi(M_\bullet) = 4\pi f_s d_H^3 \int_{0.8M_\odot}^{150M_\odot} \mathrm{d}M_\star \frac{\mathrm{d}\dot{N}_t(\gamma,\ M_\bullet,\ M_\star)}{\mathrm{d}M_\star}(0.06z_m^3 - 0.12z_m^4 + 0.095z_m^{4.5} - 0.022z_m^5), \tag{7.25}$$

is numerically evaluated for various γ and $M_\bullet$ in range $10^6 - 10^8 M_\odot$. The numerically obtained result is fit with the model given by

$$\chi(M_6) = a_1 M_6^{p_1} + a_2 M_6^{p_2} + a_3 M_6^{p_3} + a_4 M_6^{p_4} + a_5 M_6^{p_5}, \tag{7.26}$$

as shown in Fig 7.14 where $M_6 = M_\bullet/10^6 M_\odot$ where the obtained parameters, $\{a_n(\gamma),\ p_n(\gamma)\}$, are shown in Table 7.5.

Using eqns (7.11, 7.24, 7.26) and integrating over $M_\bullet$ gives

$$\dot{N}_D = \phi_\star \sum_{i=1}^{5} a_i \left(\frac{M_s}{10^6 M_\odot}\right)^{p_i} \left[\Gamma\left(\frac{1+\beta+p_i}{\epsilon}, x_{min}^\epsilon\right) - \Gamma\left(\frac{1+\beta+p_i}{\epsilon}, x_{max}^\epsilon\right)\right], \tag{7.27}$$

where a_i and p_i are the elements shown in eqn (7.26), $x_{min} = M_\bullet^{min}/M_s$ with $M_\bullet^{min} = 10^6 M_\odot$ and $x_{max} = M_\bullet^{max}/M_s$ with $M_\bullet^{max} = 10^8 M_\odot$. The number of TDEs detected in a survey time t_s is given by $N_D = \dot{N}_D t_s$, where t_s and N_D is shown for various surveys in Table 7.6. We use the total number of TDEs detected in a given duration by various surveys such as All Sky Automated Survey for SuperNovae (ASAS-SN), Palomar Transient Factor (PTF), intermediate Palomar Transient Factor (iPTF), Pan-STARRS and Galaxy Evolution Explorer (GALEX) to obtain the detection rate and compare it with the theoretical detection rate derived using Schechter luminosity function to extract the Schechter parameters.

Survey	γ	$(a_1(10^5),\ p_1)$	$(a_2(10^5),\ p_2)$	$(a_3(10^5),\ p_3)$	$(a_4(10^5),\ p_4)$	$(a_5(10^3),\ p_5)$
ASAS-SN	0.6	(-0.089, -0.396)	(0.734, 0.204)	(0.111, 0.604)	(-0.722.4, 0.304)	(-1.81, 0.804)
	0.7	(-0.117, -0.388)	(0.972, 0.212)	(0.147, 0.612)	(-0.955, 0.312)	(-2.39, 0.812)
	0.8	(-0.151, -0.387)	(1.246, 0.213)	(0.188, 0.613)	(-1.224, 0.313)	(-3.06, 0.813)
	0.9	(-0.189, -0.391)	(1.572, 0.210)	(0.237, 0.610)	(-1.542, 0.310)	(-3.85, 0.810)
	1.0	(-0.235, -0.393)	(1.955, 0.207)	(0.295, 0.607)	(-1.919, 0.307)	(-4.79, 0.807)
	1.1	(-0.290, -0.398)	(2.419, 0.202)	(0.365, 0.602)	(-2.376, 0.302)	(-5.94, 0.803)
PTF	0.6	(-2.25, -0.305)	(15.7, 0.295)	(5.492, 0.695)	(-13.6, 0.495)	(-75.5, 0.895)
	0.7	(-2.97, -0.298)	(15.3, 0.301)	(7.266, 0.701)	(-18.6, 0.501)	(-99.9, 0.902)
	0.8	(-3.81, -0.298)	(19.7, 0.302)	(9.327, 0.703)	(-23.5, 0.502)	(-128.16, 0.902)
	0.9	(-4.81, -0.301)	(24.8, 0.298)	(11.7, 0.698)	(-29.1, 0.498)	(-161.6, 0.898)
	1.0	(-5.96, -0.301)	(31.5, 0.298)	(14.6, 0.698)	(-36.2, 0.498)	(-201.4, 0.898)
	1.1	(-7.34, -0.306)	(38.1, 0.293)	(18.1, 0.693)	(-44.8, 0.493)	(-249.02, 0.894)
iPTF	0.6	(-1.26, -0.306)	(6.44, 0.293)	(3.031, 0.693)	(-7.52, 0.493)	(-41.6, 0.893)
	0.7	(-1.66, -0.300)	(8.51, 0.300)	(4.012, 0.700)	(-9.95, 0.500)	(-55.0, 0.9)
	0.8	(-2.13, -0.298)	(10.9, 0.302)	(5.149, 0.701)	(-13.6, 0.501)	(-70.6, 0.901)
	0.9	(-2.69, -0.302)	(13.8, 0.297)	(6.493, 0.697)	(-16.1, 0.497)	(-88.9, 0.898)
	1.0	(-3.33, -0.302)	(17.2, 0.298)	(8.085, 0.697)	(-20.4, 0.497)	(-110.8, 0.897)
	1.1	(-4.10, -0.307)	(21.2, 0.293)	(9.995, 0.693)	(-24.8, 0.493)	(-137.1, 0.893)
PS-MDS	0.6	(-0.266, -0.074)	(0.219, 1.026)	(-0.309, 0.926)	(0.43, 0.226)	(-0.524, 1.426)
	0.7	(-0.30, -0.07)	(0.289, 1.03)	(-0.408, 0.930)	(5.67, 0.230)	(-0.692, 1.43)
	0.8	(-0.448, 0.068)	(0.371, 1.032)	(-0.524, 0.932)	(7.27, 0.232)	(-0.889, 1.432)
	0.9	(-0.56, -0.069)	(0.468, 1.031)	(-0.666, 0.931)	(9.17, 0.231)	(-1.12, 1.431)
	1.0	(-0.696, -0.07)	(0.583, 1.028)	(-0.823, 0.928)	(1.138, 0.228)	(-1.39, 1.428)
	1.1	(-0.855, -0.075)	(0.722, 1.025)	(-1.018, 0.925)	(1.404, 0.225)	(-1.73, 1.425)
GALEX	0.6	(-0.0213, 0.312)	(0.604, 1.412)	(-1.495, 1.312)	(0.963, 1.21)	(-0.712, 1.812)
	0.7	(-0.0276, 0.317)	(0.798, 1.416)	(-1.972, 1.316)	(1.271, 1.21)	(-0.939, 1.817)
	0.8	(-0.0343, 0.319)	(1.022, 1.42)	(-2.525, 1.32)	(1.626, 1.22)	(-1.203, 1.82)
	0.9	(-0.0416, 0.320)	(1.284, 1.42)	(-3.173, 1.32)	(2.044, 1.22)	(-1.513, 1.82)
	1.0	(-0.0489, 0.319)	(1.590, 1.419)	(-3.928, 1.318)	(2.53, 1.22)	(-1.875, 1.81)
	1.1	(-0.0562, 317)	(1.952, 1.417)	(-4.822, 1.316)	(3.10, 1.21)	(-2.304, 1.81)

TABLE 7.5: The parameters $(a,\ p)$ in eqn (7.26) for various surveys and γ.

The Faber-Jackson law given by $\sigma = 150$ km sec$^{-1}(L_R/10^{10}L_\odot)^{1/4}$ with $n = 4$ (Stone and Metzger 2016) and the $M_\bullet - \sigma$ relation gives $\lambda = 4.86$ (Ferrarese and Ford 2005) which results in $\epsilon = 0.823$. The best fit to the parameters $\phi_\star,\ \beta$ and M_s are obtained by minimizing the function $F(\phi_\star,\ \beta,\ M_s)$, given by

$$F(\phi_\star,\ \beta,\ M_s) = \sum_{j=1}^{5} N^j_{D,obs}(N^j_D - N^j_{D,obs})^2, \tag{7.28}$$

where j represents the sum over all missions given in Table 7.6 and is weighted with the number of TDEs detected.

The function $F(\phi_\star,\ \beta,\ M_s)$ has multiple minima points and thus it is necessary to constrain the range for parameter search which is done on the basis of observational estimates. The approximate estimates for the Schechter parameters from observations are $\phi_\star \approx 10^{-3}$ Mpc^{-3}, $\alpha = 1.09 \pm 0.09$ which results in $\beta = -1.072 \pm 0.063$ and $L_\star \approx 10^{10}L_\odot$ (Brown *et al.* 2001; Aller and Richstone 2002) which results in $M_s \approx 10^8 M_\odot$, where $L_\odot$ is the solar luminosity. Based on these estimates, we consider the typical range $\phi_\star = 10^{-4} - 10^{-3}$ Mpc^{-3}, $\beta = -1.2$ to -0.8 and $M_s(10^6 M_\odot) = 0.01$ to 1000 to search the minimum of eqn (7.28) to obtain the Schechter parameters that are shown in Table 7.7.

For a distribution given by $\{\{x_1,\ g_1\}, \{x_2,\ g_2\}, \{x_3,\ g_3\}, ..., \{x_n,\ g_n\}\}$, the mean $\bar{g}$ and the standard deviation g_{SD} are given by

$$\bar{g} = \frac{\sum_{i=1}^{n-1} \left(\frac{g_{i+1}+g_i}{2}\right)(x_{i+1} - x_i)}{x_n - x_1}, \tag{7.29}$$

and

$$g_{SD} = \sqrt{\frac{\sum_{i=1}^{n}(g_i - \bar{g})^2}{n}}. \tag{7.30}$$

Using eqns (7.29, 7.30) with $x_i = \gamma_i$ and g_i as various Schechter parameters given in Table 7.7, the mean Schechter parameters are found to be $\phi_\star = 10^{-4}$ Mpc^{-3}, $M_s(10^6 M_\odot) = 0.592 \pm 0.09$, $\beta = -1.017 \pm 0.136$ and $\epsilon = 0.823$.

Our Schechter parameters for various γ given in Table 7.8 are compared with the parameters obtained from observations given in Table 7.11 and we found that the parameters are close for $\gamma = 0.9$. Using this the detectable rate per unit black hole mass and star mass are shown in Fig 7.15.

7.3 Discussion

The number of TDEs observed is high at low redshift as shown in Fig 2.5 as the detection is constrained by the flux sensitivity of the detector and the cadence of the survey missions. Fig 7.11 shows that the most of the TDEs are dominated by the disruption of low mass stars by low mass SMBHs. This is because the theoretical capture rate of stars decreases with increase in $M_\star$ and $M_\bullet$; thus their detection rates (MM15, Stone and Metzger 2016).

The TDE detection rate depends on the BHMF and thus the reverse can be done, that is by knowing the detection rate of TDEs through observations, one can derive the BHMF. Donley *et al.* (2002); van Velzen and Farrar (2014) have used the observed detection rates to calculate the theoretical TDEs rate per galaxy and is found to be $\sim 10^{-5}$ yr^{-1} galaxy^{-1} which is less than the observed rate by $\sim 10^{-4}$ yr^{-1} galaxy^{-1}. Stone and Metzger (2016) have used the Nuker density

profile for a sample of galaxies to calculate the TDE rates $\dot{N}_t$ and using a Schechter LF with occupation fraction f_{occ}, which is the probability of the occurrence of a black hole with mass $M_\bullet$ for a the given bulge mass, calculated the volumetric detection rate of TDEs. They also calculated the SMBH mass distribution of observed TDEs and found that it is dominated by TDEs in optical emissions. The theoretical capture rate $\dot{N}_t \propto M_\bullet^{-\beta}$ was found where $\beta = 0.19$ (Magorrian and Tremaine 1999), 0.25 (Wang and Merritt 2004), 0.404 (Stone and Metzger 2016) and 0.3 (MM15); the decrease in $\dot{N}_t$ with $M_\bullet$ is small which implies that the low observation rate of high mass SMBH TDEs is due to the BHMF. Kochanek (2016) has shown using the LF given in Shankar *et al.* (2009), that the dominance of low mass SMBHs in observed TDEs are driven by the steep slope of BHMF rather than the mass dependence TDE rates.

Kiang (1961) has found that the LF of galaxies in terms of magnitude is given by $\phi(M) \propto (M - M_0)^k$ for faint galaxies and is $\phi(M) \propto 10^{0.2M}$ for bright galaxies (Zwicky 1957), where M is the magnitude, M_0 is the limiting magnitude and k is constant. Peebles (1968) found that the bright galaxies drops sharply compared to the previous estimates with $\phi(M) \propto \exp[\alpha(M - M_0)]$, where α is a constant. Press and Schechter (1974) have shown that an initial perturbation in a self-gravitating gas condenses the mass into aggregates whose mass function is given by $\phi(m)\mathrm{d}m \propto (m/m_c)^{-1-\alpha_1} \exp(-(1/2)(m/m_c)^{2(1-\alpha_1)})\mathrm{d}m$, where m_c is the mass at initial perturbation and the mass dispersion of aggregates in volume V is $\propto V^{\alpha_1}$. If one considers that the this mass spectrum extends to galactic mass scale, then using a mass to light ratio given by $m \propto L^\beta$, one can obtain $\phi(L) \propto (L/L_\star)^{\beta-1+(1+\alpha_1)/\beta} \exp(-(1/2)(L/L_\star)^{2(1-\alpha_1)/\beta})$ where $L_\star$ is the luminosity for $m = m_s$ which follows the Schechter LF for $\alpha_1 = 0.456$ and $\beta = 1.088$.

Table 7.9 shows the various LFs in use to fit the surveys given in in Table 7.10. The observations from various galaxies at different redshifts are divided in various redshift bins and the LFs are used to fit the observed profile. The fit at various

redshift bins provides the evolution of the LF in the universe observed. The observed profile in optical and UV bands are mostly fit with the Schechter LF whereas Böhringer *et al.* (2014) have found that the profile in X-ray shows better fit with the modified Schechter function. A double power law profile is also used to fit the observations; Maloney and Petrosian (1999) found that the inner slope is similar to the fit to the Schechter function. Magnelli *et al.* (2013) using the IR band observations showed that the break luminosity increases with redshift. The hard X-ray luminosity function is fit with the LDDE model (Ueda *et al.* 2003) as done by the La Franca *et al.* (2005).

As the Schechter function shows a good fit to the observations, we have used it in our model of TDE rates along with the duty cycle and by matching it to the observed TDE rates, the obtained Schechter parameters are given in Table 7.8. The mean Schechter parameters over γ is found to be $\phi_\star = 10^{-4}$ Mpc^{-3}, $L_\star = (1.16 \pm 0.15) \times 10^{42}$ erg sec^{-1} and $\alpha = 1.021 \pm 0.16$.

By comparing the Schechter parameters obtained from previous estimates given in Table 7.11, we can see that our model with $\gamma = 0.9$ is close to the previous estimates (Brown *et al.* 2001; Montero-Dorta and Prada 2009; Wylezalek *et al.* 2014):

$$\alpha = 1.093, \quad \phi_\star = 10^{-4} \text{ Mpc}^{-3} \quad \text{and} \quad L_\star = 1.13 \times 10^{42} \text{ erg sec}^{-1}. \tag{7.31}$$

The Fig 7.15 and 7.16 show the detectable rate per unit black hole mass and star mass for various missions obtained using eqn (7.21). The rate decreases with black hole mass due to a decrease in BHMF and with star mass due to stellar initial mass function. Given the BHMF and the theoretical capture rate in a galaxy given by eqn (5.47), the galaxy averaged theoretical capture rate is given by

$$\left\langle \dot{N}_t \right\rangle = \frac{\int_{M_\bullet=10^6 M_\odot}^{10^8 M_\odot} \int_{z=0}^{1} \frac{\mathrm{d}\dot{N}_t}{\mathrm{d}M_\bullet} \Phi(M_\bullet,\ z)\, \mathrm{d}z \mathrm{d}M_\bullet}{\int_{M_\bullet=10^6 M_\odot}^{10^8 M_\odot} \int_{z=0}^{1} \Phi(M_\bullet,\ z)\, \mathrm{d}z \mathrm{d}M_\bullet}, \tag{7.32}$$

and is shown in Fig 7.17 where it is found that $\left\langle \dot{N}_t \right\rangle \sim 2 \times 10^{-5} \gamma^2$ yr^{-1}.

The observed TDE rate depends on the sample of galaxies in a given cosmological volume and is essentially the galaxy averaged capture rate as the TDE sources lie at different redshifts. We can see that the galaxy averaged capture rate from our statistical analysis of the surveys is close to the observed range. A detailed modeling of the galactic nuclei considering an anisotropic distribution and including the resonant relaxation along with the two body relaxation mechanism is however required for a better understanding of the event rates.

7.4 Summary

We summarize our results below.

- We had used Mageshwaran and Mangalam (2015) and Mageshwaran & Mangalam (2017) models to fit the light curve of sources given in Table 2.1 to extract the paramteres such as $M_\bullet$, $M_\star$, $\bar{e}$ and ℓ.
- With the distribution of $M_\bullet$ with z, we find the best fit luminosity function and Schechter parameters.
- We infer that $\gamma = 0.9$, is the optimal solution that matches the observed Schechter parameters and the best inferred Schechter parameters from our model fit is $\alpha = 1.093,\ \phi_\star = 10^{-4}$ Mpc^{-3} and $L_\star = 1.13 \times 10^{42}$ erg sec^{-1}.

- The galaxy averaged capture rate is $\left\langle \dot{N}_t \right\rangle \sim 2 \times 10^{-5} \gamma^2$ yr^{-1} which is comparable with observations. Thus, the rate tension between observation ($\sim 10^{-5}$ yr^{-1}) and theory ($\sim 10^{-4}$ yr^{-1}) for individual galaxies can be explained by the statistical average over the BHMF. More detailed dynamical models with resonant relaxation and axisymmetric nuclei, may be necessary to confirm this result.

Survey	t_s (yr)	$N_{D,obs}$
ASAS-SN	~ 4	3
PTF	~ 4	4
iPTF	~ 4	2
PS-MDS	~ 4	2
GALEX	~ 10	3

TABLE 7.6: The TDE surveys with the duration of survey t_s and the number of TDEs detected N_D for the sample of TDEs given in Table 2.1.

γ	$\phi_\star$ (Mpc^{-3})	$M_s(10^6\ M_\odot)$	β	ϵ	$F_{min}(\phi_\star,\ \beta,\ M_s)$
0.6	10^{-4}	0.78	-0.843	0.823	39.27
0.7	10^{-4}	0.66	-0.874	0.823	39.55
0.8	10^{-4}	0.56	-0.944	0.823	39.73
0.9	10^{-4}	0.57	-1.077	0.823	39.85
1.0	10^{-4}	0.538	-1.1876	0.823	39.924
1.1	10^{-4}	0.484	-1.166	0.823	39.967

TABLE 7.7: The obtained parameters by minimizing eqn (7.28) with minimum value of $F(\phi_\star,\ \beta,\ M_s)$.

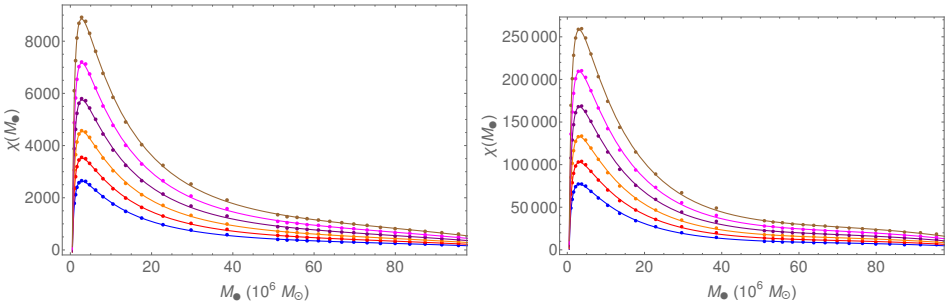

(a) ASASSN

(b) PTF

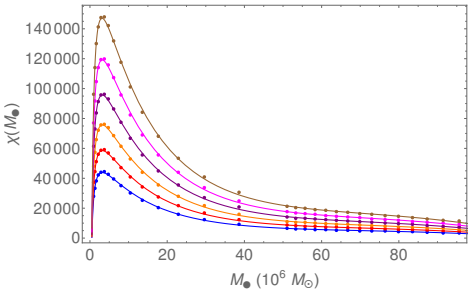

(c) iPTF

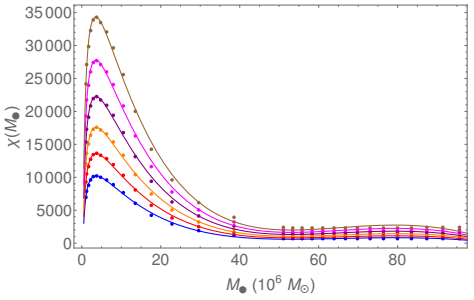

(d) PS-MDS

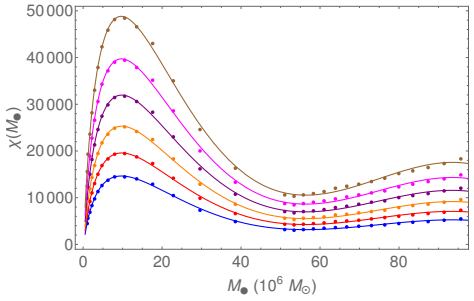

(e) GALEX

FIGURE 7.14: The $\chi(M_\bullet)$ as a function of $M_6 = M_\bullet/10^6 M_\odot$ for various $\gamma = 0.6$ (blue), 0.7 (red), 0.8 (orange), 0.9 (purple), 1.0 (magenta), 1.1 (brown) are shown. The points denotes the numerically obtained $\chi(M_\bullet)$ and solid lines denotes the fit.

γ	α	$\phi_\star$ (Mpc^{-3})	$L_\star(10^{42}$ erg sec$^{-1})$
0.6	0.809	10^{-4}	1.47
0.7	0.846	10^{-4}	1.27
0.8	0.932	10^{-4}	1.12
0.9	1.093	10^{-4}	1.13
1.0	1.228	10^{-4}	1.08
1.1	1.202	10^{-4}	0.99

TABLE 7.8: The obtained Schechter parameters from the obtained values given in Table 7.7.

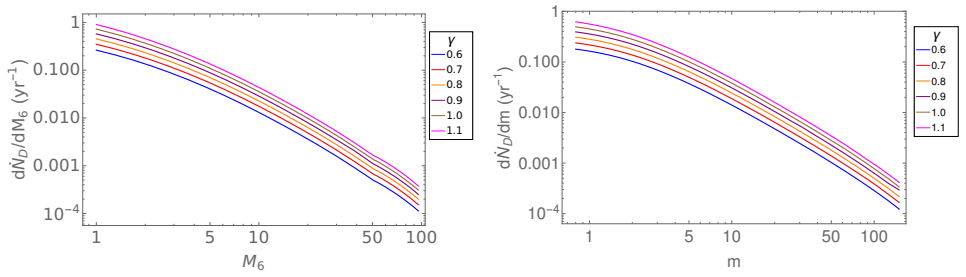

(a) ASASSN

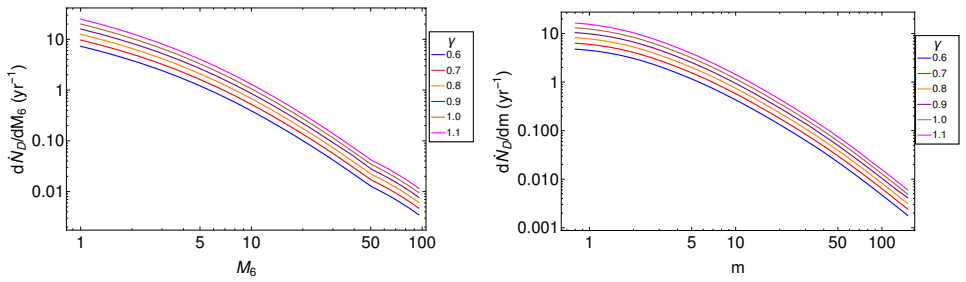

(b) PTF

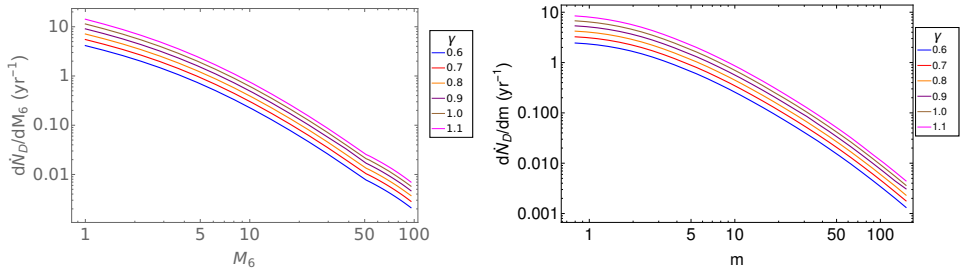

(c) iPTF

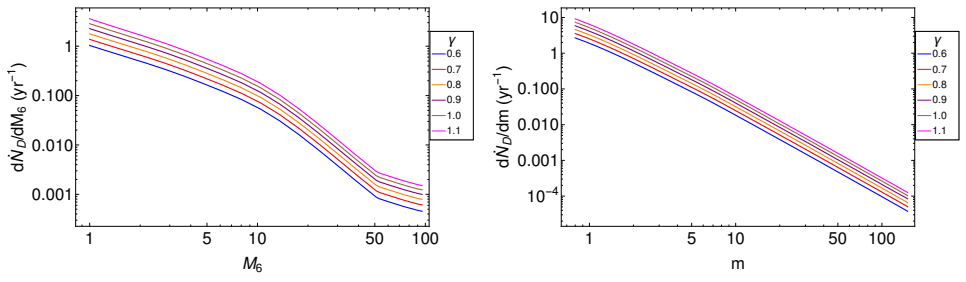

(d) Pan-STARRS

FIGURE 7.15: The detectable TDE rates per unit black hole mass (left) and star mass (right) are shown for various γ. The rate decreases with black hole mass due to decrease in BHMF and with star mass due to stellar initial mass function.

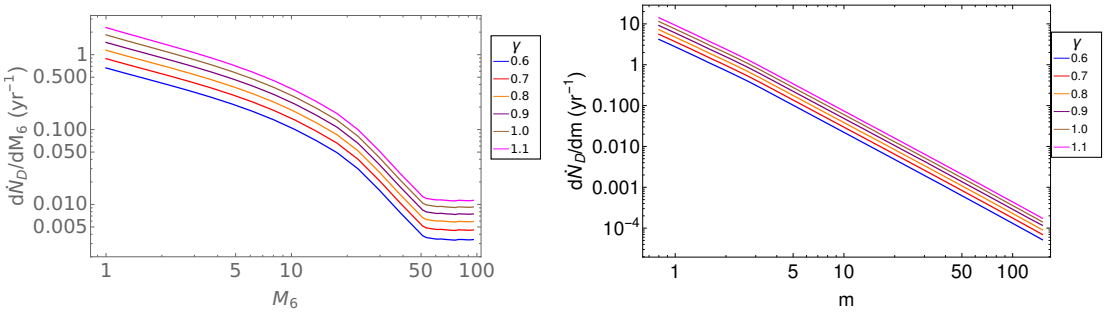

(a) GALEX

FIGURE 7.16: The detectable TDE rates per unit black hole mass (left) and star mass (right) for various γ are shown. The rate decreases with black hole mass due to decrease in BHMF and with star mass due to stellar initial mass function.

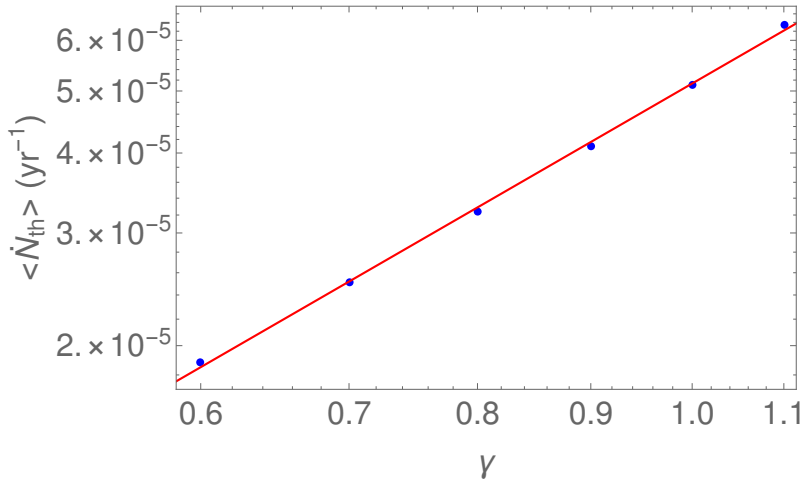

FIGURE 7.17: The galaxy averaged theoretical capture rate is shown and found to be $\left\langle \dot{N}_t \right\rangle \sim 2 \times 10^{-5} \gamma^2$ yr^{-1}.

Sl.	Model	Luminosity function	Parameters	References
1	Schechter	$\phi(L)\mathrm{d}L = \phi_\star \left(\frac{L}{L_\star}\right)^{-\alpha} \exp\left(-\frac{L}{L_\star}\right) \frac{\mathrm{d}L}{L_\star}$	$\alpha,\ \phi_\star,\ L_\star$	Schechter (1976)
		$\phi(M)\mathrm{d}M = 0.4\ln(10)\phi_\star 10^{-0.4(M-M^\star)(1-\alpha)} \exp(-10^{-0.4(M-M^\star)})\mathrm{d}M$	$\alpha,\ \phi_\star,\ M^\star$	
2	Double power law	$\phi(L)\mathrm{d}L = \phi_\star \left[\left(\frac{L}{L_\star}\right)^{k_1} + \left(\frac{L}{L_\star}\right)^{k_2}\right]^{-1} \frac{\mathrm{d}L}{L_\star}$	$\phi_\star,\ L_\star,\ k_1,\ k_2$	Maloney and Petrosian (1999) Hopkins *et al.* (2007)
3	q exponential	$\phi(L)\mathrm{d}L = \phi_\star \left(\frac{L}{L_\star}\right)^{-\alpha} \left[1 + (1-q)\frac{L}{L_\star}\right]^{\frac{1}{1-q}} \frac{\mathrm{d}L}{L_\star}$	$\phi_\star,\ \alpha,\ L_\star,\ q$	Balaguera-Antolínez *et al.* (2012) Böhringer *et al.* (2014)
4	Modified Schechter	$\phi(L)\mathrm{d}L = \phi_\star \left(\frac{L}{L_\star}\right)^{-\alpha} \exp\left(-\frac{L}{L_\star}\right) \left[1 - \left(1 + \frac{L}{\beta L_\star}\right)^{-\gamma}\right] \frac{\mathrm{d}L}{L_\star}$	$\alpha,\ \phi_\star,\ L_\star,\ \beta,\ \gamma$	Böhringer *et al.* (2014)
5	Evolution model	$\frac{\mathrm{d}\phi(L)}{\mathrm{d}\log L} = \phi_\star \left[\left(\frac{L}{L_\star}\right)^{k_1} + \left(\frac{L}{L_\star}\right)^{k_2}\right]^{-1},$	$\phi_\star,\ L_\star,\ k_1,\ k_2$	Ueda *et al.* (2003)
		Evolution factor $e(z) = \begin{cases} (1+z)^{p_1}, z < z_c \\ e(z_c)\left(\frac{1+z}{1+z_c}\right)^{p_2}, z > z_c \end{cases}$	$p_1,\ p_2,\ z_c$	
	Pure luminosity evolution (PLE)	$\frac{\mathrm{d}\phi(L/e(z))}{\mathrm{d}\log L}$		
	Pure density evolution (PDE)	$\frac{\mathrm{d}\phi(L)}{\mathrm{d}\log L} e(z)$		
6	Luminosity dependent-	$\frac{\mathrm{d}\phi(L)}{\mathrm{d}\log L} = \phi_\star \left[\left(\frac{L}{L_\star}\right)^{k_1} + \left(\frac{L}{L_\star}\right)^{k_2}\right]^{-1}, \quad \frac{\mathrm{d}\phi(L,\ z)}{\mathrm{d}\log L} = \frac{\mathrm{d}\phi(L)}{\mathrm{d}\log L} e(z,\ L),$	$\phi_\star,\ L_\star,\ k_1,\ k_2$	Ueda *et al.* (2003)
	density evolution (LDDE)	$e(z,\ L) = \begin{cases} (1+z)^{p_1}, z < z_c(L) \\ e(z_c)\left(\frac{1+z}{1+z_c(L)}\right)^{p_2}, z > z_c(L) \end{cases},$	$p_1,\ p_2,\ L_a,\ z_c^\star$	Shankar *et al.* (2009)
		$z_c(L) = \begin{cases} z_c^\star, L < L_a \\ z_c^\star \left(\frac{L}{L_a}\right)^\alpha, L > L_a \end{cases}$		

TABLE 7.9: The various luminosity functions with their fitting parameters in terms of luminosity L or absolute magnitude M are given above.

Sl.	References	Survey	Redshift	Survey area/ # of QSO	Band	Model LF
1	Gardner *et al.* (1997)	Wide-Field K-Band Survey		4.4 deg^2	K band	Schechter
2	Maloney and Petrosian (1999)	Large Bright QSO survey Homogenous Bright QSO survey Durham/AAT survey	$0.3-2.2$ $0.3-2.2$ $0.3-2.2$	1055 285 419	B band B band B band	Combining together, Double power law profile
3	Brown *et al.* (2001)	Century survey	$0.003-0.15$	64 deg^2	V and R band	Schechter
4	Norberg *et al.* (2002)	2dF Galaxy Redshift Survey	~ 0	2151.6 deg^2	b_J band	Schechter
5	Willott *et al.* (2005)	CFHT	$5.7-6.4$	3.83 deg^2	i$'$ and z$'$ bands	double power law
6	La Franca *et al.* (2005)	HELLAS2XMM sample + other catalog	$0-4$	508 AGNs	$2-10$ keV	LDDE model
7	Willmer *et al.* (2006)	DEEP2 Redshift Survey	$0.2-1.2$	11,284	B, R and V bands	Schechter
8	Zucca *et al.* (2006)	VIMOS VLT Deep Survey	$0.2-1.5$	0.61 deg^2	UBVRI bands	Schechter
9	Babbedge *et al.* (2006)	Spitzer Wide-area Infrared Extragalactic Legacy Survey	$0-4$	6.5 deg^2	3.6, 4.5, 5.8, 8 and 24 μm	Schechter Double power law
10	Vestergaard *et al.* (2008)	SDSS DR3	$0.3-5$	1644 deg^2	i-band	$\phi(M) \propto M^{\beta}$
11	Montero-Dorta and Prada (2009)	SDSS DR6	$0.02-0.17$	7425 deg^2	u band	Schechter
12	Vestergaard and Osmer (2009)	Large Bright Quasar Survey Bright Quasar Survey Fall Equatorial Stripe (SDSS)	$0.2-3.4$ $z \leq 0.5$ $3.6-5$	453.8 deg^2 10714 deg^2 182 deg^2	B_J band B_J band griz bands	$\phi(M) \propto M^{\beta}$
13	Richards *et al.* (2009)	SDSS (DR6)		8417 deg^2		
14	Rodighiero *et al.* (2010)	Deep Spitzer surveys	$0-2.5$	0.85 deg^2	8, 12, 15, 24 μm	
15	Magnelli *et al.* (2013)	Herschel -PACS far-infrared survey	$0.1-2.3$		IR (70, 100, 160 μm)	$L < L_\star:\ \phi(L) = \phi_\star(L/L_\star)^{-0.6}$ $L > L_\star:\ \phi(L) = \phi_\star(L/L_\star)^{-2.2}$
16	Böhringer *et al.* (2014)	REFLEX II	$0-0.4$	13,924 deg^2	X-ray ($0.1-2.4$ keV)	Schechter q exponential Modified Schechter
17	Wylezalek *et al.* (2014)	Spitzer snapshot program CARLA	$1.3-3.2$	420 radio loud AGNs	4.5 μm mid-IR	Schechter $M^\star$ is apparent magnitude here
18	Eardley *et al.* (2015)	Galaxy and Mass Assembly survey (GAMA)	$0.04-0.26$	1,13,000	r band	Schechter

TABLE 7.10: The surveys in various spectral bands to obtain the luminosity function are shown with fit to the LF model given in Table 7.9. The Schechter parameters are listed as (α, $L_\star$(erg sec^{-1}) or $M^\star$, $\phi_\star$(Mpc^{-3}))

Sl.	α	$\phi_\star$ (10^{-4} Mpc^{-3})	$L_\star$ (10^{45} erg sec^{-1})	References
1	0.9 ± 0.1	57.1 ± 5	2.98 ± 0.19	Gardner *et al.* (1997)
2	1.07 ± 0.09	160 ± 3	0.076 ± 0.002	Brown *et al.* (2001)
3	1.21 ± 0.3	55 ± 2	0.12 ± 0.038	Norberg *et al.* (2002)
4	1.3	2.61 ± 2.1	0.84 ± 0.004	Willmer *et al.* (2006)
5	1.0 ± 0.04	100 ± 3	0.002 ± 0.0001	Montero-Dorta and Prada (2009)
6	1.74 ± 0.087	0.005	0.302 ± 0.066	Böhringer *et al.* (2014)
7	1.01 ± 0.1	N/A	0.043 ± 0.0043	Wylezalek *et al.* (2014)
8	1.22 ± 0.02	900 ± 7	0.42 ± 0.008	Eardley *et al.* (2015)

TABLE 7.11: Schechter parameters obtained from previous surveys listed in Table 7.10.

Chapter 8

Summary, conclusions and caveats

One of the big mysteries about the black hole at the center of the galaxy is, 'Why don't we see emission from matter falling onto the black hole, or, rather, the black hole eating up its surroundings?'

Andrea M. Ghez, September 14, 2009 in EarthSky.org

This thesis is devoted to a study of the physics of transients known as tidal disruption events and their observational implications. We have studied various dynamical aspects of TDEs starting from the capture of star by the black hole to their disruption, accretion and observations by various surveys. In this chapter, we summarize the thesis, discuss the novel aspects and its impact. We will then discuss the implications for future theoretical work.

8.1 Highlights

Below, we summarize the highlights of each chapter in sequence:

- *Chapter 1:* The basic dynamics of TDEs is developed. A tidally disrupted star debris following a Keplerian orbit falls back with a rate $\propto t^{-5/3}$ at late stages. This law is considered to be the characteristic decay model of light curves for early TDE observations and is used to confirm the source as a TDE.

- *Chapter 2:* The TDEs are mostly identified through the broad Hα, Hβ and sometimes He emission lines in their spectra. The X-ray TDEs can be distinguished from AGN variability by (1) the nature of host galaxy, (2) slow decay in time suggesting coherent decay, (3) low hardness ratio suggests soft nature of the TDEs. The TDEs are observed in the distinct type of galaxies that are mostly inactive and the star-forming galaxies.

- *Chapter 3:* We studied the basic dynamics of stars around black holes in the center of galaxies. The gravitational interaction of star results in the change in energy and angular momentum leading to the diffusion of stars that results in the evolution of central sellar cusp and density attains a form $\rho \propto r^p$, where $p \simeq -7/4$ if a steady state is reached. The presence of a tidal radius results in a loss cone in phase space such that any star with angular momentum within the loss cone will be tidally disrupted. With a steady loss cone model, the theoretical capture rate is found to be $\sim 10^{-4}$ yr^{-1}.

- *Chapter 4:* The disrupted debris forms a gaseous disk which can accrete in either sub-Eddington or super-Eddington modes. The viscosity in the accretion disk results in the angular momentum transfer outwards which results in expansion of the outer radius. The microscopic viscosity is negligible in case of an accretion disk and thus a possible source of turbulent viscosity depends

on the nature of pressure in the disk that may either magnetic pressure, gas pressure or radiation pressure. The gravitational instability is also a source of viscosity which is effective for higher density where the self-gravity dominates over the external gravity; however, this is not likely for TDE disks. In the case of a sub-Eddington disk, the radiation pressure is smaller than the gas pressure and the disk is thin whereas, for a super-Eddington disk, the strong radiation pressure results in an out flowing wind and the resulting disk is a slim disk.

- *Chapter 5:* We have constructed a dynamical model of TDEs with the input physical parameters that include the black hole mass $M_\bullet$, specific orbital energy E and angular momentum J, star mass $M_\star$ and radius $R_\star$ (Mageshwaran and Mangalam (2015)). The maximum value of J is $J_{lc}(E,\ r_t)$ and as $J_{lc}(E,\ r_t) \geq 0$, the maximum value of energy is $E_m = \Phi(r_t)$. We define the dimensionless energy $\bar{e} = E/E_m$ and angular momentum $\ell = J/J_{lc}$ and the constrained in energy and angular momentum phase space is given by $\bar{e}_h = r_t/r_h < \bar{e} < 1$ and $0 < \ell < 1$. We have derived the DF for stellar density profile $\rho(r) \propto r^\gamma$ with mass function $\xi(m)\mathrm{d}m$ given in Kroupa (2001) and solved the steady state Fokker-Planck equation to obtain $\dot{N}_t$. The capture rate obtained by integrating over phase space in the range $\bar{e}_h < \bar{e} < 1,\ 0 < \ell < 1$ and $0.8 < m < 150$ where $m = M_\star/M_\odot$ is found to be $\dot{N}_t \propto M_\bullet^{-0.3}$ and $\dot{N}_t \propto \gamma^{2.1}$.

- *Chapter 5:* We have calculated the mass fallback rate of the debris as a function of E and J which includes the case of mass fallback rate obtained by Lodato *et al.* (2009) for a star on parabolic orbit with $E = 0$ and $J = \sqrt{2GM_\bullet r_t}$. Following the steady accretion model of Strubbe and Quataert (2009) with accretion rate similar to $\dot{M}_{fb}$, we simulated the light curve profiles in various spectral bands. With the given instrumental parameters such as sensitivity, cadence t_{cad} and the integration time t_{int} of the detector, the cosmological parameters and the black hole mass function of

quiescent galaxies (Hopkins *et al.* 2007; Chen *et al.* 2007), we calculated the detection rate of TDEs for optical surveys such as LSST to be 5003 yr^{-1}, Pan-STARRS 3π to be 6337 yr^{-1}, Pan-STARRS medium deep survey to be 12.5 yr^{-1} and for X-ray mission eROSITA to be 679.5 yr^{-1} (MM15). These estimates are in agreement with estimates of van Velzen *et al.* (2011) who scaled up SDSS results to other surveys.

- *Chapter 6:* We have constructed self-similar models of a time-dependent accretion disk in both sub and super-Eddington phases with wind outflows for tidal disruption events (TDEs). The physical input parameters are the black hole (BH) mass $M_\bullet$, specific orbital energy E and angular momentum J, star mass $M_\star$ and radius $R_\star$. We consider the sub-Eddington and super-Eddington phases to be gas pressure or radiation pressure dominated with the viscosity prescribed by the stress tensor, $\Pi_{r\phi} \propto \Sigma_d^b r^d$ where Σ_d is the surface density of the disk, r is the radius and b and d are constants. The specific choice of radiative or α viscosity and its parameters is decided by the expected disk luminosity and evolution time scale being in the observed range. The disk evolves due to mass loss by accretion onto the black hole and an outflowing wind, and mass gain by fallback of the debris; this results in an increasing outer radius. The bolometric luminosity of the model A is given by $L_b \propto t^{-1}(\xi_{out}^{3/4} - \xi_{in}^{3/4})$ (see eqn 6.91) and the net bolometric luminosity at late time is found to be $L_b \propto t^{-0.7}$. The bolometric disk luminosity for model B is $L_b^d \propto t^{-5/3+(3-2e)\alpha}(\xi_{out}^{9/4-2e} - \xi_{in}^{9/4-2e})$ and the outflow luminosity $L_b^w \propto (\mathcal{W}^2(t/t_0)^{(-10/3-\alpha/2)} + 1 - c_2)^4 \ln(r_{out}/r_{in})$ where α, e and c_2 are considered to be a free parameters which are obtained by fit to the observations.

- *Chapter 7:* We fit our time-dependent accretion models developed in chapter 6 to the observations given in Table 2.1. We found that the time-dependent model gives a good fit compared to the steady accretion model. We found through fits that the TDEs are dominated by disruption of low mass stars by low mass supermassive black holes; this is expected as both are dominant

populations. Using the stellar dynamical model developed in chapter 5 and the Schechter luminosity function, we obtained detectable rates for various surveys and by comparing it to the observed rate, we derived the most probable Schechter parameters as a function of γ and that are in broad agreement with the previous estimates for $\gamma = 0.9$. The galaxy averaged capture rate inferred by the TDE models applied to the survey data is smaller than the typical theoretical capture rate.

8.2 The novel aspects and their impact

1. We have included the angular momentum of the star in the stellar model for TDEs that has not taken been into account in previous work. The inclusion of angular momentum plays a crucial role in the calculation of capture rate and the mass fallback rate. We have calculated the capture rate per unit energy and angular momentum and integrated over them to calculate the net rate.

2. We calculated the TDE detectable rates by various surveys which are in good agreement with previous estimates.

3. The TDE physics we have employed includes all the essentials of accretion, fall back, and the wind; we have presented hydrodynamic criteria for the operation of the wind with $v_z^2 \propto (T - T_E)$ given by eqn (6.26). We have demonstrated in §6.2 that the timescales of evolution and magnitude of the bolometric luminosity are in good agreement with typical observed values. The detailed fits produced by models A and B in §7.1 produce good χ^2 values. This validates our simplified semi-analytic models that are calculated from a basic dynamical input set of parameters given in Table 6.1. Models A and B are clearly favored over steady models C and D.

4. We have also studied the transition dynamics from one to another disk. Since TDE disks undergo multiple phase evolution, our transition model can provide transition time and the basic parameters during the transition.

5. The simple model for the extraction of BHMF (§7.2) provides the Schechter parameters $\alpha = 1.093$, $\phi_\star = 10^{-4}$ Mpc^{-3} and $L_\star = 1.13 \times 10^{42}$ erg sec^{-1}, which is close to the previous estimates for $\gamma = 0.9$. If one is provided with the detectable rates from a larger set of observations, our model can be used to calculate the black hole mass function more precisely.

6. The galaxy averaged capture rate $\left\langle \dot{N}_t \right\rangle \sim 2 \times 10^{-5}\gamma^2$ yr^{-1} is comparable with the observations. However, the rate tension between individual galaxy and observations require more detailed dynamical models.

We have demonstrated that basic physics of the gas and stellar dynamics can provide a reasonably good explanation of the tidal disruption events. TDEs are excellent laboratories to study accretion physics: the fact that certain viscosity models in chapter 6 were eliminated indicates that they are good discriminators of the underlying physics. As more data of detections pour in from follow up surveys like LSST, zPTF, eROSITA, ASTROSAT etc, they can be used to create larger sample sets for statistical studies of black hole demographics as has been demonstrated. It will perhaps be more accurate than current methods in the future; currently it is a useful independent determinant.

8.3 Caveats

We list some of the caveats below:

1. The rate tension between the theory and observations require a more detailed modeling of the galaxy centers. A time-dependent loss cone theory with a resonant relaxation mechanism for non-spherical galactic nuclei is to be developed.

2. There is likely to be an α viscous sub-Eddington disk which would be operative during the rising phase. The typical time scale of this phase will be given by either the typical rise time in the $\dot{M}$ profile or the time taken to reach the Eddington luminosity. A detailed model during the rising phase needs to be developed.

3. If there is a super-Eddington phase to follow as determined by eqn (6.10), then the typical time scale would be given by eqn (6.65). The super-Eddington disk will be effected by radiative viscosity with a wind launched from the photosphere. During the onset and the decline of this super-Eddington phase, the wind is rendered weak in our models and we have illustrated in §6.6 a method of calculating this transition through model T so that the light curves smoothly connect to the sub-Eddington regimes. We are yet to include model T to our fits which is numerically more challenging and plan to do so in the next phase.

4. While our time-dependent models are reasonably successful in producing fits to the four diverse TDE sources chosen here, we plan on producing fits to a larger sample of light curves available in the literature with a higher resolution search in parameter space. In the fits produced thus far, we have been able to extract the mass of the star and its orbital elements, the black hole mass, and the initial accretion disk radius. The parameter search was limited by numerical resources; in the future, we plan on doing more extensive simulations.

5. The basic paradigm is sufficiently elaborate in terms of essential physics; it also transparently and adequately demonstrates the existence of two different

phases with a transition model that produces reasonably good fits. In the future, we plan to add an atmosphere to predict the details of the spectrum.

6. One can with a large statistics of detection that will soon become available, infer the basic parameters using our models and study the demographics of the black hole mass and stellar properties such as mass and evolutionary state as a function of redshift (Kochanek 2016, Stone and Metzger 2016).

8.4 Future directions

1. A more detailed modeling of the galaxy centers by including the resonant relaxation and for an axisymmetric nuclei is to be done.

2. The time-dependent accretion model developed here is for non-relativistic disks. For higher mass black holes, the tidal radius is close to the horizon and thus it is necessary to construct a time-dependent relativistic accretion model with all the essential physics of accretion, fallback and wind.

3. It is also desirable and possible in the future to add black spin and mass evolution to predict the jet phase.

4. Given the possibility of detection of gravitational waves of these events as extreme mass ratio inspirals in the frequency window of eLISA ($10^{-4} - 10^{-1}$ Hz), we need to develop theoretical tools for the dynamics and templates of detection.

Given that a high detectable event rate will become possible soon with eROSITA in X-rays and iPTF/ZTF, ASAS SN and Pan-STARRS in the optical, there are several opportunities available currently and the future. The area of TDE physics is rich, bright and exciting.

THE END!

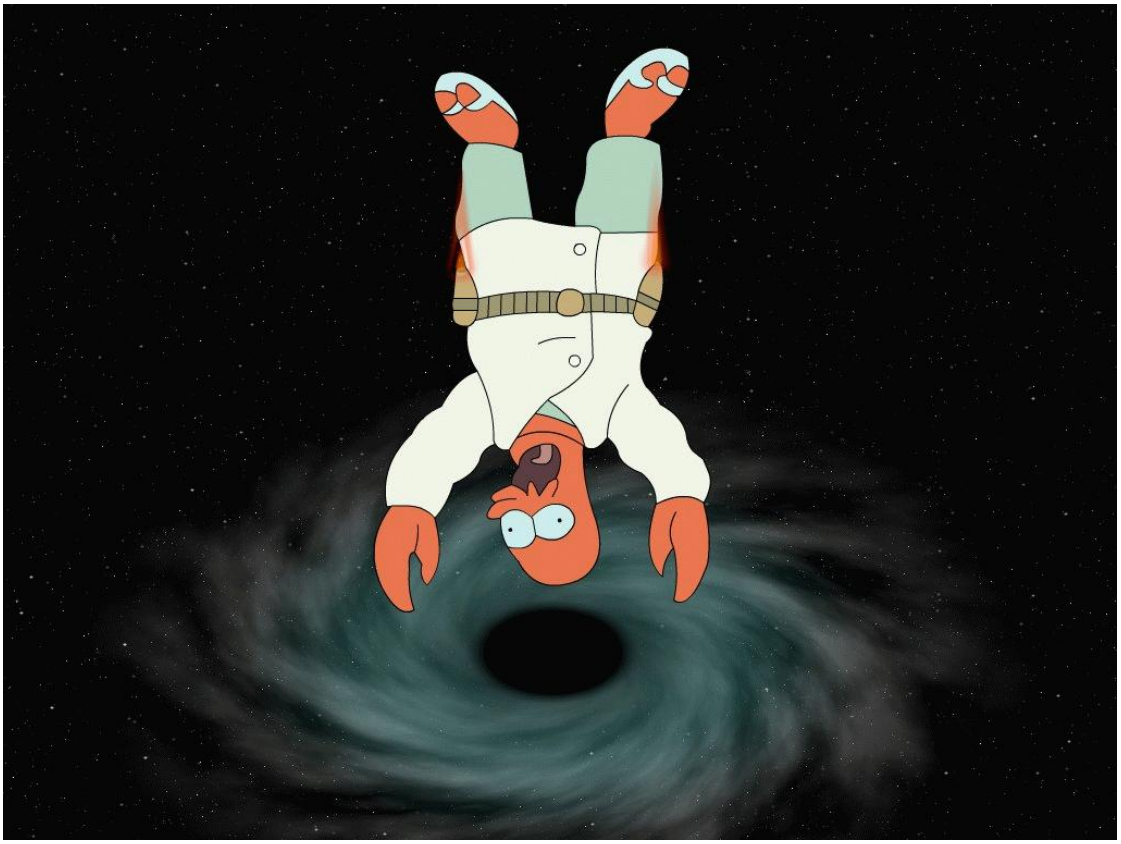

Bibliography

Abramowicz, M. A., Czerny, B., Lasota, J. P. and Szuszkiewicz, E., 1988, "Slim accretion disks", *Astrophys. J.*, **332**, 646–658. [DOI], [ADS]

Alexander, T. and Kumar, P., 2001, "Tidal Spin-up of Stars in Dense Stellar Cusps around Massive Black Holes", *Astrophys. J.*, **549**, 948–958. [DOI], [ADS], [astro-ph/0004240]

Aller, M. C. and Richstone, D., 2002, "The Cosmic Density of Massive Black Holes from Galaxy Velocity Dispersions", *Astron. J.*, **124**, 3035–3041. [DOI], [ADS], [astro-ph/0210573]

Arcavi, I., Gal-Yam, A., Sullivan, M., Pan, Y.-C., Cenko, S. B., Horesh, A., Ofek, E. O., De Cia, A., Yan, L., Yang, C.-W., Howell, D. A., Tal, D., Kulkarni, S. R., Tendulkar, S. P., Tang, S., Xu, D., Sternberg, A., Cohen, J. G., Bloom, J. S., Nugent, P. E., Kasliwal, M. M., Perley, D. A., Quimby, R. M., Miller, A. A., Theissen, C. A. and Laher, R. R., 2014, "A Continuum of H- to He-rich Tidal Disruption Candidates With a Preference for E+A Galaxies", *Astrophys. J.*, **793**, 38. [DOI], [ADS], [arXiv:1405.1415 [astro-ph.HE]]

Armijo, M. M. and de Freitas Pacheco, J. A., 2013, "PS1-10jh - a tidal disruption event with an extremely low disc temperature", *Mon. Not. Roy. Astron. Soc.*, **430**, L45–L48. [DOI], [ADS], [arXiv:1212.1140 [astro-ph.HE]]

Auchettl, K., Ramirez-Ruiz, E. and Guillochon, J., 2017, "Comparison of the X-ray emission from Tidal Disruption Events with those of Active Galactic Nuclei", *ArXiv e-prints*. [ADS], [arXiv:1703.06141 [astro-ph.HE]]

Babbedge, T. S. R., Rowan-Robinson, M., Vaccari, M., Surace, J. A., Lonsdale, C. J., Clements, D. L., Fang, F., Farrah, D., Franceschini, A., Gonzalez-Solares, E., Hatziminaoglou, E., Lacey, C. G., Oliver, S., Onyett, N., Pérez-Fournon, I., Polletta, M., Pozzi, F., Rodighiero, G., Shupe, D. L., Siana, B. and Smith, H. E., 2006, "Luminosity functions for galaxies and quasars in the Spitzer Wide-area Infrared Extragalactic Legacy Survey", *Mon. Not. Roy. Astron. Soc.*, **370**, 1159–1180. [DOI], [ADS], [astro-ph/0605305]

Bade, N., Komossa, S. and Dahlem, M., 1996, "Detection of an extremely soft X-ray outburst in the HII-like nucleus of NGC 5905.", *Astron. Astrophys.*, **309**, L35–L38. [ADS]

Bahcall, J. N. and Wolf, R. A., 1976, "Star distribution around a massive black hole in a globular cluster", *Astrophys. J.*, **209**, 214–232. [DOI], [ADS]

Balaguera-Antolínez, A., Sánchez, A. G., Böhringer, H. and Collins, C., 2012, "Constructing mock catalogues for the REFLEX II galaxy cluster sample", *Mon. Not. Roy. Astron. Soc.*, **425**, 2244–2254. [DOI], [ADS], [arXiv:1207.2138]

Baldwin, A., Phillips, M. M. and Terlevich, R., 1981, "Erratum - Classification Parameters for the Emission-Line Spectra of Extragalactic Objects", *Pub. Astron. Soc. Pac.*, **93**, 817. [DOI], [ADS]

Bardeen, J. M., Press, W. H. and Teukolsky, S. A., 1972, "Rotating Black Holes: Locally Nonrotating Frames, Energy Extraction, and Scalar Synchrotron Radiation", *Astrophys. J.*, **178**, 347–370. [DOI], [ADS]

Binney, J. and Tremaine, S., 2008, *Galactic Dynamics: Second Edition*, Princeton University Press, Princeton, NJ. [ADS]

Blagorodnova, N., Gezari, S., Hung, T., Kulkarni, S. R., Cenko, S. B., Pasham, D. R., Yan, L., Arcavi, I., Ben-Ami, S., Bue, B. D., Cantwell, T., Cao, Y., Castro-Tirado, A. J., Fender, R., Fremling, C., Gal-Yam, A., Ho, A. Y. Q., Horesh, A., Hosseinzadeh, G., Kasliwal, M. M., Kong, A. K. H., Laher, R. R., Leloudas, G., Lunnan, R., Masci, F. J., Mooley, K., Neill, J. D., Nugent, P., Powell, M., Valeev, A. F., Vreeswijk, P. M., Walters, R. and Wozniak, P., 2017, "iPTF16fnl: A Faint and Fast Tidal Disruption Event in an E+A Galaxy", *Astrophys. J.*, **844**, 46. [DOI], [ADS], [arXiv:1703.00965 [astro-ph.HE]]

Böhringer, H., Chon, G. and Collins, C. A., 2014, "The extended ROSAT-ESO Flux Limited X-ray Galaxy Cluster Survey (REFLEX II). IV. X-ray luminosity function and first constraints on cosmological parameters", *Astron. Astrophys.*, **570**, A31. [DOI], [ADS], [arXiv:1403.2927]

Bonnerot, C., Rossi, E. M., Lodato, G. and Price, D. J., 2016, "Disc formation from tidal disruptions of stars on eccentric orbits by Schwarzschild black holes", *Mon. Not. Roy. Astron. Soc.*, **455**, 2253–2266. [DOI], [ADS], [arXiv:1501.04635 [astro-ph.HE]]

Brem, P., Amaro-Seoane, P. and Sopuerta, C. F., 2014, "Blocking low-eccentricity EMRIs: a statistical direct-summation N-body study of the Schwarzschild barrier", *Mon. Not. Roy. Astron. Soc.*, **437**, 1259–1267. [DOI], [ADS], [arXiv:1211.5601]

Brown, G. C., Levan, A. J., Stanway, E. R., Tanvir, N. R., Cenko, S. B., Berger, E., Chornock, R. and Cucchiaria, A., 2015, "Swift J1112.2-8238: a candidate relativistic tidal disruption flare", *Mon. Not. Roy. Astron. Soc.*, **452**, 4297–4306. [DOI], [ADS], [arXiv:1507.03582 [astro-ph.HE]]

Brown, W. R., Geller, M. J., Fabricant, D. G. and Kurtz, M. J., 2001, "V- and R-band Galaxy Luminosity Functions and Low Surface Brightness Galaxies in the Century Survey", *Astron. J.*, **122**, 714–728. [DOI], [ADS], [astro-ph/0105186]

Bruzual, G. and Charlot, S., 2003, "Stellar population synthesis at the resolution of 2003", *Mon. Not. Roy. Astron. Soc.*, **344**, 1000–1028. [DOI], [ADS], [astro-ph/0309134]

Burrows, D. N., Kennea, J. A., Ghisellini, G., Mangano, V., Zhang, B., Page, K. L., Eracleous, M., Romano, P., Sakamoto, T., Falcone, A. D., Osborne, J. P., Campana, S., Beardmore, A. P., Breeveld, A. A., Chester, M. M., Corbet, R., Covino, S., Cummings, J. R., D'Avanzo, P., D'Elia, V., Esposito, P., Evans, P. A., Fugazza, D., Gelbord, J. M., Hiroi, K., Holland, S. T., Huang, K. Y., Im, M., Israel, G., Jeon, Y., Jeon, Y.-B., Jun, H. D., Kawai, N., Kim, J. H., Krimm, H. A., Marshall, F. E., P. Mészáros, Negoro, H., Omodei, N., Park, W.-K., Perkins, J. S., Sugizaki, M., Sung, H.-I., Tagliaferri, G., Troja, E., Ueda, Y., Urata, Y., Usui, R., Antonelli, L. A., Barthelmy, S. D., Cusumano, G., Giommi, P., Melandri, A., Perri, M., Racusin, J. L., Sbarufatti, B., Siegel, M. H. and Gehrels, N., 2011, "Relativistic jet activity from the tidal disruption of a star by a massive black hole", *Nature*, **476**, 421–424. [DOI], [ADS], [arXiv:1104.4787 [astro-ph.HE]]

Byun, Y.-I., Grillmair, C. J., Faber, S. M., Ajhar, E. A., Dressler, A., Kormendy, J., Lauer, T. R., Richstone, D. and Tremaine, S., 1996, "The Centers of Early-Type Galaxies With HST. II. Empirical Models and Structural Parameters", *Astron. J.*, **111**, 1889. [DOI], [ADS], [astro-ph/9602117]

Campana, S., Mainetti, D., Colpi, M., Lodato, G., D'Avanzo, P., Evans, P. A. and Moretti, A., 2015, "Multiple tidal disruption flares in the active galaxy IC 3599", *Astron. Astrophys.*, **581**, A17. [DOI], [ADS], [arXiv:1502.07184 [astro-ph.HE]]

Cannizzo, J. K., Lee, H. M. and Goodman, J., 1990, "The disk accretion of a tidally disrupted star onto a massive black hole", *Astrophys. J.*, **351**, 38–46. [DOI], [ADS]

Cenko, S. B., Bloom, J. S., Kulkarni, S. R., Strubbe, L. E., Miller, A. A., Butler, N. R., Quimby, R. M., Gal-Yam, A., Ofek, E. O., Quataert, E., Bildsten, L.,

Poznanski, D., Perley, D. A., Morgan, A. N., Filippenko, A. V., Frail, D. A., Arcavi, I., Ben-Ami, S., Cucchiara, A., Fassnacht, C. D., Green, Y., Hook, I. M., Howell, D. A., Lagattuta, D. J., Law, N. M., Kasliwal, M. M., Nugent, P. E., Silverman, J. M., Sullivan, M., Tendulkar, S. P. and Yaron, O., 2012a, "PTF10iya: a short-lived, luminous flare from the nuclear region of a star-forming galaxy", *Mon. Not. Roy. Astron. Soc.*, **420**, 2684–2699. [DOI], [ADS], [arXiv:1103.0779 [astro-ph.HE]]

Cenko, S. B., Krimm, H. A., Horesh, A., Rau, A., Frail, D. A., Kennea, J. A., Levan, A. J., Holland, S. T., Butler, N. R., Quimby, R. M., Bloom, J. S., Filippenko, A. V., Gal-Yam, A., Greiner, J., Kulkarni, S. R., Ofek, E. O., Olivares E., F., Schady, P., Silverman, J. M., Tanvir, N. R. and Xu, D., 2012b, "Swift J2058.4+0516: Discovery of a Possible Second Relativistic Tidal Disruption Flare?", *Astrophys. J.*, **753**, 77. [DOI], [ADS], [arXiv:1107.5307 [astro-ph.HE]]

Chandrasekhar, S., 1939, *An introduction to the study of stellar structure*, The University of Chicago press, Chicago, Ill. [ADS]

Chandrasekhar, S., 1943, "Dynamical Friction. I. General Considerations: the Coefficient of Dynamical Friction.", *Astrophys. J.*, **97**, 255. [DOI], [ADS]

Chen, Y.-M., Wang, J.-M. and Zhang, F., 2007, "Cosmological Evolution of the Duty Cycle of Quasars", in *The Central Engine of Active Galactic Nuclei*, (Eds.) Ho, L. C., Wang, J.-W., Astronomical Society of the Pacific Conference Series, 373, [ADS]

Chornock, R., Berger, E., Gezari, S., Zauderer, B. A., Rest, A., Chomiuk, L., Kamble, A., Soderberg, A. M., Czekala, I., Dittmann, J., Drout, M., Foley, R. J., Fong, W., Huber, M. E., Kirshner, R. P., Lawrence, A., Lunnan, R., Marion, G. H., Narayan, G., Riess, A. G., Roth, K. C., Sanders, N. E., Scolnic, D., Smartt, S. J., Smith, K., Stubbs, C. W., Tonry, J. L., Burgett, W. S., Chambers, K. C., Flewelling, H., Hodapp, K. W., Kaiser, N., Magnier, E. A., Martin, D. C., Neill, J. D., Price, P. A. and Wainscoat, R., 2014, "The Ultraviolet-bright, Slowly

Declining Transient PS1-11af as a Partial Tidal Disruption Event", *Astrophys. J.*, **780**, 44. [DOI], [ADS], [arXiv:1309.3009 [astro-ph.CO]]

Cohn, H. and Kulsrud, R. M., 1978, "The stellar distribution around a black hole - Numerical integration of the Fokker-Planck equation", *Astrophys. J.*, **226**, 1087–1108. [DOI], [ADS]

Donley, J. L., Brandt, W. N., Eracleous, M. and Boller, T., 2002, "Large-Amplitude X-Ray Outbursts from Galactic Nuclei: A Systematic Survey using ROSAT Archival Data", *Astron. J.*, **124**, 1308–1321. [DOI], [ADS], [astro-ph/0206291]

Dotan, C. and Shaviv, N. J., 2011, "Super-Eddington slim accretion discs with winds", *Mon. Not. Roy. Astron. Soc.*, **413**, 1623–1632. [DOI], [ADS], [arXiv:1004.1797 [astro-ph.HE]]

Dressler, A. and Gunn, J. E., 1983, "Spectroscopy of galaxies in distant clusters. II - The population of the 3C 295 cluster", *Astrophys. J.*, **270**, 7–19. [DOI], [ADS]

Eardley, E., Peacock, J. A., McNaught-Roberts, T., Heymans, C., Norberg, P., Alpaslan, M., Baldry, I., Bland-Hawthorn, J., Brough, S., Cluver, M. E., Driver, S. P., Farrow, D. J., Liske, J., Loveday, J. and Robotham, A. S. G., 2015, "Galaxy And Mass Assembly (GAMA): the galaxy luminosity function within the cosmic web", *Mon. Not. Roy. Astron. Soc.*, **448**, 3665–3678. [DOI], [ADS], [arXiv:1412.2141]

Esquej, P., Saxton, R. D., Freyberg, M. J., Read, A. M., Altieri, B., Sanchez-Portal, M. and Hasinger, G., 2007, "Candidate tidal disruption events from the XMM-Newton slew survey", *Astron. Astrophys.*, **462**, L49–L52. [DOI], [ADS], [astro-ph/0612340]

Esquej, P., Saxton, R. D., Komossa, S., Read, A. M., Freyberg, M. J., Hasinger, G., García-Hernández, D. A., Lu, H., Rodriguez Zaurín, J., Sánchez-Portal, M. and Zhou, H., 2008, "Evolution of tidal disruption candidates discovered by XMM-Newton", *Astron. Astrophys.*, **489**, 543–554. [DOI], [ADS], [arXiv:0807.4452]

Faber, S. M., Tremaine, S., Ajhar, E. A., Byun, Y.-I., Dressler, A., Gebhardt, K., Grillmair, C., Kormendy, J., Lauer, T. R. and Richstone, D., 1997, "The Centers of Early-Type Galaxies with HST. IV. Central Parameter Relations.", *Astron. J.*, **114**, 1771. [DOI], [ADS], [astro-ph/9610055]

Feldman, F. R., Weedman, D. W., Balzano, V. A. and Ramsey, L. W., 1982, "Emission-line widths in galactic nuclei", *Astrophys. J.*, **256**, 427–434. [DOI], [ADS]

Ferrarese, L. and Ford, H., 2005, "Supermassive Black Holes in Galactic Nuclei: Past, Present and Future Research", *Space Sci. Rev.*, **116**, 523–624. [DOI], [ADS], [astro-ph/0411247]

Ferrarese, L. and Merritt, D., 2000, "A Fundamental Relation between Supermassive Black Holes and Their Host Galaxies", *Astrophys. J. Lett.*, **539**, L9–L12. [DOI], [ADS], [astro-ph/0006053]

Frank, J. and Rees, M. J., 1976, "Effects of massive central black holes on dense stellar systems", *Mon. Not. Roy. Astron. Soc.*, **176**, 633–647. [ADS]

Frank, J., King, A. and Raine, D. J., 2002, *Accretion Power in Astrophysics: Third Edition*, Cambridge University Press, Cambridge, UK. [ADS]

Freitag, M. and Benz, W., 2002, "A new Monte Carlo code for star cluster simulations. II. Central black hole and stellar collisions", *Astron. Astrophys.*, **394**, 345–374. [DOI], [ADS], [astro-ph/0204292]

Gardner, J. P., Sharples, R. M., Frenk, C. S. and Carrasco, B. E., 1997, "A Wide-Field K-band Survey: The Luminosity Function of Galaxies", *Astrophys. J. Lett.*, **480**, L99–L102. [DOI], [ADS], [astro-ph/9702178]

Gezari, S., Basa, S., Martin, D. C., Bazin, G., Forster, K., Milliard, B., Halpern, J. P., Friedman, P. G., Morrissey, P., Neff, S. G., Schiminovich, D., Seibert, M., Small, T. and Wyder, T. K., 2008, "UV/Optical Detections of Candidate

Tidal Disruption Events by GALEX and CFHTLS", *Astrophys. J.*, **676**, 944–969. [DOI], [ADS], [arXiv:0712.4149]

Gezari, S., Heckman, T., Cenko, S. B., Eracleous, M., Forster, K., Gonçalves, T. S., Martin, D. C., Morrissey, P., Neff, S. G., Seibert, M., Schiminovich, D. and Wyder, T. K., 2009, "Luminous Thermal Flares from Quiescent Supermassive Black Holes", *Astrophys. J.*, **698**, 1367–1379. [DOI], [ADS], [arXiv:0904.1596 [astro-ph.CO]]

Gezari, S., Chornock, R., Rest, A., Huber, M. E., Forster, K., Berger, E., Challis, P. J., Neill, J. D., Martin, D. C., Heckman, T., Lawrence, A., Norman, C., Narayan, G., Foley, R. J., Marion, G. H., Scolnic, D., Chomiuk, L., Soderberg, A., Smith, K., Kirshner, R. P., Riess, A. G., Smartt, S. J., Stubbs, C. W., Tonry, J. L., Wood-Vasey, W. M., Burgett, W. S., Chambers, K. C., Grav, T., Heasley, J. N., Kaiser, N., Kudritzki, R.-P., Magnier, E. A., Morgan, J. S. and Price, P. A., 2012, "An ultraviolet-optical flare from the tidal disruption of a helium-rich stellar core", *Nature*, **485**, 217–220. [DOI], [ADS], [arXiv:1205.0252 [astro-ph.CO]]

Goldreich, P. and Lynden-Bell, D., 1965, "I. Gravitational stability of uniformly rotating disks", *Mon. Not. Roy. Astron. Soc.*, **130**, 97. [DOI], [ADS]

Grupe, D., Komossa, S. and Saxton, R., 2015, "IC 3599 Did It Again: A Second Outburst of the X-Ray Transient Seyfert 1.9 Galaxy", *Astrophys. J. Lett.*, **803**, L28. [DOI], [ADS], [arXiv:1504.01389 [astro-ph.HE]]

Guillochon, J. and Ramirez-Ruiz, E., 2013, "Hydrodynamical Simulations to Determine the Feeding Rate of Black Holes by the Tidal Disruption of Stars: The Importance of the Impact Parameter and Stellar Structure", *Astrophys. J.*, **767**, 25. [DOI], [ADS], [arXiv:1206.2350 [astro-ph.HE]]

Guillochon, J., Manukian, H. and Ramirez-Ruiz, E., 2014, "PS1-10jh: The Disruption of a Main-sequence Star of Near-solar Composition", *Astrophys. J.*, **783**, 23. [DOI], [ADS], [arXiv:1304.6397 [astro-ph.HE]]

Gültekin, K., Richstone, D. O., Gebhardt, K., Lauer, T. R., Tremaine, S., Aller, M. C., Bender, R., Dressler, A., Faber, S. M., Filippenko, A. V., Green, R., Ho, L. C., Kormendy, J., Magorrian, J., Pinkney, J. and Siopis, C., 2009, "The M-σ and M-L Relations in Galactic Bulges, and Determinations of Their Intrinsic Scatter", *Astrophys. J.*, **698**, 198–221. [DOI], [ADS], [arXiv:0903.4897 [astro-ph.GA]]

Hadrava, P., Řezáč, R. and Østgaard, E., 2001, "Formation of eccentric disks around black holes", in *RAGtime 2/3: Workshops on Black Holes and Neutron Stars, Opava, Czech Republic*, (Eds.) Hledík, S., Stuchlík, Z., Silesian University at Opava. Silesian University at Opava. [ADS]

Häring, N. and Rix, H.-W., 2004, "On the Black Hole Mass-Bulge Mass Relation", *Astrophys. J. Lett.*, **604**, L89–L92. [DOI], [ADS], [astro-ph/0402376]

Hayasaki, K., Stone, N. and Loeb, A., 2013, "Finite, intense accretion bursts from tidal disruption of stars on bound orbits", *Mon. Not. Roy. Astron. Soc.*, **434**, 909–924. [DOI], [ADS], [arXiv:1210.1333 [astro-ph.HE]]

Ho, L. C., Greene, J. E., Filippenko, A. V. and Sargent, W. L. W., 2009, "A Search for "Dwarf" Seyfert Nuclei. VII. A Catalog of Central Stellar Velocity Dispersions of Nearby Galaxies", *Astrophys. J. Suppl.*, **183**, 1–16. [DOI], [ADS], [arXiv:0906.4105 [astro-ph.GA]]

Holoien, T. W.-S., Prieto, J. L., Bersier, D., Kochanek, C. S., Stanek, K. Z., Shappee, B. J., Grupe, D., Basu, U., Beacom, J. F., Brimacombe, J., Brown, J. S., Davis, A. B., Jencson, J., Pojmanski, G. and Szczygieł, D. M., 2014, "ASASSN-14ae: a tidal disruption event at 200 Mpc", *Mon. Not. Roy. Astron. Soc.*, **445**, 3263–3277. [DOI], [ADS], [arXiv:1405.1417]

Holoien, T. W.-S., Kochanek, C. S., Prieto, J. L., Grupe, D., Chen, P., Godoy-Rivera, D., Stanek, K. Z., Shappee, B. J., Dong, S., Brown, J. S., Basu, U., Beacom, J. F., Bersier, D., Brimacombe, J., Carlson, E. K., Falco, E., Johnston, E., Madore, B. F., Pojmanski, G. and Seibert, M., 2016a, "ASASSN-15oi: a

rapidly evolving, luminous tidal disruption event at 216 Mpc", *Mon. Not. Roy. Astron. Soc.*, **463**, 3813–3828. [DOI], [ADS], [arXiv:1602.01088 [astro-ph.HE]]

Holoien, T. W.-S., Kochanek, C. S., Prieto, J. L., Stanek, K. Z., Dong, S., Shappee, B. J., Grupe, D., Brown, J. S., Basu, U., Beacom, J. F., Bersier, D., Brimacombe, J., Danilet, A. B., Falco, E., Guo, Z., Jose, J., Herczeg, G. J., Long, F., Pojmanski, G., Simonian, G. V., Szczygieł, D. M., Thompson, T. A., Thorstensen, J. R., Wagner, R. M. and Woźniak, P. R., 2016b, "Six months of multiwavelength follow-up of the tidal disruption candidate ASASSN-14li and implied TDE rates from ASAS-SN", *Mon. Not. Roy. Astron. Soc.*, **455**, 2918–2935. [DOI], [ADS], [arXiv:1507.01598 [astro-ph.HE]]

Hopkins, P. F., Richards, G. T. and Hernquist, L., 2007, "An Observational Determination of the Bolometric Quasar Luminosity Function", *Astrophys. J.*, **654**, 731–753. [DOI], [ADS], [astro-ph/0605678]

Hung, T., Gezari, S., Blagorodnova, N., Roth, N., Cenko, S. B., Kulkarni, S. R., Horesh, A., Arcavi, I., McCully, C., Yan, L., Lunnan, R., Fremling, C., Cao, Y., Nugent, P. E. and Wozniak, P., 2017, "Revisiting Optical Tidal Disruption Events with iPTF16axa", *Astrophys. J.*, **842**, 29. [DOI], [ADS], [arXiv:1703.01299 [astro-ph.HE]]

Jaroszynski, M., Abramowicz, M. A. and Paczynski, B., 1980, "Supercritical accretion disks around black holes", *Acta Astronomica*, **30**, 1–34. [ADS]

Kaiser, N., Aussel, H., Burke, B. E., Boesgaard, H., Chambers, K., Chun, M. R., Heasley, J. N., Hodapp, K.-W., Hunt, B., Jedicke, R., Jewitt, D., Kudritzki, R., Luppino, G. A., Maberry, M., Magnier, E., Monet, D. G., Onaka, P. M., Pickles, A. J., Rhoads, P. H. H., Simon, T., Szalay, A., Szapudi, I., Tholen, D. J., Tonry, J. L., Waterson, M. and Wick, J., 2002, "Pan-STARRS: A Large Synoptic Survey Telescope Array", in *Survey and Other Telescope Technologies and Discoveries*, (Eds.) Tyson, J. A., Wolff, S., Society of Photo-Optical Instrumentation Engineers (SPIE) Conference Series, 4836, [DOI], [ADS]

Kauffmann, G., Heckman, T. M., Tremonti, C., Brinchmann, J., Charlot, S., White, S. D. M., Ridgway, S. E., Brinkmann, J., Fukugita, M., Hall, P. B., Ivezić, Ž., Richards, G. T. and Schneider, D. P., 2003, "The host galaxies of active galactic nuclei", *Mon. Not. Roy. Astron. Soc.*, **346**, 1055–1077. [DOI], [ADS], [astro-ph/0304239]

Kesden, M., 2012, "Black-hole spin dependence in the light curves of tidal disruption events", *Physical Review D*, **86**(6), 064026. [DOI], [ADS], [arXiv:1207.6401 [astro-ph.CO]]

Kewley, L. J., Dopita, M. A., Sutherland, R. S., Heisler, C. A. and Trevena, J., 2001, "Theoretical Modeling of Starburst Galaxies", *Astrophys. J.*, **556**, 121–140. [DOI], [ADS], [astro-ph/0106324]

Kewley, L. J., Groves, B., Kauffmann, G. and Heckman, T., 2006, "The host galaxies and classification of active galactic nuclei", *Mon. Not. Roy. Astron. Soc.*, **372**, 961–976. [DOI], [ADS], [astro-ph/0605681]

Khabibullin, I., Sazonov, S. and Sunyaev, R., 2014, "SRG/eROSITA prospects for the detection of stellar tidal disruption flares", *Mon. Not. Roy. Astron. Soc.*, **437**, 327–337. [DOI], [ADS], [arXiv:1304.3376 [astro-ph.HE]]

Kiang, T., 1961, "The galaxian luminosity function", *Mon. Not. Roy. Astron. Soc.*, **122**, 263. [DOI], [ADS]

King, A. R., Pringle, J. E. and Livio, M., 2007, "Accretion disc viscosity: how big is alpha?", *Mon. Not. Roy. Astron. Soc.*, **376**, 1740–1746. [DOI], [ADS], [astro-ph/0701803]

Kippenhahn, R. and Weigert, A., 1994, *Stellar Structure and Evolution*, Springer-Verlag press, Berlin Heidelberg New York. [ADS]

Kochanek, C. S., 1994, "The aftermath of tidal disruption: The dynamics of thin gas streams", *Astrophys. J.*, **422**, 508–520. [DOI], [ADS]

Kochanek, C. S., 2016, "Tidal disruption event demographics", *Mon. Not. Roy. Astron. Soc.*, **461**, 371–384. [DOI], [ADS], [arXiv:1601.06787 [astro-ph.HE]]

Komossa, S. and Bade, N., 1999, "The giant X-ray outbursts in NGC 5905 and IC 3599:() hfill Follow-up observations and outburst scenarios", *Astron. Astrophys.*, **343**, 775–787. [ADS], [astro-ph/9901141]

Kormendy, J. and Ho, L., 2001, "Supermassive Black Holes in Inactive Galaxies", in *Encyclopedia of Astronomy and Astrophysics*, (Ed.) Murdin, P., Institute of Physics Publishing, Bristol. [DOI], [ADS]

Kormendy, J. and Richstone, D., 1995, "Inward Bound—The Search For Supermassive Black Holes In Galactic Nuclei", *Ann. Rev. Astron. Astrophys.*, **33**, 581. [DOI], [ADS]

Kroupa, P., 2001, "On the variation of the initial mass function", *Mon. Not. Roy. Astron. Soc.*, **322**, 231–246. [DOI], [ADS], [astro-ph/0009005]

La Franca, F., Fiore, F., Comastri, A., Perola, G. C., Sacchi, N., Brusa, M., Cocchia, F., Feruglio, C., Matt, G., Vignali, C., Carangelo, N., Ciliegi, P., Lamastra, A., Maiolino, R., Mignoli, M., Molendi, S. and Puccetti, S., 2005, "The HELLAS2XMM Survey. VII. The Hard X-Ray Luminosity Function of AGNs up to z = 4: More Absorbed AGNs at Low Luminosities and High Redshifts", *Astrophys. J.*, **635**, 864–879. [DOI], [ADS], [astro-ph/0509081]

Landau, L. D. and Lifshitz, E. M., 1959, *Fluid mechanics*, Oxford: Pergamon Press. [ADS]

Levan, A. J., Tanvir, N. R., Cenko, S. B., Perley, D. A., Wiersema, K., Bloom, J. S., Fruchter, A. S., Postigo, A. d. U., O'Brien, P. T., Butler, N., van der Horst, A. J., Leloudas, G., Morgan, A. N., Misra, K., Bower, G. C., Farihi, J., Tunnicliffe, R. L., Modjaz, M., Silverman, J. M., Hjorth, J., Thöne, C., Cucchiara, A., Cerón, J. M. C., Castro-Tirado, A. J., Arnold, J. A., Bremer, M., Brodie, J. P., Carroll, T., Cooper, M. C., Curran, P. A., Cutri, R. M., Ehle,

J., Forbes, D., Fynbo, J., Gorosabel, J., Graham, J., Hoffman, D. I., Guziy, S., Jakobsson, P., Kamble, A., Kerr, T., Kasliwal, M. M., Kouveliotou, C., Kocevski, D., Law, N. M., Nugent, P. E., Ofek, E. O., Poznanski, D., Quimby, R. M., Rol, E., Romanowsky, A. J., Sánchez-Ramírez, R., Schulze, S., Singh, N., van Spaandonk, L., Starling, R. L. C., Strom, R. G., Tello, J. C., Vaduvescu, O., Wheatley, P. J., Wijers, R. A. M. J., Winters, J. M. and Xu, D., 2011, "An Extremely Luminous Panchromatic Outburst from the Nucleus of a Distant Galaxy", *Science*, **333**, 199. [DOI], [ADS], [arXiv:1104.3356 [astro-ph.HE]]

Li, L.-X., Narayan, R. and Menou, K., 2002, "The Giant X-Ray Flare of NGC 5905: Tidal Disruption of a Star, a Brown Dwarf, or a Planet?", *Astrophys. J.*, **576**, 753–761. [DOI], [ADS], [astro-ph/0203191]

Lightman, A. P. and Shapiro, S. L., 1977, "The distribution and consumption rate of stars around a massive, collapsed object", *Astrophys. J.*, **211**, 244–262. [DOI], [ADS]

Lin, D., Maksym, P. W., Irwin, J. A., Komossa, S., Webb, N. A., Godet, O., Barret, D., Grupe, D. and Gwyn, S. D. J., 2015, "An Ultrasoft X-Ray Flare from 3XMM J152130.7+074916: A Tidal Disruption Event Candidate", *Astrophys. J.*, **811**, 43. [DOI], [ADS], [arXiv:1509.00840 [astro-ph.HE]]

Lin, D. N. C. and Pringle, J. E., 1987, "A viscosity prescription for a self-gravitating accretion disc", *Mon. Not. Roy. Astron. Soc.*, **225**, 607–613. [DOI], [ADS]

Lin, H., Kirshner, R. P., Shectman, S. A., Landy, S. D., Oemler, A., Tucker, D. L. and Schechter, P. L., 1996, "The Luminosity Function of Galaxies in the Las Campanas Redshift Survey", *Astrophys. J.*, **464**, 60. [DOI], [ADS], [astro-ph/9602064]

Lodato, G. and Rossi, E. M., 2011, "Multiband light curves of tidal disruption events", *Mon. Not. Roy. Astron. Soc.*, **410**, 359–367. [DOI], [ADS], [arXiv:1008.4589 [astro-ph.CO]]

Lodato, G., King, A. R. and Pringle, J. E., 2009, "Stellar disruption by a supermassive black hole: is the light curve really proportional to $t^{-5/3}$?", *Mon. Not. Roy. Astron. Soc.*, **392**, 332–340. [DOI], [ADS], [arXiv:0810.1288]

Loeb, A. and Laor, A., 1992, "Accretion flows near black holes mediated by radiative viscosity", *Astrophys. J.*, **384**, 115–128. [DOI], [ADS]

LSST Science Collaboration, Abell, P. A., Allison, J., Anderson, S. F., Andrew, J. R., Angel, J. R. P., Armus, L., Arnett, D., Asztalos, S. J., Axelrod, T. S. and et al., 2009, "LSST Science Book, Version 2.0", *ArXiv e-prints*. [ADS], [arXiv:0912.0201 [astro-ph.IM]]

Mageshwaran, T. and Mangalam, A., 2015, "Stellar and Gas Dynamical Model for Tidal Disruption Events in a Quiescent Galaxy", *Astrophys. J.*, **814**, 141. [DOI], [ADS], [arXiv:1510.07828]

Magnelli, B., Popesso, P., Berta, S., Pozzi, F., Elbaz, D., Lutz, D., Dickinson, M., Altieri, B., Andreani, P., Aussel, H., Béthermin, M., Bongiovanni, A., Cepa, J., Charmandaris, V., Chary, R.-R., Cimatti, A., Daddi, E., Förster Schreiber, N. M., Genzel, R., Gruppioni, C., Harwit, M., Hwang, H. S., Ivison, R. J., Magdis, G., Maiolino, R., Murphy, E., Nordon, R., Pannella, M., Pérez García, A., Poglitsch, A., Rosario, D., Sanchez-Portal, M., Santini, P., Scott, D., Sturm, E., Tacconi, L. J. and Valtchanov, I., 2013, "The deepest Herschel-PACS far-infrared survey: number counts and infrared luminosity functions from combined PEP/GOODS-H observations", *Astron. Astrophys.*, **553**, A132. [DOI], [ADS], [arXiv:1303.4436]

Magorrian, J. and Tremaine, S., 1999, "Rates of tidal disruption of stars by massive central black holes", *Mon. Not. Roy. Astron. Soc.*, **309**, 447–460. [DOI], [ADS], [astro-ph/9902032]

Magorrian, J., Tremaine, S., Richstone, D., Bender, R., Bower, G., Dressler, A., Faber, S. M., Gebhardt, K., Green, R., Grillmair, C., Kormendy, J. and Lauer,

T., 1998, "The Demography of Massive Dark Objects in Galaxy Centers", *Astron. J.*, **115**, 2285–2305. [DOI], [ADS], [astro-ph/9708072]

Maksym, W. P., Ulmer, M. P. and Eracleous, M., 2010, "A Tidal Disruption Flare in A1689 from an Archival X-ray Survey of Galaxy Clusters", *Astrophys. J.*, **722**, 1035–1050. [DOI], [ADS], [arXiv:1008.4140 [astro-ph.HE]]

Maksym, W. P., Ulmer, M. P., Eracleous, M. C., Guennou, L. and Ho, L. C., 2013, "A tidal flare candidate in Abell 1795", *Mon. Not. Roy. Astron. Soc.*, **435**, 1904–1927. [DOI], [ADS], [arXiv:1307.6556 [astro-ph.HE]]

Maloney, A. and Petrosian, V., 1999, "The Evolution and Luminosity Function of Quasars from Complete Optical Surveys", *Astrophys. J.*, **518**, 32–43. [DOI], [ADS], [astro-ph/9807166]

Mangalam, A., 2001, "Formation of a proto-quasar from accretion flows in a halo.", *Astron. Astrophys.*, **379**, 1138–1152. [DOI], [ADS], [astro-ph/0110591]

Mangalam, A., 2003, "Physics of Supermassive Disks: Formation and Collapse", *Bulletin of the Astronomical Society of India*, **31**, 207–213. [ADS], [astro-ph/0308227]

Marconi, A. and Hunt, L. K., 2003, "The Relation between Black Hole Mass, Bulge Mass, and Near-Infrared Luminosity", *Astrophys. J. Lett.*, **589**, L21–L24. [DOI], [ADS], [astro-ph/0304274]

Marzke, R. O., Huchra, J. P. and Geller, M. J., 1994, "The luminosity function of the CfA Redshift Survey", *Astrophys. J.*, **428**, 43–50. [DOI], [ADS]

McConnell, N. J. and Ma, C.-P., 2013, "Revisiting the Scaling Relations of Black Hole Masses and Host Galaxy Properties", *Astrophys. J.*, **764**, 184. [DOI], [ADS], [arXiv:1211.2816]

Medvedev, M. V. and Narayan, R., 2000, "Axisymmetric Self-similar Equilibria of Self-gravitating Isothermal Systems", *Astrophys. J.*, **541**, 579–586. [DOI], [ADS], [astro-ph/9910277]

Merloni, A., Predehl, P., Becker, W., Böhringer, H., Boller, T., Brunner, H., Brusa, M., Dennerl, K., Freyberg, M., Friedrich, P., Georgakakis, A., Haberl, F., Hasinger, G., Meidinger, N., Mohr, J., Nandra, K., Rau, A., Reiprich, T. H., Robrade, J., Salvato, M., Santangelo, A., Sasaki, M., Schwope, A., Wilms, J. and German eROSITA Consortium, t., 2012, "eROSITA Science Book: Mapping the Structure of the Energetic Universe", *ArXiv e-prints 1209.3114*. [ADS], [arXiv:1209.3114 [astro-ph.HE]]

Merritt, D., 1997, "Cusps and Triaxiality", *Astrophys. J.*, **486**, 102–109. [DOI], [ADS], [astro-ph/9701154]

Merritt, D., 2006, "Dynamics of galaxy cores and supermassive black holes", *Reports on Progress in Physics*, **69**, 2513–2579. [DOI], [ADS], [astro-ph/0605070]

Merritt, D., 2010, "The Distribution of Stars and Stellar Remnants at the Galactic Center", *Astrophys. J.*, **718**, 739–761. [DOI], [ADS], [arXiv:0909.1318]

Merritt, D., 2013a, "Loss-cone dynamics", *Classical and Quantum Gravity*, **30**(24), 244005. [DOI], [ADS], [arXiv:1307.3268 [astro-ph.GA]]

Merritt, D., 2013b, *Dynamics and Evolution of Galactic Nuclei*, Princeton University Press, Princeton. [ADS]

Merritt, D., 2015a, "Gravitational Encounters and the Evolution of Galactic Nuclei. I. Method", *Astrophys. J.*, **804**, 52. [DOI], [ADS]

Merritt, D., 2015b, "Gravitational Encounters and the Evolution of Galactic Nuclei. II. Classical and Resonant Relaxation", *Astrophys. J.*, **804**, 128. [DOI], [ADS], [arXiv:1506.03010]

Merritt, D. and Ferrarese, L., 2001, "Relationship of Black Holes to Bulges", in *The Central Kiloparsec of Starbursts and AGN: The La Palma Connection*, (Eds.) Knapen, J. H., Beckman, J. E., Shlosman, I., Mahoney, T. J., Astronomical Society of the Pacific Conference Series, 249, [ADS], [astro-ph/0107134]

Merritt, D. and Poon, M. Y., 2004, "Chaotic Loss Cones and Black Hole Fueling", *Astrophys. J.*, **606**, 788–798. [DOI], [ADS], [astro-ph/0302296]

Merritt, D. and Valluri, M., 1999, "Resonant Orbits in Triaxial Galaxies", *Astron. J.*, **118**, 1177–1189. [DOI], [ADS], [astro-ph/9903452]

Merritt, D. and Vasiliev, E., 2011, "Orbits Around Black Holes in Triaxial Nuclei", *Astrophys. J.*, **726**, 61. [DOI], [ADS], [arXiv:1005.0040]

Merritt, D. and Vasiliev, E., 2012, "Spin evolution of supermassive black holes and galactic nuclei", *Physical Review D*, **86**(10), 102002. [DOI], [ADS], [arXiv:1208.6274 [astro-ph.GA]]

Merritt, D., Alexander, T., Mikkola, S. and Will, C. M., 2011, "Stellar dynamics of extreme-mass-ratio inspirals", *Physical Review D*, **84**(4), 044024. [DOI], [ADS], [arXiv:1102.3180 [astro-ph.CO]]

Milosavljević, M., Merritt, D. and Ho, L. C., 2006, "Contribution of Stellar Tidal Disruptions to the X-Ray Luminosity Function of Active Galaxies", *Astrophys. J.*, **652**, 120–125. [DOI], [ADS], [astro-ph/0602289]

Misner, C. W., 1968, "The Isotropy of the Universe", *Astrophys. J.*, **151**, 431. [DOI], [ADS]

Mobasher, B., Sharples, R. M. and Ellis, R. S., 1993, "A Complete Galaxy Redshift Survey - Part Five - Infrared Luminosity Functions for Field Galaxies", *Mon. Not. Roy. Astron. Soc.*, **263**, 560. [DOI], [ADS]

Montero-Dorta, A. D. and Prada, F., 2009, "The SDSS DR6 luminosity functions of galaxies", *Mon. Not. Roy. Astron. Soc.*, **399**, 1106–1118. [DOI], [ADS], [arXiv:0806.4930]

Montesinos Armijo, M. and de Freitas Pacheco, J. A., 2011, "Tidal Disruption Flares: The Accretion Disk Phase", *Astrophys. J.*, **736**, 126. [DOI], [ADS], [arXiv:1105.2060 [astro-ph.HE]]

Muriel, H., Nicotra, M. A. and Lambas, D. G., 1995, "The Luminosity Function of Elliptical Galaxies", *Astron. J.*, **110**, 1032. [DOI], [ADS]

Narayan, R. and Yi, I., 1995, "Advection-dominated Accretion: Underfed Black Holes and Neutron Stars", *Astrophys. J.*, **452**, 710. [DOI], [ADS], [astro-ph/9411059]

Natarajan, P., 2011, "The mass assembly history of black holes in the Universe", *ArXiv e-prints*. [ADS], [arXiv:1105.4902]

Norberg, P., Cole, S., Baugh, C. M., Frenk, C. S., Baldry, I., Bland-Hawthorn, J., Bridges, T., Cannon, R., Colless, M., Collins, C., Couch, W., Cross, N. J. G., Dalton, G., De Propris, R., Driver, S. P., Efstathiou, G., Ellis, R. S., Glazebrook, K., Jackson, C., Lahav, O., Lewis, I., Lumsden, S., Maddox, S., Madgwick, D., Peacock, J. A., Peterson, B. A., Sutherland, W., Taylor, K. and 2DFGRS Team, 2002, "The 2dF Galaxy Redshift Survey: the b_J-band galaxy luminosity function and survey selection function", *Mon. Not. Roy. Astron. Soc.*, **336**, 907–931. [DOI], [ADS], [astro-ph/0111011]

Osterbrock, D. E., 1977, "Spectrophotometry of Seyfert 1 galaxies", *Astrophys. J.*, **215**, 733–745. [DOI], [ADS]

Paczyński, B. and Wiita, P. J., 1980, "Thick accretion disks and supercritical luminosities", *Astron. Astrophys.*, **88**, 23–31. [ADS]

Padovani, P., Alexander, D. M., Assef, R. J., De Marco, B., Giommi, P., Hickox, R. C., Richards, G. T., Smolčić, V., Hatziminaoglou, E., Mainieri, V. and Salvato, M., 2017, "Active galactic nuclei: what's in a name?", *Astron. Astrophys. Rev.*, **25**, 2. [DOI], [ADS], [arXiv:1707.07134]

Pasham, D. R., Cenko, S. B., Levan, A. J., Bower, G. C., Horesh, A., Brown, G. C., Dolan, S., Wiersema, K., Filippenko, A. V., Fruchter, A. S., Greiner, J., O'Brien, P. T., Page, K. L., Rau, A. and Tanvir, N. R., 2015, "A Multiwavelength Study of the Relativistic Tidal Disruption Candidate Swift J2058.4+0516 at Late Times", *Astrophys. J.*, **805**, 68. [DOI], [ADS], [arXiv:1502.01345 [astro-ph.HE]]

Peebles, P. J. E., 1968, "Significance of the First Brightest Galaxies in Rich Clusters", *Astrophys. J.*, **153**, 13. [DOI], [ADS]

Peebles, P. J. E., 1972, "Star Distribution Near a Collapsed Object", *Astrophys. J.*, **178**, 371–376. [DOI], [ADS]

Phinney, E. S., 1989, "Manifestations of a Massive Black Hole in the Galactic Center", in *The Center of the Galaxy*, (Ed.) Morris, M., IAU Symposium, 136, Kluwer Academic Publishers, Dordrecht. Kluwer Academic Publishers, Dordrecht. [ADS]

Planck Collaboration, Ade, P. A. R., Aghanim, N., Armitage-Caplan, C., Arnaud, M., Ashdown, M., Atrio-Barandela, F., Aumont, J., Aussel, H., Baccigalupi, C. and et al., 2013, "Planck 2013 results. XXIX. Planck catalogue of Sunyaev-Zeldovich sources", *ArXiv e-prints*. [ADS], [arXiv:1303.5089]

Planck Collaboration, Ade, P. A. R., Aghanim, N., Arnaud, M., Ashdown, M., Aumont, J., Baccigalupi, C., Banday, A. J., Barreiro, R. B., Bartlett, J. G. and et al., 2016, "Planck 2015 results. XIII. Cosmological parameters", *Astron. Astrophys.*, **594**, A13. [DOI], [ADS], [arXiv:1502.01589]

Press, W. H. and Schechter, P., 1974, "Formation of Galaxies and Clusters of Galaxies by Self-Similar Gravitational Condensation", *Astrophys. J.*, **187**, 425–438. [DOI], [ADS]

Pringle, J. E., 1981, "Accretion discs in astrophysics", *Ann. Rev. Astron. Astrophys.*, **19**, 137–162. [DOI], [ADS]

Raichur, H., Das, M., Herrero, A. A., Shastri, P. and Kantharia, N. G., 2015, "Late time X-ray, IR and radio observations of the tidal disruption event galaxy NGC 5905", *Astrophys. Space Sci.*, **357**, 32. [DOI], [ADS], [arXiv:1304.2235]

Ramirez-Ruiz, E. and Rosswog, S., 2009, "The Star Ingesting Luminosity of Intermediate-Mass Black Holes in Globular Clusters", *Astrophys. J. Lett.*, **697**, L77–L80. [DOI], [ADS], [arXiv:0808.3847]

Rees, M. J., 1988, "Tidal disruption of stars by black holes of 10 to the 6th-10 to the 8th solar masses in nearby galaxies", *Nature*, **333**, 523–528. [DOI], [ADS]

Richards, G. T., Myers, A. D., Gray, A. G., Riegel, R. N., Nichol, R. C., Brunner, R. J., Szalay, A. S., Schneider, D. P. and Anderson, S. F., 2009, "Efficient Photometric Selection of Quasars from the Sloan Digital Sky Survey. II. ˜1,000,000 Quasars from Data Release 6", *Astrophys. J. Suppl.*, **180**, 67–83. [DOI], [ADS], [arXiv:0809.3952]

Rodighiero, G., Vaccari, M., Franceschini, A., Tresse, L., Le Fevre, O., Le Brun, V., Mancini, C., Matute, I., Cimatti, A., Marchetti, L., Ilbert, O., Arnouts, S., Bolzonella, M., Zucca, E., Bardelli, S., Lonsdale, C. J., Shupe, D., Surace, J., Rowan-Robinson, M., Garilli, B., Zamorani, G., Pozzetti, L., Bondi, M., de la Torre, S., Vergani, D., Santini, P., Grazian, A. and Fontana, A., 2010, "Mid- and far-infrared luminosity functions and galaxy evolution from multiwavelength Spitzer observations up to z ˜ 2.5", *Astron. Astrophys.*, **515**, A8. [DOI], [ADS], [arXiv:0910.5649]

Rosenbluth, Marshall N., MacDonald, William M. and Judd, David L., 1957, "Fokker-Planck Equation for an Inverse-Square Force", *Phys. Rev.*, **107**, 1–6. [DOI]URL:
`http://link.aps.org/doi/10.1103/PhysRev.107.1`

Rybicki, G. B. and Lightman, A. P., 1986, *Radiative Processes in Astrophysics*, Wiley-VCH. [ADS]

Sambhus, N. and Sridhar, S., 2000, "Stellar Orbits in Triaxial Clusters around Black Holes in Galactic Nuclei", *Astrophys. J.*, **542**, 143–160. [DOI], [ADS], [astro-ph/0007355]

Saxton, R. D., Read, A. M., Esquej, P., Komossa, S., Dougherty, S., Rodriguez-Pascual, P. and Barrado, D., 2012, "A tidal disruption-like X-ray flare from the quiescent galaxy SDSS J120136.02+300305.5", *Astron. Astrophys.*, **541**, A106. [DOI], [ADS], [arXiv:1202.5900]

Saxton, R. D., Read, A. M., Komossa, S., Rodriguez-Pascual, P., Miniutti, G., Dobbie, P., Esquej, P., Colless, M. and Bannister, K. W., 2014, "An X-ray and UV flare from the galaxy XMMSL1 J061927.1-655311", *Astron. Astrophys.*, **572**, A1. [DOI], [ADS], [arXiv:1410.1500 [astro-ph.HE]]

Saxton, R. D., Read, A. M., Komossa, S., Lira, P., Alexander, K. D. and Wieringa, M. H., 2017, "XMMSL1 J074008.2-853927: a tidal disruption event with thermal and non-thermal components", *Astron. Astrophys.*, **598**, A29. [DOI], [ADS], [arXiv:1610.01788]

Schechter, P., 1976, "An analytic expression for the luminosity function for galaxies.", *Astrophys. J.*, **203**, 297–306. [DOI], [ADS]

Shakura, N. I. and Sunyaev, R. A., 1973, "Black holes in binary systems. Observational appearance.", *Astron. Astrophys.*, **24**, 337–355. [ADS]

Shankar, F., Weinberg, D. H. and Miralda-Escudé, J., 2009, "Self-Consistent Models of the AGN and Black Hole Populations: Duty Cycles, Accretion Rates, and the Mean Radiative Efficiency", *Astrophys. J.*, **690**, 20–41. [DOI], [ADS], [arXiv:0710.4488]

Shankar, F., Weinberg, D. H. and Miralda-Escudé, J., 2013, "Accretion-driven evolution of black holes: Eddington ratios, duty cycles and active galaxy fractions", *Mon. Not. Roy. Astron. Soc.*, **428**, 421–446. [DOI], [ADS], [arXiv:1111.3574]

Shapiro, S. L., Lightman, A. P. and Eardley, D. M., 1976, "A two-temperature accretion disk model for Cygnus X-1 - Structure and spectrum", *Astrophys. J.*, **204**, 187–199. [DOI], [ADS]

Shen, R.-F. and Matzner, C. D., 2014, "Evolution of Accretion Disks in Tidal Disruption Events", *Astrophys. J.*, **784**, 87. [DOI], [ADS], [arXiv:1305.5570 [astro-ph.HE]]

Shiokawa, H., Krolik, J. H., Cheng, R. M., Piran, T. and Noble, S. C., 2015, "General Relativistic Hydrodynamic Simulation of Accretion Flow from a Stellar

Tidal Disruption", *Astrophys. J.*, **804**, 85. [DOI], [ADS], [arXiv:1501.04365 [astro-ph.HE]]

Soltan, A., 1982, "Masses of quasars", *Mon. Not. Roy. Astron. Soc.*, **200**, 115–122. [ADS]

Spitzer, L., 1987, *Dynamical evolution of globular clusters*, Princeton University Press, Princeton, NJ. [ADS]

Stone, N. C. and Metzger, B. D., 2016, "Rates of stellar tidal disruption as probes of the supermassive black hole mass function", *Mon. Not. Roy. Astron. Soc.*, **455**, 859–883. [DOI], [ADS], [arXiv:1410.7772 [astro-ph.HE]]

Strubbe, L. E. and Quataert, E., 2009, "Optical flares from the tidal disruption of stars by massive black holes", *Mon. Not. Roy. Astron. Soc.*, **400**, 2070–2084. [DOI], [ADS], [arXiv:0905.3735 [astro-ph.CO]]

Syer, D. and Ulmer, A., 1999, "Tidal disruption rates of stars in observed galaxies", *Mon. Not. Roy. Astron. Soc.*, **306**, 35–42. [DOI], [ADS], [astro-ph/9812389]

Tadhunter, C., 2008, "An introduction to active galactic nuclei: Classification and unification", *New Astronomy Reviews*, **52**, 227–239. [DOI], [ADS]

Toomre, A., 1964, "On the gravitational stability of a disk of stars", *Astrophys. J.*, **139**, 1217–1238. [DOI], [ADS]

Tundo, E., Bernardi, M., Hyde, J. B., Sheth, R. K. and Pizzella, A., 2007, "On the Inconsistency between the Black Hole Mass Function Inferred from M-σ and M-L Correlations", *Astrophys. J.*, **663**, 53–60. [DOI], [ADS], [astro-ph/0609297]

Turner, E. L. and Gott, III, J. R., 1976, "Groups of Galaxies. II. The Luminosity Function", *Astrophys. J.*, **209**, 6–11. [DOI], [ADS]

Ueda, Y., Akiyama, M., Ohta, K. and Miyaji, T., 2003, "Cosmological Evolution of the Hard X-Ray Active Galactic Nucleus Luminosity Function and the Origin

of the Hard X-Ray Background", *Astrophys. J.*, **598**, 886–908. [DOI], [ADS], [astro-ph/0308140]

Ulmer, A., 1999, "Flares from the Tidal Disruption of Stars by Massive Black Holes", *Astrophys. J.*, **514**, 180–187. [DOI], [ADS]

Valluri, M. and Merritt, D., 1998, "Regular and Chaotic Dynamics of Triaxial Stellar Systems", *Astrophys. J.*, **506**, 686–711. [DOI], [ADS], [astro-ph/9801041]

van Velzen, S. and Farrar, G. R., 2014, "Measurement of the Rate of Stellar Tidal Disruption Flares", *Astrophys. J.*, **792**, 53. [DOI], [ADS], [arXiv:1407.6425]

van Velzen, S., Farrar, G. R., Gezari, S., Morrell, N., Zaritsky, D., Östman, L., Smith, M., Gelfand, J. and Drake, A. J., 2011, "Optical Discovery of Probable Stellar Tidal Disruption Flares", *Astrophys. J.*, **741**, 73. [DOI], [ADS], [arXiv:1009.1627 [astro-ph.CO]]

Vasiliev, E. and Merritt, D., 2013, "The Loss-cone Problem in Axisymmetric Nuclei", *Astrophys. J.*, **774**, 87. [DOI], [ADS], [arXiv:1301.3150 [astro-ph.GA]]

Vestergaard, M. and Osmer, P. S., 2009, "Mass Functions of the Active Black Holes in Distant Quasars from the Large Bright Quasar Survey, the Bright Quasar Survey, and the Color-selected Sample of the SDSS Fall Equatorial Stripe", *Astrophys. J.*, **699**, 800–816. [DOI], [ADS], [arXiv:0904.3348 [astro-ph.CO]]

Vestergaard, M., Fan, X., Tremonti, C. A., Osmer, P. S. and Richards, G. T., 2008, "Mass Functions of the Active Black Holes in Distant Quasars from the Sloan Digital Sky Survey Data Release 3", *Astrophys. J. Lett.*, **674**, L1. [DOI], [ADS], [arXiv:0801.0243]

Wang, J. and Merritt, D., 2004, "Revised Rates of Stellar Disruption in Galactic Nuclei", *Astrophys. J.*, **600**, 149–161. [DOI], [ADS], [astro-ph/0305493]

Weedman, D. W., Feldman, F. R., Balzano, V. A., Ramsey, L. W., Sramek, R. A. and Wuu, C.-C., 1981, "NGC 7714 - The prototype star-burst galactic nucleus", *Astrophys. J.*, **248**, 105–112. [DOI], [ADS]

Weinberg, S., 1971, "Entropy Generation and the Survival of Protogalaxies in an Expanding Universe", *Astrophys. J.*, **168**, 175. [DOI], [ADS]

Will, C. M., 2012, "Capture of non-relativistic particles in eccentric orbits by a Kerr black hole", *Classical and Quantum Gravity*, **29**(21), 217001. [DOI], [ADS], [arXiv:1208.3931 [astro-ph.GA]]

Willmer, C. N. A., Faber, S. M., Koo, D. C., Weiner, B. J., Newman, J. A., Coil, A. L., Connolly, A. J., Conroy, C., Cooper, M. C., Davis, M., Finkbeiner, D. P., Gerke, B. F., Guhathakurta, P., Harker, J., Kaiser, N., Kassin, S., Konidaris, N. P., Lin, L., Luppino, G., Madgwick, D. S., Noeske, K. G., Phillips, A. C. and Yan, R., 2006, "The Deep Evolutionary Exploratory Probe 2 Galaxy Redshift Survey: The Galaxy Luminosity Function to z˜1", *Astrophys. J.*, **647**, 853–873. [DOI], [ADS], [astro-ph/0506041]

Willott, C. J., Delfosse, X., Forveille, T., Delorme, P. and Gwyn, S. D. J., 2005, "First Results from the Canada-France High-z Quasar Survey: Constraints on the z = 6 Quasar Luminosity Function and the Quasar Contribution to Reionization", *Astrophys. J.*, **633**, 630–637. [DOI], [ADS], [astro-ph/0507183]

Wylezalek, D., Vernet, J., De Breuck, C., Stern, D., Brodwin, M., Galametz, A., Gonzalez, A. H., Jarvis, M., Hatch, N., Seymour, N. and Stanford, S. A., 2014, "The Galaxy Cluster Mid-infrared Luminosity Function at $1.3 < z < 3.2$", *Astrophys. J.*, **786**, 17. [DOI], [ADS], [arXiv:1403.2390]

Wyrzykowski, Ł., Zieliński, M., Kostrzewa-Rutkowska, Z., Hamanowicz, A., Jonker, P. G., Arcavi, I., Guillochon, J., Brown, P. J., Kozłowski, S., Udalski, A., Szymański, M. K., Soszyński, I., Poleski, R., Pietrukowicz, P., Skowron, J., Mróz, P., Ulaczyk, K., Pawlak, M., Rybicki, K. A., Greiner, J., Krühler, T., Bolmer, J., Smartt, S. J., Maguire, K. and Smith, K., 2017, "OGLE16aaa - a signature of a hungry supermassive black hole", *Mon. Not. Roy. Astron. Soc.*, **465**, L114–L118. [DOI], [ADS], [arXiv:1606.03125]

Yang, Y., Zabludoff, A. I., Zaritsky, D., Lauer, T. R. and Mihos, J. C., 2004, "E+A Galaxies and the Formation of Early-Type Galaxies at z˜0", *Astrophys. J.*, **607**, 258–273. [DOI], [ADS], [astro-ph/0402062]

Zauderer, B. A., Berger, E., Soderberg, A. M., Loeb, A., Narayan, R., Frail, D. A., Petitpas, G. R., Brunthaler, A., Chornock, R., Carpenter, J. M., Pooley, G. G., Mooley, K., Kulkarni, S. R., Margutti, R., Fox, D. B., Nakar, E., Patel, N. A., Volgenau, N. H., Culverhouse, T. L., Bietenholz, M. F., Rupen, M. P., Max-Moerbeck, W., Readhead, A. C. S., Richards, J., Shepherd, M., Storm, S. and Hull, C. L. H., 2011, "Birth of a relativistic outflow in the unusual γ-ray transient Swift J164449.3+573451", *Nature*, **476**, 425–428. [DOI], [ADS], [arXiv:1106.3568 [astro-ph.HE]]

Zauderer, B. A., Berger, E., Margutti, R., Pooley, G. G., Sari, R., Soderberg, A. M., Brunthaler, A. and Bietenholz, M. F., 2013, "Radio Monitoring of the Tidal Disruption Event Swift J164449.3+573451. II. The Relativistic Jet Shuts Off and a Transition to Forward Shock X-Ray/Radio Emission", *Astrophys. J.*, **767**, 152. [DOI], [ADS], [arXiv:1212.1173 [astro-ph.HE]]

Zucca, E., Ilbert, O., Bardelli, S., Tresse, L., Zamorani, G., Arnouts, S., Pozzetti, L., Bolzonella, M., McCracken, H. J., Bottini, D., Garilli, B., Le Brun, V., Le Fèvre, O., Maccagni, D., Picat, J. P., Scaramella, R., Scodeggio, M., Vettolani, G., Zanichelli, A., Adami, C., Arnaboldi, M., Cappi, A., Charlot, S., Ciliegi, P., Contini, T., Foucaud, S., Franzetti, P., Gavignaud, I., Guzzo, L., Iovino, A., Marano, B., Marinoni, C., Mazure, A., Meneux, B., Merighi, R., Paltani, S., Pellò, R., Pollo, A., Radovich, M., Bondi, M., Bongiorno, A., Busarello, G., Cucciati, O., Gregorini, L., Lamareille, F., Mathez, G., Mellier, Y., Merluzzi, P., Ripepi, V. and Rizzo, D., 2006, "The VIMOS VLT Deep Survey. Evolution of the luminosity functions by galaxy type up to z = 1.5 from first epoch data", *Astron. Astrophys.*, **455**, 879–890. [DOI], [ADS], [astro-ph/0506393]

Zwicky, F., 1957, *Morphological astronomy*, Springer: Berlin. [ADS]